POLITECNICO DI MILANO

PhD SCHOOL

PhD IN ENERGY AND NUCLEAR SCIENCE AND TECHNOLOGY

POLITECNICO
MILANO 1863

Density Functional Theory simulations as an effective tool to investigate optical, electronic and vibrational properties of sp and hybrid sp-sp^2 carbon-based materials

Supervisor: Prof. Carlo S. Casari
Co-supervisors: Dr. Alberto Milani, Dr. Daniele Fazzi

PhD thesis of:
Patrick Serafini

ACADEMIC YEAR 2021-2022

Contents

Abstract

sp and hybrid sp-sp^2 carbon based materials are gathering an increasing popularity, both for their peculiar properties and for the promising applications. In these materials, structural features affect the degree of π-electron conjugation resulting in different optical, electronic and vibrational properties. How topology, connectivity and system size are related with the final properties is fundamental to understand structure-property relationships and to tailor the properties by proper structure design. In this ground, my thesis work is focused on computational investigations, by means of state-of-the-art Density Functional Theory calculations, of peculiar carbon nanostructures characterized by sp and mixed sp-sp^2 hybridization. I started my activity with the study of optical, electronic and vibrational properties of sp-hybridized carbon atom wires (CAWs), through the study of their UV-Vis absorption and Raman/SERS spectroscopic responses, and how these properties are affected by extension and terminal groups. Following a bottom-up approach, I extended the analysis to molecular γ-graphdiyne molecular fragments consisting in hexagonal rings containing sp^2 hybridized carbon atoms, linked toghether by sp hybridized linear diacetylenic units. For these systems, electronic behaviour is explored, by evaluating the band gap, changing the type of fragment, the length and connection type of the sp units, the extension of the fragments themselves and other parameters. Also vibrational properties of these structures are investigated, revealing the possibility to find different classes of molecules, providing further interpretation useful for the characterization of novel systems. Following the same approach, much more extended systems as 1D γ-graphdiyne nanoribbons and the 2D γ-graphdiyne crystal are then investigated. Electronic and vibrational properties are analyzed in order to give a detailed characterization of grapdiyne nanoribbons and give an interpretation of their electronic properties with the aim to apply them as possible novel materials in nanoelectronics. The overall research activity was completed with the investigation of different and new forms of 2D graphdiyne-based crystals. Indeed, relative energies and band structures analyses are explored, depending on carbon sp/sp^2 ratio, and correlated to peculiar topological effects. Raman and IR spectra were also computed to find specific classes of molecules with peculiar vibrational response and to find marker bands able to uniquely characterize different graphdiyne crystals.

The aim of my thesis work is to find potential candidates among all the investigated sp and hybrid sp-sp^2 systems for different engineering fields, passing from energy conversion to nanoeletronic devices.

Introduction

In the recent 30 years nanostructured carbon-based materials have reached a great importance in the field of nanoscience and nanotechnology. Fullerene, graphene, nanotubes and other forms of carbon are some examples of this big interest towards these type of materials. The continous research towards other exotic forms of carbon makes the recent period "The era of carbon allotropes" [1]. Moreover, the absence of a real experimental sp allotrope, theoretically investigated and called carbyne, has stimulated different reasearch groups in the study of sp-carbon based materials [2]. These systems are considered as possible novel nanostructures with innovative and peculiar electronic properties. More recently, carbon atom wires (CAWs) started to be studied as possible novel materials in the field of molecular electronics [3]. These structures are studied both with experimental and theoretical/computational methods. From the experimental point of view, different techniques have been implemented to produce carbon atom wires [4] and, at the same time, different characterization techniques have been employed to determine their structural, vibrational and electronic properties. Parallel to experimental works, many computational investigations, focused on the prediction of the properties of sp-carbon chains, further revealed the interesting behaviour and the promising properties of these systems [3].

In this context, my thesis work is focused on theoretical investigations, by means of state-of-the-art Density Functional Theory calculations, of peculiar carbon nanostructures characterized by sp and mixed sp-sp^2 hybridization. The starting point of my activity were sp-hybridized carbon atom wires (CAWs), consisting in the simplest sp carbon-based molecular systems. The analysis concerns on the investigation of their optical, electronic and vibrational properties, through the study of their UV-Vis absorption and Raman/SERS spectroscopic responses, and how they depend on extension and terminal groups. The discussion was also supported by the comparison between theoretical and experimental data. Then, taking into consideration a different set of molecular carbon wires, limits of Density Functional Theory in describing electronic and structural properties of systems with marked multiconfigurational character were analyzed. At the same time, a preliminary investigation of the properties relevant for electronic transport, made for the same set of molecules, was per-

formed in order to assess the potentiality of these molecules as active materials in organic electronic devices.

Then, following a bottom-up approach, I extended the analysis to molecular γ-graphdiyne fragments made by hexagonal rings containing sp^2 hybridized carbon atoms, linked toghether by linear diacetylenic units characterized by sp hybridization. The aim of this study is to give theoretical details on their electronic and vibrational properties, especially as a reference for chemical synthesis [5–10]. Indeed, I focused on the understanding of their electronic behaviour, by evaluating the band gap, changing the type of fragment, the length and connection type of the sp units, also through the analysis of a topological index, the extension of the fragments themselves and other parameters. The aim was to understand how these properties can be tuned, in a molecular design way, in order to synthetize different systems with desired properties. Moreover, studying the vibrational properties and in particular the Raman spectra of these structures, it is possible to find different classes of molecules and to provide a further interpretation useful for the characterization of novel systems properly designed and synthetized. Going on with the investigation of much more extended systems, I decided to focus my attention on the theoretical investigation of 1D γ-graphdiyne nanoribbons and the 2D γ-graphdiyne crystal. Also in this case, electronic and vibrational properties were analyzed. Band gap and Raman spectra of different type of nanoribbons were investigated as a function of their width and their edge-type. The aim of this study was to give a detailed characterization of grapdiyne nanoribbons and give an interpretation of their electronic properties in order to apply them as possible novel materials in nanoelectronics.

The overall research activity was completed with the investigation of different forms of 2D graphdiyne-based crystals. Indeed, with the support of an algorithm, we were able to systematically generate different systems having different structures and sp/sp^2 carbon ratios. The aim was to analyze how structural and topological effects can tune the relative stability and the electronic behavior, to propose a rationale for the development of new systems with tailored properties. To this aim, relative energies and band structures were analyzed, depending on carbon sp/sp^2 ratio, and correlated to peculiar topological effects. At the same time, Raman and IR spectra were also computed in order to find specific classes of molecules with peculiar vibrational response, but also to find marker bands able to uniquely characterize different graphdiyne crystals.

The first chapter of the thesis is dedicated to the description of what sp and hybrid sp-sp^2 materials are and what has been already reported in literature about them. Chapter two will describe the theoretical basis of the computational approaches that I have used for all the investigation described in the thesis. The following three chapters (3,4 and 5) are dedicated to the

description of the results. In particular, chapter 3 will discuss the analysis of electronic, vibrational and optical properties of Carbon Atom Wires (CAWs), while in chapters 4 and 5 γ-graphdiyne and graphdiyne-based materials will be analyzed in detail.

All the results of my PhD research activity, whose logical discussion follows a bottom-up approach, are characterized by the common objective of applying sp and hybrid sp-sp^2 systems in different engineering fields, passing from energy conversion to nanoeletronic devices, having a vision for an all carbon-based science and technology.

Chapter 1

Carbon Atom Wires (CAWs) and hybrid sp - sp^2 carbon-based materials

The last 30 years have seen carbon materials and nanostructures playing a relevant and increasing role in science and technology. The discovery of fullerenes, nanotubes, and conductive polymers and the advent of graphene are some examples of fundamental milestones. The existence of other exotic forms of carbon and the foreseen potential of developing novel systems make this period "The era of carbon allotropes", as proposed by A. Hirsch in 2010 [1]. Indeed, among carbon materials, the case of the "lacking allotrope" consisting of sp-hybridized carbon atoms found a significant interest in the past [2] and its importance is expected to increase progressively in the future, in view of recent theoretical predictions and achievements of new hybrid sp–sp^2 materials developed and investigated in the last 10 years [3]. In this context, I will give a brief introduction about sp and sp-sp^2 carbon-based nanomaterials in the current chapter.

1.1 Carbyne

The most shared definition describes carbyne as the one-dimensional infinite linear chain formed only by covalently bonded sp-carbon atoms. It is, thus, the true one dimensional atomic chain characterized by a diameter of only one atom. Its existence has been then questioned, due to the high reactivity of the chains and their tendency to crosslink to form sp^2 or sp^3 carbon. For this reason, the production of single sp-carbon chains long enough to be reliably considered as an infinite one is nowadays challenging. The longest chains (up to 6000 atoms) identified up to now have been recently detected inside double-wall carbon nanotubes [11]. The longest wire in isolated form has been

synthesized by Tykwinski and Chalifoux with lengths of more than 40 carbon atoms [12]. For small chains it can be shown that their behaviour is ruled by end-effects while for long chains, with more than 50 carbon atoms, Peierls distortion takes place and rules the chain behaviour [13]. There are two possible forms of carbyne that possess different electronic and vibrational properties. One structure consists of equivalent (equalized) double bonds. This is referred to as polycumulene (or simply cumulene) and it can be described as a 1-D crystal with a monoatomic unit cell. It will be characterized by a negligible bond length alternation ($BLA = r_1$-r_2, with r_1 and r_2 bond distances of the single and triple bonds respectively, Fig. 1.1). The other arrangement is characterized by a sequence of alternating triple and single bonds (polyyne) consisting in a 1-D crystal with a unit cell containing two carbon atoms. Due to this, the structure will be characterized by a certain non-negligible BLA. Due to the so-called Peierls distortion, occurring for an infinite chain, the only

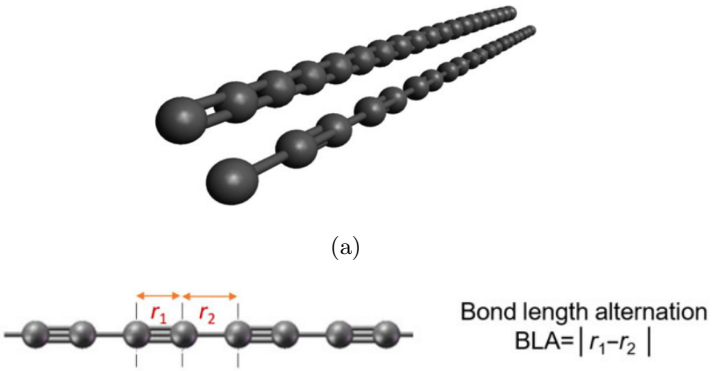

Figure 1.1: *(a) The structure of ideal carbyne with the two possible configurations: cumulene (top) and polyyne (bottom) and (b) the bond length alternation (BLA) as the parameter to describe the structure of a finite wire [3]*

stable form is the polyynic one. Theoretical predictions point towards exceptional properties making carbyne a promising champion material. Some of these outstanding properties are: very high effective surface (higher than 13000 m^2/g) [14], very high Young modulus (up to 32 TPa), specific stifness of about 10^9 Nm/kg (much higher than all the other materials, including carbon nanotubes, graphene and diamond) [15], extremely high values of thermal conductivity (80-200 kW/mK for cumulenes and polyynes at room temperature) attributed to high phonon frequencies and long phonon mean free path, allowing ballistic thermal transport up to the microscale [16]. Moreover, for what concerns electronic properties, cumulene is expected to be a metal since the conduction band is half filled (one carbon atom contributes to one elec-

tron for each of the two 2p orbitals). In polyynes, however, the double unit cell provides two electrons in each orbital and results in a half Brillouin zone. Hence, the valence band is completely filled by electrons while the conduction band, separated by the band gap opened at the edge of the Brillouin zone, is empty thus leading to a semiconductor [17](Fig. 1.2) with large electron mobilities and peculiar conductance behaviour, including ballistic transport even with spin polarization [18, 19]. Indeed, it is a peculiar electron conjuga-

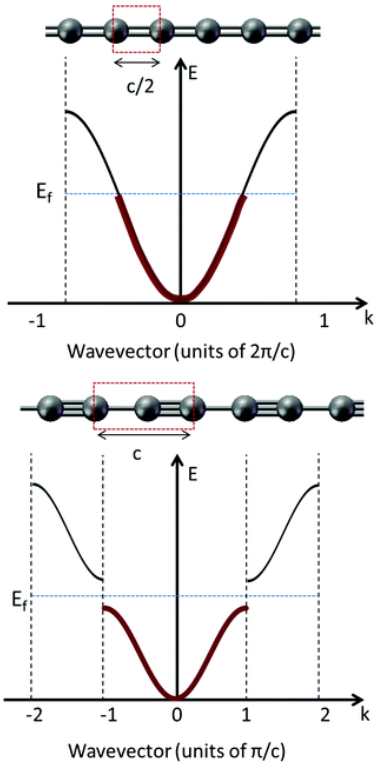

Figure 1.2: *Sketch of the two possible geometric arrangements of carbyne with the corresponding band structure according to a solid-state physics approach: an equalized double-bond structure (polycumulene, top), and alternate quasi simple–quasi triple bonds (polyyne, bottom). The band filling reveals the metal and semiconducting character of cumulene and polyyne, respectively.*

tion that makes carbyne such an interesting system. In fact, since the chain is formed by sp-carbon atoms with a high degree of π-electron delocalization, the electronic behavior strictly depends on the conjugation properties of these carbon atoms. Such behavior directly follows the case of many other poly-conjugated molecules (polyacetylene and oligoenes, polythiophenes, polycyclic aromatic molecules, etc.). Moreover, BLA significantly affects the electronic structure of the sp-carbon chain, driving the transition from a metallic to a semiconducting system, which also influences both the optical and vibrational properties. Due to the well-known electron–phonon coupling that exists in all

π-conjugated systems, it is reasonable to expect that changes in BLA might also significantly influence the vibrational properties of carbyne. Indeed, considering cumulene first, the description of its phonon dispersion is elementary and constitutes a classical textbook example for introducing the concept of phonons in a monoatomic infinite chain as a 1-D crystal [20]. Cumulene displays only acoustic phonon branches (one longitudinal acoustical, 1LA and 2TA, respectively), and the system would not present any optical activity. The polyyne case corresponds to a homo-atomic chain with different bond strengths so that the unit cell is composed by two atoms. As a result, there are three acoustic and three optical phonon branches (Fig. 1.3). In other words, upon moving from cumulene to polyyne the major effect is the appearance of optical phonon branches. The physical origin of this phenomenon is the electron–phonon coupling typical of these systems, even in the presence of π-electron delocalization

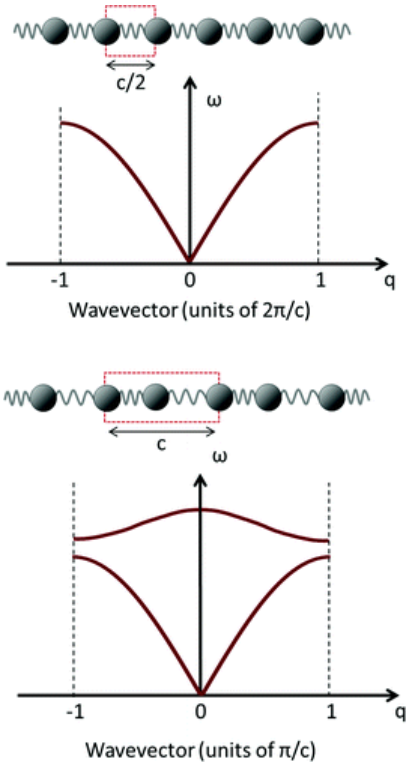

Figure 1.3: *Sketch of the phonon dispersion branches of a bond equalized (cumulene, top) and alternate (polyyne, bottom) infinite wire (i.e., carbyne as a 1-D crystal).*

1.2 CAWs: examples of carbyne-like systems

In the last 20 years more and more attention has been focused on sp carbon atom wires (CAWs). Hydrogen-capped polyynes are a particularly simple and interesting example of these systems for which both synthesis, made by Cataldo [21], but also theoretical investigations were done [17]. In the second case, the trend of the BLA as a function of the increasing length of the *sp*-chain were analyzed in details. What it is found is that BLA decreases for increasing length of the chains due to the increase of π-electron conjugation. This sctructural variation is followed by a lowering of the gap between the highest occupied and the lowest unoccupied molecular orbitals (HOMO-LUMO gap). Obviously it is impossible to reach the 0 gap case of cumulene structure because at some length Peierls distortion occurs but chemical strategies have been developed to this aim for short systems. Indeed for small molecules made by relatively short carbon chains, the predominant effect in inducing a cumulenic or polyynic structure along the chain is given by the end groups [22]. Indeed, moving from ideal (i.e., infinite chain) to real (i.e., finite length) structures, the endgroup effects play a leading role: for these wires the presence of end-group effects is essential [13] and the carbon chain structure is mainly determined by the chemical nature of the endgroups, as highlighted by the values of BLA and CC bond lengths reported in Fig. 1.4 for a few series of sp-carbon molecules [23]. In fact, in hydrogen endcapped wires, the CH single bonds require the presence of a triple bond on the adjacent CC linkage, so that a single bond is formed on the next CC and so on, thus inducing a polyyne-like structure. However, a vinylidene endgroup (i.e., $= CH_2$) induces CC double bonds at the terminal parts of the sp-chain, resulting in a more equalized cumulene-like structure. Hence, for the same number of C atoms in the sp-chain, the vinylidene endgroups result in a substantially smaller BLA with respect to hydrogen endgroups. Clearly,

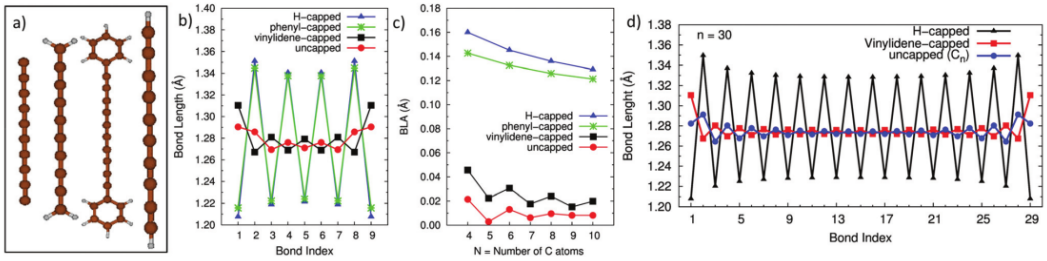

Figure 1.4: *(a) Structure of the considered wires (from left to right): uncapped, vinylidene-, phenyl- and H-endcapped; (b and c) bond length and bond length alternation (BLA) as a function of the number of carbon atoms for different types of wires. (d) Bond lengths in long wires (i.e., 30 carbon atoms) with different terminations. Data are from DFT calculations [24].*

this behaviour facilitates the design of new sp-carbon compounds with tun-

able properties by means of a proper choice of the end-groups and a synthetic approach. An example for this approach is represented by the recent work by Tykwinski et al. [25, 26], where long cumulene-like CAWs (up to 9 C=C bonds) have been obtained by rational chemical synthesis. Indeed, these *sp*-carbon chains have been terminated by an sp^2-carbon atom connected to two substituted phenyl groups, creating a chemical connection similar to that presented by ideal vinylidene-capped molecules. So, thanks to these end-groups, the *sp*-carbon chains are forced to display a cumulenic equalized geometry [25]. It should be noted that in finite-length wires, the cumulene-like geometry does not correspond to the ideal case with BLA = 0. Finite cumulenes are systems showing small BLA values, which are markedly different from those found in polyynes. Besides investigating the structural properties of cumulenes, pioneering studies revealed a diradicaloid character of the ground electronic state wavefunction for various cumulenic species. Such diradicaloid character was suggested to be very elusive, depending by the electronic coupling and the reciprocal orientations between the carbon chain and the end-capping groups. Hartzler [27], Diederich [28] and Tykwinski [29] were amongst the first to suggest possible resonance forms, encompassing diradicaloid and charge-separated (zwitterionic) structures, for carbon chains. Recently, Munz [30] reported a detailed computational contribution documenting the diradical character and excited-state aromaticity of differently end-capped cumulenes, as potential candidates for optical applications. The diradicaloid character was suggested to be the key for tuning the nonlinear optical properties of carbon chains, thus maximizing the quantum yield of processes such as two-photon absorption and singlet exciton fission [30–36].

Raman spectroscopy has emerged as one of the techniques of choice for unambiguous identification and investigation of sp-carbon. Differently from Raman of sp^2-carbon systems that have Raman fingerprint signals in $1300 - 1600$ cm^{-1} region, Raman signals that characterize sp-carbon chains are located at $1800 - 2300$ cm^{-1} , that is a spectral region completely uncovered by signals from other carbon systems. In Fig. 1.5, some examples of Raman spectra of some sp-carbon based systems are shown in comparison with sp^2-carbon. Graphite, amorphous carbon, CNTs, and fullerene have all first-order Raman features below 1600 cm^{-1}, while sp-rich carbon films, H-terminated polyynes, phenyl-terminated polyynes show bands in the 1800–2300 cm^{-1} range. In particular, Raman spectra of hydrogen end-capped polyynes show a similar pattern as polyenes, namely a very intense line that corresponds to the so called Effective Conjugation Coordinate (ECC) mode [37, 38], and this has also been named as "α-line" in the literature. Vibration associated to this line consists in the simultaneous stretching of the triple bonds coupled with the shrinking of the single ones. Size-selected polyynes show a peak position downshifting for increasing wire length, thanks to the strong electron-phonon coupling of

this system, allowing size detection according to the frequency position of the main peak.

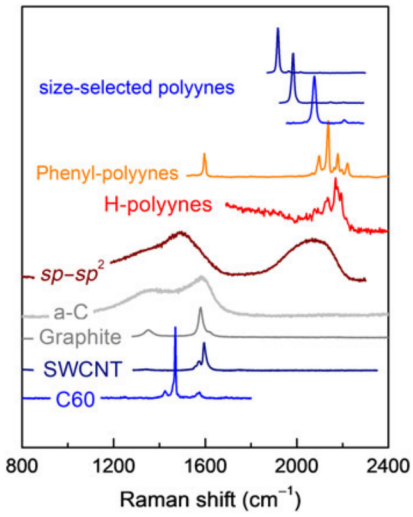

Figure 1.5: *Raman spectra of sp–sp^2 carbon and carbon atom wires (H-polyynes, diphenyl polyynes, and size-selected polyynes. The spectra of other sp^2 carbon systems (microcrystalline graphite and amorphous carbon (a–C) and nanostructures (fullerite C_{60} and single-wall carbon nanotube SWCNT) are shown for comparison.*

Today, many techniques can be found in the literature for the synthesis of sp-carbon systems. The different techniques are based on both physical and chemical strategies mainly in a bottom-up approach [4]. Techniques based on physical vapour deposition methods depend on the production of a carbon vapour or plasma that is rapidly quenched to induce clustering of carbon atoms under out-of-equilibrium conditions. The carbon vapour can be produced by arc discharge or laser ablation, and quenching can be accomplished by the use of inert gas molecules or liquids (see Fig. 1.6). An easy-to-use and cost-effective technique for the synthesis of polyynes in solution is the arc discharge in liquids developed by F. Cataldo [39]. This technique also allows one to control the chain termination by selecting suitable solvents. Chemical synthesis has been often used to synthesize systems in solution. Two approaches are often pursued. The first employs a polymerization strategy, as has been reviewed by Kudryavtsev [40, 41].These syntheses are based on, for example, dehydropolycondensation of acetylene, polycondenation reactions of halides, and dehydrohalogenation of polymers, e.g., chemical carbonization of poly(vinylidene halides). In these cases, the resulting sp-carbon wires can be efficiently formed in a single step, but the products are polydisperse due to the nature of the synthetic protocol. Furthermore, solution state characterization of the resulting product is often challenging. The second approach

targets molecules with a defined length and endgroup constitution, typically via the dimerization reaction of ethynyl groups (Glaser reaction) [42], with a defined length and specific endgroups, and the salient examples can be found in reviews by Szafert and Gladysz [43], Jevric and Nielsen [44], and Chalifoux and Tykwinski [12]. In these cases, a homologous series of molecules can be made and studied as a function of length, allowing the prediction of properties of carbyne, as well as molecules that are not yet synthetically assessable.

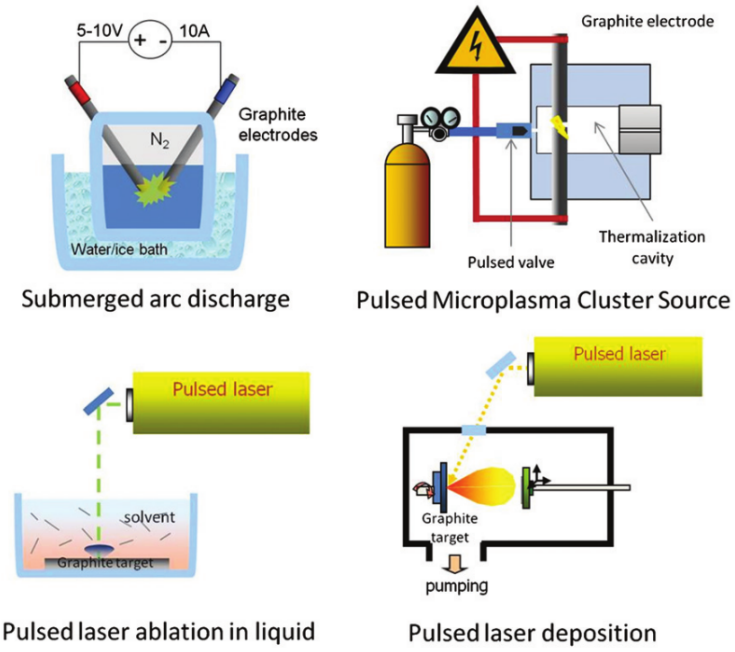

Figure 1.6: *Sketches representing several known physical methods adapted to synthesize linear sp-carbon wires [17].*

Polyynes are typically easier to produce than cumulenes probably due to higher stability, and nowadays polyynes up to 20 carbon atoms and more can be produced in solution even as size-selected samples [4, 38, 45]. Step-wise syntheses offer the possibility of different terminating groups [43]. On the other hand, cumulenes are more difficult to produce and there are far fewer reports on their synthesis and study in the literature. Short cumulenes can be synthesized in a similar way by controlling the termination-induced electronic arrangement. Such a strategy has been discussed in the review by Cadierno et al. [46], and the synthesis of cumulene wires has been reported by Cataldo [4] and more recently by Tykwinski and co-workers [25, 26], which describes cumulene wires up to 8 sp-carbon atoms produced by means of stepwise chemical synthesis. In all of these systems, the choice of terminal groups for the cumulene is fundamental for multiple reasons. For example, aromatic endgroups can strongly

couple with the sp-chain, which then propagates through the wire structure. On the other hand, bulky endgroups are necessary in order to prevent intermolecular interactions among wires, and thus avoiding cross-linking reactions and conversion into amorphous sp^2-carbon, as discussed also for polyynes.

1.3 Novel $sp - sp^2$ carbon-based materials

Carbon atom wires can be fundamental units also for more complex nanostructured and novel materials, characterized by peculiar and tunable properties. In particular we will focus on novel $sp-sp^2$ systems, such as graphyne, graphdiyne and related fragments reported in Fig. 1.7.

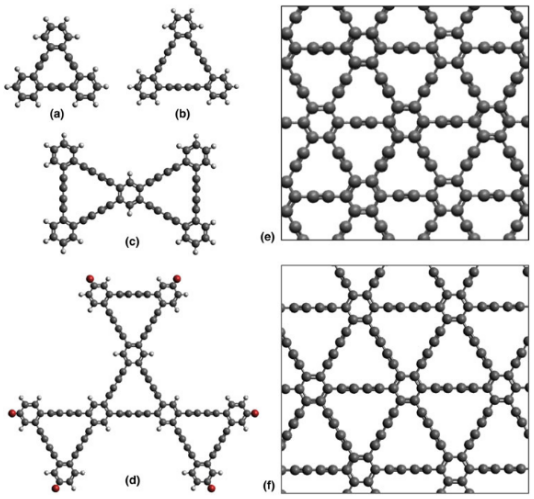

Figure 1.7: *Structures of $sp \rightarrow sp^2$ molecular fragments of graphyne (a) and graphdiyne of increasing size (b→d). In model (d), the red spheres represent bis-terbutyl substituted phenyl groups. The structure of extended 2D graphyne and graphdiyne is reported in (e) and (f), respectively. [3]*

1.3.1 Graphynes (GY) and Graphdiynes (GDY)

Generally speaking, graphynes (GY) and graphdiynes (GDY) are flat one-atom-thin carbon-based networks (like graphene), which can be constructed by replacing some =C=C= bonds in graphene by uniformly distributed acetylenic linkages -C≡C- (graphynes) or diacetylenic linkages -C≡C-C≡C- (graphdiynes). In both cases, the resulting networks include two non-equivalent types of carbon atoms: three-fold coordinated sp^2-hybridized atoms together with two-fold coordinated sp-hybridized atoms. In this context, these flat carbon networks can be viewed as "intermediate" (sp^2 + sp) systems between two well-known

carbon allotropes: graphene (comprises exclusively sp^2 -like atoms) and carbyne (comprises exclusively sp-like atoms [12]). As a result, such flat carbon (sp^2 and sp) networks with a high π-conjugation, uniformly distributed pores, density much smaller than for graphene and tunable electronic properties are considered now as possible promising materials for nanoelectronics, as membranes, for energy storage applications or as candidates for anode materials in batteries [47].

Such structures have been first outlined in 1987 by Baughman, Eckhardt and Kertesz [2]. One simple example is given by using the linear –C≡C– bonds to connect sp^2 carbon hexagons thus producing the so-called γ-graphyne or 6,6,6-graphyne. Another possibility is to construct a honeycomb structure formed by the linear bonds only, as a sp-carbon counterpart of graphene, called α-graphyne or 18,18,18-graphyne (Fig. 1.8). The nomenclature is based on three numbers indicating the number of carbon atoms in the smallest ring, in the next ring that is connected to the first one by a linear –C≡C– bond, and in the ring that is in the ortho-position with respect to the previous two rings, respectively. According to this, α-graphyne is 18,18,18-graphyne while γ-graphyne is 6,6,6-graphyne. The sp-carbon content can vary from 75% in α-graphyne, to 66.67% in 12,12,12-graphyne (β-graphyne), 55% for 6,6,12-graphyne, and down to 50% for 6,6,6-graphyne.

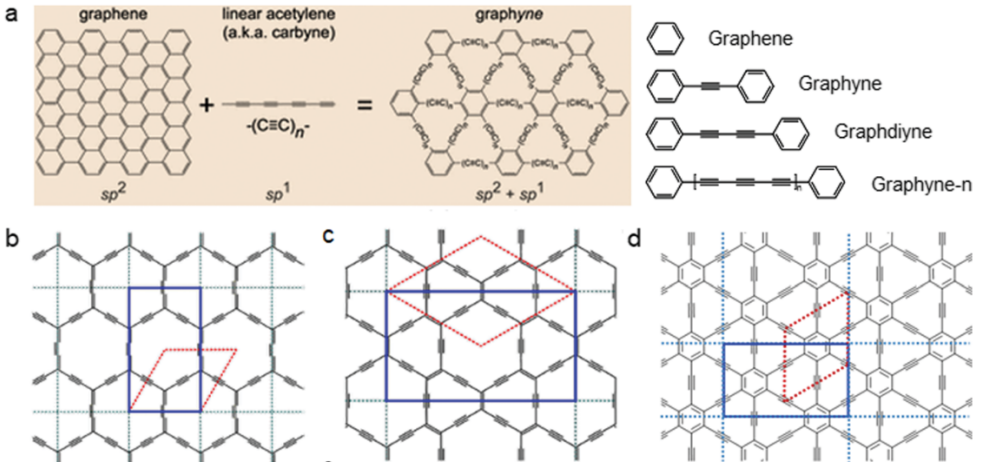

Figure 1.8: *Nomenclature and chemical structures of graphynes. (a) Schematic structures of graphene and graphynes. Graphynes are formed after replacing one-third of the graphitic carbon bonds of GR by an arbitrary number (n) of "–C≡C–" linkages. Structural diagram of different kinds of single-layer graphynes (b) α-graphyne; (c) β-graphyne; (d) γ-graphyne [48]*

On the other hand, in all of the described graphynes the sp^2 atoms are bonded by "single" -C≡C- linkages. Therefore, one more way of construction of graphyne-like networks is to increase the length of linear carbyne-like atomic chains between sp^2 atoms, i.e. to replace (-C≡C-) by (-C≡C-C≡C-) or

(-C≡C-C≡C-C≡C-) etc. chains, which connect either hexagons C_6, or pairs of sp^2 atoms, or individual sp^2 atoms. Historically, among the very rich variety of possible graphyne-like (sp and sp^2) networks, the family of so-called graphdiynes (GDY) is considered separately. Generally, these structures (Fig. 1.7, panel f) may be described as GY networks, where all acetylenic linkages are replaced by diacetylenic linkages -C≡C-C≡C-. Thus, the term "graphdiyne" comes from the term "graphyne", taking into account the aforementioned replacement of acetylenic by diacetylenic units [2]. Certainly, like for graphynes, a huge set of graphdiynes may be proposed.

Several strategies have been reported in literature for the production of finite GY- and GDY-based systems. On-surface synthesis is one of the most important production technique. Indeed, on-surface reaction process is a method to construct covalently bonded molecular structures on metal surfaces using designed precursors [49]. This process could appear both in STM systems under ultrahigh vacuum (UHV) conditions and in chemical vapor deposition (CVD) systems under a certain atmosphere. The former was regarded as an effective way to produce and in situ observe GDY-based substructures, which could facilitate the monitoring of the coupling process, intermediates, and byproducts in real time. Wei Xu et al. [50] designed specific precursors (7–9) with terminal alkynyl bromide, which could couple with each other on the Au(111) surface through the dehalogenative homocoupling reaction. Owing to the lower bonding energy of the C–Br bond than the C–H bond, this method could yield higher selectivity and fewer byproducts, thereby producing an ordered 2D porous network with acetylenic linkages. The second sinthetic approach that is worth to mention is based on a bottom-up approach by chemical synthesis that has been explored with different techniques in several studies [5–10, 51]. Indeed, Haley and co-workers reported the successful synthesis of various molecular fragments (see Fig. 1.9) using inter- and intra-molecular cyclization approaches based on Sonogashira cross-coupling reactions between precursors with alkynylated groups, thus obtaining acceptable overall yields and easy product isolation and purification. In the case of GY, molecular fragments made by aromatic rings connected with monoacetylenic units were also theoretically studied for the first time by Tahara and coworkers [52], aiming in understanding how topology, conncetivity and extension affects electronic and aromatic properties of deydrobenzoannulenes (DBAs) (see Fig. 1.7-a).

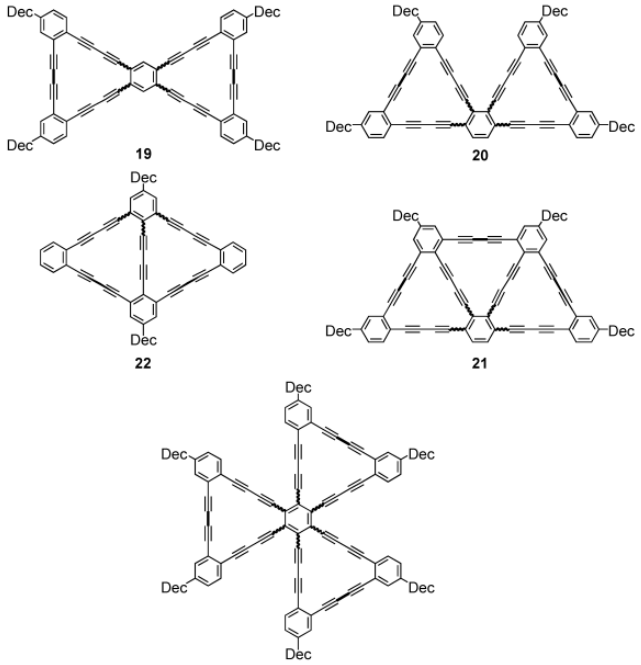

Figure 1.9: *Different GDY-based molecular fragments synthesized by the Haley group [10]*

For what concerns GY- and GDY- based crystals, the presence of acetylenic (diacetylenic) linkages (i.e. sp hybridized atoms) in 2D carbon networks decreases their stability in comparison with graphene and some other sp^2-like graphene allotropes. In turn, the relative stability of GYs and GDYs was probed in many works. So, as early as 1987, Baughman et al. [2] estimated the gas phase formation energies for a set of GYs within semi-empirical MNDO (modified neglect of diatomic overlap) calculations. The obtained values of formation energies (H_f) (in kcal/mol) for the considered graphynes (in Baughman's designation) increase in the following sequence: 14.9 (6,6,6) < 17.8 (6,6,12) < 19.3 (6,6,14) < 23.7 (14,14,1 4) = 23.7 (12,12,12) < 25.2 (14,14,18) < 26.3 (18,18,18). This means that with the growth of the number of sp atoms (or of acetylenic linkages -C≡C-) in GY-like networks, their stability will decrease. Estimations [53] of the energy within the DF-TB approach for series of sp^2- and sp-like 2D carbon networks allow us to conclude that their stability decreases when the ratio of sp/sp^2 atoms increases, or, in other words, when the relative number of C≡C bonds is increased (Fig. 1.10).

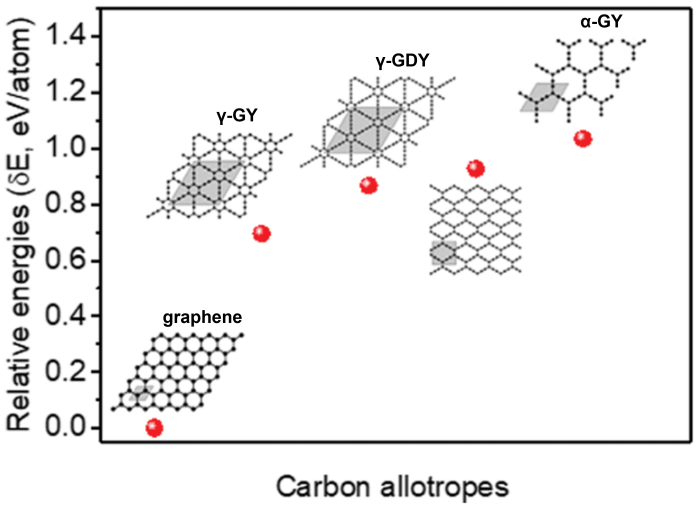

Figure 1.10: *Calculated energies for different graphynes with respect to graphene (E=0) [53].*

Graphynes and graphdiynes can be also constructed, through the use of different algorithms, as possible modification of graphene by interconnecting sp^2-carbon hexagons with linear sp-carbon chains of different lengths (a single or a double acetylenic bond for GY and GDY, respectively), generating new systems with peculiar and tunable electronic and optical properties. Moreover, starting from GY and GDY, many other ideal 2D hybrid sp-sp^2 carbon systems can be proposed by playing with geometry and topology, offering countless possibilities in the design and tailoring of carbon allotropes, both theoretically and experimentally [54]. These structures are also a part of a larger family of two-dimensional π-conjugated covalent organic frameworks (COFs), showing the occurrence of Dirac cones [55, 56], flat bands, and tunable bands gap (Fig. 1.11). Such phenomena observed in the electronic structure of COFs have been explained based on peculiar topological effects also in connection to their influence on the charge transport behavior [57, 58].

1.3.2 2D γ-GDY

As already mentioned above, graphdiyne is a one-atom-thin carbon network (like graphene), which can be constructed by replacing some =C=C= bonds in graphene with uniformly distributed diacetylenic linkages -C≡C-C≡C-. Among the different types of graphdiyne, we will focus our attention on the γ-graphdiyne whose structure is reported in Fig. 1.12. The C-C bonds in the hexagons and in diacetylenic linkages are not uniform, reflecting different bonding types for each pair of carbon atoms. This diversity leads to greater structural flexibility of GDYs as compared with graphene, thus enhancing the fracture strain accordingly. From the electronic point of view, γ-GDY is a semiconductor with

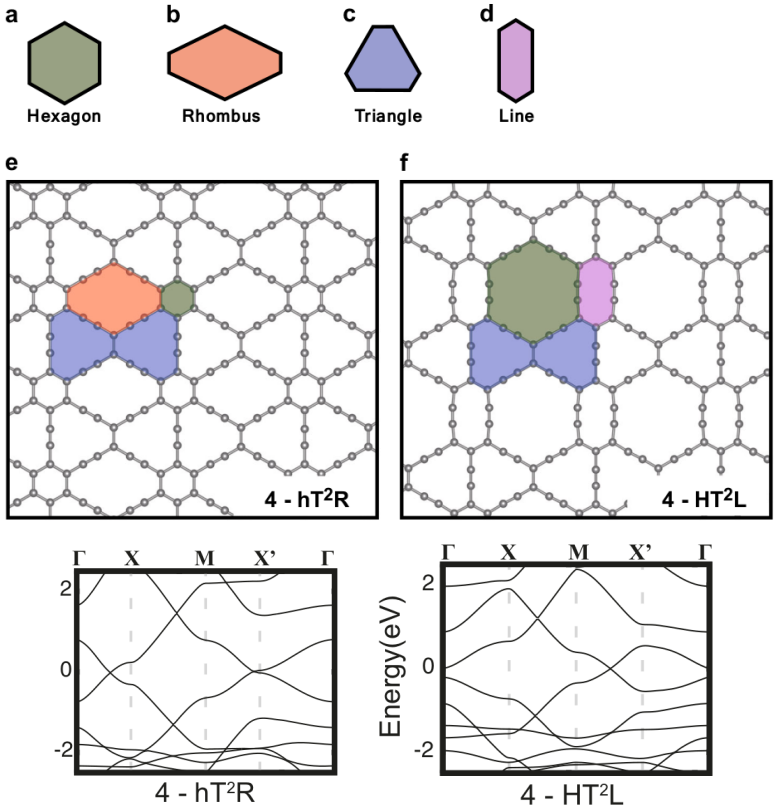

Figure 1.11: *The design for 2D sp–sp^2 hybrid carbon sheets. Building blocks for designing the layers:* ***a*** *hexagon,* ***b*** *triangle,* ***c*** *rhombus, and* ***d*** *line shapes where sp^2-bonded carbon atoms lie on the edge sites of the blocks and zero or even-numbered sp-bonded carbon atoms lie on the line.* ***e***, ***f*** *show examples for the designed 2D sp–sp^2 hybrid carbon atomic layers, together with their electronic band structures. The grey-colored spheres represent carbon atoms and the blocks of a unit cell are colored [54].*

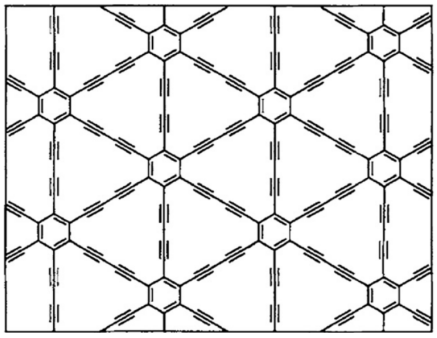

Figure 1.12: *Structure of γ-graphdiyne [47]*

direct band gap at Γ point of the Brillouin zone (wavevector k=0).

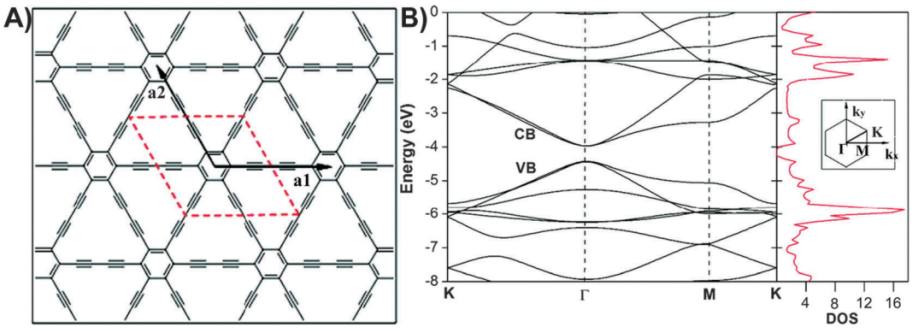

Figure 1.13: *Schematic representation of a single GDY sheet. Band structure and density of states for a single GDY sheet, obtained from DFT calculations. The Brillouin zone is also shown. [59]*

The band structure includes deep σ-type bands, whereas the low-energy $\pi(\pi^*)$ bands form the edges of the gap (Fig. 1.13). The reported band gaps usually go from 0.46 to 1.22 eV depending on the applied methods and the exchange-correlation functionals used [47]. In Table 1.1 some values of the band gap are reported. Moreover, the mobility is a key parameter that characterizes the electrical properties of semiconductor materials, and it also determines their applications in the field of electronics. As a novel semiconductor material, γ-GDY has an intrinsic electron mobility of 10^5 cm^2 V^{-1} s^{-1} at room temperature, and the hole mobility is one order of magnitude lower than the electron one.

γ-GDY has an hexagonal simmetry and belongs to the two-dimensional space-group *P6/mmm* (D_{6h}) in the Hermann-Maugin notation [60]. For the first-order Raman scattering, the process is limited to phonons at the Brillouin zone center Γ point respecting the law of momentum conservation. The calculated Raman spectra and atomic motions of vibrational modes of γ-GDY are

Table 1.1: *Lattice constant and band gap values of GDY taken from the literature and calculated with different methods and exchange-correlation functionals [47].*

	GDY
a (Å)	9.44^b ; 9.464^d ; 9.48^h ; 9.37^i
BG (eV)	0.53^b ; $0.52/1.18^d$; 1.22^e ; $044/1.10^g$; 0.46^h ; 0.53^i

b	FP-LCAO	*d*	VASP: GGA-PBE/Crystal06: B3LYP
e	hybrid exchange-correlation functional (HSE06)	*g*	ABINIT-YAMBO: LDA/GW
h	VASP-PAW: GGA/PBE	*i*	CASTEP: GGA/PBE

shown in Fig. 1.14 [61].

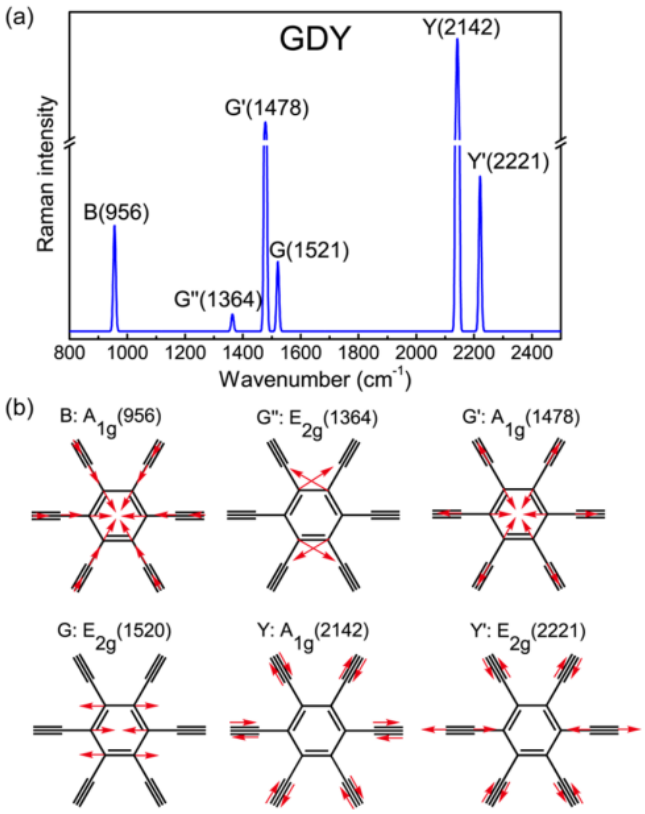

Figure 1.14: *Raman spectra and vibrational modes of GDY. (a) Raman spectrum (b) Atomic motions of intense Raman-active modes, in which the red arrows show the motion directions of the main contributors. [61]*

The γ-graphdiyne has six intense Raman peaks: the breathing vibration of the hexagonal benzene rings is B, the vibrations related to sp^2 carbon are G,G' and G" (similar to other carbon-based sp^2 materials), and the alkyne-related

modes are Y and Y'. The G peak comes from stretching of aromatic bonds as in graphene, but it is characterized by low intensity and wavenumber. The Y peak comes from the synchronous stretching/contracting of triple bonds, which is a fully symmetric mode. The G" peak is connected to the scissoring vibration of atoms in benzene ring. The G' peak comes from the vibrations of C-C bonds between triply coordinated atoms and theirs doubly coordinated neighbors (G' is even stronger than G). The Y' peak is another stretching mode of alkyne triple bonds, but the vibrations of different triple bonds are out-of-phase: one-third of triple bonds are stretching while the remaining two-thirds are shortening.

1.3.3 γ-GDY nanoribbons

As is well known, a finite graphene sheet has edges, which comprise atoms with different coordination numbers and dangling bonds. These structures, which are termed nanoribbons (NRs), exhibit properties different from the ideal infinite graphene sheet and have been widely investigated [62, 63]. It is not surprising that attention was paid also to similar structures: *sp*-sp^2 nanoribbons of GYs (GY-NRs) and GDYs (GDY-NRs). Ribbon width, edge morphology, edge functionalization and other parameters can be modified to tailor electronic, chemical, mechanical and magnetic properties. Generally two main types of the most symmetric variants of edge configurations of ribbons, designed by "cutting" through infinite GY and GDY networks, may be analyzed: zigzag and armchair [47] (Fig. 1.15).

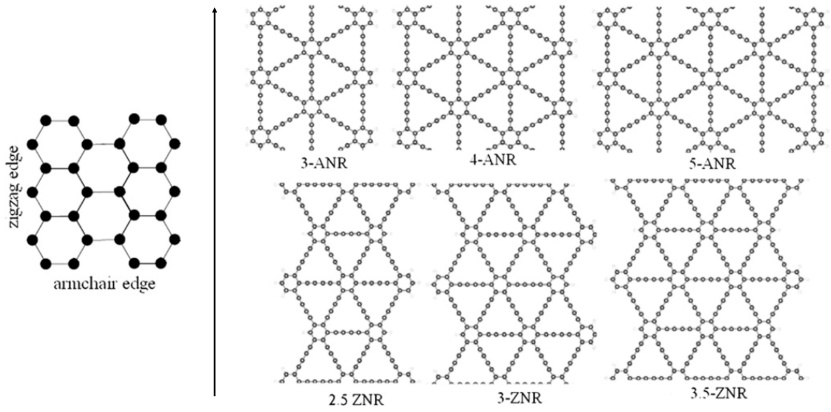

Figure 1.15: *The structures of armchair (ANR) and zigzag (ZNR) graphdiyne nanoribbons labeled according to the number of chains of C_6 hexagons. On the left: the configurations of zigzag and armchair edges for graphene ribbons are illustrated. The arrow inicates the periodic axis of the nanoribbons [47]*

Focusing on γ-GDY nanoribbons, a simple nomenclature of NRs was pro-

posed, where the index n indicates the number of repeated units ($-C_6 - C \equiv C - C \equiv C - C_6 - C \equiv C - C \equiv C - C_6$-) that can be counted along the width of the ribbon. Within this scheme, armchair nanoribbons (ANRs) are defined by only integers value of n, whereas for zigzag nanoribbons (ZNRs) the number of repeated units n can be also an half integer. Examples of such structures are shown in Fig. 1.15.

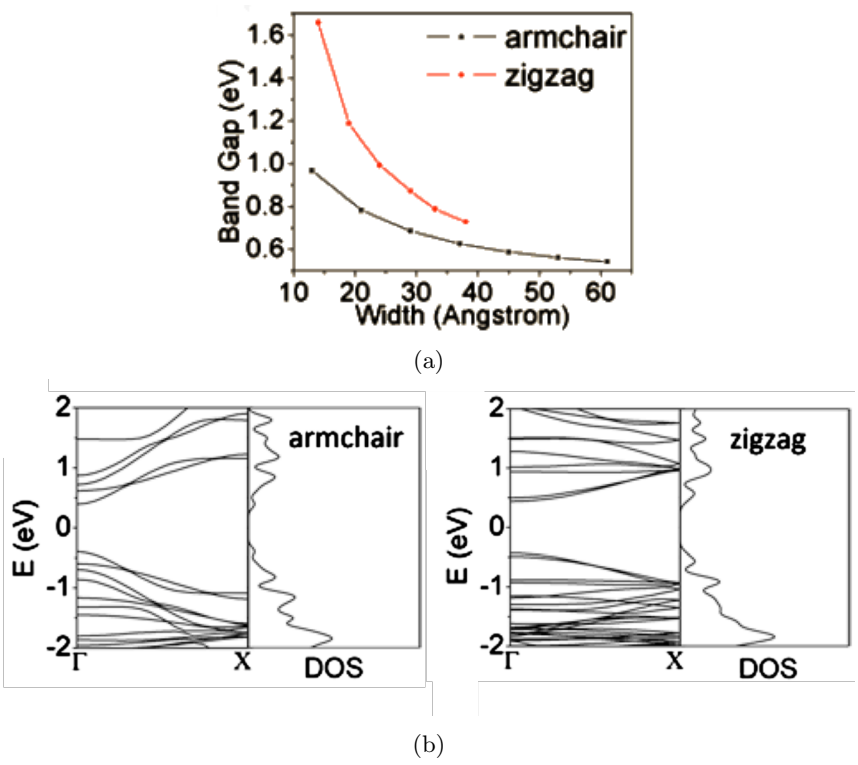

Figure 1.16: *Above: Trend in the band gap as a function of the nanoribbons' width for zigzag and armchair NRs [64]. Below: Band structures and density of states (DOS) for zigzag and armchair nanoribbons with n=3 are reported. LDA functional was used for the calculations [64]*

A lot of computational studies have been carried out to study electronic properties of these structures. ANRs and ZNRs with variable width were analyzed and it was found that all these ribbons are still semiconductors and their band gaps decrease as the ribbon width increases approaching, as expected, the limit of the 2D-GDY as reported in Fig. 1.16 [64, 65]. Analyzing the stability of NRs passivated by H atoms at the edges, it was found that they are more stable than the "parent" 2D networks; besides, stability of graphdiyne nanoribbons decreases as their widths increase. Moreover, the extimation of the Young's modules of GDY ribbons demonstrate that the elastic stiffness of graphdiyne NRs is much smaller than for graphene ribbons [65].

1.3.4 Possible applications of GDYs

For their peculiar structural, mechanical and electronic properties, studied in detail by several theoretical works, graphdiynes have a lot of possible applications as superb contenders for nanoscale semiconductors with adjustable gaps, as new materials with direction-dependent mechanical properties for possible nanomechanical applications, for electronic and opto-electronic devices, for hydrogen storage [47]. Sun et al have studied graphdiyne sheets decorated with lithium and the calculations show that these sheets can host a large amount of lithium, suggesting these materials to be designed as anodes for lithium batteries [66]. Another possible application of graphdiyne sheets could be their use as separation membranes for hydrogen purification from syngas, that usually contain undesired molecules like CH_4 and CO. Due to their thickness of one atom, they seem to be the most promising candidates because the efficiency of the membrane decreases with the increase of its thickness [67]. High carrier mobility, natural moderate bandgap, highly conjugated structure, and uniformly distributed pores facilitate the application of graphdiyne as an ideal candidate for photocatalysis and photoelectrocatalysis. Wang and Dan et al. synthesized a titania nano-particles (P25)/GDY hybrid composite by a hydrothermal method and reported its excellent photocatalytic performance [68]. Wu and Zhang et al. attempted to use GDY as the hole-transfer layer to fabricate quantum dots (QDs)-sensitized photocathodes for PEC water splitting [69]. In their work, 4-mercaptopyridine surface-functionalized CdSe QDs were synthesized and assembled on the surface of GDY nanowalls through π–π stacking, which was evidenced by the ultraviolet photoelectron spectroscopy and Raman spectroscopy. Water desalination through nanoporous membranes has been suggested as an energy-efficient method that could substitute commercial technologies, such as reverse osmosis. Buehler et al. demonstrated that a carbon "nanoweb" allowing both barrier-free permeation of water molecules and perfect rejection of salt ions would be an ideal candidate for water desalination [70]. A carbon nanoweb can be built from a monolayer of GY or GDY, robust and porous, with well defined atomic triangular pores. The search for new GDY-based materials and their applications is today still at its initial stage and will probably expand in future research in the vision of an all carbon-based science and technology.

Chapter 2

Theoretical Background

2.1 Quantum Chemistry Theory for Crystalline and Molecular Simulations

In this chapter the basic principles of quantum chemistry [71] and, in particular, of *Density Functional Theory* will be exposed [72–80]. After a brief treatment of correlated methods based on Hartree-Fock, DFT will be analyzed in detail.

2.1.1 Born-Oppenheimer approximation

Imagine to have a system of M nuclei and N electrons that can be described respectively by position vectors $\vec{R}_A$ and $\vec{r}_i$. We define $\vec{r}_{iA}$ the distance between the i electron and the nucleus A, $\vec{R}_{AB}$ the distance between nuclei A and B and $\vec{r}_{ij}$ the distance between the i and the j electron :

$$\vec{R}_{AB} = \vec{R}_A - \vec{R}_B \quad \vec{r}_{iA} = \vec{r}_i - \vec{r}_A \quad \vec{r}_{ij} = \vec{r}_i - \vec{r}_j \tag{2.1}$$

Now we can write the Hamiltonian associated to this system :

$$\hat{\mathcal{H}} = -\sum_{i=1}^{N} \frac{1}{2}\nabla_i^2 - \sum_{A=1}^{M} \frac{1}{2M_A}\nabla_A^2 - \sum_{i=1}^{n}\sum_{A=1}^{M} \frac{Z_A}{r_{iA}} + \sum_{i=1}^{N}\sum_{j>1}^{N} \frac{1}{r_{ij}} + \sum_{A=1}^{M}\sum_{B>A}^{M} \frac{Z_A Z_B}{R_{AB}} \tag{2.2}$$

where M_A represents the ratio between the mass of the A nucleus and the mass of the electron while Z_A is the A nucleus' atomic number. The first two terms are respectively the kinetic energies of electrons and nuclei in the system, the third term is the attraction term between electrons and nuclei while the other two remaining terms are the repulsive contributions between two electrons and two nuclei respectively. To deal with the physical problem of M nuclei interacting with N electrons we have to do a lot of approximations, due to its complexity. The first important semplification that we have to consider is the so called Born-Oppenheimer or adiabatic approximation. It is based on

the fact that nuclei are thousand of times heavier with respect to electrons, which means that their velocity will be very lower with respect to that of electrons. With this in mind, we can solve the elctronic problem of the system considering nuclei as frozen. In this way, the kinetic energy of the nuclei can be neglected (adiabatic term) and the nuclei-nuclei repulsion can be considered as a constant. So the electronic problem can be solved separately and will depend only parametrically on nuclei coordinates; the Hamiltonian of the system of N particles in a field of M nuclei can be written in the following way:

$$\hat{\mathcal{H}}_{elec} = -\sum_{i=1}^{N} \frac{1}{2}\nabla_i^2 - \sum_{i=1}^{N}\sum_{A=1}^{M} \frac{Z_A}{r_{iA}} + \sum_{i=1}^{N}\sum_{j>i}^{N} \frac{1}{r_{ij}} \tag{2.3}$$

Then, the stationary state Schrödinger equation for the electrons will become :

$$\hat{\mathcal{H}}_{elec}\Psi_{elec}(r_i; R_A) = \varepsilon_{elec}(R_A)\Psi_{elec}(r_i; R_A) \tag{2.4}$$

In which both wavefunction and eigenvalues depends parametrically on nuclear coordinates. The electronic problem is solved at first and then the nuclear problem can be considered. In this way we can take into account the effect of electrons on nuclei considering their mean field. Total energy for the nuclei can be written, adding the nuclear repulsion term, as:

$$\varepsilon_{tot} = \varepsilon_{elec} + \sum_{A=1}^{M}\sum_{B>A}^{M} \frac{Z_Z Z_B}{R_{AB}} \tag{2.5}$$

And, accordingly, the Hamiltonian for nuclei will be:

$$\hat{\mathcal{H}}_{nucl} = -\sum_{A=1}^{M} \frac{1}{2M_A}\nabla_A^2 + \varepsilon_{tot}(R_A) \tag{2.6}$$

This method allows to consider nuclei moving on the potential energy surface obtained from the solution of the electronic problem. In this context, the solution of the Schrödinger equation for nuclei will give information on vibrations of the system. The total wavefunction, under the Born-Oppenheimer approximation, will be the product between the electronic and the nuclear one:

$$\Psi_{tot}(r_i; R_A) = \Psi_{elec}(r_i; R_A)\Psi_{nucl}(R_A) \tag{2.7}$$

2.1.2 Hartree-Fock approximation

Taking a system constituted by N electrons, we can describe its wavefunction with a Slater determinant made by single particle wavefunctions:

$$\big|\Psi_0\big\rangle = |\psi_1\psi_2...\psi_a\psi_b...\psi_N\big\rangle \tag{2.8}$$

According to the variational principle, the "best" molecular orbitals are those which minimize the electronic energy:

$$E_0 = \langle \Psi_0 | \hat{\mathcal{H}} | \Psi_0 \rangle \tag{2.9}$$

We can systematically vary the orbitals mantaining as the only constrain the orthonormality between them until the energy E_0 results to be a minimum. With this procedure, it is possible to derive the equation for the optimized orbitals, the Hartree-Fock equation:

$$f(i)\psi = \varepsilon\psi \tag{2.10}$$

where f(i) is the Fock operator :

$$f(i) = -\frac{1}{2}\nabla_i^2 - \sum_{A=1}^{M} \frac{Z_A}{r_{iA}} + \nu^{HF}(i) \tag{2.11}$$

in which ν^{HF} is an effective one-electron potential operator, called the Hartree-Fock potential, which represents the mean potential felt by the i electron generated by all the other electrons. In this way the many-body problem is reduced to a one-body due to the fact that the electron-electron repulsion is treated as a mean effect. However, the Fock operator has a functional dependence on the solutions ψ_a of the pseudo-eigenvalue equation. Indeed, to solve this problem it is necessary to use an iterative procedure called SCF (*Self-Consistent-Field*). The procedure starts with the selection of the trial orbitals, and at first the equation is used to evaluate the mean field with these ones. Then, with the calculated mean field, the equation is solved to compute the new orbitals that will be used to evaluate the new mean field of the system. This procedure is repeated until it converges to a certain value of mean field, so when the potential found in the last step is equal to the next one and the orbitals used to build the Fock operator are equal to its wavefunctions. At this point it is said that the system reached the *self-consistency*. The Slater determinant written with the computed orbitals is the wavefunction of the fundamental state. The remaining orbitals are called virtual orbitals and are empty. So a finite basis set, as explained later, is used and the more it's extended, the lower is the energy evaluated. The Fock operator can be written as the sum of three terms; the first one is:

$$h(1) = -\frac{1}{2}\nabla_1^2 - \sum_A \frac{Z_A}{r_{1A}} \tag{2.12}$$

consisting in the sum between the kinetic and potential energy related to elctron-nucleus attraction. The other two are two-electron terms that constitute ν^{HF}. The first one is the *Coulomb* operator that represents the coulombic repulsion between electrons:

$$\hat{\mathcal{F}}_b(1) = \int dx_2 \psi_b(2)^2 r_{12}^{-1} \tag{2.13}$$

it represents the average local potential at x_1 arising from an electron in the ψ_b state. The second term, arising from the antisymmetric nature of the single determinant, is the *exchange* operator. It does not have a simple classical interpretation like the coulomb term. Its expression is defined for its effect on the orbital ψ_a:

$$\hat{\mathcal{K}}_b(1)\psi_a(1) = \left[\int dx_2 \psi_b^*(2) r_{12}^{-1} \psi_a(2)\right]\psi_b(1) \tag{2.14}$$

Finally the Hartree-Fock equation can be written in the following way:

$$\left[h(1) + \sum_{b\neq a} \hat{\mathcal{F}}_b(1) - \sum_{b\neq a} \hat{\mathcal{K}}_b(1)\right]\psi_a(1) = \varepsilon_a \psi_a(1) \tag{2.15}$$

and, in a more compact way, we can write also the Hartree-Fock operator as:

$$\nu^{HF}(1) = \sum_b \hat{\mathcal{F}}_b(1) - \hat{\mathcal{K}}_b(1) \tag{2.16}$$

so that the Fock operator becomes the sum of the core Hamiltonian and the Hartree-Fock operator previously defined:

$$f(1) = h(1) + \nu^{HF}(1) \tag{2.17}$$

2.1.3 Roothan-Hall equations

The Hartree-Fock equation cannot be implemented efficiently in numerical algorithms because reliable procedures to compute numerical solutions have not been yet found in order to solve the integro-differential equation. However, thanks to Roothan, it is possible to write it in a matrix form in order to be solved with numerical calculations. The idea to bypass the limitation was to write the wavefunctions, so the molecular orbitals, as a set of known functions. In this way the HF equation becomes an algebraic equation resolvable by matrix algebra. Therefore the molecular orbitals were expressed as a linear combination of atomic orbitals and these atomic orbitals are themselves approximated with gaussian contractions. Indeed, introducing a certain set of K known functions called basis set, we can write MO (molecular orbitals) as a linear expansion:

$$\psi_i = \sum_{\mu=1}^{K} C_{\mu i}\phi_\mu \quad i = 1, 2, ..., K \tag{2.18}$$

The accuracy of the approximation becomes higher the more you expand the set of atomic orbitals, so an exact expansion for an infinite basis set would be obtained. But for computational limitations a finite basis set must be used.

Now considering the closed-shell Hartree-Fock equation in which we have only the spatial dependence of the wavefunction:

$$f(r_1)\psi_j(r_1) = \varepsilon_j\psi_j(r_1) \tag{2.19}$$

and by left multiplying for $\phi^*_\mu(1)$ and integrating over $d\vec{r}_1$ the (1.28) after that we have substituted the linear expansion, we obtain a matrix expression of the equation. In fact, defining the overlap matrix:

$$S_{\mu\nu} = \int dr_1\phi^*_\mu(1)\phi_\nu(1) \tag{2.20}$$

and the Fock matrix:

$$F_{\mu\nu} = \int dr_1\phi^*_\mu f(1)\phi_\nu(1) \tag{2.21}$$

the matrix equation becomes:

$$\sum_\nu F_{\mu\nu}C_{\nu i} = \varepsilon_i \sum_\nu S_{\mu\nu}C_{\nu i} \quad i = 1, 2, ..., K \tag{2.22}$$

from which we can write the final expression of the Roothan-Hall equations:

$$\mathbf{FC} = \mathbf{SC}\varepsilon \tag{2.23}$$

$\mathbf{C}$ is the square $K \times K$ matrix of the expansion coefficients $C_{\mu i}$ while ε is the diagonal matrix composed by the orbitals' energies. $F_{\mu\nu}$ is the sum of two contributions, the first one:

$$H^{core}_{\mu\nu} = \int dr_1\phi^*_\mu(1)h(1)\psi_\nu(1) \tag{2.24}$$

is the core Hamiltonian, while the second, $G_{\mu\nu}$, is the two electron part of the Fock matrix and can be written in terms of matrix density $P_{\mu\nu}$:

$$P_{\mu\nu} = 2\sum_a^{\frac{N}{2}} C_{\mu a}C^*_{\nu a} \tag{2.25}$$

Using the following expression:

$$F_{\mu\nu} = H^{core}_{\mu\nu} + G_{\mu\nu} = H^{core}_{\mu\nu} + \sum_{\lambda\sigma} P_{\lambda\sigma}[(\mu\nu|\sigma\lambda) - \frac{1}{2}(\mu\lambda|\sigma\nu)] \tag{2.26}$$

The Fock matrix depends on the density matrix, and, consequently, on the expansion coefficients. This means that Roothan equations are nonlinear and, for this reason, an iterative procedure is needed to solve them. It is possible also to orthonormalize the equation loosing the dependence on the overlap matrix and make it a simple eigenvalue problem, obtaining the transformed Roothan equations:

$$\mathbf{F'C'} = \mathbf{C'}\varepsilon \tag{2.27}$$

From which we can evaluate C and then solve the above cited iterative procedure.

2.1.4 SCF procedure

The SCF is defined as the iterative procedure to solve the electronic problem using the matrix Roothan equations. It is characterized by the following passages:

1. Characteristics of the molecule: nuclear coordinates, atomic numbers, number of electrons, basis set.
2. Calculation of the integrals: $S_{\mu\nu}, H_{\mu\nu}^{core}, (\mu\nu|\lambda\sigma)$.
3. Diagonalization of the overlap matrix $S_{\mu\nu}$ and evaluation of the transformation matrix.
4. Guess of the density matrix **P**.
5. Computation of the **G** matrix from density matrix and double integrals $(\mu\nu|\lambda\sigma)$.
6. Addition of **G** to $H_{\mu\nu}^{core}$ to obtain the Fock matrix.
7. Calculation of the transformed Fock matrix **F'**.
8. Diagonalization of **F'** to obtain **C'** and ε
9. Evaluation of **C** from **C'**
10. Computation of a new matrix density from **C**
11. If the new matrix density is the same of the previous one, having defined a certain tolerance for the convergence, the problem is solved. If it is not, the procedure is repeated from the point 5 with the new density matrix.
12. If the procedure reaches convergence, **C**, **P** and **F** are used to obtain all the quantities of interest.

SCF procedure for crysalline systems can be also generalized for calculations made in Periodic Boundary Conditions (PBC). Indeed, using Bloch's functions as basis set, we can rewrite the Fock matrix in the following way:

$$F_{\mu\nu}(\vec{k}) = \sum_{\vec{T}_n} e^{i\vec{k}\vec{T}_n} F_{\mu\nu}(\vec{T}_n) \tag{2.28}$$

In which $F_{\mu\nu}(\vec{T}_n)$ are the matrix elements of the Fock operator between the μ_{th} AO located in the 0 cell and the ν_{th} AO located in the $\vec{T}_n$ cell. So the Roothan-Hall equation becomes:

$$\mathbf{F}(\vec{k})\mathbf{C}(\vec{k}) = \mathbf{S}(\vec{k})\mathbf{C}(\vec{k})\mathbf{E}(\vec{k}) \tag{2.29}$$

Theoretically the equation can be solved for an infinite set of k values within the first Brillouin zone. Practically it is done only for a narrow range of k values. The Fock operator in the reciprocal space is obtained as the Fourier transform of the Fock operator in the direct space as:

$$F_{\mu\nu}(k) = \sum_{m} e^{i\vec{k}\vec{m}} \left\langle \psi_{\mu}^{0} | \hat{F} | \psi_{\nu}^{\vec{m}} \right\rangle \tag{2.30}$$

where $\vec{m}$ is a direct lattice vector. Now using this expression of $F(\vec{k})$ and using the Roothan-Hall equations previously written we can solve the same problem using SCF procedure also for crystals.

2.1.5 Basis-set

As previously seen, in order to do the iterative procedure and solve the electronic problem related to molecules or crystals it is necessary to define a starting basis set made by atomic orbitals. A reliable expression for them is the Slater-type orbital (STO) function:

$$\phi_i(\zeta, n, l, m; \vec{r}, \theta, \phi) = N r^{n-1} e^{-\zeta \vec{r}} Y_{ln}(\theta, \phi) \tag{2.31}$$

In which n,l,m are quantum numbers, N is a normalization constant and ζ is the exponent of the STO. Due to the computational costliness of these type of orbitals, especially for the calculation of double integrals, Gaussian-type orbitals (GTO) are used to express the basis set in which the Slater functions are substituted with gaussian ones:

$$g(\alpha, l, m, n; x, y, z) = N e^{-\alpha x^2} x^l y^m z^n \tag{2.32}$$

Now n,l,m are not quantum numbers but simply exponents. These, which are positive numbers larger than zero, determine the diffuseness or "size" of the basis functions; a large exponent implies a small dense function, a small exponent implies a large diffuse function. Usually the single atomic orbital is expressed in terms of a linear combination of Gaussian functions called primitive functions g_p:

$$\psi_{\mu} = \sum_{p=1}^{L} d_{p\mu} g_p(\alpha_{p\mu}, \vec{r}) \tag{2.33}$$

Where both contraction coefficients, d_{pm}, and exponents are determined to best-fit the shape of the atomic orbitals and they remain fixed during the SCF process. The "*minimal*" basis set is the one in which the single ground-state orbital is described by a single contraction. A first evolution consists in the "*split-valence*" basis set in which a distinction between valence and core orbitals is introduced. The core ones are described by only one contraction,

while the valence orbitals are described by more than one contraction. Examples of these orbitals are the split-valence basis sets arising from the group of John Pople, typically expressed as X-YZg [81]. In this case, X represents the number of primitive Gaussians comprising each core atomic orbital basis function. The Y and Z indicate that the valence orbitals are composed of two basis functions each, the first one composed of a linear combination of Y primitive Gaussian functions, the other composed of a linear combination of Z primitive Gaussian functions. One example of this family is the widely used 6-31G in which we have 6 primitives to describe the core orbitals and two contractions, made respectively by 3 and 1 primitives, to describe the outer shell orbitals. Moreover it is possible to introduce polarization functions in which d orbitals on heavy atoms and p orbitals for hydrogen are added to the basis set and are indicated with * (6-31G* or 6-31G**) or as 6-31G(d,p). They are inserted as non-contracted gaussian's primitives and they unavoidably increase the computational cost. Anions, compounds with lone pairs, and hydrogen-bonded dimers have significant electron density at large distances from the nuclei. To improve the accuracy for such compounds, the 6-31+G* basis set is formed from the previously described 6-31G* set by the addition of four highly diffuse functions (1s, p_x , p_y, p_z) on each nonhydrogen atom. A highly diffuse function is one with a very small orbital exponent (typically, 0.01 to 0.1). The 6-31++G* set also include a highly diffuse s function on each hydrogen atom. Dunning and co-workers have developed the contracted gaussian type functions (CGTF) basis sets cc-pVDZ, cc-pVTZ, cc-pVQZ, cc-pV5Z, and cc-pV6Z (collectively denoted as cc-pVnZ, where n goes from 2 to 6), designed for use in calculation methods that include electron correlation [82]. Here, cc-pVDZ stands for correlation-consistent, polarized valence double-zeta. Unlike the Pople-type functions, where the number of d functions used varies from set to set, the cc family of functions always uses five d functions, seven f functions, etc... but they successively include larger shells of polarization.

Until now we have considered molecular problems, so single molecule calculations. In order to deal with crystals the concept of CO-LCAO (crystalline orbitals as a linear combination of atomic orbitals) must be introduced. As we have done for molecules, we can write crystalline orbitals as a linear combination of atomic orbitals:

$$\Psi_i = \sum_{\mu} C_{i\mu} \Phi_{\mu} \tag{2.34}$$

But in this case the translational invariance must be taken into account, so the atomic orbitals are written as Bloch's functions :

$$\Phi_{\mu}(\vec{r};\vec{k}) = \frac{1}{\sqrt{N}} \sum_{\vec{T}_n} e^{i\vec{k}\vec{T}_n} \psi_{\mu}^{\vec{T}_n}(\vec{r} - \vec{r}_{\mu}) \tag{2.35}$$

where $\psi_{\mu}^{\vec{T}_n}(\vec{r}-\vec{r}_{\mu})$ is the μ_{th} atomic orbital referred to cell 0 and having origin in

$\vec{r}_\mu$. These ψ_μ atomic obitals are built using gaussian contractions, as previously discussed. In other words, they constitute the basis set for the SCF procedure described in the previous section also for crystalline systems.

2.1.6 Correlation Energy

The four sources of error in ab initio molecular electronic calculations are

(1) Neglect/incomplete treatment of electron correlation

(2) Incompleteness of the basis set

(3) Relativistic effects

(4) Deviations from the Born–Oppenheimer approximation

Deviations from the Born–Oppenheimer approximation are usually negligible for ground-state molecules and relativistic effects will not be discussed in this thesis. In calculations on molecules without heavy atoms, (1) and (2) are the main sources of error. Almost all computational methods expand the MOs in a basis set of one-electron functions. For the problem to be solved basis set must have a finite number of members and hence is incomplete by definition. Molecular correlation energy is defined as the difference between the nonrelativistic true molecular energy and the restricted Hartree–Fock (HF) nonrelativistic energy calculated with a complete basis set: $E_{corr} = E_{nonrel} - E_{HF}$. The existence of a nonzero E_{corr} in HF theory can be ascribed to its failure to account for the instantaneous correlations between motions of electrons. This source of E_{corr} is called dynamic correlation. There is a second reason why E_{HF} may differ from E_{nonrel}: in some situations, the single-Slater-determinant HF wavefunction is a poor representation of the system's state, thereby making E_{HF} deviate very considerably from the true nonrelativistic E, and making E_{corr} substantial. This contribution to E_{corr} is called static correlation. To deal with static correlation, one replaces the single determinant used in the HF method with a linear combination of the configuration state functions (CSFs) that make substantial contributions to the wavefunction. This gives a multiconfiguration (MC) wave function.

2.1.7 Configuration Interaction

To overcome the deficiencies of the Hartree–Fock wave function (for example, improper behavior as internuclear distances go to infinity and very inaccurate dissociation energies), one can introduce configuration interaction (CI), thus going beyond the Hartree–Fock approximation. Using the set of occupied and virtual spin-orbitals found through classical HF calculations, one can form antisymmetric many-electron functions that have different orbital occupancies.

Each such many-electron function Φ_i is a Slater determinant or a linear combination of a few Slater determinants. Each Φ_i is called a configuration state function (CSF) or a configuration function. In this way, we can express the total wavefunction of a system as a linear combination of these configuration functions:

$$\Psi = \sum_i b_i \Phi_i \tag{2.36}$$

In summary, to do a CI calculation, we choose a one-electron basis set ψ_i, iteratively solve the Hartree–Fock equations to determine one-electron atomic (or molecular) orbitals ϕ_i as linear combinations of the basis set, form many-electron configuration functions Φ_i using the orbitals ϕ_i, express the wave function Ψ_i as a linear combination of these configuration functions. Then, solving the following equation:

$$det(H_{ij} - ES_{ij}) = 0 \tag{2.37}$$

for the energy, and solving the associated simultaneous linear equations for the coefficients b_i in (2.36) the problem is solved. The configuration functions in a CI calculation are classified as singly excited, doubly excited, triply excited, ... , according to whether 1, 2, 3, ... electrons are excited from occupied to unoccupied (virtual) orbitals.

2.1.8 Multiconfiguration SCF (MCSCF) method

Differently from simple CI calculation, in MCSCF method one writes the molecular wavefunction as a linear combination of CSFs Φ_i and varies not only the expansion coefficients b_i in $\Psi = \sum_i b_i \Phi_i$, but also the forms of the molecular orbitals in the CSFs. The molecular orbitals are varied by varying the expansion coefficients c_{ri} that relate the MOs ϕ_i to the basis functions ψ_r. The most commonly used kind of MCSCF method is the complete active space SCF (CASSCF or CAS) method. Here, as usual, one writes the molecular orbitals ϕ_i to be used in the CSFs as linear combinations of basis functions ψ_i. One divides the orbitals in the configuration state functions into inactive and active ones. The inactive orbitals are kept doubly occupied in all CSFs. The electrons not in the inactive orbitals are called active electrons. One writes the wavefunction as a linear combination of all CSFs Φ_i that can be formed by distributing the active electrons among the active orbitals in all possible ways and that have the same spin and symmetry eigenvalues as the state to be trated: $\Psi = \sum_i b_i \Phi_i$. One then does a MCSCF calculation to find the optimum coefficients c_{ri} and b_i. A reasonable choice is to take the active orbitals as those MOs that arise from the valence orbitals of the atoms that form the molecule. The notation CASSCF(n,m) denotes that n active electrons were distributed among m active molecular orbitals. The choice of active orbitals is often not obvious and, also, the SCF process in CASSCF sometimes converges

to a function that is not the true energy minimum. For these reasons, this technique cannot be used as a "black box", instead it requires chemical skills to avoid unrealiable results.

2.1.9 Principles of Density Functional Theory

The electronic wavefunction of an n-electron molecule depends on 3n spatial and n spin coordinates. Since the Hamiltonian operator contains only one- and two-electron spatial terms, one finds that the molecular energy can be written in terms of integrals involving only six spatial coordinates. In this context, the aim of Density Functional Theory (DFT), differently from the Hartree-Fock theory, is to shift the focus from the wavefunction to the electron density. If the wavefunction, in a generic system of N electrons, depends on 3N spatial coordinates the electron density will depend only on three variables (x,y and z); it's evident the convenience of a method based only on density. This theory consists in writing all the quantities of the fundamental state of a system as functionals of the electronic density $\rho(\vec{r})$. In particular, the energy of the ground state can be written as a functional of the density and it rapresents the minimum possible energy if the density is exact. It is an exact theory because, as will be seen, it contains an exchange-correlation potential that theoretically, if its exact expression would be known, would give an exact result. The negative aspect is that we have no information on how to build it, which results in the necessity of using some approximations.

Kohn-Sham method

The Hohenberg-Kohn theorems are considered as the cornerstone of the DFT theory, thanks to which it was possible to formulate a physico-mathematical theory based on electronic density. Here we reported the two theorems:

Th. 1 The external potential $\nu(\vec{r})$ is uniquely determined by the electronic density, apart from an additive constant.

Th. 2 Be $\tilde{\rho}(r)$ a non negative density normalized by N. So $E_0 < E_\nu[\tilde{\rho}]$ where $E_\nu[\tilde{\rho}]$ is the functional of the state which external potential is determined from an electronic density of the fundamental state $\tilde{\rho}$. The ground-state density can be evaluated using a variational method that involves only the density

Given the elctronic hamiltonian as:

$$\hat{\mathcal{H}}_{elec} = \hat{\mathcal{T}}_e + \hat{\mathcal{V}}_{ext} + \hat{\mathcal{U}}_{ee} \tag{2.38}$$

Using the above cited theorems, if it is true that the electronic density adapts itself to reach the minimal configuration due to the external potential, it is

also true the contrary. So the nuclear configuration is determined from the density. This enables to write the total energy of the system as a functional of the electronic density:

$$E[\rho] = T_e[\rho] + V_{ext}[\rho] + \frac{1}{2}\int\int \frac{\rho(\vec{r})\rho(\bar{r}')}{|\vec{r}-\bar{r}'|}d\vec{r}d\vec{r}' + E_{xc}[\rho] \tag{2.39}$$

In which U_{ee} is splitted in two terms. The first one is the classical energy repulsion term between electrons while the second is the exchange-corelation term in which non classical contributions are taken into account. The solution of the problem was given by the Kohn-Sham method that is based on substituting the real system with one formed by independent electrons, characterized by the same density of the real system. The kinetic energy term of interacting particles was substituted with a non interactive one. This system is taken with the same electronic density of the interacting system but the electrons are considered independent. The part of the kinetic energy that considers the electron-electron interaction is embedded in the exchange-correlation term. So total energy functional becomes:

$$E_{KS}[\rho] = T_0[\rho] + V_{ext}[\rho] + U_{cl}[\rho] + E_{xc}[\rho] \tag{2.40}$$

In the E_{xc} is contained the only one approximation of the density functional theory, because an exact exchange-correlation functional is unknown. Various type of approximations have been proposed but they cannot be used precisely for all the chemical systems. We can introduce the hamiltonian of the non-interactive system:

$$\hat{\mathcal{H}}_0 = \sum_{i=1}^{N}\Big(-\frac{\nabla_i^2}{2} + \nu_{eff}(\vec{r}_i)\Big) \tag{2.41}$$

In which the eigenstates can be expressed in the form of Slater determinant where fictitious Kohn-Sham orbitals are present ϕ_i^{KS} with electronic density $\rho(r) = \sum_{i=1}^{N}|\phi_i^{KS}(\vec{r})|^2$. Applying a variational method on E_{KS}, the following equation can be derived:

$$\nu_{eff}(r) = \nu(\vec{r}) + \int \frac{\rho(\bar{r}')}{|\vec{r}-\bar{r}'|}d\bar{r}' + \mu_{xc}[\rho(\vec{r})] \tag{2.42}$$

in which $\mu_{xc}[\rho(\vec{r})] = \frac{\delta E_{xc}[\rho(\vec{r})]}{\delta\rho(\vec{r})}$. So at the end we can write the Kohn-Sham selfconsistent equations:

$$\Big\{-\frac{\nabla^2}{2} + \nu_{eff}(\vec{r})\Big\}\phi_i(\vec{r}) = \varepsilon_i\phi_i(\vec{r}) \tag{2.43}$$

Indeed, the same iterative procedure that we have used in Hartree-Fock theory to solve this equation can be adopted here. So, once orbitals energies are

calculated, the total energy can be expressed in the following way:

$$E_{KS}[\rho] = \sum_{i}^{N} \varepsilon_i - \frac{1}{2} \int \int \frac{\rho(\vec{r})\rho(\bar{r}')}{|\rho(\vec{r}) - \rho(\bar{r}')|} d\vec{r} d\bar{r}' + \left\{ E_{xc}[\rho] - \int \rho(\vec{r}) \mu_{xc}[\rho] d\vec{r} \right\} \tag{2.44}$$

These equations can be cast in a form similar to HF equations, and, for this reason, they can be implemented in a calculation code. But, differently from the Hartree-Fock equations, in the KS ones the ν_{eff} takes into account both exchange and correlation. So, using a system of N non-interacting electrons but with the same electronic density of the interacting one allows to solve in an exact way the many body Schrödinger equations. For what concerns the KS orbitals we can say that their meaning is only related to the associated electronic density $\rho(\vec{r})$.

E_{xc} functionals

The exchange-correlation functional can be written as:

$$E_{xc}[\rho] = \frac{1}{2} \int \int \frac{\rho(\vec{r})\rho(\bar{r}')}{|\vec{r} - \bar{r}'|} [\tilde{g}(\vec{r}, \bar{r}') - 1] d\vec{r} d\bar{r}' \tag{2.45}$$

In which $\tilde{g}(\vec{r}, \bar{r}')$ is the two-body direct correlation function, called also pair correlation function, averaged depending on the force of the electronic contribution. Now defining the exchange-correlation hole $\tilde{\rho_{xc}}(\vec{r}, \bar{r}') = \rho(\bar{r}')[\tilde{g}(\vec{r}, \bar{r}') - 1]$, the following expression can be obtained:

$$E_{xc}[\rho] = \frac{1}{2} \int \int \frac{\rho(\vec{r})\tilde{\rho_{xc}}(\vec{r}, \bar{r}')}{|\vec{r} - \bar{r}'|} d\vec{r} d\bar{r}' \tag{2.46}$$

Written in this way, E_{xc} represents the interaction between the electronic charge distribution and the electronic charge distribution affected by the exchange-correlation effects. The simpler approximation that can be done on electronic density is the *Local Density Approximation* (LDA) in which a locally homogeneous system is considered, so the electronic density is approximated to the one of an homogeneous electron gas. In these terms the exchange-correlation functional becomes:

$$E_{xc}^{LDA}[\rho] = \int \rho(\vec{r}) \varepsilon_{xc}^{LDA}[\rho] d\vec{r} \tag{2.47}$$

In which $\varepsilon_{xc}^{LDA}[\rho] = \int \frac{\tilde{\rho}_{xc}^{LDA}(\vec{r}, \bar{r}')}{|\vec{r} - \bar{r}'|} d\vec{r}$ is the exchange-correlation energy. It is a very strong approximation, and should be limited to systems with slowly varying electronic distribution. Perdew demonstrated that since LDA is based on a real physical system, it works not so bad also with molecules [75]. Moreover, it is a real *first principle* approximation because it doesn't depend on any empirical parameter. We can re-formulate the same approximation considering

also the spin, obtaining the LSDA (Local Spin Density Approximation). An evolution of the LSDA approximation is the GEA(*Gradient Expansion Approximation*) that consists on a Taylor expansion of the E_{xc} functional. The GGA (*Generalized Gradient Approximation*) is a particular type of GEA in which the expansion is truncated at the first order:

$$E_{xc}[\rho] = \int f[\rho, \nabla\rho] d\vec{r} \tag{2.48}$$

The main strategy of this approach is to separate the term of exchange with that of correlation: $E_{xc}[\rho] = E_x[\rho] + E_c[\rho]$. The most important exchange functionals are B88, PW86 and PW91 while among the most important correlation functionals there are the LYP, PW86 and the PW91. It can be noticed that all these functionals, apart from the PW91, contain empirical parameters fitted on experimental data. So DFT cannot be defined a real *ab-initio* method, because the functional depends strongly on these empirical parameters.

PBE functional and hybrid methods

GGA functionals are not satisfying for what concern the exchange part. For this reason hybrid functionals, in which the exchange part is substituted by the exact HF exchange, were formulated and implemented. The method is based on the *Adiabatic Connection* formula :

$$E_{xc} = \int_0^1 E_{xc,\lambda} d\lambda \tag{2.49}$$

In this way the exchange-correlation functional is represented with only one expression that is a function of the coupling constant λ. If $\lambda = 1$ the system is considered completely correlated while for $\lambda = 0$ the correlation is 0. The functionals that are built in this way are called "hybrid". Several hybrid schemes have been proposed and the most widely used include three empirical parameter to rule the mixing of HF exchange and DF exchange and correlation:

$$E_{xc}^{ACM3} = E_{xc}^{LSD} + a_1\big(E_x^{HF} - E_x^{LSD}\big) + a_2 \Delta E_x^{GGA} + a_3 \Delta E_c^{GGA} \tag{2.50}$$

In this context, one of the most important three-parameters hybrid functional is the B3LYP one. Recently, Becke has suggested that just one coefficient is sufficient to rule the HF/DF exchange ratio according to:

$$E_{xc}^{ACM1} = E_{xc}^{GGA} + a_1\big(E_x^{HF} - E_x^{GGA}\big) \tag{2.51}$$

These methods (usually referred to as ACM1) are quite successful. Perdew and co-workers have next shown that the optimum value of a_1 coefficient can be adjusted *a priori* taking into account that fourth-order perturbation theory is

sufficient to get accurate numerical results for molecular systems. This leads to a family of adiabatic connection functionals thereafter referred to as ACM0 with the same number of adjustable parameters as their GGA's constituents:

$$E_{xc}^{ACM0} = E_{xc}^{GGA} + \frac{1}{4}\left(E_x^{HF} - E_x^{GGA}\right) \tag{2.52}$$

So using the PBE functional and HF exchange with predefined coefficients it is possible to exploit a parameter free density functional approach that is rapresented by the famous PBE0 hybrid functional. It is a very good functional which couples a good accuracy for molecular structures and properties along the whole periodic table to a direct connection to physical principles. It will be also one of the functional adopted for our computational calculations.

Range-separated hybrid functionals

If general hybrids (GHs) guarantee a systematic performance improvement with respect to semilocal density functionals and a successful modeling of a large number of ground- and excited-state properties, they still suffer from a density overdelocalization in the long-range (LR) regime. Instead of correctly behaving as $-r_{12}^{-1}$, $r_{12} = |r_2 - r_1|$ being the electron-electron distance, the asymptote of their exchange potential behaves instead as $-a_x r_{12}^{-1}$. This drawback leads systematically to an underestimation of the energy properties of molecular systems such as ionization potentials (IPs), intramolecular/intermolecular charge-transfer excitations, or the dissociation of open-shell complexes. Thanks to a concomitant wide implementation and an excellent performance improvement, the range-separated exchange (RSX) scheme remains among the most popular alternative to GHs. It consists in a physically sound solution to impose to the exchange potential a $-r_{12}^{-1}$ asymptotic behavior by splitting the Coulomb operator into a short-range and a long-range (SR and LR, respectively) term:

$$\frac{1}{r_{12}} = \frac{1 - [\alpha + \beta erf(\mu r_{12})]}{r_{12}} + \frac{\alpha + \beta erf(\mu r_{12})}{r_{12}} \tag{2.53}$$

The error function erf smoothly connects the SR to the LR part of the operator under the governance of a range-separation parameter μ, which is usually determined empirically. The resulting RSX exchange-correction hybrid energy is written as:

$$E_{xc,\mu}^{RSX-H} = E_{xc}^{GH} + (1 - a_x)E_{x,\mu}^{HF} - (1 - a_x)E_{x,\mu}^{GGA} \tag{2.54}$$

In which $\alpha = a_x$ and $\alpha + \beta = 1$. The parameter μ is homogeneous to the inverse of a distance, and it measures how fast the range separation switches from the SR to the LR regime. By using Eq. (1.54), numerous challenging applications were tackled in an accurate way. We especially mention some conceptually

simple systems particularly prone to one-electron self-interaction error (SIE) such as cationic rare gas dimers in their dissociation limit or more complex properties like bond-length alternations (BLAs) in conjugated chains and long through-space charge-transfer excitations.

2.1.10 Fractional Occupation Number Weighted Electron Density (ρ^{FOD})

Quantum chemical methods for electronic structure require the inclusion of electron correlation (EC, also called "many-body") effects when aiming at quantitative accuracy as we discussed in previous sections. Molecular systems with strong static electron correlation (SEC) are represented, for example, by covalent bond breaking, bi- or polyradicals, or certain classes of transition-metal complexes. They are usually characterized by small energy gaps between frontier orbitals and hence, appearance of many equally important determinants in electronic wavefunctions' composition, while systems dominated by dynamic EC exhibit a large HOMO–LUMO gap and are well described by a single Hartree–Fock (HF) or Kohn–Sham (KS) configuration. The accurate account of SEC is challenging in wave function theory (WFT) as well as density functional theory. For these reasons, Grimme et al. [83] introduced a simple, yet physically sound real-space measure of SEC based on fractional orbital occupation (FO), finite-temperature DFT (also called "Fermi-smearing" technique). Indeed, they proposed a real-space function ρ^{FOD} of position vector r termed fractional orbital density (FOD) given by:

$$\rho^{FOD}(r) = \sum_{i}^{N} (\delta_1 - \delta_2 f_i) |\phi_i(r)|^2 \tag{2.55}$$

where ϕ_i are the molecular orbitals, f_i are the associated fractional occupation numbers ($0 \leq f_i \leq 1$) and the sum is taken over all electronic single-particle levels in the system. They are obtained by solving self-consistently the KS-SCF equations which minimize the free-electronic energy G_{el} that is:

$$G_{el} = E_{el} - T_{el} S_{el} \tag{2.56}$$

With E_{el} being the SCF calculated energy S_{el} being the entropy, expressed through the following way:

$$S_{el} = k \sum_{i}^{N} f_i ln(f_i) + (1 - f_i) ln(1 - f_i) \tag{2.57}$$

At electronic temperature T_{el}. In Equation (2.55) the constants δ_1 and δ_2 are chosen to be unity if the level is lower than the Fermi energy E_F while they are

zero and -1, respectively, for levels higher than E_F. By this definition only the fractionally occupied (i.e., f_i different from zero or one, respectively) levels sum up, or in other words, the so defined FOD yields for each point in real space only the contribution of "hot" or strongly correlated electrons. Moreover, the integration of the fractional occupation density (ρ^{FOD}) over all space yields a single size-extensive number (named N_{FOD}) which can be used to globally quantify SEC.

2.2 IR absorption, Raman scattering and UV-Vis absorption for molecules and crystals

2.2.1 Classical theory of vibrations in polyatomic molecules

To deal with this problem we consider a system with many degrees of freedom within the harmonic approximation. The approach consists in introducing a certain coordinate system using which it is possible to reduce the many body quantum vibrational problems in terms of a set of independent one dimensional quantum oscillators. We can write the classical Hamiltonian associated to this problem:

$$H = T + V = \frac{1}{2}\sum_i m_i \dot{u}_i^2 + \frac{1}{2}\sum_{ij} u_i k_{ij} u_j \tag{2.58}$$

The kinetic energy term is a diagonal quadratic form, so it is expressed as a sum of independent terms. While the potential energy term in general couples all pairs of displacement through the $k_{ij} = \left(\frac{\partial^2 V}{\partial x_i \partial x_j}\right)_{x_i = x_i^0}$ coefficients. The aim is to find an equivalent formulation but in which the Hamiltonian becomes fully diagonal. The Hamiltonian can be written also in terms of matrices in the following way:

$$\mathbf{H} = \frac{1}{2}\dot{\xi}^t\dot{\xi} + \frac{1}{2}\dot{\xi}^t\mathbf{W}\dot{\xi} \tag{2.59}$$

where W is defined as :

$$\mathbf{W} = \mathbf{M}^{-1/2}\mathbf{K}\mathbf{M}^{-1/2} \tag{2.60}$$

and expresses the potential V as a quadratic form with respect to the set of mass-weighted coordinates ξ. $\mathbf{K}$ and $\mathbf{M}$ represent respectively the matrix made by the spring constants and the matrix associated to the masses of nuclei. Now considering the diagonal representation of $\mathbf{W}$:

$$\mathbf{W}\mathbf{L} = \mathbf{L}\Lambda \tag{2.61}$$

it is possible to rewrite the Hamiltonian as:

$$\mathbf{H} = \frac{1}{2}\dot{\xi}^t\mathbf{L}\mathbf{L}^t\dot{\xi} + \frac{1}{2}\dot{\xi}^t\mathbf{L}\Lambda\mathbf{L}^t\dot{\xi} \tag{2.62}$$

Introducing a new set of coordinates called *normal coordinates* $\bar{q} = \mathbf{L}^t\bar{\xi}$, it is possible to write the Hamiltonian as a diagonal form both for the kinetic and the potential energy:

$$\mathbf{H} = \frac{1}{2}\dot{\bar{q}}^t\dot{\bar{q}} + \frac{1}{2}\dot{\bar{q}}^t\mathbf{\Lambda}\dot{\bar{q}} \tag{2.63}$$

where eigenvalues Λ represent squares of angular frequencies ω_i^2. Writing the equations of motion for normal coordinates:

$$q_i(t) = q_i^0 sin(\omega_i t + \psi_i) \tag{2.64}$$

it is possible to write the displacements in terms of normal coordinates q:

$$\bar{u} = (\mathbf{M}^{-1/2}\mathbf{L})\bar{q} \tag{2.65}$$

Normal coordinates are fundamental for what concerns the relationship between chemical structure and specific vibration transitions. Solving the secular equation reported in (1.61) it is possible to derive vibrational eigenvectors and frequencies for a system composed by electrons and ions. To visualize the normal modes the idea is to represent the eigenvectors calculated solving the above mentioned equation as animations of the atoms' motion for a selected i-th normal mode.

2.2.2 Quantum theory for vibrations in a polyatomic molecule

It is possible to write the quantum Hamiltonian for a polyatomic molecular system as :

$$\hat{H} = \hat{T} + \hat{V} = \sum_i \left[-\frac{\hbar^2}{2}\frac{\partial^2}{\partial q_i^2} + \frac{1}{2}\omega_i^2 q_i^2 \right] \tag{2.66}$$

It is convenient to use a dimensionless form of the Hamiltonian. Then defining the so called dimensionless position operator $t_i = q_i\sqrt{\omega_i\hbar}$ we obtain:

$$\hat{H} = \sum_i \frac{\hbar\omega_i}{2}\left[\frac{\partial^2}{\partial t_i^2} + t_i^2\right] = \sum_i \hbar\omega_i\hat{h}(t_i) \tag{2.67}$$

The eigenvalues and eigenvectors of the one-dimensional quantum oscillator described by the Hamiltonian $\hat{H}_{vib}(t_i) = \hbar\omega_i\hat{h}(t_i)$ are:

$$\hat{H}_{vib}(t_i)|n_i> \; = \hbar\omega_i\left(n_i + \frac{1}{2}\right)|n_i> \tag{2.68}$$

In which n_i are the eigenvectors of the vibrational problem that are related to normal coordinates and so to displacements. It is possible to show that for a many body Hamiltonian given by the sum of independent one-body Hamiltonians, the total wavefunction of the system is given by the product of the

eigenfunctions of each one-body Hamiltonian and the total energy eigenvalue is the sum of the one-body eigenvalues:

$$\hat{H}\phi(t_1, t_2, t_3, ..., t_M) = E\phi(t_1, t_2, t_3, ..., t_M) \tag{2.69}$$

$$\phi(t_1, t_2, t_3, ..., t_M) = \prod_{i=1}^{M} \phi_{n_i}(t_i) \tag{2.70}$$

$$E = \sum_{i=1}^{M} \hbar\omega \left(n_i + \frac{1}{2} \right) \tag{2.71}$$

M is the number of vibrational normal modes obtained as eigensolutions of the secular equation. The eigenfunctions of vibrational Hamiltonian $\phi_{n_i}(t_i)$ can be expressed in terms of Hermite polynomials (H_n) in the following way:

$$\phi_{n_i}(t_i) = C_n e^{-\frac{t^2}{2}} H_n(t) \tag{2.72}$$

Where C_n are sustainable normalization contants and Hermite polynomials H_n are given by:

$$H_0(t) = 1 \tag{2.73}$$

$$H_1(t) = 2t \tag{2.74}$$

$$H_2(t) = 4t^2 - 2 \tag{2.75}$$

$$H_3(t) = 8t^3 - 12t \tag{2.76}$$

Adopting Cartesian displacements to describe molecular motions, three translations of the molecule as a rigid body and three rotations can be identified. Therefore true vibrations are $M = 3N - 6$. Rototranslations are associated to solutions with $\omega = 0$.

2.2.3 Infrared (IR) absorption spectroscopy

Perturbation theory and dipole operator

Infrared spectroscopy is a particular optical spectroscopy in which quantum transitions between different vibrational states are observed. The transition probability between two stationary states ,$|i>$ and $|f>$, promoted by a time dependent perturbation written in the form of $\hat{H}'(t) = \hat{V}\cos(\omega_0 t + \varphi)$, with the $\hat{V}$ operator being time independent, is given by:

$$P_{i\to f} = \frac{2\pi}{\hbar} \left| \langle i|\hat{V}|f\rangle \right|^2 \delta(E_f - E_i - \hbar\omega_0) \tag{2.77}$$

The previous equation represents the so called Fermi golden rule, $|i>$ and $|f>$ are known eigenstates of a given Hamiltonian $\hat{H}$ for which $\hat{H}'$ can be taken as

a weak enough perturbation. For a collection of charges forming the molecule and neglecting magnetic effects, the perturbative Hamiltonian operator $\hat{H}'(\mathrm{t})$ which describes the interaction of the molecule with the external electric field $E(t)$ is given by:

$$\hat{H}'(t) = \sum_I -E_0(eZ_I R_I)\cos(\omega_0 t + \varphi) + \sum_i E_0(er_i)\cos(\omega_0 t + \varphi) \tag{2.78}$$

In the previous equation the sum over I rapresents the sum over all the nuclei while the sum over i rapresents the sum over the electrons. Since $E_0 cos(\omega_0 t + \varphi) = E(t)$, we can write:

$$\hat{H}'(t) = -\left[\sum_I eZ_I R_I - \sum_i er_i\right] E(t) = -\hat{\mu}E(t) \tag{2.79}$$

where μ is the dipole operator. So the time-independent part of the operator $\hat{H}'(\mathrm{t})$ is:

$$\hat{V} = -\hat{\mu}E_0 \tag{2.80}$$

Therefore the evaluation of the matrix element showing in Fermi golden rule is reduced to:

$$\langle i|\hat{V}|f\rangle = -\langle i|\hat{\mu}|f\rangle E_0 \tag{2.81}$$

The projection of the transition dipole moment $\langle i|\hat{\mu}|f\rangle$ on the polarization vector of the incoming optical field governs photon absorption, which drives the quantum transition of the molecule from state $|i>$ to state $|f>$.

Vibrational transitions

IR absorption spectroscopy is characterized by an excitation where the initial and final quantum states of the molecule are two different vibrational states belonging to the same electronic states. The matrix elements of the transition operator for the $i \to f$ quantum transition can be written in the following way:

$$\langle\langle i|\hat{\mu}|f\rangle\rangle = \langle g|\prod_j (0_j|[\hat{\mu}_n + \hat{\mu}_e]\prod_k |n_k)|g\rangle = \prod_j (0_j|\langle g|\hat{\mu}_n + \hat{\mu}_e|g\rangle\prod_k |n_k) \tag{2.82}$$

in which $\langle g|\hat{\mu}_n + \hat{\mu}_e|g\rangle = \mu(\vec{R})$ represents the expectation value of the molecular dipole due to charge distribution of both electrons and nuclei in the ground electronic state, that is a function of the set of atomic positions $(\vec{R})$. $(0_j|$ is the generic initial vibrational state while $|n_k)$ is the generic vibrational final state. As already well known, the set of atomic positions can be expressed in terms of normal coordinates $\vec{q}$; therefore also $\mu(\vec{q})$ can be expressed as a function of these. As a first approximation, we can express the dependence of

the expectation value of the dipole as a function of the molecular geometry as a Taylor expansion arrested at the first order:

$$\mu(q) \approx \mu_0 + \sum_j \left(\frac{\partial \mu}{\partial q_j}\right)_0 q_j \tag{2.83}$$

Substituting this relation inside the (1.72) and doing the calculations we can write the final result:

$$\left\langle \left\langle i|\hat{\mu}|f \right\rangle \right\rangle = \sum_s \left(\frac{\partial \mu}{\partial q_s}\right)_0 (0_s|q_s|n_s) \prod_{j \neq s} (0_j|n_j) \tag{2.84}$$

Observing the equation above, we can see that the value of the static molecular dipole at equilibrium does not influence IR absorption for a purely vibrational transition. The specific normal mode, characterized by a certain normal coordinate, will be IR active if there is a variation of the dipole moment with respect to that normal coordinate. Finally, the IR absorbance (A_k) of a given one-quantum transition associated to mode k is given by:

$$A_k \propto \frac{1}{2}\left(\frac{\hbar}{\omega_k}\right)\left(\frac{\partial \mu}{\partial q_k}\right)_0^2 \tag{2.85}$$

With ω_k equal to the frequency associated to the quanta of the specific normal mode.

2.2.4 Raman scattering

The classical theory of Raman scattering is based on the idea that the electromagnetic field of the incident light induces in the system a time dependent dipole moment $M(t) = \sum_i e_i r_i(t)$ where e is the electron's charge and r is the position vector. Let $E = E_0 \cos \omega_L t$ be the electric vector of the incident light. For the dipole moment M induced by E one can write:

$$M = \alpha E + \frac{1}{2}\beta E^2 + ... \tag{2.86}$$

in which α is the electronic polarizability and β is a third rank tensor, called hyperpolarizability that will be neglected in this treatment. In general α is a second-rank tensor, but we will consider only the isotropic system's case where M is parallel to E. α depends on the electric charge distribution ρ of the system ($\alpha = \alpha(\rho)$). If the atomic configuration changes during the vibration, ρ and hence α will also change. Considering a single normal mode of vibration, expanding α in a Taylor series we obtain:

$$\alpha_0 + \left(\frac{\partial \alpha}{\partial Q}\right)_0 Q + \frac{1}{2}\left(\frac{\partial^2 \alpha}{\partial Q^2}\right)_0 Q^2 \tag{2.87}$$

The *first-order Raman effect* is determined by the term linear in Q, the *second-order Raman effect* by the term quadratic in Q and so on. We will only refer to first-order Raman scattering. If the molecule vibrates with frequency ω_s we have $Q = Q_0 cos\omega_s t$ and obtain

$$\alpha(t) = \alpha_0 + \left(\frac{\partial\alpha}{\partial Q}\right)_0 Q_0 cos\omega_s t \tag{2.88}$$

Substituting (2.88) in (2.87) and using known trigonometric formulae the following expression can be obtained:

$$M(t) = \alpha cos\omega_L t + b[cos(\omega_L - \omega_s)t + cos(\omega_L + \omega_s)t] \tag{2.89}$$

where:

$$\alpha = \alpha_0 E_0, \qquad b = \frac{1}{2}\left(\frac{\partial\alpha}{\partial Q}\right)_0 Q_0 E_0 \tag{2.90}$$

The equation shows that the induced dipole moment M vibrates not only with the frequency ω_L of the incident light, but also with the frequencies $\omega_L \pm \omega_s$. These latter frequencies arise from the modulation of the electronic polarizability α by the vibration of the atoms. From the expression of M(t) we can derive the intensity of the emitted radiation:

$$I(t) = AE_0^2\left[k_0^2 \cos^2\omega_L t + k_1^2 \cos^2\left(\omega_L - \omega_s\right)t + k_2^2 \cos^2\left(\omega_L + \omega_s\right)t\right] + crossterms \tag{2.91}$$

where:

$$k_0^2 = \alpha_0^2 \omega_L^4 \tag{2.92}$$

$$k_1^2 = \frac{1}{4}\left(\frac{\partial\alpha}{\partial Q}\right)_0^2 Q_0^2(\omega_L - \omega_s)^4 \tag{2.93}$$

$$k_2^2 = \frac{1}{4}\left(\frac{\partial\alpha}{\partial Q}\right)_0^2 Q_0^2(\omega_L + \omega_s)^4 \tag{2.94}$$

Neglecting the cross terms, we expect that scattered light will have peaks at the frequencies ω_L and $\omega_L \pm \omega_s$. This can be demonstrated calculating the frequency dependence of the scattered light, the power spectrum, obtained as a fourier transform of M(t). Making the calculation we obtain:

$$P(\omega) = \pi AE_0^2\left\{k_0\delta\left(\omega - \omega_L\right) + k_1^2\delta\left[\omega - \left(\omega_L - \omega_s\right)\right] + k_2^2\delta\left[\omega - \left(\omega_L + \omega_s\right)\right]\right\} \tag{2.95}$$

The first term is the power scattered per unit solid angle at the frequency ω_L of the incident radiation and is known as *elastic scattering* or *Rayleigh scattering*. The second and the third terms rapresent the *inelastic* or *Raman scattering* that consists in a radiation scattered at the Stokes frequency $\omega_L - \omega_s$ and at the anti-Stokes frequency $\omega_L + \omega_s$ respectively. Each term is proportional to

k_i^2 which, at the same time, is proportional to the square of the polarizability derivative with respect to the normal coordinate. It means that if this derivative is 0, the Stokes and anti-Stokes peaks disappear for that specific normal mode; this fact rapresents the so called selection rules for Raman scattering. The classical theory correctly predicts the existence of the Stokes and anti-Stokes lines, but it leads to an incorrect ratio of their intensities. Infact, from the equations above, the ratio between the Stokes and anti-Stokes peaks should be:

$$\frac{I_{Stokes}}{I_{anti-Stokes}} = \frac{\left(\omega_L - \omega_s\right)^4}{\left(\omega_L + \omega_s\right)^4} \tag{2.96}$$

which is certainly less than unity, whereas experimentally it is found that the Stokes lines are more intense than the anti-Stokes ones. This error is corrected by using a quantum theory for the interpretation of the Raman effect. Whether or not a normal mode is Raman active depends on the simmetry of the equilibrium configuration and of the symmettry of the normal modes Q_s. If the structure and symmetry of the vibrating system is known, it is possible to predict the number of Raman active modes for each symmetry species of the symmetry group under consideration.

2.2.5 Raman and IR intensities prediction by the analytical energy gradient minimum

While the vibrational eigenstates of a molecule or crystal can be derived by the solution of the secular equation described in the previous sections, an accurate prediction of the full IR and Raman spectra requires knowledge of the dipole moment and polarizability as functions of the nuclear coordinates. In the harmonic approximation, the intensities corresponding to the fundamental modes are simply given in terms of the dipole and polarizability derivatives with respect to the appropriate normal coordinates as reported in the previous chapters. The dipole and static polarizability derivatives at the equilibrium geometry R_0 with respect to an arbitrary nuclear coordinate R_a, are can be written as derivatives of the total energy $E(\varepsilon)$ in the following way:

$$\mu^0_{\alpha,a} = \left.\frac{\partial \mu^0_\alpha}{\partial R_a}\right|_{R=R^0} = \left.\frac{\partial^2 E(\varepsilon)}{\partial R_a \partial \varepsilon_a}\right|_{R=R^0 \varepsilon=0} \tag{2.97}$$

$$\alpha_{\alpha\beta,a} = \left.\frac{\partial \alpha_{\alpha\beta}}{\partial R_a}\right|_{R=R^0} = \left.\frac{\partial^3 E(\varepsilon)}{\partial R_a \partial \varepsilon_a \partial \varepsilon_b}\right|_{R=R_0 \varepsilon=0} \tag{2.98}$$

where μ^0_α is a component of the permanent dipole moment μ^0 and $\alpha_{\alpha\beta}$ is a component of the polarizability tensor α. Through the calculation of these derivatives it is possible to obtain Raman activities and IR intensities for molecules and crystals.

2.2.6 Vibronic transitions: UV-Vis absorption spectroscopy

In UV-Vis absorption spectroscopy the photon energy is large enough to promote an electronic transition, i.e., a change of the electronic part of the molecular wave function from the ground state $|g\rangle$ to some excited state $|e\rangle$. This transition may not necessarily occurs as a purely electronic transition. It may be accompanied by vibrational transitions which happen simultaneously to the electronic excitation process. In other words the final state $|f\rangle\rangle$ can be represented as:

$$|f\rangle\rangle = |e\rangle \prod_j |n_j)_e \tag{2.99}$$

With the occupation vector n of the final vibrational state possibly being different from the zero vector (0). We add as a pedix the dependence of the vibrational eigenfunctions upon the electronic state, since the Hessian (and thus normal modes and eigenstates) does depend on the potential energy surface of the k-th electronic state, given by $V_{nn}(R) + \varepsilon_k(R)$. As we have done for IR spectroscopy, we still consider that the initial state is the electronic ground state and the vibrational state with zero occupation for every normal mode:

$$|i\rangle\rangle = |g\rangle \prod_j |0_j)_g \tag{2.100}$$

Similarly to the derivation carried out for IR absorption, we may integrate over all electronic degrees of freedom and introduce the transition dipole moment upon g $\rightarrow$ e excitation, denoted μ_{ge}, which will be of course a function of the atomic positions or, better, of the set of normal coordinates q:

$$\langle\langle i|\widehat{\mu}|f\rangle\rangle = \langle g| \prod_j {}_g(0_j|[\widehat{\mu}_n+\widehat{\mu}_e] \prod_k |n_k)_e|e\rangle = \prod_j {}_g(0_j|\langle g|\widehat{\mu}|e\rangle \prod_k |n_k)_e = \prod_j {}_g(0_j|\mu_{ge}(q) \prod_k |n_k)_e \tag{2.101}$$

Two very useful approximations adopted in discussing UV-Vis absorption spectroscopy are named after Franck-Condon (FC) and Herzberg-Teller (HT). The FC approximation simply states that since the electronic transition process is way faster than nuclear motion (just out of the Born-Oppenheimer (BO) approximation), one can merely consider the "static" value of the transition dipole moment, evaluated at the equilibrium position of the electronic ground state (from which the transition occurs). Actually this approach can also be justified considering the Taylor expansion procedure introduced before in discussing IR absorption and the ground state dipole moment. In the FC approximation the Taylor expansion is essentially arrested at the zero-th level. The HT approximation moves one step further than FC and takes into consideration the linear terms in the Taylor expansion. So to summarize:

$$\mu_{ge}(q) \approx \mu^0_{ge} + \sum_j \left(\frac{\partial \mu_{ge}}{\partial q_j}\right)_0 q_j \tag{2.102}$$

Quite obviously the HT approximation becomes crucial in justifying UV-Vis absorption phenomena in correspondence of transitions for which the evaluation of μ^0_{ge} yields zero (these are also named dipole-forbidden transitions). Under those circumstances, absorption may still be observed as due to the presence of so-called HT vibronic coupling terms, i.e., $(\partial\mu_{ge}/\partial q_j)_0 \neq 0$.

Let us consider the FC approximation and let us evaluate the transition dipole moment:

$$\langle\langle i|\widehat{\mu}|f\rangle\rangle = \prod_j {}_g(0_j|\mu^0_{ge}\prod_k |n_k)_e = \mu^0_{ge}\prod_j {}_g(0_j|\prod_k |n_k)_e = {}_g(0|n)_e\mu^0_{ge} \quad (2.103)$$

Now, the evaluation of the integral over vibrational eigenstates of the ground over excited states, i.e., $g(0|n)e$, originates some issues. This is essentially due to the fact that the set of normal coordinates of the excited state simply does not correspond to the set of normal coordinates of the ground state. This is the result of two facts:

(i) the equilibrium geometry of the ground and excited states generally are not the same;

(ii) the Hessian of the ground and excited state energy surfaces are not the same.

Nevertheless, since the set of normal coordinates of the ground and excited states form a complete set for describing relative nuclear displacements there must be a relation which may express the set of q e coordinates as a function of q_g coordinates. A linear representation of this connection is the so-called Duschinsky rotation:

$$q_e = Jq_g + \Delta \quad (2.104)$$

Where:

$$J = L_e^{-1}L_g = L_e^t L_g\Delta = L_e^t M^{\frac{1}{2}}(x^0_e - x^0_g) \quad (2.105)$$

Where the symbols L, M, x have been discussed in dealing with the description of vibrational states reported in previous chapters. Thanks to the Duschinsky linear relation it is possible to compute multidimensional FC overlaps $g(0|n)e$, but the formulas are cumbersome and recursive. It is useful to examine the case where one can neglect Duschinsky rotation (i.e., neglect mode mixing and assume the coupling matrix to be unity $J = 1$). Under these circumstances the normal coordinates of the excited state are just origin-shifted with respect to those of the ground state and there is a one-to-one correspondence between normal modes:

$$q_{e,k} = q_{g,k} + \Delta_k \quad (2.106)$$

Hence the multidimensional FC overlap simply reduces to the product of individual FC factors, mode by mode:

$$g(0|n)e = \prod_k {}_g(0_k|n_k)_e \tag{2.107}$$

By introducing the dimensionless displacement parameter B_k:

$$B_k = \left(\frac{\omega_k}{\hbar}\right)^{1/2} \Delta_k \tag{2.108}$$

it is possible to analytically evaluate the FC overlap terms compactly and determine the relative intensities of a vibronic progression as follows:

$$A_{i\to f} \propto (\mu^0_{ge})^2 |_g(0_k|n_k)_e|^2 = (\mu^0_{ge})^2 e^{-B_k^2/2} \frac{B_k^{2n_k}}{2^{n_k} n_k!} \tag{2.109}$$

The FC overlaps are the basis of the UVFC program, developed by Prof. Matteo Tommasini from the Politecnico di Milano, that has been used in my PhD work to compute UV-Vis spectra.

Chapter 3

Carbon Atom Wires (CAWs): theoretical analysis of their optical, electronic and vibrational properties

3.1 Introduction

The starting point of my PhD work consists in the investigation of sp-hybridized linear systems, focusing in particular in the analysis of the optical, electronic and vibrational properties of carbon atom wires (CAWs). These structures, as already discussed in the first chapter, are carbon-based linear atomic wires that can appear in two different forms: polyynic and cumulenic. The strong coupling between structural and electronic properties causes a considerable difference in the electronic, vibrational and optical behaviour of the two structures. For this reason, my analysis starts with the study of Raman and UV-Vis spectra of polyynes with different end groups and lengths to understand how properties depend on their termination and extension. Then, interaction between polyynes and silver nanoparticles has been investigated, together with the computation of the Raman spectrum, with a twofold aim: describe the peculiar physicochemical interaction that takes place between the linear carbon chain and the metal nanoparticle and correctly interpret and support the experimentally-obtained Surface Enhanced Raman Scattering (SERS) spectra. Finally, the attention was shifted to the analysis of cumulenes with different terminations and lengths for the prediction of the electronic properties of these molecules, focusing in particular on the investigation of their ground and excited state properties in order to find promising candidates for organic electronic applications.

3.2 UV-Vis and Raman spectra analysis of polyynes with different end-capping groups

Characterization of polyynes can be performed by UV–Vis and Raman spectroscopy. The size-dependent electronic structure leads to a sequence of vibronic bands in UV–Vis spectra which shift to higher wavelength by increasing the number of carbon atoms. Vibrational properties can be investigated by Raman spectroscopy, showing peaks located in the 1800–2300 cm^{-1} spectral range as a fingerprint of sp-carbon [24]. The red-shift of the Raman peaks with increasing the wire length can be used to characterise the size distribution [84]. In case of weak Raman signal of isolated sp-carbon chains, or when the polyynes concentration in solution is too low, surface-enhanced Raman scattering (SERS) has proven to enhance the sensitivity up to 6 order of magnitude by exploiting silver in form of nanoislands supported on surfaces or colloidal nanoparticles. While computed UV-Vis and Raman spectra are treated in this section and compared with experimental data, SERS effect will be discussed in the following section. First-principles calculations of the vibronic spectra of C_n polyynes with different terminations (hydrogen, methyl and cyano) were carried out by employing time-dependent DFT (TDDFT) calculations, adopting the Coulomb-attenuated range separated exchange–correlation functional CAM-B3LYP, and the Dunning's correlation consistent cc-pVTZ basis set. All calculations were performed by using the package Gaussian09 [85]. For each C_n, after the ground state geometry optimisation, vertical excited state transitions were computed at TDDFT level. For the most relevant dipole-active state (mainly described by single-particle HOMO-LUMO transition) a further TDDFT geometry optimisation and force field calculation have been performed. Based on ground and excited state equilibrium geometries and vibrational force fields, the Huang-Rhys factors and the vibronic spectra were evaluated, as reported in the Theoretical Background chapter.

Also Raman spectra have been computed for polyynes, but at PBE0/cc-pVTZ level of theory. Indeed, previous experience in the prediction of the Raman response of several sp-carbon-based molecular systems shows that this functional provides a good agreement vs experimental data [37, 86, 87]. Vibrational frequeny obtained from calculations have been appropriately scaled, using a scaling factor of 0.961 for the specific adopted level of theory, according to the Computational Chemistry Comparison and Benchmark DataBase (CCCBDB, [88])

3.2.1 Hydrogen-capped polyynes

Fig. 3.1 shows the experimental UV–Vis absorption spectra of size-selected hydrogen-capped polyynes HC_nH (n = 6–16) synthesised in water [89]. Spectra

have been normalised for better comparison even though the intensity decreases up to three order of magnitude for longer polyynes. The observed absorption bands are related to the vibronic progression mainly governed by the ECC vibrational mode, characteristic fingerprint of the carbon atom wires and directly connected to the conjugation of the chain as already explained in the first chapter of my thesis. The absorption energy decreases to longer wavelengths by increasing chain length, as in the case of other polyconjugated materials. To support the interpretation of the experimental results I performed TDDFT calculations, coupled with the use of the UVFC program, to simulate UV-Vis absorption spectra. This method has the capability to find the active excited state of a molecule and then, once the minimum energy configuration of the excited state is found, to compute the vibronic progression, as described in the last section of the Theoretical Background chapter. Indeed, as reported in Tab. 3.1 for the case of HC_8H system, oscillator strength (f_{os}) different from zero, considering the first 10 excited states, is obtained only for a single state for all the polyynic systems. This will cause the presence of a single vibronic progression in the computed UV-Vis absorption spectra of these molecules.

Wavelength (nm)	f_{os}
354	0
342	0
342	0
240	0
231	0
200	4
187	0
180	0
180	0
174	0

Table 3.1: *Table reporting the first 10 active excited states for the HC_8H polyyne*

Predicted spectra, as can be seen in Fig. 3.1, are in good agreement with experimental data. All the predicted spectra have been rigidly shifted by 19.5 nm to match the experimental data of C_8. This has been done due to the very well known difficulty by the DFT method to estimate π-electron conjugation along the chain. Indeed, as can be seen from the spectra, the more the chain length the more the underestimation of the electronic conjugation, resulting in a blue-shift of the computed UV-Vis spectra with respect to the experimental ones (especially for n>10). This effect can be inferred to a partial multireference character of the polyyne excited states, not considered by DFT-based methods, that increases with the chain length and which would affect the computed excitation energy. The concept of multiconfigurationality

of the ground state of carbon atom wires will be discussed in the last section of this chapter. These results show that TDDFT calculations allow to predict vibronic spectra of polyynes as they can be experimentally detected by HPLC thus opening to the investigation of novel polyyne systems. Analyzing in detail the UV-Vis experimental absorption spectra, some low frequency peaks, characterized by very low intensity, can be distinguished (see Fig. 3.1 for the case of HC_8H). The origin of these bands, that cannot be predicted from DFT calculations, is probably due to some dark excited states, positioned at lower energy with respect to the main active absorption band, that, for some reasons not completely understood, in experimental conditions become weakly active and generate the presence of these absorption bands at high wavelengths.

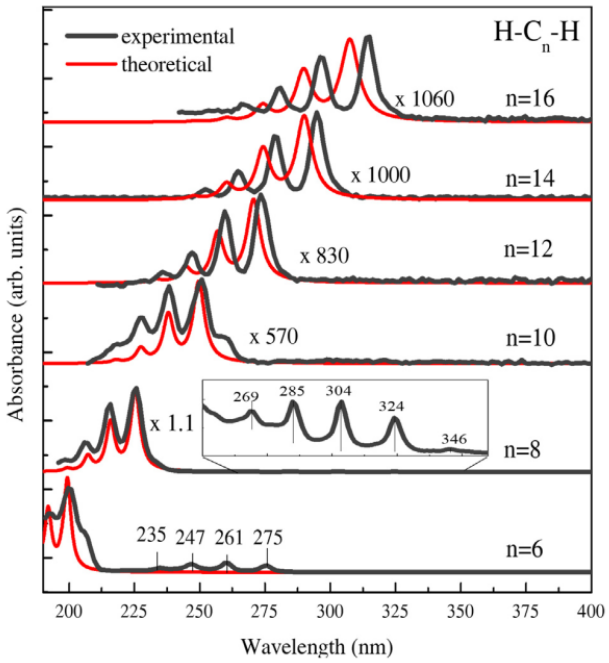

Figure 3.1: *In black, normalised absorption spectra of hydrogen-capped polyynes HC_nH (n = 6–16) in water separated and collected by HPLC. In red, TD-DFT calculations of UV–Vis spectra compared with experimental data. The inset shows the low intensity peaks of HC_8H magnified. [89]*

The vibronic progression of each HC_nH is mainly dominated by one vibrational normal mode, attributed to the in-phase C≡C/C-C stretching/shrinking of the carbon chain and which corresponds also to the most intense Raman active vibration. This pattern is clearly visible from Fig. 3.2, that is reporting the ECC pattern for the HC_8H system as a reference and in which the two different colours stand for opposite phases of bonds' vibration (i.e. shrinking/stretching) while the thickness of the coloured line indicates the amplitude

of the vibration. Indeed, in Fig. 3.2 we reported the Raman spectra for HC_nH with n ranging from 6 to 16 and, as can be seen, the ECC mode dominates the spectra for all the systems. Moreover, it suffers a redshift in vibrational frequency for increasing length of the chain, passing from 2332 cm^{-1} for HC_6H to 2122 cm^{-1} for $HC_{16}H$. This is due to the increase in the electronic conjugation of the system, already discussed with the analysis of the UV-Vis spectra and also reflected by the Raman spectra. Indeed, the increase in electronic conjugation is coupled with the decrease in the force constant associated to the triple bonds, with a consequent strengthening of the single ones, with an associated decrease in the BLA.

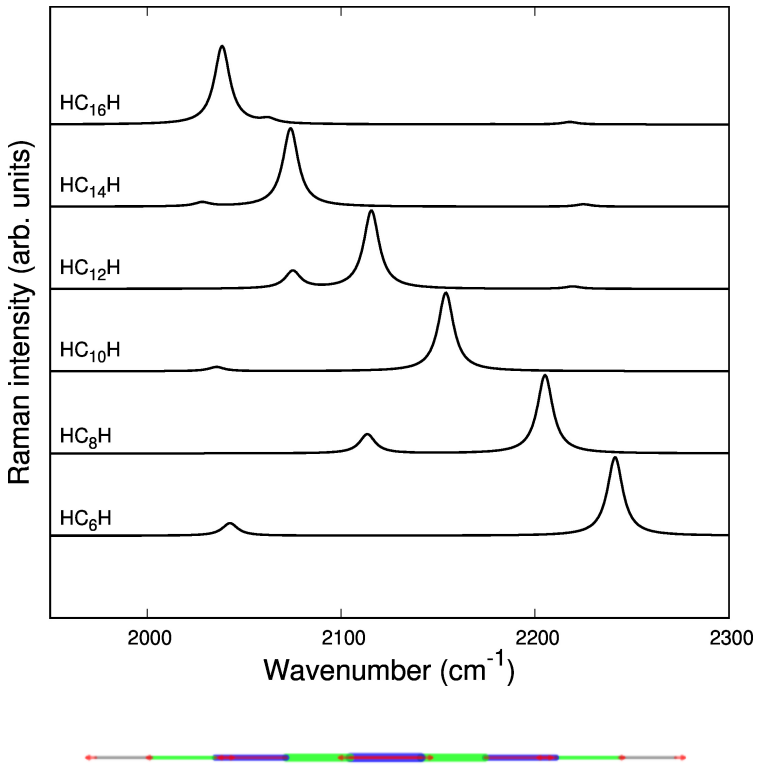

Figure 3.2: *Above: DFT-computed Raman spectra of HC_nH polyynes with n ranging from 6 to 16. Below: typical ECC vibrational pattern for a polyyne (HC_8H in this case) in which red arrows indicate atomic displacements while green and blue colors indicate the active bond stretching vibrations in each normal mode. The different colors indicate different phases of the vibration, while the line width is proportional to its amplitude.*

Although the Raman spectra is in very good accordance with the experimental UV-Vis spectra analysis, from the experimental point of view is very difficult to obtain pure Raman spectra. The reason is that polyynes are usually produced in solution at very low concentrations, ranging from 10^{-6} to 10^{-9} M,

and this prevents the possibility to obtain intense enough signal from the Raman scattering processes. For this reason, surface-enhanced Raman scattering (SERS) has been employed experimentally to solve this issue and in Fig. 3.3 spectra are reported for HC_nH with n = 6, 8, 10. Comparing these spectra with the ones obtained from calculations, one can appreciate the appearance of a low frequency band, for all the three systems, around 1900 cm^{-1}. This band has been attributed to the interaction of the polyynes with the metal nanoparticles, present in solution and responsible for the chemical and physical enhancement of the signal. This interaction has not be considered to obtain DFT calculated spectra reported in Fig. 3.2, but it will be deeply investigated in one of the following section.

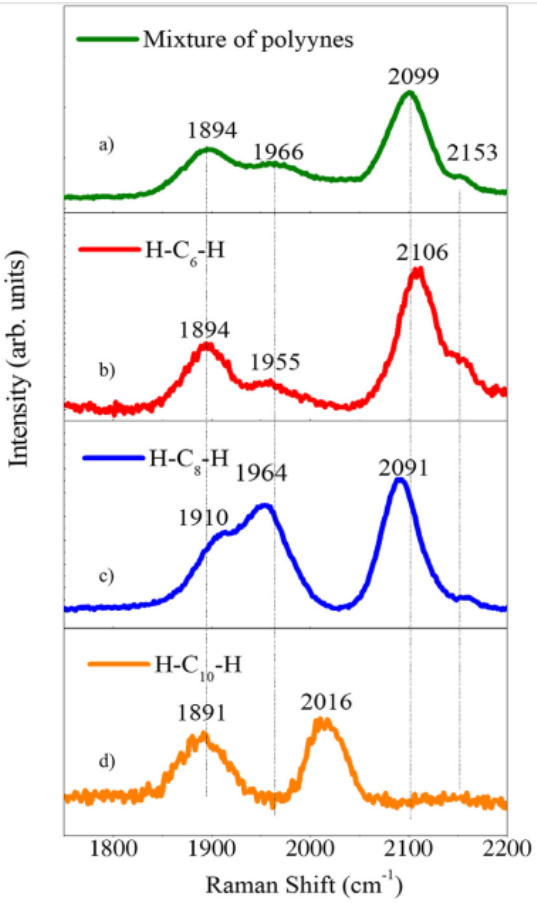

Figure 3.3: *Experimental SERS spectra of (a) the polyynes mixture, (b) size-selected hydrogen polyynes (HC_nH with n = 6, (c) n = 8 and (d) n = 10.) [89]*

3.2.2 Methyl- and cyano-capped polyynes

For methyl- ($HC_nC_nH_3$) and cyano-capped (HC_nCN) polyynes, similar considerations can be done. Indeed, also for these cases the UV-Vis spectra has been computed and compared with experimental data [90] (see Fig. 3.4).As already done for the hydrogen polyynes case, predicted data were rigidly shifted to match the spectra of C_8, considered as a reference system. Also for these systems, we found only one active excited state with f_{osc} different from 0. Transition energies are well described using the TD-DFT model, even if, by increasing the length of the chain, the discrepancy with respect to the experimental values increases, as already explained for HC_nH systems.

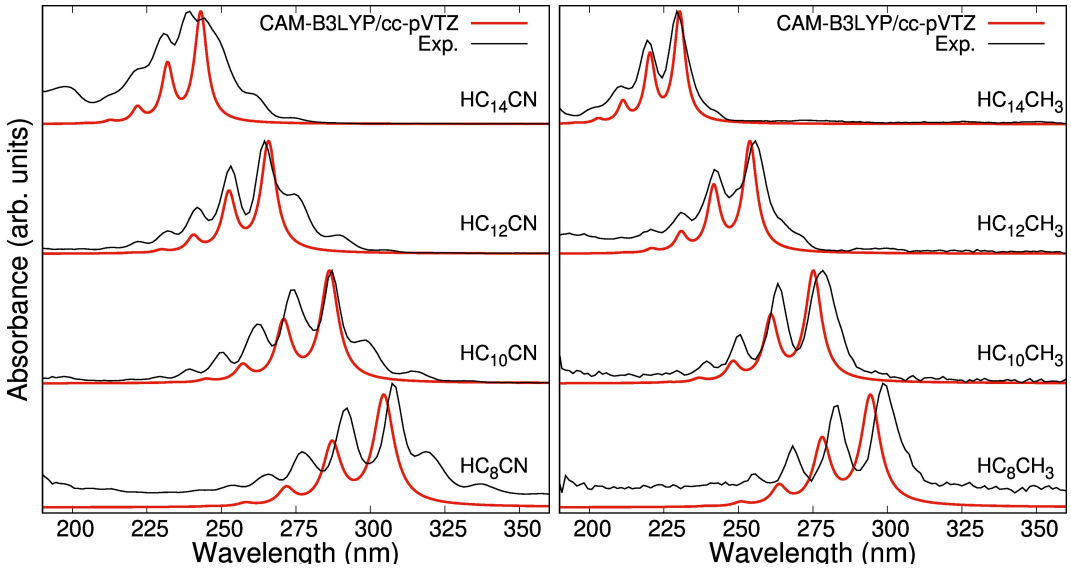

Figure 3.4: *Normalized experimental (thin black lines) and simulated (thick red lines) UV-vis spectra of CN-polyynes (left) and CH_3-polyynes (right) [90]*

By analyzing spectra reported in Fig. 3.4, the influence of the terminal group in determining the electronic conjugation of the chain can be noticed. Indeed, by comparing the computed UV-Vis spectra of HC_nCH_3 and HC_nCN, considering the same value of n, a more red-shifted spectra is obtained for cyano-capped polyynes with respect to methyl-capped ones. Indeed, referring to the most intense absorption of the vibronic progression (usually refered to the 0-0 transition), focusing the attention on n = 12, a transition positioned at 287 nm is obtained for $HC_{12}CN$ systems compared to $HC_{12}CH_3$ whose transition is located at 276 nm. This visible difference can be attributed to the different conjugation allowed by the different terminal groups. In HC_nCH_3 systems, the π-electron chain is able to to couple only slightly with the s orbitals of the 3 hydrogens in a phenomenon called hyperconjugation. On the contrary, in the case of HC_nCN polyynes, the π orbitals of the carbon atoms can

strongly couple with the π orbitals of the C≡N group, thus counting almost as an additional carbon atom in the conjugated chain. As a term of comparison, the simulated UV-Vis 0-0 transition for the $HC_{12}H$ system is located at 271 nm. This phenomenon is well described also by looking at the molecular HOMO and LUMO orbitals for the different species reported in Fig. 3.5 for a single reference length. Indeed, lobes describing the eigenstates are more delocalized on the terminals for the CN-terminated polyynes with respect to the CH_3-terminated polyyne. Moreover, both systems present an higher π-electron delocalization with respect to the hydrogen-terminated carbon wire.

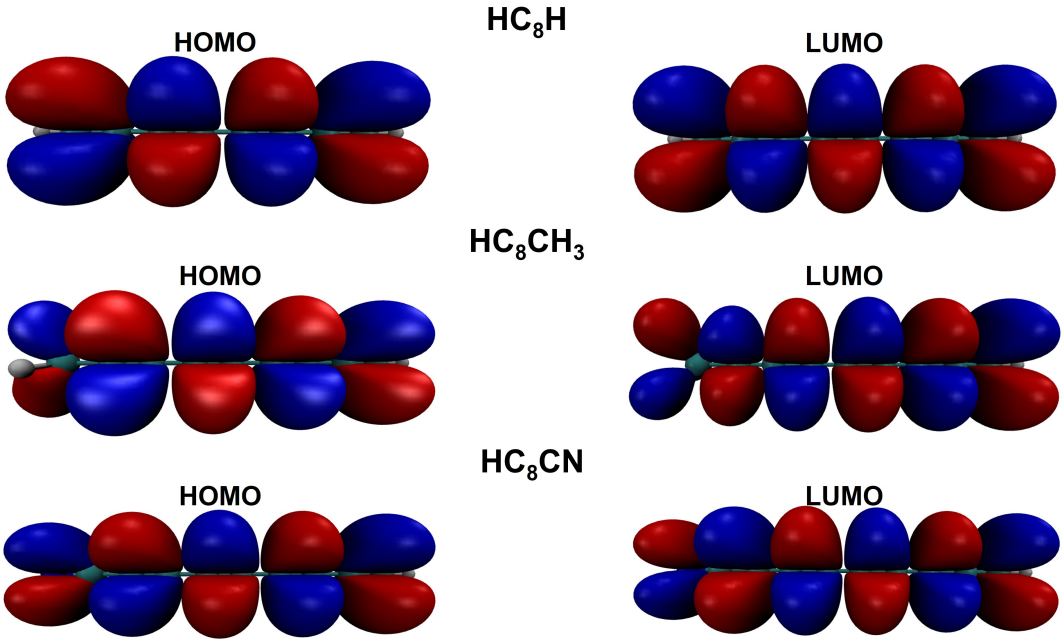

Figure 3.5: *HOMO and LUMO molecular orbitals for HC_8H, HC_8CH_3 and HC_8CN carbon wires*

Polyynes of the same size and different terminations have been investigated, both computationally (Fig. 3.6) and experimentally (Fig. 3.7), via Raman spectroscopy [90]. Indeed HC_8H, HC_8CH_3 and HC_8CN has been taken as benchmark for the analysis. As can be seen from Fig. 3.6, the Raman active band related to the ECC mode, whose peculiar pattern can be recognized by the skecthes, is dominating the spectra of all the three systems. What is clearly visible is that, as already discussed in the case of UV-Vis spectroscopy, due to the higher electronic conjugation present in HC_8CN system, the ECC vibrational frequency is very red-shifted (2262 cm^{-1}) with respect to methyl (2289 cm^{-1}) and hydrogen (2295 cm^{-1}) one. The reason is the different coupling between the π orbitals in the carbon chain and the terminal groups, as already discussed for the interpretation of the UV-Vis spectra. This trend is

also present in the experimental SERS spectra (see Fig. 3.7): two main broad bands appear below and above 2000 cm^{-1} in all three measurements [90]. The band below 2000 cm^{-1} usually appears in the SERS spectra of polyynes due to the interaction between the molecule and the metal cluster, as already previosly explained for the case of hydrogen-capped polyynes, whereas the band at a higher wavenumber corresponds to the ECC mode. Concerning the ECC mode, a nearly symmetrical peak at 2079 cm^{-1} can be observed in HC_8H , a band centered at 2073 cm^{-1} in HC_8CH_3 and a doublet in HC_8CN, for which the most intense peak is located at 2067 cm^{-1} and a secondary one at 2093 cm^{-1}. A mismatch between simulated and experimental peak positions is observed due to the interaction with silver colloids that is not included in our calculations, but that will be treated in the next section.

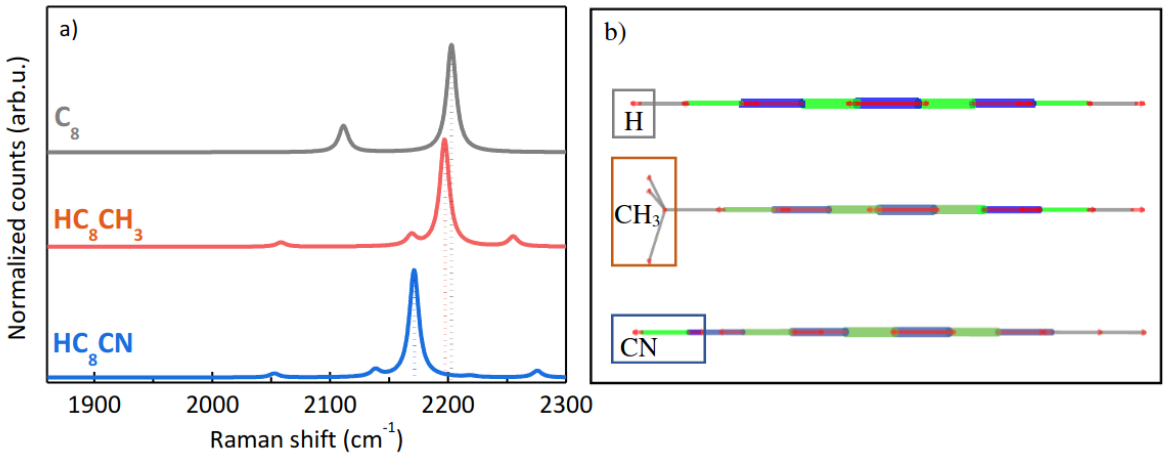

Figure 3.6: *DFT-computed Raman spectra of HC_8H, HC_8CH_3 and HC_8CN polyynes. Normal modes associated to ECC vibration are also reported on the right in which red arrows indicate atomic displacements while green and blue colors indicate the active bond stretching vibrations in each normal mode. The different colors indicate different phases of the vibration, while the line width is proportional to its amplitude.*

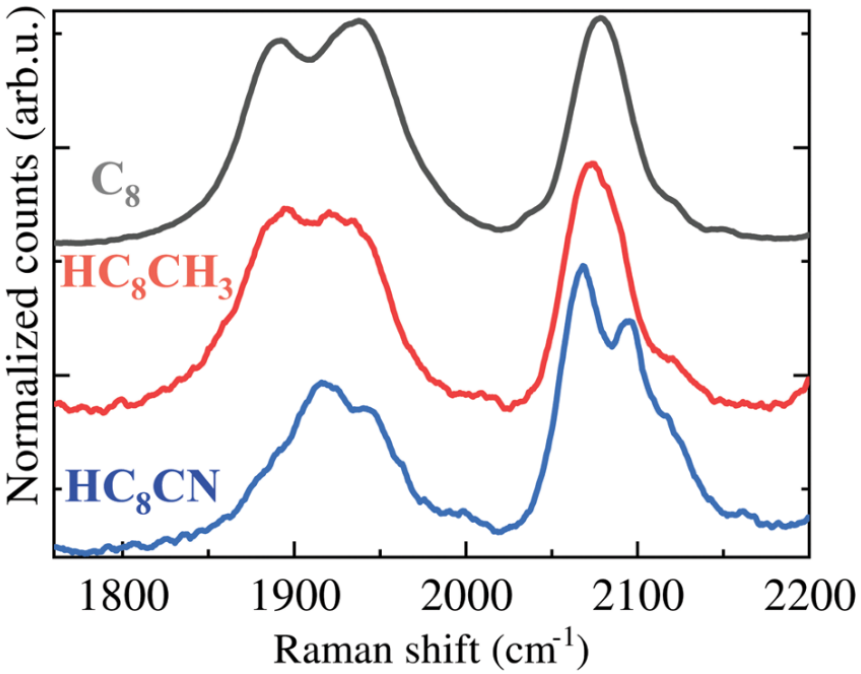

Figure 3.7: *Experimental SERS spectra of HC_8H, HC_8CH_3 and HC_8CN polyynes [89]*

3.3 Analysis of the interaction between polyynes and metal nanoparticles

This section focuses on the computational investigation of the interaction between metal nanoparticles and polyynes, responsible for the chemical enhancement visible in experimental SERS analyses. Different systems have been analyzed, consisting in hydrogen-, methyl- and cyano- terminated polyynes of various lengths, interacting with silver clusters of different sizes, to understand the effect of the dimensions on the obtained results. Such polyynes represent relatively simple molecules, already studied and for which experimental data are available.

3.3.1 Optimization of computational setup

The optimization of the computational setup will be presented in this section. The choice of hydrogen-polyynes as benchmark for the optimization setup is mainly due to the fact that these carbon atom wires are the most studied from both the computational and experimental point of view. Furthermore, they are polyynes having the simplest and minimal chemical structure. The benchmarking of the different parameters' performances has been done on the basis

of analyses and comparisons of the predicted Raman spectra and interaction energies for different systems.

The basis-sets that have been analyzed are the well known cc-pVTZ, the AUG-cc-pVTZ and the 6-311++G(d,p). The first one proved to be a very good compromise between accuracy and computational time for the simulation of Raman spectra of polyynes [90]. The second basis-set is instead an augmented version of the first one, as it incorporates diffuse functions, useful when describing larger and more complex systems due to their ability in the evaluation of inter-molecular and intra-molecular long-range interactions. The choice of 6-311++G(d,p) is based on the fact that it's a smaller basis-set with respect to the cc-pVTZ but, at the same time, it features diffuse functions. The investigated systems are, as said, hydrogen-polyynes, of different lengths, i.e. 4 and 8 atoms (denoted as HC_4H and HC_8H), interacting with Silver nanoparticles of different size, i.e. 4 and 8 atoms (denoted as Ag_4 and Ag_8). The test dimers were formed by same-length polyynes interacting with different sized clusters and different length polyynes interacting with cluster of the same size. To be able to differentiate the influence of this parameter, the same functional, PBE0, has been used. The spectra obtained from the different combinations of polyynes and metal clusters, by using cc-pVTZ, the AUG-cc-pVTZ and the 6-311++G(d,p) basis sets, are characterized by peaks having the same shape, whoose vibrational frequencies are also positioned at almost the same frequency. As a term of comparison, Raman spectra of HC_4H interacting with Ag_8, evaluated with the 3 different basis sets, are reported in Fig. 3.8.

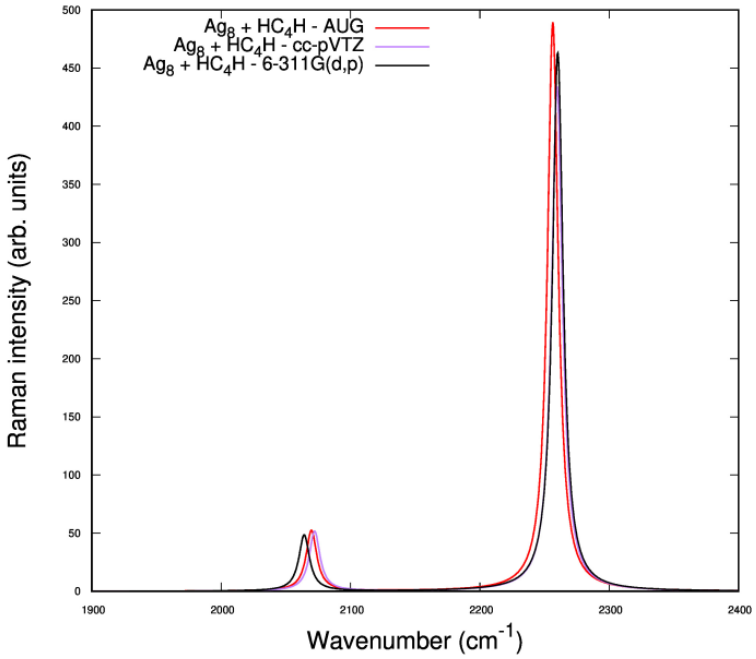

Figure 3.8: *Effect of different basis-sets (cc-pVTZ, AUG-cc-pVTZ and 6-311++G(d,p)) on the Raman spectra of system* Ag_8 + HC_4H

Another parameter that we considered as a benchmark of the computational setup's accuracy is the interaction energy defined by the following relationship:

$$E_{INT} = E_{complex} - (E_{chain} + E_{cluster}) \tag{3.1}$$

where $E_{complex}$ is the energy of the complex formed by the Silver cluster and the CAW, while E_{chain} and $E_{cluster}$ are the energies of the hydrogen-polyyne and cluster respectively. The calculated values, reported in table 3.2, are consistent with the use of different basis-sets; indeed, a trend was individuated for all the systems.

species	AUG-cc-pVTZ	cc-pVTZ	6-311++G(d,p)
Ag_4+HC_4H	-3.12	-2.85	-4.23
Ag_8+HC_4H	-5.34	-5.20	-7.5
Ag_4+HC_8H	-4.90	-4.64	-6.13
Ag_8+HC_8H	/	-6.03	-8.67

Table 3.2: *Interaction energies, in kcal/mol, calculated by adopting PBE0 functional in combination with different basis-sets are reported in the table.*

Therefore, considering the spectra and interaction energies, the choice of one of the three proposed basis-sets does not seem to be crucial. Therefore,

6-311++G(d,p) has been selected for modeling the interaction. In this way, it is possible to have diffuse functions in the description of the different systems, i.e. hydrogen-polyynes, methyl-polyynes and cyano-polyynes, without having to sustain the burden of the higher complexity and computational cost of the AUG-cc-pVTZ.

In order to investigate the effect of the functional choice on the modeling of CAW-silver nanoparticle system, the same analysis, already done for the basis set choice, was performed using B3LYP hybrid functional and comparing the results obtained with the PBE0 one, both briefly introduced in the theoretical background chapter. PBE0 has been used in previous studies [22, 24] giving good results in the evaluation of Raman spectra of sp systems featuring π conjugation. On the other hand B3LYP is widely used in DFT studies, and has given good results for a variety of systems. In order to study the effect of the exchange-correlation functional employed, metallic clusters of 8, 16 atoms interacting with polyyne length of 4, 8 atoms were investigated. To have comparable results cc-pVTZ was used for both cases. Raman spectra calculated with both functional for a single dimer, Ag_8+HC_8H, are reported in Figure 3.9.

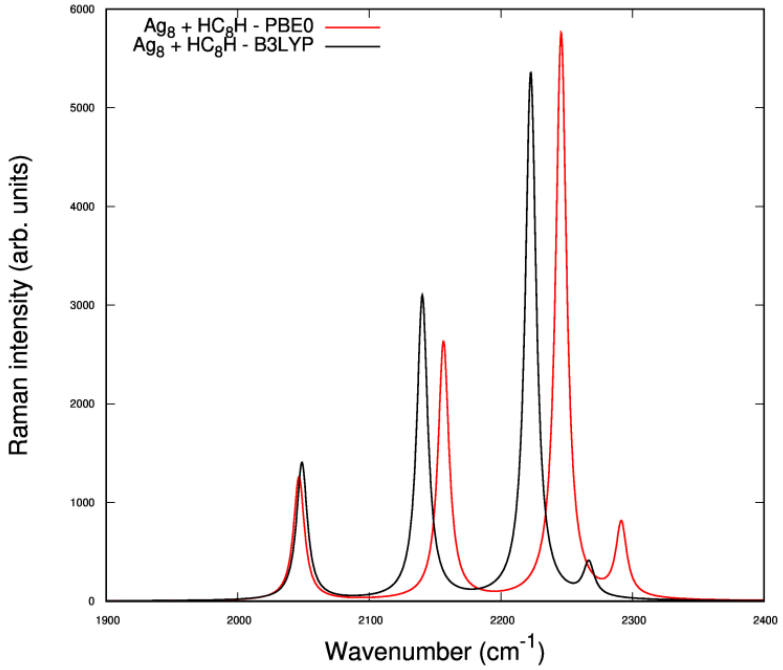

Figure 3.9: *Effect of the two different functionals (PBE0 and B3LYP) for Ag_8 + HC_8H*

Comparing the spectra obtained by using the two functionals, a general difference in the vibrational frequencies predicted for the main Raman active bands can be noticed. Indeed, focusing on the high frequency region of the spectra (2000-2400 cm^{-1}), the maximum shift measured for the case of the 4

atom long polyyne (HC_4H is 10 cm^{-1} for the peaks with the highest intensities located at 2250 (B3LYP) and 2260 (PBE0) cm^{-1}. In the case of the 8 atom long polyyne the highest difference consists in 23 cm^{-1} and is measured for the peaks at 2223 (B3LYP) and 2246 cm^{-1} (PBE0), those with the highest intensities, as in the previous case. For the HC_4H polyyne interacting with the cluster of 16 atoms, the maximum calculated shift is 20 cm^{-1} and still measured for the peaks with the highest intensity (at 2249 and 2269 cm^{-1}). The differences are more evident in the case of Ag_8 + HC_8H, since probably PBE0 overestimates π conjugation with respect to B3LYP (which in turns underestimates it). From the analysis of the interaction energies, a significant discrepancy between values predicted with the two functionals is found for different dimers, but this is expected due to the differences of the two in estimating the exchange-correlation energy. Specifically, the B3LYP functional predicts a much more weaker interaction with respect to PBE0. However, it is already possible to find a trend: the energy of the shorter polyyne (HC_4H with the different clusters) is lower with respect to the longer (HC_8H) one. The differences observed in the spectra and in the interaction energies may originate from the characteristics of the functionals, especially considering their different mathematical definition. Considering the overall shape of the spectra and the trend identified in the interaction energies, the choice of the functional seems to not alter significantly the results. Therefore PBE0 was selected, also considering the satisfying results obtained in the previously mentioned studies, where this functional was used to investigate sp hybridized systems (and in particular their Raman spectra).

The effect of intermolecular van der Waals interactions has also been considered in the overall evualuation of the computational parameters. Indeed, one of the problems that affects DFT based calculations is the poor evaluation of weak interactions, such as Van der Waals interactions, even if wide basis-sets featuring diffuse functions are used. The assessment of the effect of dispersion corrections, introduced by Grimme et al. [91] and known as GD3 corrections, has been done on a single dimer, formed by the 8 atoms-long polyyne (HC_8H) and the silver nanoparticle with 8 atoms (Ag_8). Again, the analysis of the spectra and interaction energies was considered to check whether the corrections introduced any notable differences. From these analysis, one can understand that the implementation of the GD3 corrections does not affect the overall shape of the spectra and the calculated values of the interaction energies are consistent with that computed neglecting Van Der Waals interactions. For this reason, consisting GD3 corrections an additional computational cost to the standard calculations, I have decided not to consider them in the final computational setup adopted.

3.3.2 Analysis of Hydrogen-capped polyynes

Once the basis-set and the exchange-correlation functional were selected (PBE0/6-311++G(d,p)), with such setup the analysis of hydrogen-capped polyynes interacting with different silver clusters has been performed. The systems investigated are the same employed for the setup optimization, i.e. silver nanoparticles of size 4 (Ag_4) and 8 (Ag_8) atoms, and hydrogen-polyynes of different length, 4 (HC_4H) and 8 (HC_8H) atoms long. In Fig. 3.10 we reported the optimized geometries representing all the 4 possible combinations between clusters (Ag_4, Ag_8) and polyynes (HC_4H, HC_8H) to help the overall discussion.

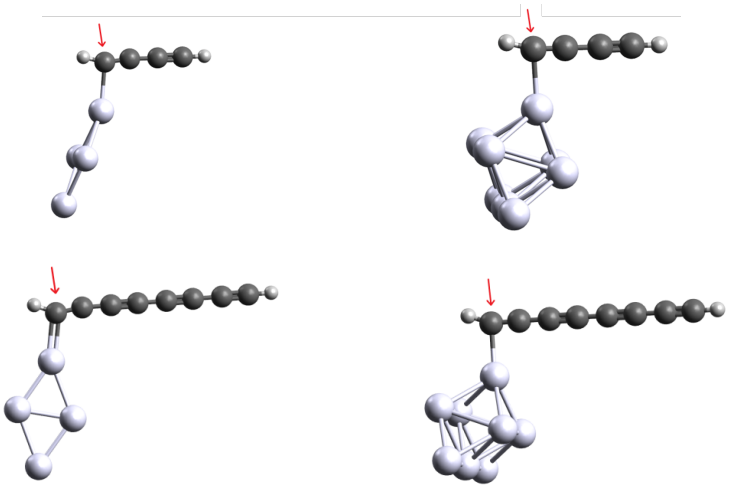

Figure 3.10: *Optimized geometries of: Ag_4 + HC_4H, Ag_8 + HC_4H, Ag_4 + HC_8H, Ag_8 + HC_8H. The red arrow indicates the first carbon atom of the chain.*

Raman spectra and interaction energies analysis

The influence of chain length and size of the cluster has been investigated upon comparisons between the spectra and interaction energies obtained for the different systems. Firstly, the spectra of hydrogen-polyynes have been analyzed, to check whether the distinctive peaks referred to sp carbon hybridization were correctly predicted. In Fig. 3.11 it is indeed possible to observe in both cases the ECC mode, assigned to the most intense peak, and, in the spectrum of HC_8H, it is well visible also the β mode peak, at a lower frequency. Their eigenvectors are also reported in Fig. 3.11.

The analysis of the interaction energies (see table 3.3) suggests that the interaction is stronger with increasing size of the cluster and increasing length of the linear carbon chain. If the size of the cluster is fixed, i.e. considering the effect of the length of the chain, a difference of 1.9 kcal/mol between Ag_4 + HC_4H and Ag_4 + HC_8H is measured. For the other two systems, i.e. Ag_8

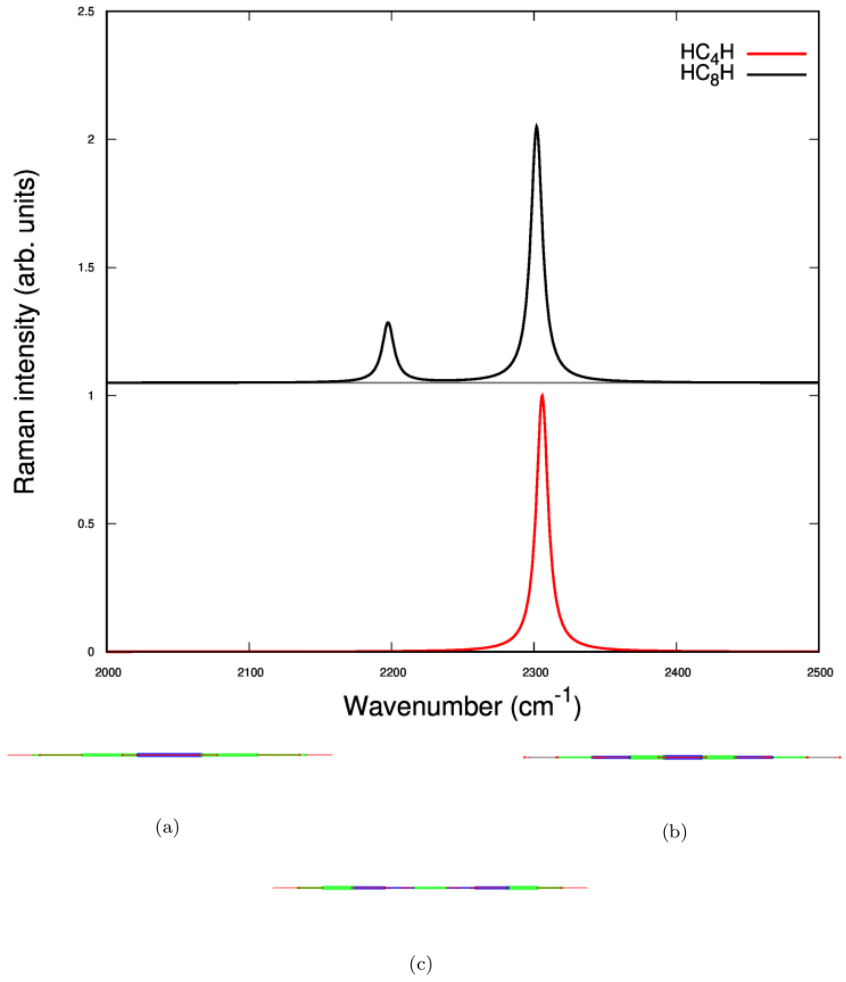

Figure 3.11: *Top: Normalized spectra for isolated hydrogn-polyynes. Bottom: Eigenvector of the two hydrogen-polyynes: a) ECC mode of HC_4H, at 2306 cm^{-1}; b) ECC mode of HC_8H, at 2302 cm^{-1} ; c) β mode of HC_8H, at 2198 cm^{-1}. Red arrows indicate atomic displacements while green and blue colors indicate the active bond stretching vibrations in each normal mode. The different colors indicate different phases of the vibration, while the line width is proportional to its amplitude.*

+ HC_4H and Ag_8 + HC_8H the gap reduces to 1.17 kcal/mol. On the other hand, if the length of the chain is fixed, it is possible to highlight the effect of the size of the cluster: for the systems Ag_4 + HC_4H and Ag_8 + HC_4H the difference in the interaction energies is of 3.27 kcal/mol; for Ag_4 + HC_8H and Ag_8 + HC_8H systems such difference decreases to 2.54 kcal/mol. In both cases, i.e. for fixed size of the cluster and then for fixed length of the chain, the difference between the interaction energies of the considered systems is reducing (1.9 $\rightarrow$ 1.17 kcal/mol and 3.27 $\rightarrow$ 2.54 kcal/mol). It is therefore

possible to hypothesize that such difference will reach a plateau, meaning that, at some point, the increase in the size of the cluster at fixed chain length or the increase of the chain length at fixed cluster dimensions, will not produce an appreciable increase in the interaction energies.

species	Ag_4	Ag_8
HC_4H	-4.23	-7.50
HC_8H	-6.13	-8.67

Table 3.3: *Predicted interaction energies, in kcal/mol, for hydrogen-polyynes interacting with silver nanoparticles.*

Another result obtained from this evaluation is that the system with the longest chain and biggest cluster is the most stable. This can be explained by the presence of a higher number of molecular orbitals available for the interaction between the cluster and the chain. The optimized geometry, corresponding to the more stable configuration, for every system predicts the interaction of the silver cluster with the first carbon atom of the chain, corresponding to the closest with the hydrogen atom. An interesting insight is provided by the analysis of the spectra, which confirm the interaction of the chain and the cluster. In fact, a general enhancement of the signal is measured, and in addition new peaks arise due to the activation of new normal modes. Raman spectra related to the polyyne C_4 interacting with Ag_4 and Ag_8 clusters are discussed and reported in Fig 3.12.

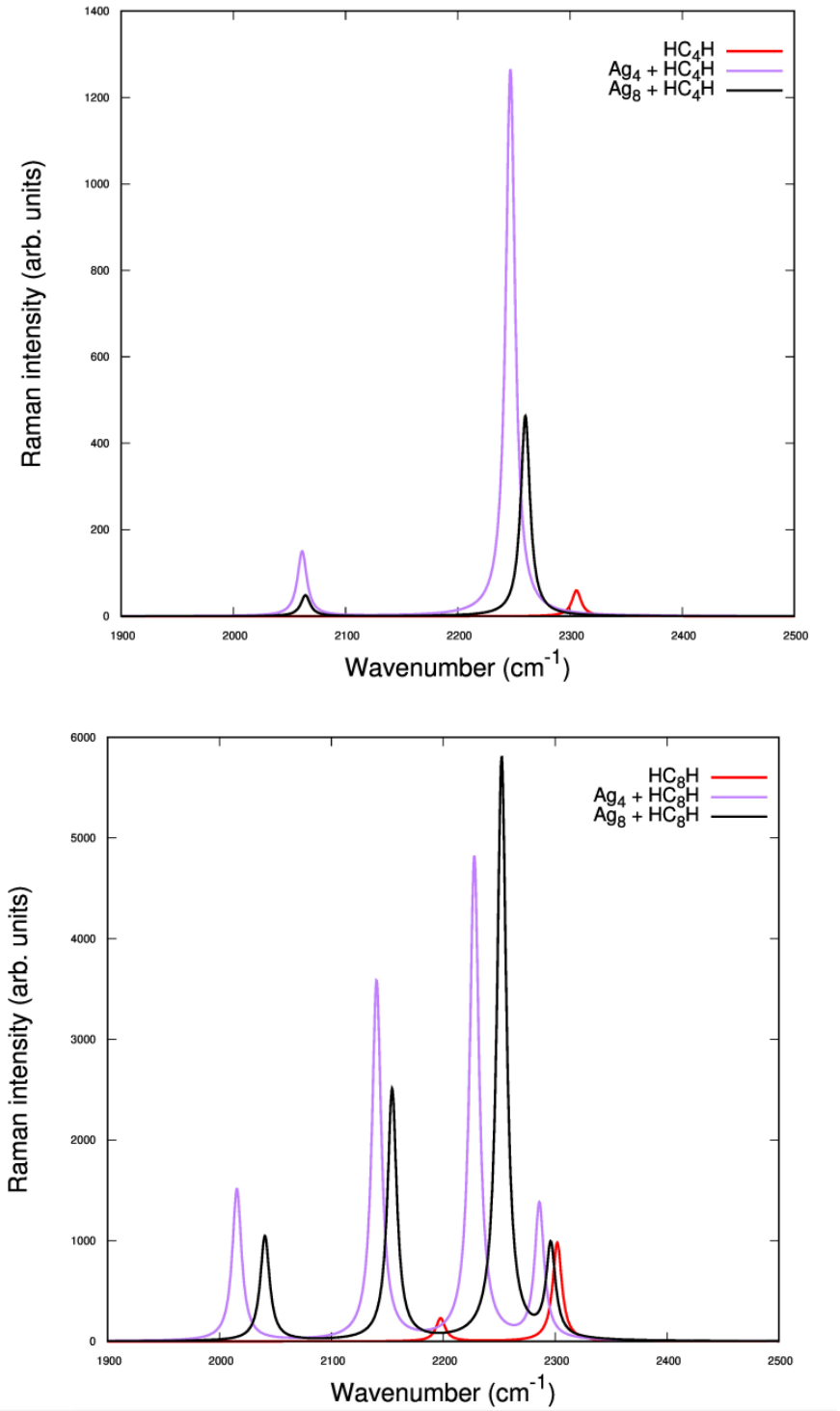

Figure 3.12: *Predicted SERS spectra of systems composed by polyyne of 4 (above) and 8 (below) atoms long and different sized clusters.*

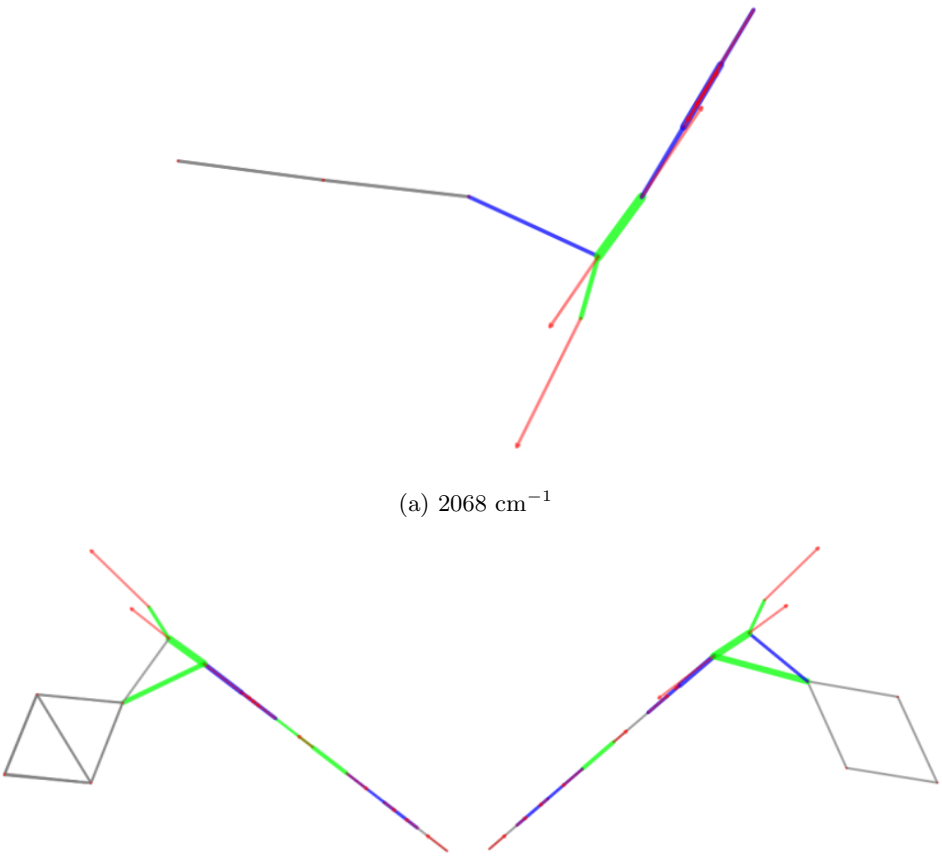

(a) 2068 cm^{-1}

(b) 2042 cm^{-1} (c) 2020 cm^{-1}

Figure 3.13: *Normal modes of vibration associated to the low frequency bands, for Ag_i + HC_iH systems, that appear due to the interaction between chain and cluster. Vibrational frequencies are also reported for each mode. Red arrows indicate atomic displacements while green and blue colors indicate the active bond stretching vibrations in each normal mode. The different colors indicate different phases of the vibration, while the line width is proportional to its amplitude.*

It is possible to observe a downshift of the most intense peak and the appearance of a peak at lower frequencies (at 2068 cm^{-1} for Ag_4 and 2072 cm^{-1} for Ag_8), which is not predicted for the isolated polyyne. The shape of the spectra suggests that the cause behind the increase in the intensities of the signals and the redshift of the peaks is not related to the interaction energy, since the latter is higher for the system with the bigger cluster (see table 3.3). Instead, by looking at the different optimized geometries, it is possible to associate the redshift and the appearance of new bands to the degree of distortion of the chain caused by the interaction with the cluster as can be appreciated in Fig. 3.10. The higher distortion seems indeed caused by the smaller cluster, which produces a more red-shifted spectrum for both HC_4H and

HC_8H (see Fig. 3.12). The rise of newly activated normal modes, not predicted for the isolated chain, is caused in principle by the peculiar interaction with the cluster, which has also the effect of distorting the chain, which in turns loses its symmetry. A possible interpretation for the smaller distortion induced by the bigger cluster (see Fig. 3.10) is that the relative difference between the size of the cluster and the polyyne is too big. In this case, it has to be expected that for longer chains the deformation produced by the bigger cluster is noticeable and more evident when compared to this situation. The appearance and nature of the low frequency peak in both dimers has been investigated with the inspection of the related vibrational eigenvectors. Taking as example the case of Ag_4 + HC_4H, since similar considerations are possible also for Ag_8 + HC_4H, it is possible to observe, in Fig 3.13, a strong contribution due to the stretching of the triple bond of the two carbon atoms in the immediate vicinity of the silver cluster, with the other bonds having an opposite behavior. This suggest a strong interaction taking place between such atoms and the cluster, causing the appearance of the associated peak at low frequencies. As for the other active mode, it resembles a modified ECC mode, further suggesting a rupture of the collective oscillation of the bonds in the isolated hydrogen-polyyne, due to its interaction with the nanoparticle. The same general considerations apply also for the case of polyyne $HC_{\ 8}H$, even if the predicted spectra are much different. Indeed, as in the case of the shorter polyyne, new peaks appear, related to new active modes, which are produced, in same fashion of the Ag_i + HC_4H systems, by the effect of the peculiar interaction with the cluster. Previously, the spectrum of the isolated HC_4H was showing a single peak while now, due to the interaction with the nanoparticle, two distinct and redshifted modes are observable; the same situation is verified for the 8 atom long polyyne: the spectra of HC_8H features two active normal modes, while the interaction with the cluster produces the activation of a total of four new modes, which are still redshifted with respect to those belonging to the isolated polyyne (3.12). The frequencies at which the peaks related to such active modes are located are: 2020, 2142, 2223, 2282 cm^{-1} for Ag_4 + HC_8H, and 2041, 2154, 2252, 2296 cm^{-1} for Ag_8 + HC_8H. The spectra for the systems Ag_i + HC_8H are also reported in Fig. 3.12. For these systems, the intensities of the peaks associated to the different clusters are much more similar in opposition with the HC_4H chain, indicating a similar deformation of the chain for each interacting cluster (see Fig. 3.10). Similarly to the case of the shorter polyyne, also in this systems the shift of the peaks can be related to the peculiar effect of the cluster that increases the conjugation of the chain. In this regard, the values of the BLA and HOMO-LUMO gap of the molecule have been calculated for HC_8H and Ag_8 + HC_8H. Specifically, the BLA is calculated as the difference between the average length of the triple bonds and the average of the single bonds of the chain; the energy gap is instead calculated during the optimization process.

The values reported in table 3.4 highlight the effect of the cluster in increasing the conjugation of the chain, as indeed both parameters decrease when the polyyne is interacting with the cluster.

System	BLA (Å)	HOMO-LUMO gap (eV)
HC_8H	0.135	4.735
Ag_8 + HC_8H	0.122	2.041

Table 3.4: *Bond length alternation, in Angstroms, and energy gap, in eV for HC_8H and Ag_8 + HC_8H. Both parameters show decreasing values upon the interaction with the cluster.*

By comparing the two plots in Fig. 3.12, it seems that the shift is independent on the size of the polyyne or of the cluster, a phenomenon that is manifesting upon the interaction of the isolated polyyne with the nanoparticle. Indeed, taking into account the eigenvectors related to the peaks located at 2247 cm^{-1} for the Ag_4 + HC_4H and the one located at 2228 cm^{-1} for the Ag_4 + HC_8H system, a similarity in the oscillation of the bonds is found. The behavior can be associated to a modification and localization of the ECC mode and it is caused again by the interaction with the cluster (see Fig. 3.13. Thus, the downshift of the considered normal mode is consistent for both systems.

In order to further quantify the interaction between carbon atoms near the cluster and the cluster itself, we decided to analyze the distance between the first two carbon atoms of the chain and the nearest silver atom. Indeed, it is possible to predict an ideal Van der Waals type of interaction whence the bond length of two atoms is equal to the sum of the their Van der Waals radii:

$$L_{bond} \approx R_1^{VdW} + R_2^{VdW} \tag{3.2}$$

The Van der Waals radii of carbon and silver are 1.70 Å and 1.72 Å respectively, while the bond lengths we are considering are 2.262 Å for the first atom, and 2.578 Å for the second one, and thus both are much shorter than the sum of the Van der Waals radii (3.42 Å). This could justify an interaction between the carbon atoms and the silver one that is stronger than a simple Van der Waals interaction, adding another interesting result in the investigation of the interaction occurring between the chain and the nanoparticle. For comparison, the values of such bond length obtained for all of the systems are reported in table 3.5.

System	Bond length (C_1-Ag)	Bond length (C_2-Ag)
Ag_4 + HC_4H	2.370	2.874
Ag_4 + HC_8H	2.241	2.865
Ag_8 + HC_4H	2.339	2.596
Ag_8 + HC_8H	2.262	2.578

Table 3.5: *Analysis of the bond lengths between the first and second carbon atom of the chain (see Fig. 3.10) and the closest silver atom belonging to the cluster. The reported values are measured in Angstroms.*

It is possible to observe that the lowest value for the first carbon are obtained for Ag_4 + HC_8H and Ag_8 + HC_8H, suggesting that the higher the conjugation on the chain, the stronger the interaction with the cluster. On the other hand, the length of the bond of the second carbon atom and the cluster is lower when the cluster itself is bigger. Thus the effects that mostly influence this parameter, and therefore the interaction between the chain and the nanoparticle are the conjugation on the chain and the size of the cluster.

Comparison with experimental data

The comparison with experimental data is necessary to check whether there exists an agreement between the computation and the experiments. The spectra reported in Fig.3.14 represent the experimental SERS spectra of a sample containing silver nanoparticles interacting with HC_8H polyyne.

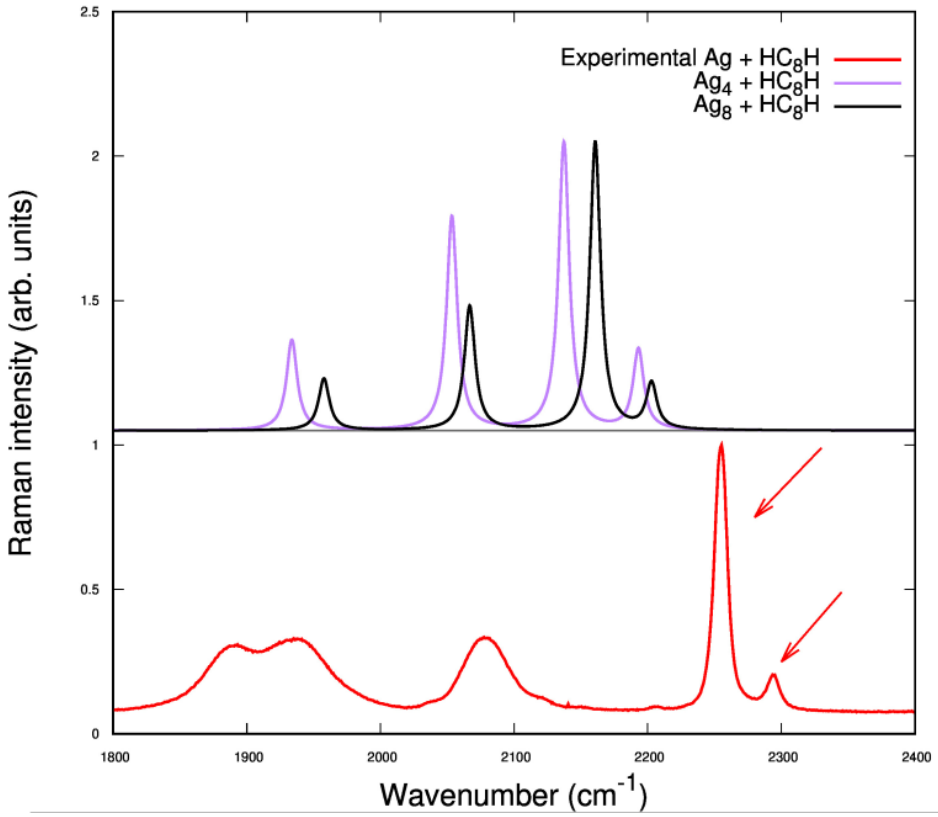

Figure 3.14: *Experimental SERS spectrum of liquid solutions of size-selected polyynes with four triple bonds [90]. The calculated spectra, in purple and black, have been scaled down. The arrows indicate the peaks related to the acetonitrile.*

The spectra obtained from the computations have been scaled down to account for the well known overestimation of the π conjugation by the hybrid exchange-correlation functional adopted (PBE0). The scale factor for the specific functional and basis-set used (i.e. PBE0 and 6-311++G(d,p)) is 0.9594, taken from the Computational Chemistry Comparison and Benchmark DataBase (CCCBDB, [88]). The red line represents the spectrum obtained experimentally, and features five peaks, which are located at about 1890, 1930, 2070, 2250, 2290 cm^{-1}. The right most peaks, i.e. at 2250 and 2290 cm^{-1} , indicated in Fig. 3.14 by the red arrows, are related to the acetonitrile solution. The peaks which represent the polyynes interacting with silver nanoparticles are those at 1890, 1930, 2070 cm^{-1}. It can be observed that there exists a non-negligible shift between the experimental measures [90] and the predicted ones even after the scaling of the values. This may be caused by the different size of the silver nanoparticles in solution, that are bigger than the model ones used in the computations. As evident, the peaks measured in the experiment are broad and cover a wide range of frequencies. This behavior is caused by the

effect of the dimensional distribution of the nanoparticles in the solution, which is in agreement with the results of the computations: the calculated spectra are in fact influenced by the dimension of the cluster. The solution experimentally prepared features silver nanoparticles of non-zero dimensional distribution and, moreover, a convolution of the measured signals, for the whole set of of different systems (i.e. silver nanoparticle interacting with the polyynes) had to be performed, thus resulting in the broadening of the mentioned peaks. In this regard, a correspondence with the calculated spectra can be individuated: broad bands arise in the experimental spectra in the range of 1850 and 1950 cm^{-1} and between 2050 and 2110 cm^{-1}. These features may be related to the different peaks predicted for hydrogen-polyynes interacting with the silver clusters.

3.3.3 Analysis of Methyl-capped and Cyano-capped polyynes

After the analysis of hydrogen polyynes interacting with silver nanopartciles, considered as a model system to test the computational setup and to obtain preliminary results, the study has been extended towards more complex CAW-based systems, i.e. methyl- and cyano-capped polyynes. The computations have been performed using the same optimized setup discussed in the previous section, i.e. PBE0 as exchange-correlation functional and 6-311++G(d,p) as basis-set. In this context this analysis was focused on the effect of the terminal group, and therefore we considered a unique chain length (i.e. 8 atoms) and cluster size (i.e. Ag_8). The predicted results have then been compared with experimental SERS data [90].

Investigation of different possible configurations between polyyne and cluster

As a first investigation of the polyyne-cluster interaction in the case of methyl-terminated chain, the interaction energies of the two possible configurations were calculated: the first one featuring the methyl group on the same side of the chain as the cluster, the other one with the CH_3 group and the nanoparticle at opposite sides of the polyyne. The calculated values are reported in table 3.6, where it is possible to see that one of the two configurations is more stable and energetically favoured, i.e. the one in which the cluster interacts with the chain in the vicinity of the CH group.

System	E_{INT} (kcal/mol)
Ag_8 + HC_8H	-6.24
Ag_8 + HC_8CH_3	-6.40
Ag_8 + CH_3C_8H	-4.88
Ag_8 + CNC_8H	-6.91

Table 3.6: *Calculated values of the interaction energies for the two different stable configurations of methyl-polyyne and the only one of cyano-polyyne. The value of Ag_8 + HC_8H is reported for comparison.*

The interaction energy increases of about 0.16 kcal/mol from Ag_8 + HC_8H to Ag_8 + HC_8CH_3, and since the values obtained differ by less then 1 kcal/mol, the obtained results are comparable with the numerical error related to the basis-sets (e.g. basis-set superposition error), or in the inaccurate description of the dispersion interactions. As for the less stable configuration, it could be suggested that the presence of the methyl group in the vicinity of the cluster has some effects on the interaction between the silver atom and the first carbon of the chain: the steric hindrance is the cause for the lower interaction energy.

Additional insights can be obtained by the analysis of the BLA and energy gap between the HOMO and LUMO, as done for the case of Ag_8 + HC_8H in the previous section. The trend of such parameters is reported in table 3.7. A comparison between the two parameters, i.e. BLA and HOMO-LUMO gap, shows that methyl and hydrogen polyyne interacting with the cluster, both approaching the same CH group, are characterized by very similar electronic conjugation and the influence of the metal nanoparticles is very similar for the two systems. Values reported for the two methyl-polyyne configurations, i.e. Ag_8 + HC_8CH_3 and Ag_8 + CH_3C_8H, indicate that the position of the methyl terminal group is slightly influencing the conjugation on the chain, but the small discrepancies of the values indicate that its effect on the interaction with the cluster has to be further analyzed.

For what concerns cyano-capped polyynes, as for the case of methyl-polyynes, the relative position of the cyano group with respect to the cluster has to be investigated. Two possible initial configurations were prepared and optimized, i.e. one featuring the cyano group and the silver cluster on the same side, the other on opposite sides but, differently from the methyl polyyne, both the optimization processes converged to very similar geometries, each of them featuring the silver cluster on the opposite side of the cyano group; this suggests only one energetically possible configuration for these interacting monomers, as the CN group does not represent a preferential site for the interaction with

the cluster. Focusing the attention on the analysis of the interaction energies, as for the comparison with the values obtained in the hydrogen-polyynes, the difference is 0.67 kcal/mol as can be seen in table 3.6. This increase can be associated to the higher electronic conjugation of the chain, already discussed for the case of methyl-polyyne and present also in cyano-polyyne. Indeed, the values reported for the Ag_8 + HC_8CN dimer (table 3.7) indicate a strong decrease in both BLA and energy gap, as already seen in the case of both the hydrogen-polyynes and methyl-polyynes.

System	BLA (Å)	HOMO-LUMO gap (eV)
Ag_8 + HC_8H	0.122	2.041
Ag_8 + HC_8CH_3	0.121	2.095
Ag_8 + CH_3C_8H	0.127	2.204
Ag_8 + HC_8CN	0.103	1.361

Table 3.7: *Calculated values of the BLA, in Angstroms, and energy gap, in eV for the two different stable configurations of methyl-polyyne. The value of Ag_8 + HC_8H is reported for comparison.*

The implications related to the two different configurations have been also investigated by the analysis of the spectra for the methyl-polyyne. The spectra for both the configurations are compared to the spectrum of the isolated methyl-polyyne in Fig. 3.15. Some differences are visible: for the case of Ag_8 + HC_8CH_3 there is a modification in the overall shape of the Raman spectrum, possibly caused by the way the chain interacts with the cluster and the magnitude of such interaction. On the other hand, the spectrum of the system with the cluster and the methyl end group on the same side resembles the one of the isolated chain, but is redshifted.

Raman spectra analysis

The same effect shown for the case of hydrogen-polyynes can be observed for the system Ag_8 + HC_8CH_3: the interaction of the cluster with the carbon atoms in its vicinity influences the activation of a normal mode, which localizes in the portion of the chain closest to the nanoparticle, at about 2050 cm^{-1}. Also in this case we can hypothesize that a decrease in the force constant of the triple bond of the two carbon atoms interacting with the cluster is taking place, and this is caused by the interaction itself. This results in the activation of that low frequency normal mode.

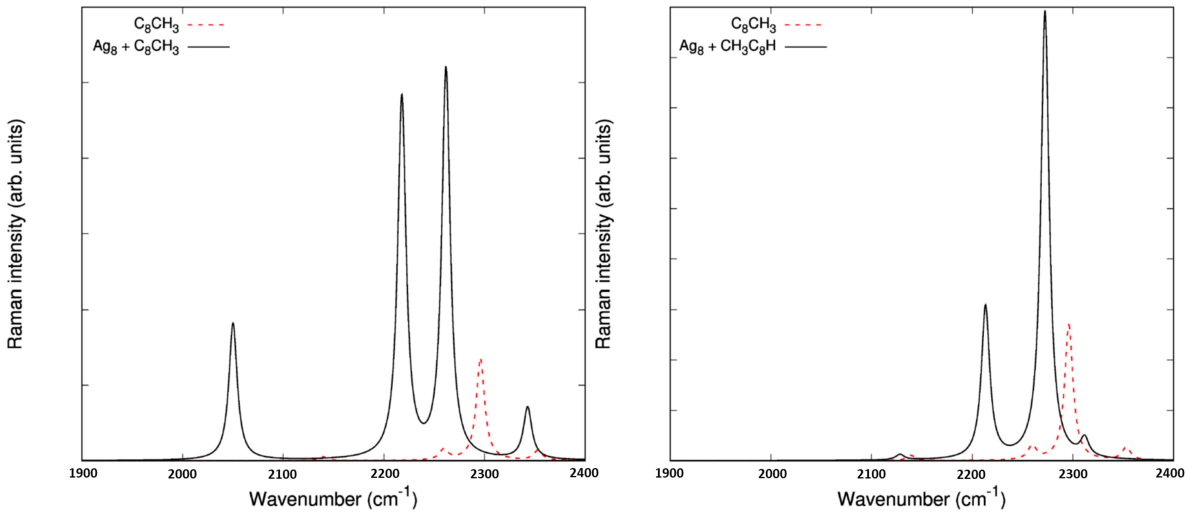

Figure 3.15: *Non-normalized spectra of:* HC_8CH_3 *and* Ag_8 *+* HC_8CH_3 *(left);* HC_8CH_3 *and* Ag_8 *+* CH_3C_8H *(right).*

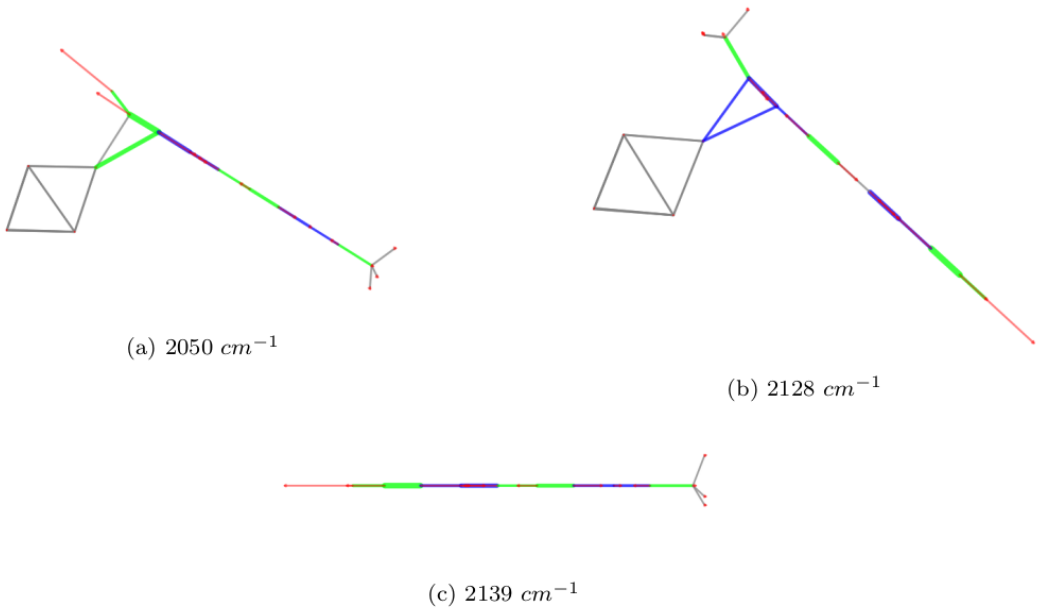

(a) 2050 cm^{-1}

(b) 2128 cm^{-1}

(c) 2139 cm^{-1}

Figure 3.16: *Eigenvectors associated to the low frequency normal mode for a)* Ag_8 *+* HC_8CH_3*, b)* Ag_8 *+* CH_3C_8H*, c)* HC_8CH_3*. The difference in the oscillation between a) and b), c) is visible. The frequencies of the normal modes are also reported.*

Furthermore, the enhancement of the peak at 2218 cm^{-1} is due to a modification of the ECC mode, that is now focused on the specific part of the chain where the nanoparticle interacts with the polyyne; such peculiar interaction is

also the cause for the modification of the ECC mode. The same consideration applies for the peak at 2343 cm^{-1}. Instead, for the Ag_8 + CH_3C_8H system, the presence of the methyl group on the same side of the cluster weakens the interaction of the cluster itself with the carbon atoms, resulting only in a shift of the signals, as indeed the overall shape of the spectrum is similar to the isolated polyyne case: there is an enhancement in the intensity of each mode, and the low frequency peak does not appear. To better assess such enhancement of the signals due to the interaction with the cluster, the non-normalized spectra are reported in Fig. 3.15 for both configurations. The analysis of the eigenvectors associated to the normal modes, reported in Fig. 3.16, could provide some interesting insights: a similar shape between the eigenvectors of the normal modes of the system Ag_8 + $CH_3C_{\ 8}H$ and the isolated methyl-polyyne can be expected, while a modification in the nature of the oscillation of the bonds should be expected in the case of Ag_8 + HC_8CH_3 , especially for the low frequency normal mode, similarly to the case of the hydrogen-polyynes. In this regard, the eigenvectors related to the low frequency normal mode of Ag_8 + HC_8CH_3, Ag_8 + CH_3C_8H and HC_8CH_3 are reported. In Fig. 3.16 it is possible to see a comparison of the low frequency mode for both the configurations and the isolated polyyne. The different behavior of the Ag_8 + HC_8CH_3, highlighted in Fig. 3.16a, is caused by the interaction with the cluster, that is inducing a modification in the triple bond of the first two carbon atoms of the chain. By looking at the eigenvectors related to Ag_8 + CH_3C_8H and HC_8CH_3, it is possible to observe similarities with the one of Ag_8 + HC_8CH_3, but the analysis of the spectra underlines huge differences: an higher relative intensity and especially a noticeable shift (of about 100 cm^{-1}) are predicted for the peak of Ag_8 + HC_8CH_3 with respect to the isolated polyyne. The behavior of Ag_8 + CH_3C_8H is instead different with respect to Ag_8 + HC_8CH_3: the low frequency peak is absent, and the reason is the position of the methyl group on the same side of the cluster, that weakens the interaction of the silver cluster with the first two atoms of the chain. The observation of the eigenvectors associated to the most intense peak, located between 2260 and 2300 cm^{-1}, reported in Fig. 3.17 further confirms the different behavior induced by the position of the end group. In fact, the oscillations of the bonds in the case of the Ag_8 + CH_3C_8H are associated to the ECC mode, visible also in the isolated polyyne; on the other hand, the same normal mode for the system Ag_8 + HC_8CH_3 highlights a localization of the oscillations on a specific part of the chain, and this is mainly caused by the peculiar interaction with the cluster. Moreover, the oscillations of the bonds of Ag_8 + HC_8CH_3 (Fig. 3.17a) can be related to a modified ECC mode, focused only on a specific part of the chain; on the other hand, a collective ECC oscillation is visible in the case of both the isolated methyl-polyyne (Fig. 3.17c) and the Ag_8 + CH_3C_8H system. The nature of the interaction with the cluster is again the probable cause for the differences

in the eigenvectors: for the Ag_8 + HC_8CH_3 system, the interaction with the cluster is stronger, and causes the activation of localized normal modes. On the other hand, the methyl group on the same side of the cluster has a shielding effect, which results in a weakened interaction between the nanoparticle and the polyyne, preventing the strong localization of the ECC mode, and thus causing the similarities in the eigenvectors of Ag_8 + CH_3C_8H and HC_8CH_3. The situation changes again for the other two peaks, located at about 2200 cm^{-1} and at about 2350 cm^{-1}. For each system, the peak at $\approx$ 2200 cm^{-1} can be associated to a different collective oscillation of the carbon-carbon bonds. Moreover, the strong interaction with the cluster is underlined by the high intensity of the peak of Ag_8 + HC_8CH_3 with respect to the other two systems. As for the Ag_8 + CH_3C_8H system, we have seen that the overall behavior is basically the same showed in the isolated polyyne, but the oscillation is more localized on the triple bond of the two initial carbon atoms of the chain. The right-most peak, at $\approx$ 2350 cm^{-1}, is instead related to a localized oscillation on the side of the methyl group in the case of the HC_8CH_3 and Ag_8 + HC_8CH_3 systems. As it is possible to see in the spectra (3.15), these peaks are predicted in both those systems, and have a similar frequency and intensity, with a downshift in the case of the interaction with the silver cluster, due to the already discussed effect of the interaction of the cluster itself with the chain, causing an increased conjugation on the chain. On the other hand it is evident a difference in the spectrum of the other systems, i.e. Ag_8 + CH_3C_8H. In this case, the position of the methyl group on the same side of the cluster results in a lower frequency and intensity; the cause of this behavior is the presence of the cluster itself, which screens the effect of the methyl group on the chain. Summarizing, the analysis of the spectra and the eigenvectors highlights a very different behavior caused by the relative positions of the end group and the silver cluster. In one case, with the cluster opposite to the methyl group, the behavior observed is similar to the case of hydrogen-polyynes, suggesting a strong interaction between the molecular orbitals of the nanoparticle and those of the first carbon atoms of the polyyne, causing the appearance of the low frequency mode. The geometry of the chain is also influenced, and this is visible by the enhancement of the signals and by the localization of the collective oscillations on the side of the cluster. On the other hand, when the cluster is on the same side of the methyl group, the interaction effect is weakened, and in fact the low frequency mode is not detected, since the interaction is different with respect to the Ag_8 + HC_8CH_3 system. Furthermore, the shape of the spectra is similar to that of the isolated polyyne, with the difference in the enhancement of the intensity of the peaks, as visible in Fig. 3.15. The cause could be the hindering effect of the methyl group, which weakens the interaction between the chain and the cluster, thus preventing the modification of the ECC mode. The interaction with the nanoparticle also causes differences in the behavior of the other peaks

as well: the one close to 2200 cm^{-1} is a result of the modification of the ECC mode, and its intensity is grater for Ag_8 + HC_8CH_3, while mildly increased in the case of Ag_8 + CH_3C_8H. The last peak, located at about 2350 cm^{-1}, moves closer to the high intensity peak in the case of Ag_8 + CH_3C_8H due to the fact that the methyl group is on the same side of the cluster, and thus the bonds influenced by such end group are involved also in the interaction with the cluster, while in the other two cases are free to vibrate, and indeed the peaks for HC_8CH_3 and Ag_8 + HC_8CH_3 are similar in frequency and intensity.

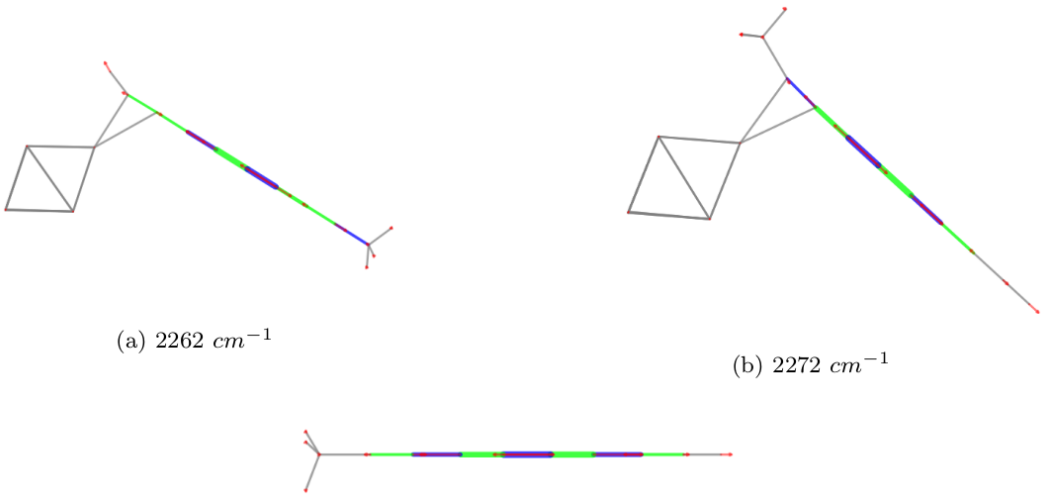

(a) 2262 cm^{-1}

(b) 2272 cm^{-1}

(c) 2296 cm^{-1}

Figure 3.17: *Eigenvectors associated to the highest intensity normal mode for a) Ag_8 + HC_8CH_3, b) Ag_8 + CH_3C_8H, c) HC_8CH_3. The frequencies of the normal modes are also reported.*

For the case of cyano-terminated polyynes, the predicted spectra were investigated and are reported in Fig. 3.18. The observation that can be done are in general those already reported for the other studied systems, i.e. hydrogen-polyynes and methyl-polyynes. An enhancement of the peaks can be observed (Fig. 3.18), with the already mentioned low frequency mode arising in the left side of the spectra, at 2020 cm^{-1} and 1999 cm^{-1} for the Ag_8 + HC_8CN and Ag_8 + CNC_8H respectively. The nature of this peak can be assessed by the inspection of the eigenvectors, that are very similar to the case of hydrogen-polyynes and methyl-polyynes (see Fig. 3.12 and 3.15). Indeed, the same behavior showed in the case of hydrogen-polyynes and methyl-polyynes, is observed. The peak located at about 2010 cm^{-1} is associated to the oscillation of the triple bond interacting with the cluster.

The eigenvectors of the system Ag_8 + HC_8CN are very different from the

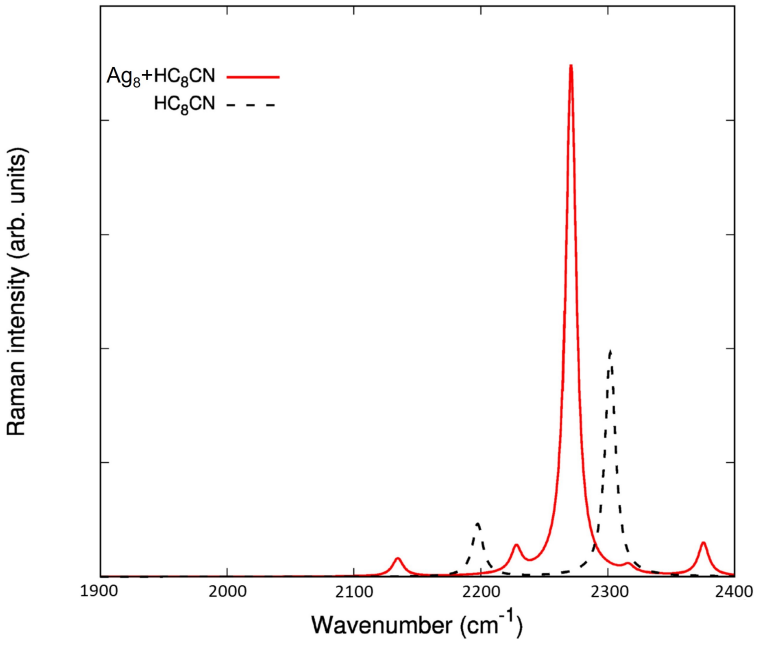

Figure 3.18: *Non-normalized spectra of HC_8CN and Ag_8 + HC_8CN.*

ones of the isolated cyano-polyyne. The nature of the low frequency peak is then determined by the peculiar interaction between the polyyne and the nanoparticle. Similarly to the other investigated systems, a modification in the internal force constants is expected, as well as a modification of the bond lengths. Due to the increase interaction energy calculated for cyano-polyynes with respect to methyl- and hydrogen-polyynes, a shorter silver-carbon bond (i.e. between the closest silver atom and the closest two atoms of the chain) should also be predicted. As for the peak located at 2169 cm^{-1} for Ag_8 + HC_8CN, the analysis of the eigenvectors suggests a behavior already seen in the other cases (methyl and hydrogen): the modes resemble the ECC one, but localized only on the extreme of the chain. Also in this case the eigenvectors are similar for both dimers, while are very different from those of the isolated polyyne. The effect of the cluster is then again underlined: it modifies the nature of the normal modes of the chain. Another peak is predicted at 2287 cm^{-1} for Ag_8 + HC_8CN and represents again a localized mode on the central bonds of the chain. This peak is not predicted for the isolated polyyne: this may indicate that such normal mode is enhanced by the interaction with the cluster. At last, the peak at high frequencies, specifically at 2363 cm^{-1} is associated to the vibration of the triple bond of the C≡N group. This is observed also for the isolated polyyne. The fact that its characteristics are not altered by the presence of the cluster is due to the distance that these

two have between them and also by the fact that the cyano triple bond is one of the strongest in nature. In this regard, a possible explanation for the instability of system featuring the cluster on the same side of the CN group could be suggested on the base of the electronegativity of such terminal group: the high electronic density found on the CN group at the end of the chain, differently from the CH terminal group, may be the cause of the impossibility to instantiate a stable interaction with the cluster. However, more in detail analysis should be carried out in order to better investigate this behavior.

Comparison with experimental data

As a final investigation, the predicted results for methyl- and cyano-terminated polyynes have been compared with the experimental data obtained by Peggiani et al. [90], in order to verify whether the results obtained from the calculations may be in agreement with experimental measures. In Fig. 3.19 are reported the comparison between computed and experimental Raman spectra for the analyzed species. The experimental spectra has been obtained from a solution of acetonitrile, which is causing an high intensity peak at 2350 cm^{-1}. The frequencies considered and reported in the spectra do not show the peaks related to the acetonitrile solution, which contains cyano- and methyl-polyynes of the same length of those investigated in this chapter, interacting with silver nanoparticles of various dimensions. As for the case of hydrogen polyynes, the calculated spectra have to be scaled down, with a factor of 0.9594 in order to correct the approximations assumed by using DFT methods regarding the chain's conjugation. The scale factors for the specific functional and basis-set used (i.e. PBE0 and 6-311++G(d,p)) are again taken from the Computational Chemistry Comparison and Benchmark DataBase (CCCBDB [88]).

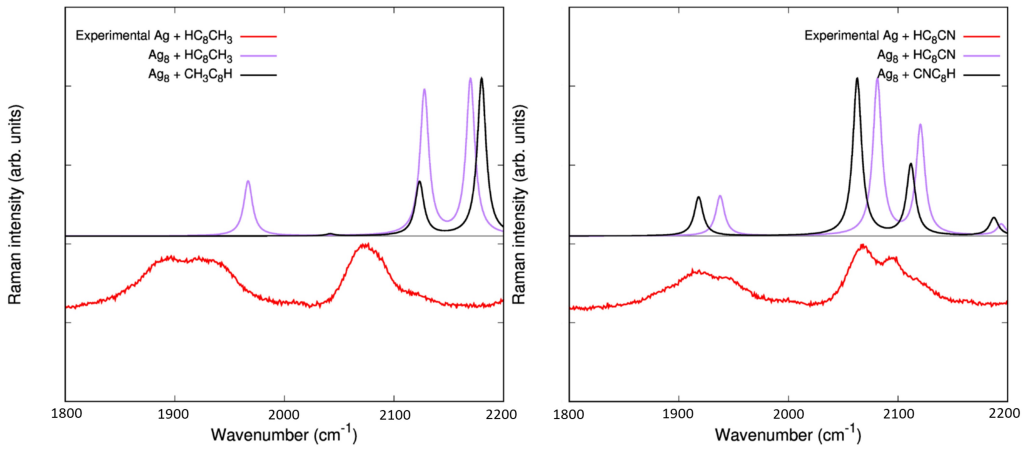

Figure 3.19: *Experimental SERS spectrum of liquid solution of size-selected polyynes. On the left: comparison of SERS experimental measure with predicted SERS signals of methyl-polyynes. On the right: comparison of experimental SERS and predicted SERS for cyano-polyynes [90].*

The peaks measured for methyl-polyynes are found at about 1910 and 2080 cm^{-1}. The calculated spectra predict peaks for the methyl-polyynes at about 1950 cm^{-1} for the low frequency peak, and between 2100 and 2200 cm^{-1} for the other high intensity bands. It would seem that both the low frequency signal and the other peaks are not precisely located at similar frequency, but overall the proposed model featuring a silver cluster interacting with the polyyne successfully describes the low frequency band, whereas the charged species model fails to do so. The reason behind the discrepancies between the experimental data and the calculations may be the influence of the size of the nanoparticle, which is larger in the case of the experiment, and therefore causes a downshift of the normal modes, as hypothesized when discussing the effect of the shape of the cluster in the analysis of the calculated results for cyano-polyynes. The broadening of the peaks measured in the experiment may be caused by the already discussed effect of the convolution of the various signal for the systems present in solution, i.e. polyynes interacting with nanoparticles of different sizes. It would seem that the low frequency normal mode in the experimental spectrum suffers more from this effect, even if the predicted spectra only show a high intensity low frequency peak for the Ag_8 + HC_8CH_3 system. However, a lower equilibrium energy was calculated for the Ag_8 + CH_3C_8H system, which indicates that most of the synthesized dimers should possess the Ag_8 + HC_8CH_3 configuration. Furthermore, the broadening effect may also be influenced by the specific interaction with the nanoparticle: the dimensions of the cluster is much greater with respect to the size of the chain, and thus a small difference in the local interaction site may result in the broadening of the

peaks. However, the effect of the local properties of the interaction sites have been correctly assessed by the studied model. As for the signal at about 2080 cm^{-1}, it may be associated to the high intensity normal modes reported in the calculated spectra. As visible, the broadening of the measured peak is not intense as for the case of the low frequency mode. Finally, the peaks predicted in the case of the calculated spectra at frequencies greater than 2200 cm^{-1} have probably a too low intensity to be detected in the experimental analysis. As for the cyano-polyynes, the frequencies measured in the experiment are similar to those of the methyl-polyynes, i.e. the low frequency normal mode is located at about 1910 cm^{-1} and the other at about 2070 cm^{-1}. For the latter, the presence of a shoulder is to be noted, representing a similar effect highlighted also by the asymmetry of the same band measured in the methyl-polyynes: the shape of peaks underlines the presence of different systems in solution. On the other hand, the predicted spectra is in good agreement concerning the frequency related to the low frequency peak, which is located at around 1900 cm^{-1}. The other peaks appearing in the experimental spectrum are predicted to be between 2030 and 2110 cm^{-1}. The shape of the experimentally measured peaks is also in agreement with the calculations. Indeed, for the low frequency normal mode, the broadening of the signal may be due to the effect of the different possible cluster's configurations, as already discussed, and in this case particularly visible by observing the predicted spectra (in black and purple, in Fig. 3.19). As for the measured peaks at about 2080 cm^{-1}, it may be observed a good agreement with the predicted spectra. Indeed, the convolution of the theoretical spectrum for the Ag_8 + HC_8CN resembles the experimental spectrum, which is in fact a confirmation on the hypothesis proposed for the effect of the different cluster's shape. As visible, in both the calculated spectra, the peak at about 2110 cm^{-1} is less intense than the close peak at 2030 cm^{-1}, so that the former may appear as a shoulder of the latter. Finally, similarly to the case of methyl-polyynes, the peaks at frequencies above 2180 cm^{-1} are related to modes that are probably too weak to be detected in the experimental measures.

For future developments, it would be interesting to extend the computational set to more extended clusters that more resemble the dimension of a real SERS nanoparticle. On the other hand, it is not straightforward to predict the interaction between bigger clusters (Ag_i with i>8) and polyynes. Indeed, bigger nanoparticles would result in a very high computational cost by using the selected levels of theory. For bigger nanoparticles (Ag_i with 8<i<60), the use of LANL2DZ pseudopotential and basis sets [92] would be useful to give good results at a reasonable computational cost. Increasing the cluster dimension more than 8 atoms, following the discussed trend, we expect an increase in the interaction energy between polyyne and nanoparticle, tending towards saturation. The frequency dependence of the main bands is more complex to be

predicted because I noticed that it depends on the local interaction between cluster and polyyne. Following the observed trend, we would expect a progressive lower frequency shift of the peaks increasing the size of the cluster but also the local arrangement of the cluster atoms (coordination number of the Ag atoms approaching the wire) would play an important role in determining enhancement and shift of the main Raman active bands.

3.4 Diradical ground state character in end-capped cumulenes and analysis of their charged states for transport properties prediction

In this section I combined complementary computational techniques, spanning from broken symmetry (BS) DFT-based approach to fractional occupation orbital density analysis (FOD) and CASSCF-based methods for the analysis of different end-capped cumulenic species. The aim was to highlight the diradicaloid character of their electronic structure, representing the fingerprint of multi-reference electronic configurations involved in the description of the ground state wavefunction. Within the frame of BS-DFT approach, I have computed the BLA pattern for each synthesized end-capped species comparing our data with experimental results. Then, after the evidence of a diradical ground state character, investigation of the excited states, together with the calculation of the reorganization energies, was done for the same set of cumulenes, but also for hydrogen polyynes, taken as a reference model of polyynic systems. Indeed, the reorganization free energy describes the electrostatic response of the surrounding medium to changes in the charge state of an active region, such as in a charge transfer between two neighboring molecules, thus being fundamental to describe charge transport properties of organic materials. This analysis was stimulated by the fact that the diradicaloid character was suggested to be the key for tuning the nonlinear optical properties of carbon chains, thus maximizing the quantum yield of processes, such as two-photon absorption and singlet exciton fission, that could be fundamental in optoelectronic devices.

3.4.1 Computational Details

DFT calculations were employed for the geometry optimization and vibrational frequency calculation of each end-capped cumulenic species, namely n[H], n[Ph], n[Mes], n[tBuPh], n[Fl], with n the number of carbon-carbon (CC) bonds in the chain. Each system was firstly optimized in its singlet closed shell ground electronic state, hereafter referred as CS-DFT. All molecules investigated in our study are depicted in Figure 3.20. The BLA parameter was calculated as the absolute value of the difference between the central bond length of the chain

and the mean bond length value between the two adjacent bonds (BLA = $R_{central} - R_{nn}$), as defined by Tykwinski et al. [93] Only molecules with odd n were investigated, allowing the comparison between the theoretical and the experimental results [25].

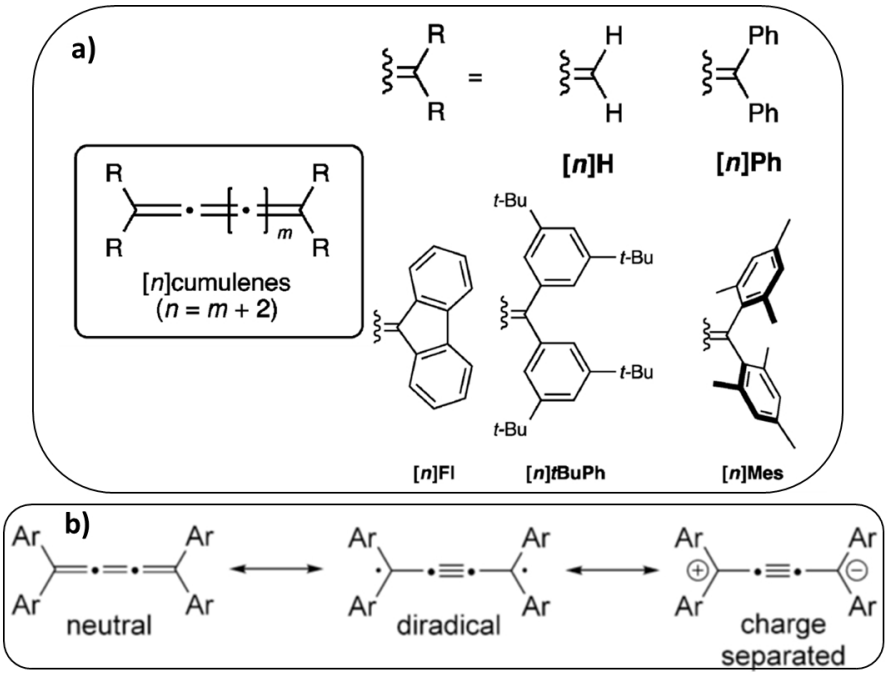

Figure 3.20: *Panel a): chemical structures of the end-capped cumulene species analysed in this work. End groups are: vinylidene (n[H]), phenyl (n[Ph]), di-tert-butylphenyl (n[tBuPh]), mesityl (n[Mes]) and fluorene (n[Fl]), as taken from Ref. 12. Panel b): different exemplary electronic resonance forms for tetraaryl[3]cumulene are reported at the bottom, taken from Ref. [29]*

To verify the presence of possible lower energy solutions in the ground and excited states of these cumulenes, we performed a DFT wavefunction stability check by adopting the BS scheme within the spin-polarized unrestricted DFT approach (BS-UDFT), also referred as open-shell singlet [35,94]. If a wavefunction instability is found, both the electronic and nuclear structures are further re-optimized following the BS-UDFT potential energy surface (PES), as already deeply described in literature [95–97]. The BLA was then recomputed accordingly and compared with the CS-DFT solutions. When possible, computational data were compared with respect to the experimental values [26]. A BS solution at the DFT level implies the presence of at least a low-lying triplet state (T) [98]. This T state was also optimized at the UDFT level for each system. Given the ground state energies, we calculated the energy difference between the open-shell (BS-UDFT) and the closed shell (CS-DFT) singlet

states, such as ΔE_{BS-CS} = E(BS)-E(CS), and between the triplet (T) and the closed shell singlet (CS) ground state solutions, namely ΔE_{T-CS} = E(T)-E(CS) for each chain length. Yamaguchi correction scheme [99] was applied for the singlet-triplet gap as follows:

$$E_{T^i} - E_{S^i} = \frac{\langle S^2_{T^i}\rangle (E_{T^i} - E_{BS^i})}{\langle S^2_{T^i}\rangle - \langle S^2_{BS^i}\rangle} \tag{3.3}$$

E_T, E_S, and E_{BS} represent the energy of the triplet, singlet, and BS solutions, respectively, and $\langle S^2_{T^i}\rangle$ and $\langle S^2_{BS^i}\rangle$ are the expectation value of the square of the total spin operator for the triplet and BS solutions, respectively. To access the electronic correlation effects and to compute the number of correlated electrons for each system we performed, both for ground and excited states, finite-temperature (FT)-DFT calculations within the frame of the fractional occupation number weighted electron density (FOD) analysis, as introduced by Grimme and Hansen [83]. The FOD analysis revealed to be a practical tool for the characterization of static electron correlation (SEC) in diradicaloid systems [100, 101], and it has been recently used in combination with BS-UDFT analysis to address and quantify the diradicaloid character in conjugated molecules and polymers [97, 98]. To strengthen our BS-UDFT and FOD analyses, we computed the diradical/tetraradical indices y_0/y_1 for each cumulenic species. These indices, as introduced by Nakano [98], are defined by the occupation number (n) of the lowest unoccupied natural orbitals (LUNO and LUNO+1, respectively), and they can be considered as descriptors of the diradical/tetraradical character of a molecule. y_0 and y_1 were computed as: $y_0 = n_{LUNO} = 2 - n_{HONO}$, $y_1 = n_{LUNO+1} = 2 - n_{HONO-1}$, where n was derived by the FT-DFT calculations. All calculations were performed adopting the range-separated functional CAM-B3LYP and (for some cases) the ωB97X-D. The choice for a range-separated functional was motivated to minimize the self-interaction energy (SIE) and to possibly mitigate SEC effects peculiar of the DFT method. The basis set considered belongs to the Dunning's correlation consistent sets, namely the triple-split cc-pVTZ. For long chains (n = 7,9) or bulky terminals ([Mes], [tBuPh]), a reduced Pople 6-31G** set was adopted. Both CAM-B3LYP and ωB97X-D resulted in open-shell singlet BS solutions for certain lengths of the chains. To take into account correlation effects in a different way, though still within the DFT frame, we performed calculations considering the B97-3c functional. The latter was recently introduced by Grimme et al. [102] to effectively treat strongly correlated systems, and it was particularly suggested for compounds showing partial multi-reference character. To complete our analysis and to corroborate the broken-symmetry DFT results, which suggest a partial multireference character of the ground state wavefunction, we performed also CASSCF calculations on vinylidene-capped cumulenes n[H]. The CASSCF active spaces were initially designed on the basis

of the FOD analysis. All orbitals showing a fractional occupancy lower than 1.98 or higher than 0.02 were included in the active space. Energies of the ground and excited CASSCF states were corrected via the 2^{nd}-order n-electron valence state perturbation theory (NEVPT2) corrections [103]. All calculations were performed by combining the use of Gaussian09 [85] and ORCA 4.2.1 [104] codes. Lastly, I also calculated, by means of the so-called four-point scheme, the inner-sphere contributions to the reorganization energy for all the analysed molecules according to the following equation:

$$\lambda_{in} = [E^C_{tot}(R_n) + E^N_{tot}(R_C)] - [E^C_{tot}(R_C) + E^N_{tot}(R_N)] \tag{3.4}$$

Denoting E^C_{tot} and E^N_{tot} the total energies of charged and neutral donor and acceptor fragments, respectively, and by R_C and R_N the equilibrium geometries adopted by the charged and neutral fragments. Indeed, the reorganization free energy occurring in polaron hopping rate theories is in general a long-range property describing the electrostatic response of the surrounding medium to changes in the charge state of an active region, such as in a charge transfer between two neighboring sites.

3.4.2 Appearance of broken-symmetry DFT solutions by lengthening the carbon chain: evidences of diradicaloid resonant structures

For each species we considered chain lengths from n = 3 to 9, to be able to compare our results with published experimental data. As reported in Table 1, we can observe that by increasing the chain length a broken-symmetry solution (BS-UDFT) appears, generally starting from n $\geq$ 5 or 7. The stabilized energy for the BS solution with respect to the CS one (ΔE_{BS-CS}) increases by lengthening the chain, reaching -0.2 eV for 9[Fl]. At the same time, the triplet state T stabilises by increasing the chain length, lowering its energy with respect to the CS DFT solution, and reaching ΔE_{T-CS} values even lower than 0.2 eV (Table 3.8). Such behaviour agrees with and justifies the presence of low-lying BS solutions (i.e., open-shell singlet state) [105–107] for long cumulenic chains. ΔE_{T-BS_Y} values corrected by applying the Yamaguchi scheme, i.e. taking into account the spin contamination values, are also reported in Table 3.8. Considering the effect of the end-groups, BS solutions are much stabilised by the fluorene terminals and less by the vinylidene ones. Diaryl-based terminations, such as [Ph], [Mes] and [tBuPh] show similar effects, lying in between the vinylidene and fluorene groups.

species	ΔE_{BS-CS}(eV)	ΔE_{T-CS}(eV)	ΔE_{T-BS}	$\langle S^2\rangle_{BS}$	N_{FOD}	y_0/y_1
3[H]	-	1.42	-	-	0.06	0.029/0.000
5[H]	-	0.89	-	-	0.21	0.100/0.006
7[H]	0*	1.93	1.93	0	0.44(0.44)	0.186/0.032
9[H]	-0.04	1.55	2.07	0.46	0.70(0.74)	0.270/0.079
3[Ph]	-	1.00	-	-	0.39	0.164/0.005
5[Ph]	-	0.55	-	-	0.59	0.264/0.011
7[Ph]	-0.04	0.27	0.37	0.30	0.83(0.93)	0.344/0.045
9[Ph]	-0.15	0.05	0.44	1.09	1.09(1.25)	0.411/0.104
3[Mes]	-	1.47	-	-	0.37	0.157/0.006
5[Mes]	-	0.70	-	-	0.59	0.256/0.014
7[Mes]	-0.02	0.41	0.46	0.12	0.84 (0.88)	0.344/0.054
9[Mes]	-0.10	0.19	0.53	0.90	1.12 (1.21)	0.417/0.117
3[tBuPh]	-	1.00	-	-	0.43	0.184/0.006
5[tBuPh]	0*	0.54	0.54	0	0.66 (0.67)	0.291/0.013
7[tBuPh]	-0.05	0.27	0.40	0.38	0.90 (0.99)	0.367/0.053
9[tBuPh]	-0.16	0.06	0.59	1.26	1.17 (1.31)	0.431/0.117
3[Fl]	-	0.82	-	-	0.63	0.294/0.008
5[Fl]	0*	0.45	0.46	0.02	0.84 (0.87)	0.392/0.008
7[Fl]	-0.08			0.48	1.08 (1.20)	0.473/0.040
9[Fl]	-0.20	-0.02	0.44	1.22	1.33 (1.50)	0.535/0.094

Table 3.8: *Numerical values of NFOD, y_0/y_1, ΔE_{BS-CS} (eV), ΔE_{T-S} (eV),ΔE_{T-BS_Y} (eV, corrected by the Yamaguchi scheme), $\langle S^2\rangle$ (of the BS–UDFT solution) for all the analysed molecules, calculated at CAM-B3LYP/cc-pVTZ level of theory (CAM-B3LYP/6-31G(d,p) for n[Mes] and n[tBuPh] species). The * stands for an energy difference between the BS and the CS solutions lower than 10^{-4} eV*

The appearance of BS solutions would suggest (within the DFT limits) the presence of a multi-reference electronic structure, showing diradicaloid character, with spin-α and β spatially separated and localized at the extremes of the linear chain [95, 100]. Values for the spin contamination ($\langle S^2\rangle$) of the BS solutions are also reported in Table 3.8, in order to evaluate the quality and range of validity of our DFT calculations. BS-UDFT solutions are by definition spin-contaminated [108–112], however in our case $\langle S^2\rangle$ is moderate and acceptable up to n = 7. For the case of n[H] species we considered chain lengths up to n = 20, and the BS solutions for n > 9 result to be highly contaminated, with $\langle S^2\rangle$ larger than 1 as reported in Table 3.9. The same occurs for the chain length n = 9 of [Ph], [Mes], [tBuPh] and [Fl] (Table 3.9), however we considered instructive to report such species in the main text for comparing (see next section) their structural parameters with respect to the experimental available data.

species	$\langle S^2 \rangle$
7[H]	0.00
9[H]	0.46
11[H]	1.61
13[H]	2.78
15[H]	3.58
17[H]	4.00
19[H]	4.17
9[Ph]	1.09
9[Mes]	0.90
9[tBuPh]	1.26
9[Fl]	1.22

Table 3.9: $\langle S^2 \rangle$ *(of the BS–UDFT solution) for n[H] cumulenes, with n ranging from 7 to 20, and 9[Ph], 9[Mes], 9[tBuPh] and 9[Fl], calculated at CAM-B3LYP/cc-pVTZ level of theory (CAM-B3LYP/6-31G(d,p) for n[Mes] and n[tBuPh] species)*

To better quantify the diradicaloid character and the electronic correlation effects of cumulenes, we computed the N_{FOD} and the diradical/tetraradical y_0/y_1 numbers, as reported in Table 3.8. Both N_{FOD} and y_0/y_1 indexes increase by lengthening the chain, reaching significant high values (> 1.00) for the [Fl] species with $n \geq 7$ (see Table 3.8). Generally, $N_{FOD} \geq 0.5$-0.6 would suggest strong correlation effects and the presence of multireference wavefunctions, as reported in literature [83]. Parallel, $y_0 \geq 0.2$ would indicate a marked diradicaloid character [105]. For long chains, $n = 7, 9$, N_{FOD} is approaching or exceeding 1 for the diaryl- and fluorene end-capped species, with y_0 reaching values up to 0.4. Such values are consistent with the presence of BS solutions, suggesting a pronounced diradicaloid character for long (generally $n \geq 5$ or 7) cumulenic chains. Considering the different end-capped species, both N_{FOD} and y_0/y_1 parameters increase by following the trend [H] < [Ph] < [Mes] < [tBuPh] < [Fl], therefore showing marked diradicaloid character for diaryl-tert-butyl and fluorene terminal groups. Within the diaryl end-capped chains, [tBuPh] groups show higher N_{FOD} and y_0/y_1 than [Ph] and [Mes]. Our calculations confirm the parallelism between the presence of BS-UDFT solutions and high N_{FOD}, y_0/y_1 values, leading to multireference diradicaloid structures, as previously suggested by Negri et al. [100] To further corroborate the multireferencial character of the cumulenic species with long chain-lengths ($n \geq 7$), we performed CASSCF/NEVPT2 calculations on the vinylidene species n[H]. The configuration of the ground state wavefunction, as shown in Table 3.10, clearly shows a not negligible contribution of doubly-excited determinants of the form [H,H]→[L,L], thus resulting in a multireference character. The contribution of the doubly-excited determinant to the ground state wavefunction increases by lengthening the chain, following the trend previously discussed of an increased

stability of the BS solution, as well as high N_{FOD} and y_0/y_1 values for long chains.

3[H]	5[H]	7[H]	9[H]
0.92744 : 222000	0.92237 : 222000	0.82103 : 22220000	0.82268 : 22220000
0.03211 : 220200	0.03301 : 202200	0.04733 : 22022000	0.04203 : 22022000
0.02267 : 202020	0.02652 : 220020	0.02921 : 22200200	0.02883 : 22200200
0.00580 : 022200	0.00982 : 211110	0.02631 : 21121010	0.02176 : 21121010
0.00549 : 122100	0.00494 : 022200	0.01898 : 12210101	0.01874 : 12210101

Table 3.10: *Ground state compositions of n[H] cumulenes for n=3,5,7,9, calculated with CASSCF using an active space of [8x8]*

From this preliminary analysis we can confidently conclude that:

i) by increasing the length of the cumulene chain broken-symmetry DFT solutions appear, generally for n $\geq$ 5 or 7

ii) the presence of BS solutions goes on par with high NFOD ($\geq$ 0.7) and y_0/y_1 (0.2/0.05), suggesting a diradicaloid (multireference) character of the ground state electronic structure

iii) CASSCF/NEVPT2 calculations confirm the multireference character for long (n $\geq$ 7) chains, corroborating the BS-UDFT calculations

iv) the end-groups influence the diradical character, leading to different BS stabilisations, NFOD and y_0/y_1 values

v) diaryl- and fluorene end-groups stabilise the diradical structures, with [Fl] showing the strongest effect.

To show the impact of the BS solution on the structural properties of the carbon chains, we initially focused on the vinylidene species, reporting in Figure 3.21 the BLA pattern for 7[H] and 9[H]. Unfortunately, there are no crystallographic data for such species, so a direct comparison with experimental values is not possible. Nevertheless, we can consider such systems as ideal models to catch some general trends. The first remarkable observation is the comparison between the CS-DFT and the BS-UDFT solutions. As discussed previously, both 7[H] and 9[H] show a low energy BS solution with relatively high N_{FOD} and y_0/y_1 values (see Table 3.8). Furthermore, the spin contamination for both species is either none or limited (Table 3.9). For the case of 7[H] the BS solution is almost degenerate with the CS one ($\Delta E_{BS-CS} \sim 0$), and in fact the computed bond lengths are very similar for both cases (see black (CS) and red (BS) lines in Figure 3.21). For the case of 9[H], where the BS solution is considerably more stable than the CS (ΔE_{BS-CS} = -0.04 eV), the bond length pattern of

the BS-UDFT (red, Figure 3.21) is more alternated than the CS-DFT (black, Figure 3.21). This result is quite significant, showing a non-negligible (and not null) BLA for the more stable BS solution of cumulenes (BLA(7[H]) = 0.012 Å and BLA(9[H]) = 0.040 Å), thus resembling the bond length alternation pattern of a polyyinic structure with single- and triple-like bonds. In fact, the central bond of [H]cumulene (number 5 in Figure 3.21) is more single at the BS-UDFT level as it would be as predicted by the canonical (but unstable) CS-DFT solution, likewise the nearest bonds 4 and 6 are more triple than the CS-DFT prediction. Such result is the clear computational evidence of a diradicaloid structure, as provided by the BS-UDFT solution. Such diradicaloid structure can resemble the resonance forms sketched in Figure 3.20, as it was already hypothesized and suggested by initial pioneering experimental studies [25, 26, 93]. As a term of comparison, the BLAs for hydrogen-capped polyynes with 7 and 9 CC bonds are computed as well, being 0.150 Å and 0.145 Å, respectively. These values are certainly higher than those derived for cumulenes within the BS approach (BLA(7[H]) = 0.012 Å and BLA(9[H]) = 0.040 Å), nevertheless the comparison suggest a polyynic-like trend in the bond length pattern of diradicaloid cumulenic species.

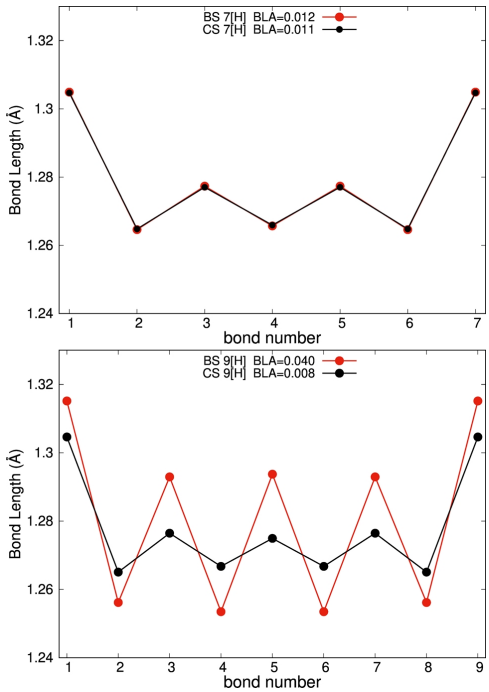

Figure 3.21: *Computed (CAM-B3LYP/cc-pVTZ) bond lengths (Å) for 7[H] (above panel) and 9[H] (below panel). CS-DFT (black) and BS-UDFT (red) solutions are reported together with the calculated BLA parameter*

3.4.3 Electronic and structural analysis of experimentally available end-capped cumulenes: the cases of [Ph], [Mes], [tBuPh] and [Fl] groups

As for the case of n[H] series we computed the BLA parameter of n[Ph], n[tBuPh], n[Mes] and n[Fl] species and compared them with those derived from the experimental crystallographic (X-Ray diffraction, XRD) data [93]. In Figure 3 the computed BLA values for the CS (black line, circles) and, when present, the BS solutions (red line, circles) are reported and compared with the experimental data (purple line, squares, when available).

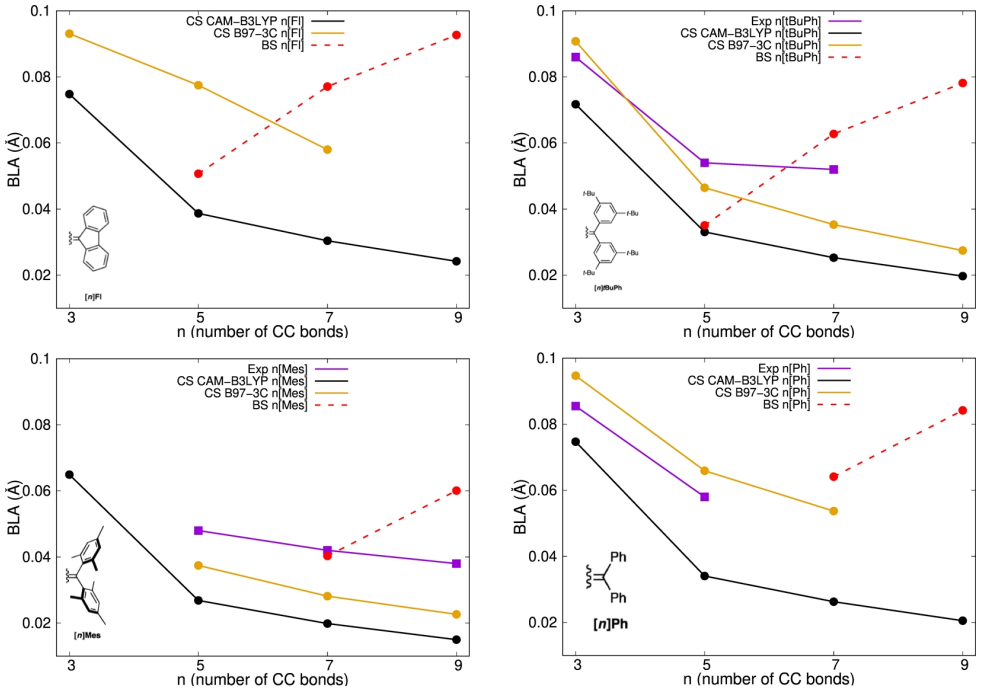

Figure 3.22: *Computed BLA values are reported for CS (black line, circles) and BS (red line, circles) DFT solutions of n[Fl] and n[Ph] (CAM-B3LYP/cc-pVTZ), and n[Mes], n[tBuPh] (CAM-B3LYP/6-31G(d,p)). Experimental values [26,93] are reported in purple line, squares. BLA values were also computed at B97-3c/cc-pVTZ level of theory (yellow line, circles).*

Generally, as observed experimentally for [Mes], [tBuPh] and [Ph], the longer is the cumulene chain the lower is the BLA, as an effect of the extended electron delocalisation. The experimental BLA parameters show quite high values, spanning from 0.086 Å (3[tBuPh]) to 0.038 Å (9[Mes]), however they do not vanish for long chain lengths. Moreover, a not negligible impact of the end-groups can be observed in the experimental data. Diaryl-terminations have distinctively different BLA parameters, wether they are [Mes], [Ph] or [tBuPh]. [Ph] and [tBuPh] show higher BLAs than [Mes], suggesting a delicate coupling between the terminal groups and the carbon chain, leading to

fine modulations of the BLA. As already reported by Tykwinski [25], the experimental values are markedly higher than the computed ones, the latter being canonical CS-DFT calculations. In Figure 3.22 CS-DFT calculations are reported for each species, confirming their underestimation and rapid dispersion of the BLA parameter with respect to the experimental results. Focusing on n = 5,7 [Mes] and [tBuPh] species, where experimental data are available, the CS-DFT solution underestimates the experimental BLA parameter by more than 0.02 Å. Moreover, for the case of [tBuPh] the experimental BLA dispersion versus the chain length seems to already reach saturation for n $\geq$ 5, while CS-DFT data rapidly decrease. As discussed in the previous section and reported in Table 3.8, from n $\geq$ 5 a broken-symmetry (open-shell singlet) solution can appear, showing the diradicaloid character of the cumulenic species. Consequently, as in the case of vinylidene species (n[H], see Figure 3.21), the BLA changes, increasing with respect to the CS-DFT solution. In Figure 3.22 we reported the calculation of the BLA parameter at the BS-UDFT level (when present), for each species. It is possible to observe a larger BLA parameter with respect to the canonical CS solution, closely matching for some cases the experimental data. In this regard, it is worth to analyse the cases of 7[Mes] and 7[tBuPh] (Figure 3.22). The calculated BLA parameter for 7[Mes] increases from 0.020 Å at the CS-DFT level, to 0.040 Å for the BS solution, approaching the experimental value of 0.042 Å. For 7[tBuPh] the situation is very similar: BLA increases from 0.025 Å (CS-DFT) to 0.063 Å (BS-DFT), improving the comparison with the experimental data (0.052 Å). As reported for n[H] (Figure 3.21), the appearance of broken-symmetry DFT solutions for long chains (typically n $\geq$ 5) is the manifestation of a diradicaloid (localised) character of the electronic structure, resulting in enhanced BLA and higher electronic gap than the canonical CS-DFT (over-delocalised) solutions. For 7[Mes] and 7[tBuPh] the spin contamination (see Table 3.8) is relatively small, 0.12 and 0.38 respectively, therefore we can consider acceptable the BS-UDFT approximation resulting in an open-shell (diradicaloid) singlet ground state electronic wavefunction for such species. For longer chains, namely n $\geq$ 9, the spin contamination increases (see Table 3.8), leading to pronounced and unreliable BS-UDFT BLAs, as reported in Figure 3.22. A typical case is 9[Mes], in which the computed BS-UDFT BLA parameter is larger than the experimental value. Furthermore, the dispersion behaviour of the BS-UDFT BLA vs. the chain length does not match the experimental trend. Despite the high spin contamination of the BS-UDFT solutions for n = 9, we decided anyway to report the computed BLA parameter for all species in Figure 3.22, documenting the more alternated structure with respect to the CS-DFT solution. We forsee that for long chains (n $\geq$ 9) the experimental values should lie in between the underestimated CS-DFT values and the overestimated BS-UDFT ones, the former being affected by severe electron delocalisation, self-interaction energy (SIE)

and static electronic contribution (SEC) problems, the latter being affected by high spin-contamination. A proper solution for the prediction of the structural parameters of long cumulenic chains would be to adopt multireference wavefuntion based methods (e.g., CASSCF/CASPT2) or hybrid approaches, such as DFT/MRCI [113]. However, either the investigated cumulenic species are computationally prohibitive at these levels of theory, or no analytical gradients have been implemented yet (see DFT/MRCI), being therefore not possible to overcome the current limits of the DFT approach. For such reasons, our BS-UDFT findings do not pretend to be quantitative or predictive, rather to raise a warning about the blind and wild applicability of DFT methods in the prediction of the structure-property relationships of long cumulene chains, regardless their terminals. Ultimately, our BS-UDFT data are valuable because they show the existence of a diradicaloid character (otherwise missed at the CS-DFT level) for medium-large cumulene chain-lengths. Furthermore, for those cases in which the spin-contamination is reasonable ($\langle S^2 \rangle < 0.4$), the comparison with the structural experimental data match very well. For cases like 5[Fl] or 5[tBuPh] (see Table 3.8 and Figure 3.22), where the BS solution is quasi-degenerate with respect to the CS-DFT one, the BLA increases, however not enough to match the experimental data. Here, BS-UDFT is suggesting the presence of a diradicaloid structure, and therefore the necessity to go beyond single-reference approximations for a quantitative description of the properties of such chain length. In general, we can partially summarise our findings as follow:

i) BS-UDFT solutions appear starting from n $\geq$ 5 depending on the end-groups, and they lead to higher BLA than the canonical CS-DFT.

ii) For the chain length n = 7 the BS-UDFT solution is energetically well separated by the CS-DFT (ΔE_{BS-CS} > -0.01 eV) with limited spin contamination, leading to a very good match with the available experimental data for [Mes] and [tBuPh] species.

iii) For long chains (n $\geq$ 9) the validity of the BS-UDFT approach is challenged by the high spin contamination, resulting in large BLA higher than the observed values.

To circumvent the BS solution, still keeping the computational benefits provided by a DFT approach, we computed the structure of each species at the B97-3c level, which has been demonstrated to be a reasonable exchange-correlation functional to describe multi-reference systems [102]. Notably, the computed BLA parameters at the B97-3c level are higher than the CS-DFT (CAM-B3LYP and/or ωB97X-D) data, being for short chains very close to the experimental results (Figure 3.22). However, for long chains (n $\geq$ 7) the BLA dispersion versus the chain length at the B97-3c does not match the experimental trend and approaches the CS-DFT one. For the cases of 7[Mes] and

7[tBuPh], B97-3c underestimates the BLAs with respect to the experimental data, even though the values are higher than those computed at the CS-DFT (CAM-B3LYP and/or ωB97X-D) level, approaching the BS-UDFT solutions. Overall, B97-3c seems to mitigate the SIE/SEC errors, however it is not appropriate to quantitatively reproduce the observed structural data. Given the above scenario, we focus our attention to the case of n = 7 in order to better understand the effects induced by different terminal groups on the carbon chain. In Figure 3.23 we reported the computed BLA patterns for n = 7 by varying the end-capping groups, namely [Ph], [Mes], [tBuPh] and [Fl].

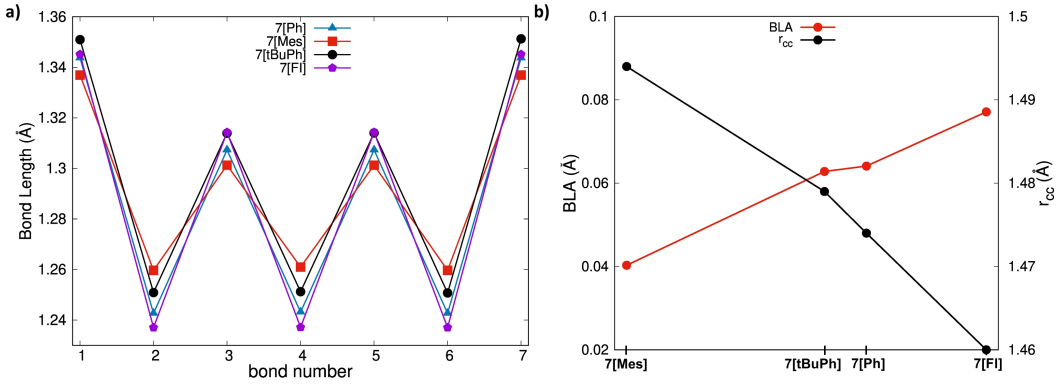

Figure 3.23: *Panel a): computed bond lengths (Å) at the BS-UDFT level for n = 7 by varying the end-capping groups, such as [Ph] (blue), [Mes] (red), [tBuPh] (black) and [Fl](purple) (CAM-B3LYP/cc-pVTZ for [Ph] and [Fl], and CAM-B3LYP/6-31G(d,p) for [Mes] and [tBuPh). Panel b): BLA parameter (red) and bond length of the terminal carbon-carbon bonds (r_{CC}) (black) by varying the end-groups.*

As reported in Figure 3.23a our calculations show that the bond length alternation pattern is highly influenced also by the terminal groups of the carbon chain, confirming some initial observations by Tykwinski et al. [25]. Fluorene ([Fl]) induces the highest bond length alternation in the chain leading to pronounced triple- and single-like bond pattern. Diaryl-mesityl ([Mes]) instead shows the lowest BLA (Figure 3.23 and Figure 3.22). Diphenyl ([Ph]) and diaryl-tert-butyl- ([tBuPh]) show intermediate BLA between [Mes] and [Fl]. This result can be attributed to the stabilization of the diradical character by the end-groups and nicely matches the trends already suggested by N_{FOD} and y_0/y_1, as discussed previously and reported in Table 3.8. N_{FOD} and y_0/y_1 increase as [Ph] < [Mes] < [tBuPh] < [Fl]; similarly the BLA pattern (Figure 3.23) and parameter (Figure 3.22) increase as [Mes] $\approx$ [Ph] < [tBuPh] < [Fl]. It is instructive to analyse the trend of the BLA parameter as a function of the terminal groups, as reported in Figure 3.23b, and to correlate it to the bond length of the terminal carbon-carbon bonds (r_{CC}), which connects the chain to the end-groups. Moving from [Mes], [tBuPh]/[Ph] to [Fl] the BLA increases

from 0.04 Å to 0.08 Å. At the same time r_{CC} decreases from 1.495 Å to 1.460 Å, showing a shortening of the terminal bonds. Such behaviour is consistent with a radicaloid character of the carbon chain, leading to a polyyinc-like structure (Figure 3.20). Amongst the diaryl groups 7[tBuPh] shows a predicted BLA parameter (0.065 Å) larger than the one computed for 7[Mes] (0.040 Å). This trend, disclosed only throughout our BS-UDFT calculations, perfectly matches the experimental observation by Tykwinski et al., reporting an accentuated long/short bonding pattern for [tBuPh] as compared to [Mes] [25]. Furthermore, we can predict that the fluorene group induces a higher degree of diradicaloid character (i.e., larger BLA parameter and shorter r_{CC}, Figure 3.23b) than the diaryl end-terminals. Such feature can be traced back to the planar structure of the fluorene moieties, allowing for a larger delocalisation of the electronic structure. This characteristic can be observed as well by looking at the computed spin densities of the open-shell (BS-UDFT) singlet state for all the end-capped species (n = 7), as reported in Figure 3.24. Indeed, from Figure 3.24 we can observe that the spin density of [Fl] species is more delocalised than the diaryl end-terminals ([Mes], [Ph], [tBuPh]), leading for the former to a pronounced bond length alternation and diradicaloid character of the carbon chain.

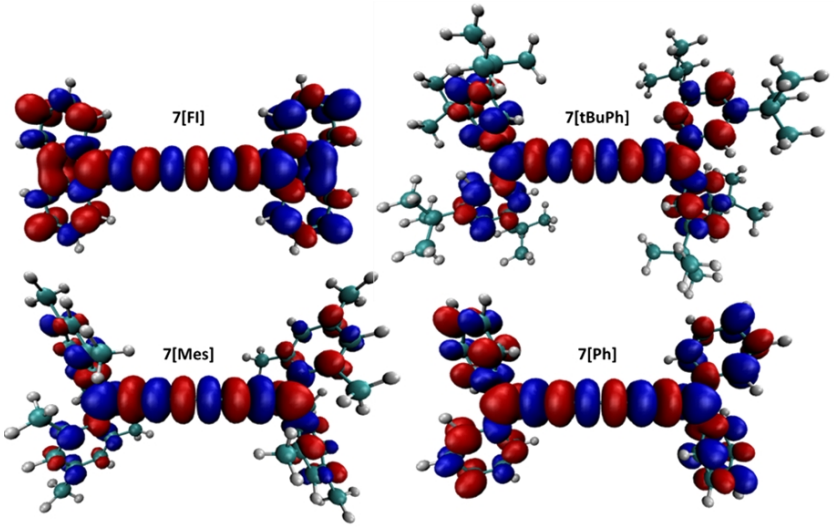

Figure 3.24: *Spin densities for BS-UDFT solutions of 7[Ph], 7[Mes], 7[tBuPh] and 7[Fl], calculated at the CAM-B3LYP/cc-pVTZ level of theory (7[Ph] and 7[Fl]) and at the CAM-B3LYP/6-31G(d,p) one (7[Mes] and 7[tBuPh])*

To further investigate the effect induced by the terminal groups on the carbon chain bond length alternation, we correlated the computed BLA parameters with respect to the averaged dihedral angle of the diaryl ([Mes], [Ph], [tBuPh]) and fluorene end-groups, as reported in Figure 3.25, together with the

experimental data taken from Refs [26,93]. Due to the steric hindrance induced by the mesityl, tert-butyl-phenyl or phenyl rings, the aryl units can feature different orientations and exploit various dihedral angles with respect to the carbon chain, as observed via XRD experiments by Tykwinski et al [25,26,93]. These conformations can affect the local electronic coupling between the end-terminals and the cumulene chain, inducing consequently a variation of the BLA pattern. Generally, as reported in Figure 3.25, n[Mes] species show a larger (average) dihedral angle than n[tBuPh], the former having a smaller BLA parameter than the latter. Correlating the BLA parameter to the dihedral angle in Figure 3.25, experimental and computational data agree reasonably well, suggesting a linear relationship. We can observe that the larger is the dihedral angle (i.e., the more the end-terminals are distorted with respect to the carbon chain) the lower is the bond length alternation of the chain, suggesting a more equalized (i.e., cumulenic-like) structure. Small dihedral angles, at the limit of a flat structure like for [Fl] species, induce pronounced BLAs, enhancing the diradicaloid character of the carbon chain and leading to alternated polyynic-like structures.

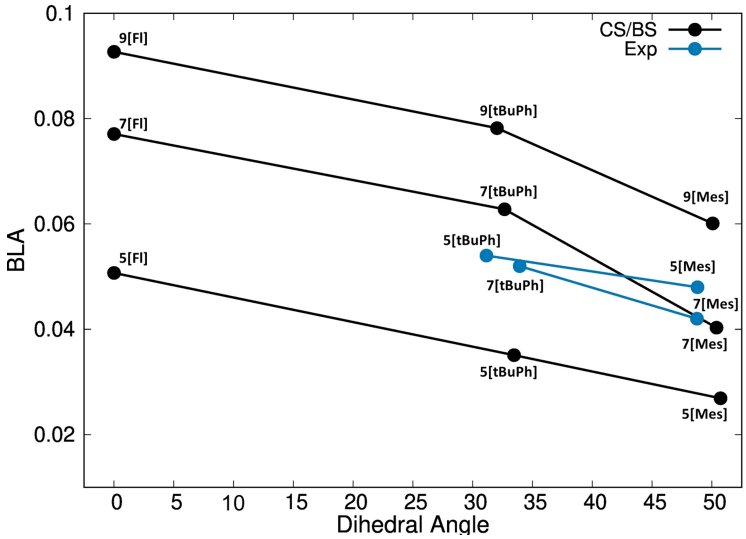

Figure 3.25: *Computed (black) and experimental (blue) BLAs as a function of the mean dihedral angle for n[Mes] and n[tBuPh] species. CAM-B3LYP/6-31G(d,p) data*

3.4.4 Cationic and anionic ground state analysis of carbon atom wires with different terminations

After the deep analysis on the ground state properties of cumulenes, focusing the attention on their diradical character, I decided to focus my attention on the analysis of the charged states of these systems, with the aim of predicting charge transport behaviours, through the analysis of the reorganization energies, for

a view of applying these systems as active materials in optoelectronic organic devices (such as OFET or OPV).

The analysis started with the reorganization energies investigation of vinylidene-capped cumulenes and hydrogen terminated polyynes, representing the simplest system, both cumulenic and polyynic, to be investigated. We started the analysis using a CAM-B3LYP/cc-pVTZ level of theory. By plotting the reorganization energy values as a function of the chain length of the investigated carbon atom wire (CAW), I discovered that the energy values, both for polyynes and cumulenes, did not fit the usual trend obtained for other polyconjugated materials (Fig. 3.26, panel a and b).

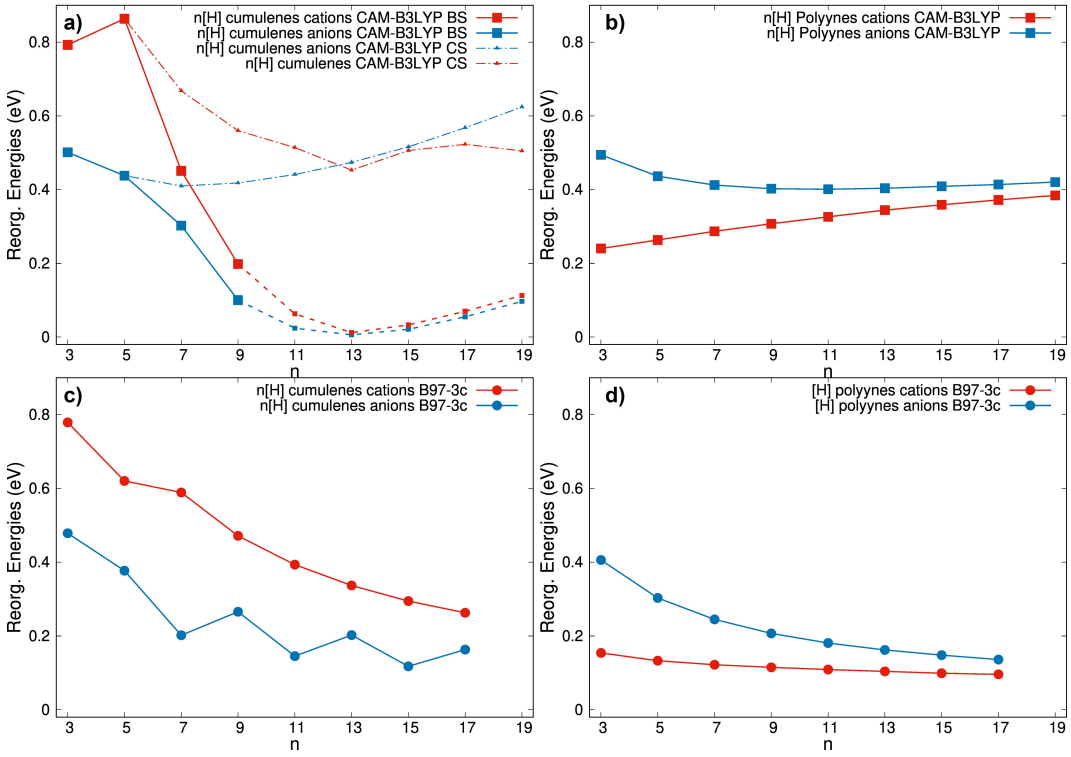

Figure 3.26: *Reorganization energy plots for vinylidene-capped cumulenes (panels a and c) and hydrogen terminated polyynes (panels b and d) as a function of the chain length. Energy values were calculated adopting two different levels of theory: CAM-B3LYP/cc-pVTZ (panels a and b) and B97-3c/cc-pVTZ (panels c and d)*

Indeed, for n[H] cumulenes an oscillating trend is shown in Fig. 3.26 (panel a, dotted line and triangular points) depending on the number of bonds along the chain, both for cationic and anionic species. On the other hand, polyynes showed an initial decrease of the anionic reorganization energy but then, after reaching a minimum for 11[H], it starts to increase with n (Fig. 3.26, panel b). The cationic trend shows a more unusual behaviour: the energy seems to

exponentially increase with the increasing number of carbon atoms. To give an explanation to this result, we made spin-polarized BS calculations on both polyynes and cumulenes. We found that for the ground state of cumulenes a lower energy broken-symmetry solution exits; for this reason, we found another nuclear configuration for the neutral species and, consequently, new values of the reorganization energies that are reported in Fig. 3.26 (panel a, solid and dotted lines, squared points). This effect, deeply discussed in the previous section, is due to the intrinsic multiconfigurationality found for the ground state of the investigated systems. For very long cumulenic species (n>9), spin contamination for the ground state showed very high values which makes BS energy values strongly unreliable for these lengths; for this reason we decided to represent this data region with dotted lines. Polyynes have quite different behaviour: we didn't find any broken symmetry solution, neither in ionic nor in ground states. Even if lower energy ionic and ground state solutions have not been found using BS approach, we performed TDDFT calculation on cations and anions of polyynes and we found roots at very low energies (lower than 0.01 eV). This result usually suggests a multiconfigurational character for the specific state under investigation. Moreover, we also calculated the N_{FOD} for the ionic species of polyynes and we found very high values of this indicator (N_{FOD} >1) also for very short polyynic species (Tab. 3.11) while for cumulenes, apart for long cumulenic chains, N_{FOD} are almost comparable with that obtained for the ground states. With this in mind, we re-calculated the reorganization energies, both for polyynes and cumulenes, adopting the B97-3c functional that is known to describe better the static electronic correlation, as explained in the computational details section. With these calculations much more reliable data of the energies are obtained for polyynes, for which the usual trend expected for polyconjugated systems as a function of the CC bonds' number is recovered (Fig. 3.26, panel d). For cumulenes the progression of the reorganization energies calculated with B97-3c functional is reliable only for cationic species while for anionic ones an oscillating behaviour is obtained when n>7 as reported in Fig.3.26, panel c.

species	$N_{FOD}^{neutral,CS}$	N_{FOD}^{cation}	N_{FOD}^{anion}
n[H] Polyynes			
3[H]	0.02	1.02	1.05
5[H]	0.08	1.06	1.08
7[H]	0.16	1.15	1.14
9[H]	0.26	1.25	1.23
11[H]	0.36	1.37	1.33
13[H]	0.47	1.49	1.43
15[H]	0.58	1.61	1.55
17[H]	0.69	1.74	1.66
n[H] Cumulenes			
3[H]	0.06	0.25	0.16
5[H]	0.21	0.53	0.35
7[H]	0.44	0.81	0.6
9[H]	0.7	1.07	0.86
11[H]	0.98	1.31	1.09
13[H]	1.26	1.55	1.32
15[H]	1.52	1.74	1.53
17[H]	1.78	1.94	1.74
3[Mes]	0.37	1.23	0.84
5[Mes]	0.59	1.4	1.8
7[Mes]	0.84	1.58	1.02
9[Mes]	1.12	1.77	1.22
3[Ph]	0.39	0.92	0.81
5[Ph]	0.59	1.07	0.87
7[Ph]	0.83	1.25	1.03
9[Ph]	1.09	1.44	1.24
3[tBuPh]	0.43	1.16	0.9
5[tBuPh]	0.66	1.29	0.95
7[tBuPh]	0.9	1.47	1.1
9[tBuPh]	1.17	1.65	1.3
3[Fl]	0.63	1.44	0.77
5[Fl]	0.84	1.56	0.87
7[Fl]	1.08	1.71	1.05
9[Fl]	1.33	1.88	1.26

Table 3.11: *Table reporting numerical values for N_{FOD} for all the analysed molecules, calculated for the neutral (closed shell) and charged ground states.*

In light of these findings, with the aim of further investigating the obtained values for the reorganization energies, we calculated the distortions, in terms of bond lengths difference, between the charged and the ground states for vinylidene-capped cumulenes and hydrogen terminated polyynes, evaluated at

both CAM-B3LYP and B97-3c levels of theory. Distortions are plotted in Fig. 3.27 as histograms located at the specific bonds of the cumulenic linear chain, representing in blue the anionic and in red the cationic distortions. The first interesting result coming from these data is that the two functionals, i.e. CAM-B3LYP and B97-3c, report very similar distortions, both in magnitude and in the relative amplitude, between anion and cations. Indeed, both functionals, for polyynes and cumulenes, predict a delocalization of the polaron along all the π-conjugated wire, resulting in a general decrease in the absolute values of the bond length distortions increasing the number of CC bonds in the chain. Moreover, starting from vinylidene-capped cumulenes, both levels of theory predict a higher distortion for the molecule creating a negative charge with respect to the creation of a positive one.

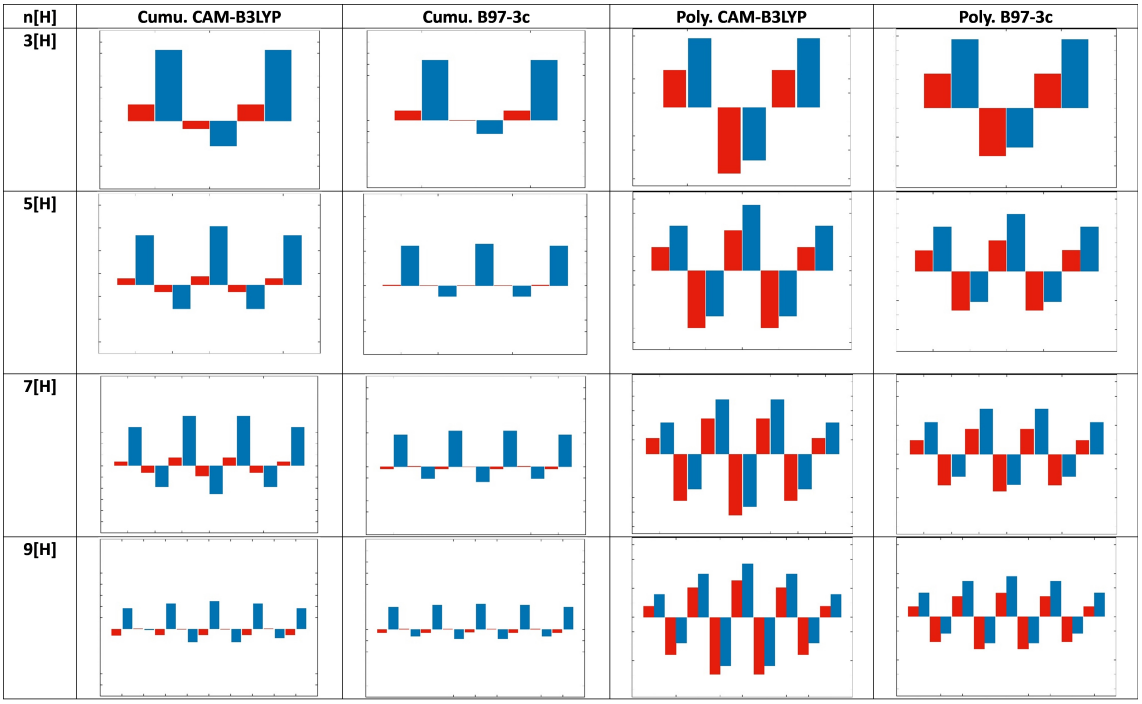

Figure 3.27: *Figure reporting histograms of the bond length distortions (in Å) between anionic (blue) and cationic (red) states with respect to the ground one, calculated for vinylidene-capped cumulenes and hydrogen-terminated polyynes adopting both DFT functionals (CAM-B3LYP and B97-3c).*

This result is in contrast with values of the anionic reorganization energies found for cumulenes, because both the levels of theory adopted predict a lower reorganization energy for the creation of an anion with respect to a cation; this should reflect a lower distortion induced in the molecule when inserting charge instead of giving. For this reason, we evaluated the dihedral angles

formed by the vinyl groups between each other, for each molecular length, and we reported them in Tab. 3.12. As we can see from the values of the angles, we obtain, with both CAM-B3LYP and B97-3c levels of theory, higher torsion angles between the terminal groups when we eject charge from the molecule rather than injecting. Indeed, looking at the values calculated at CAM-B3LYP broken-symmetry level of theory we can appreciate a difference between angles of cationic and anionic species of around 30° for 3[H] and 5[H] species. This difference becomes much more pronounced when we reach higher lengths of the chain, reaching a difference of almost 40° in the case of 7[H] and 9[H]. Data obtained at B97-3c are more scattered and quite unreliable, due to the beginning of the oscillating trend at n=9, but the global result is quite the same. These higher distortions, in terms of dihedral angles between vinyl groups, that can be found in cationic species with respect to the anionic ones, could be the cause of the lower reorganization energy obtained for anionic species of cumulenes, even if the anionic bond distortions are bigger with respect to the cationic ones.

species	Anion (CAM-B3LYP)	Cation (CAM-B3LYP)	Anion (B97-3c)	Cation (B97-3c)
3[H]	10.1	39.7	22.5	40.7
5[H]	11.2	41.7	27.1	42.5
7[H]	1.5	41.9	1.9	43.2
9[H]	0.6	40.6	30.41	43.6

Table 3.12: *Table reporting the torsion angle between the terminal groups for vinylidene-capped cumulenes with different chain length, computed at two different levels of theory (CAM-B3LYP/cc-pVTZ and B97-3c/cc-pVTZ)*

For the case of polyynes the situation is like that of cumulenes. Indeed, as reported in Fig. 3.27, bond length distortions for anionic and cationic states with respect to the ground are predicted in a very similar way with both functionals (i.e. CAM-B3LYP and B97-3c). Looking at the histograms, we can appreciate a slightly higher distortion for the anions with respect to cations; this is in accordance with the reorganization energies that predicts, with both levels of theory, lower values when creating a hole than an electron in the molecule. Moreover, the distortion that the molecule suffers when creating an anion or a cation becomes more and more the same increasing the length of the chain and, at the same time, also the reorganization energy values for cationic and anionic species approach with themselves.

After the investigation of vinylidene-capped cumulenes and hydrogen-terminated polyynes, I moved my attention to the analysis of reorganization energies for n[Mes], n[tBuPh], n[Ph] and n[Fl] cumulenes with different lengths with the aim of deeply investigating the role of the different end-capping groups. Also

here, a BS approach was adopted to revise the reorganization energies' data where needed. Indeed, we found lower energy solutions for the ground states of all the analysed cumulenes, as already deeply discussed in the previous sections, starting for n>5 in n[Fl] and n[tBuPh] and for n>7 in n[Mes] and n[Ph] species. In Fig. 3.28 we reported the reorganization energies for all the 4 classes of differently terminated cumulenes.

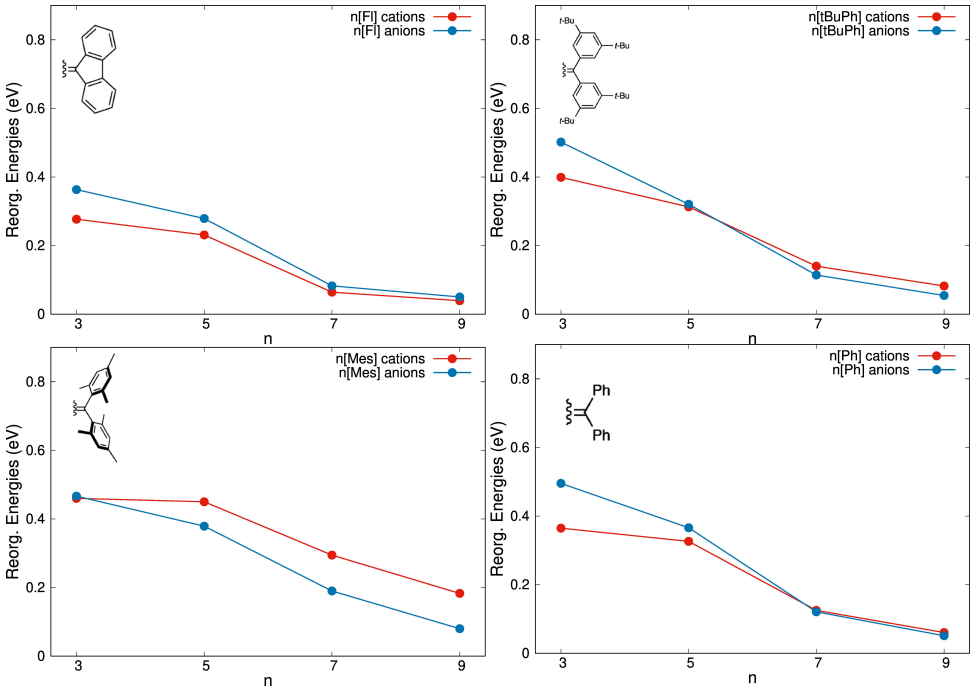

Figure 3.28: *Reorganization energy plots for aryl-terminated cumulenes with different end-capping groups (n[Mes], n[Ph], n[tBuPh] and n[Fl]).*

In parallel to the calculation of the reorganization energies, in Fig. 3.29 we also reported the analysis of the ionic state distortions with respect to the ground state, as we made for hydrogen-terminated polyynes and vinylidene-capped cumulenes in previous section. The first thing to notice is that, independently from the terminal groups, the energy needed to create an electron or a hole on a single molecule is quite the same. This result suggests an ambipolar charge transport character for these materials. One exception to this trend is represented by the n[Mes] series that, apart from the 3[Mes] molecule, shows lower reorganization energies for the anionic states with respect to the cationic ones, suggesting an effective electron-transport behaviour. Indeed, the different behaviour can be attributed to the less diradical character that characterize [Mes] terminated cumulenes, as already discussed in previous sections. Fluorene-capped cumulenes show the lowest values of the reorganization energies and the less distorted structure in the ionic state, and this is much more

pronounced for small lengths. Indeed, for n[Fl] we obtain energy values of 0.277 and 0.363 eV, that are the lowest values with respect to n[Ph], n[tBuPh] and n[Mes]. For this length, n[Ph] and n[tBuPh] show the largest energy values, around 0.5 eV. When number of CC bonds increases to 5, energies for 5[Ph] and 5[tBuPh] (0.366, 0.326 eV and 0.320, 0.313 eV) fall at lower values with respect to 5[Mes] (0.379, 0.450 eV) but still higher than 5[Fl] (0.279, 0.231 eV). Increasing more the chain length, reorganization energy values for all the species decrease dramatically at values around 0.1 eV apart for 7[Mes] that show still highest values in energy (0.190, 0.294 eV). These effects are very coherent with distortions of the ionic state, with respect to the ground, reported in Fig. 3.29, in which the highest distortion is found for 7[Mes] and the lowest one for 7[Fl]. For the maximum analysed length, i.e. n=9, for which we obtain the highest spin contamination, the reorganization energies of the species dramatically decreases touching very low values (<0.1); this could be caused by the very spin-contaminated ground state wavefunction. Indeed, only for 9[Mes] species, for which we found the lowest value of the ground state spin contamination, energy values higher than 0.1 eV are obtained, suggesting a slightly higher reliability of the calculated datum. At the same time, almost all the differently terminated species for n=9 show an almost negligible distortion between the charged and the ground states.

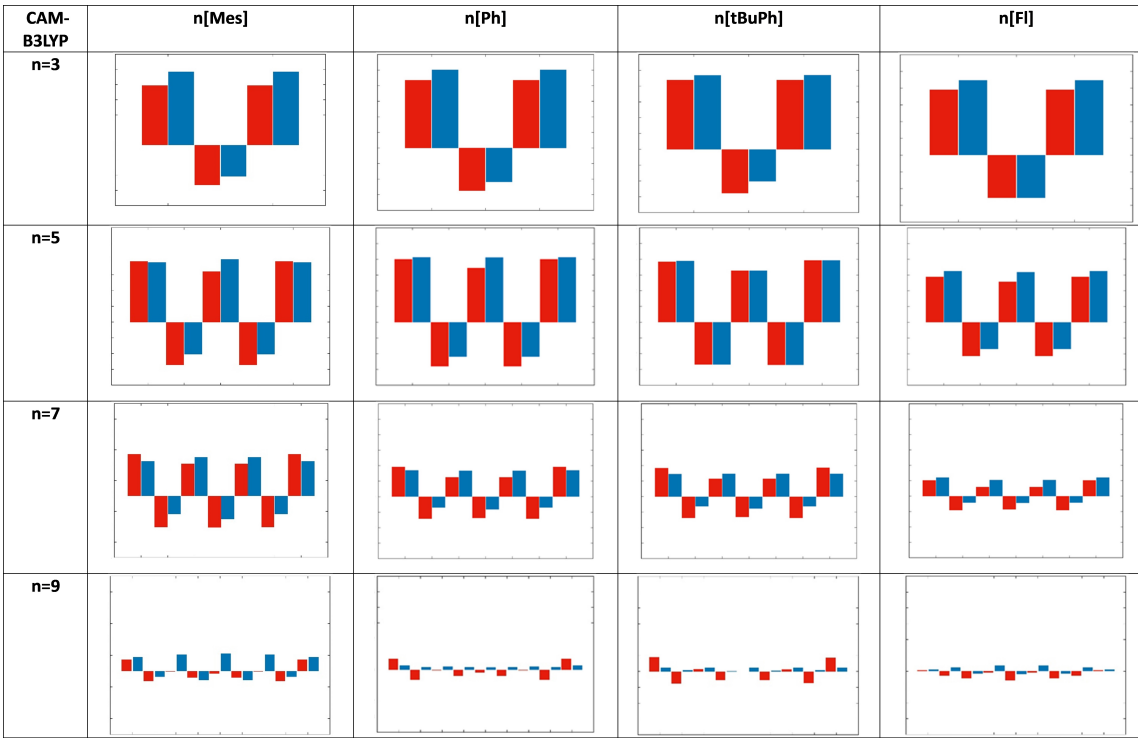

Figure 3.29: *Figure reporting histograms of the bond length distortions between anionic (blue) and cationic (red) states with respect to the ground one, calculated for aryl-terminated cumulenes adopting both DFT functionals (CAM-B3LYP and B97-3c).*

Having a look at the averaged dihedral angles of the diaryl end-capped groups ([Mes], [Ph], [tBuPh]), for the neutral, anionic, and cationic states and for a different number of CC bonds in the sp chain, reported in Tab. 3.13, some conclusions can be drawn. Indeed, the first thing to notice is that only for the n[Mes] species the differences between the anionic and neutral dihedral angles are higher with respect to the differences between cationic and neutral ones. In fact, focusing on an intermediate length like n=7, anionic states of n[Ph] and n[tBuPh] species present higher difference in angles with the neutral states (5.15° and 3.85° respectively) with respect to the cationic ones (2.15° and 2.89°). For 7[Mes] molecule the situation is reversed, having a difference in dihedral angles of the anionic state with the neutral one of 1.97°, in contrast with the 4.4° difference between cationic and neutral dihedral angles. Therefore, although the bond length distortions between ionic and neutral state seem to be almost independent on the creation of a hole rather than an electron in the molecule, dihedral angle differences between ionic and neutral states are telling us that n[Mes] species distort less when creating an anion other than a cation while for the other two species (i.e. n[Ph], n[tBuPh]) the behaviour is reversed. This result is coherent with the trend in reorganization energies observed in Fig.

3.28, in which n[Mes] show lower energy for the creation of an electron, almost independently from the number of CC bonds in the chain, while for the other two cases, n[Ph] and n[tBuPh], lower energies can be found for the creation of an hole instead of an electron, at least for small cumulenic lengths.

species	Neutral	Anion	Cation
3[Mes]	50.1	46.0	44.9
5[Mes]	50.2	47.3	45.3
7[Mes]	49.9	48.0	45.5
9[Mes]	49.6	48.4	45.7
3[Ph]	32.4	23.0	28.5
5[Ph]	32.7	24.5	28.5
7[Ph]	30.7	25.6	28.6
9[Ph]	29.7	26.4	28.7
3[tBuPh]	34.5	26.5	30.4
5[tBuPh]	31.2	24.8	27.8
7[tBuPh]	30.5	26.6	28.6
9[tBuPh]	29.7	27.3	28.6

Table 3.13: *Table reporting dihedral angles between the terminal groups for neutral, anionic and cationic states of differently terminated cumulenes with different chain lengths (n[Mes], n[Ph], n[tBuPh] and n[Fl])*

Chapter 4

Bottom-up investigation of γ-graphdiyne: from γ-GDY molecular fragments to 1D nanoribbons and 2D crystal

4.1 Introduction

Once sp-hybridized systems, i.e. CAWs, have been studied, focusing in particular on how electronic and vibrational properties are affected by different parameters (extension, end-capping groups ...), the attention was shifted towards hybrid sp-sp^2 carbon-based systems. To this aim, investigation of electronic and vibrational properties of different types of GDY fragments has been performed, as a starting point, to study how modulation of these properties is affected by structural features and size [114]. Then, following a bottom-up approach, the analysis of graphdiyne nanoribbons (GDYNRs) as a function of the nanoribbon width and edge-type (armchair or zigzag) is shown, disclosing the modulation of the band gap, together with the analysis of peculiar markers in IR and Raman that are sensitive to the lateral confinement and to the molecular structure of the edges [115]. Finally, computations of the electronic structure of 2D γ-GDY by periodic DFT simulations adopting different functionals and basis sets is shown. Thereafter, we focused on the prediction and assignment of its IR and Raman spectra [115].

4.2 γ-graphdiyne molecular fragments

By analysing a large number of GDY-based molecular fragments I investigated how topology affects the electronic and vibrational properties of these system, in particular how HOMO-LUMO gap depends on the degree of conjugation,

described by the three types of connectivity of the sp-domains to the aromatic 6-membered rings (i.e. para, ortho and meta, see Fig. 4.1-a). Some examples of the investigated 2D GDY fragments are reported in Fig. 4.1-b, together with the nomenclature adopted to highlight the presence and number of para paths of different lengths. Indeed, the length of the para, ortho and meta pathways is referred to the number of the diacetylenic units that are connected in that connectivity type; the number of carbon bonds in the single units remains unchanged (i.e. four sp-carbon atoms). In the case of the 2D GDY-based molecular fragments, for the number of para, ortho and meta pathways we refer to the multiplicity of the different pathway-types in the structures. Starting from the fundamental unit characterized by a "triangular ring" named T1 the nomenclature TXC or TX(PY)$_z$ indicates how many of these rings are present (X), if they are condensed (C, that is if they share one diacetylenic linkage), which is the length (Y) of the para-conjugated paths that they form (i.e. how many diacetylenic units are connected in para-position with respect to the aromatic rings) and how many of these paths are present (Z).

DFT calculations have been employed for geometry optimization, HOMO-LUMO gap evaluation and Raman spectra prediction of these GDY-based molecular fragments. Some of these models were built to consider also the molecules synthetized in previous studies. Calculations have been carried at PBE0/6-31G(d,p) level of theory by using GAUSSIAN09 package [85]: this choice has been done also to compare the results found for finite systems with infinite ones. Indeed, one-dimensional polymeric model systems showing different conjugation paths (para-, ortho- and meta) and configurations (cis and trans for meta cases) have been also considered, carrying out periodic boundary conditions DFT calculations at the same level of theory using the CRYSTAL17 code [116] to fully optimize their geometry and compute the band gap. For the optimizations of the 1D polymers the tolerance on integral screening (TOLINTEG parameters) have been fixed to 9,9,9,9,80, while the shrink parameters defining Monkhorst-Pack sampling points have been fixed to 50. All the studied finite and infinite systems were optimized keeping a planar geometry, thus not taking into account the effect of distortion from planarity. PBE0 functional has been adopted because it proved to give a very reliable description in the trends found in the electronic and vibrational properties for a large variety of sp-hybrized carbon systems [24] and this is why it has been adopted also here.

With the aim of finding structure-property correlations for the analyzed molecules harmonic oscillator model of aromaticity (HOMA) parameter for the aromatic rings is calculated according to the following expression:

$$HOMA = 1 - \frac{\alpha}{n}(\sum(R_{opt} - R_i)^2) \tag{4.1}$$

In this definition, n is the number of bonds taken into the summation and α is an empirical constant (α=257.7 Å^{-2}) chosen to give HOMA=0 for the

hypothetical Kekulé structure of an aromatic system and HOMA=1 for the system with all bonds equal to the optimal value R_{opt} (R_{opt}=1.388 Å [117]). R_i are the bond lengths of the CC bonds in the aromatic rings. According to this definition, the limiting cases of graphene and benzene show HOMA values of 0.76 and 0.99, respectively. The value of R_{opt} is calculated according to the following expression:

$$R_{opt} = [R(s) + 2R(d)]/3 \tag{4.2}$$

Where R(s) and R(d) are taken respectively as the carbon-carbon bond lengths of the experimentally measured single and double bonds of butadiene-1,3 molecule in gas phase. The HOMA values are computed as average values of all the aromatic rings in each structure.

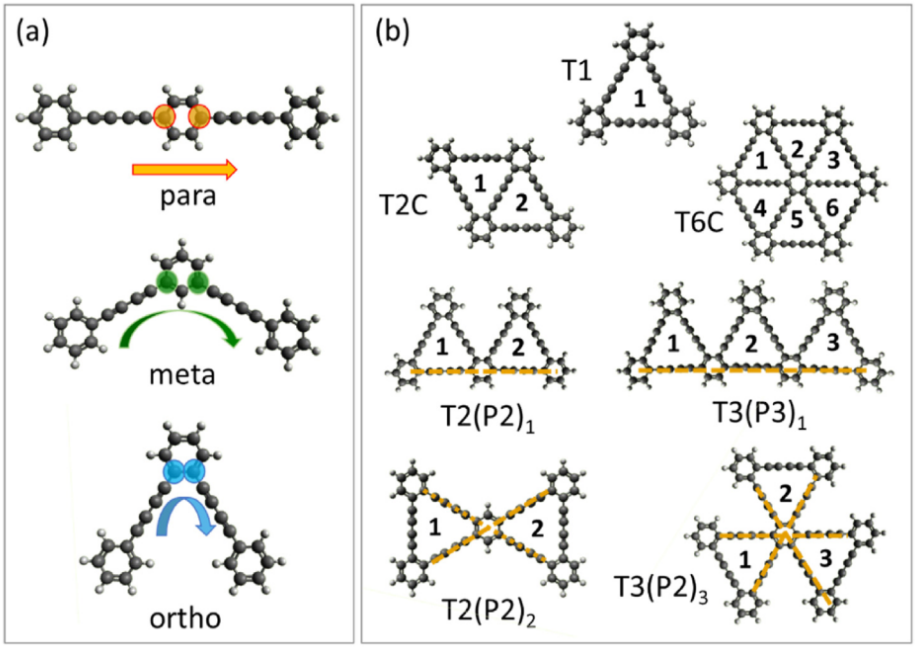

Figure 4.1: *a) Sketches of para, meta and ortho conjugation paths; b) Sketches of some of the 2D-GDY fragments investigated and related nomenclature [114].*

4.2.1 Gap modulation in 1-D molecular fragments

We started the analysis by considering one-dimensional models as the simplest systems to investigate the extent of conjugation across the different path types as a function of the dimension of the fragment. Starting from the monomeric building block (i.e. a di-phenyl polyyne with 4 sp-carbon atoms [118]) oligomers of increasing length and connected in para, ortho and meta (cis and trans) position were studied and compared to the infinite polymer described as a 1D crystal in periodic boundary conditions. The HOMO-LUMO gap as a function

of the fragment length is reported in Fig. 4.2 for all the possible configurations. The gap values of 2D fragments composed of "triangular" units (each one formed by three sp-chains and aromatic rings) are reported for comparison, up to the infinite limit which corresponds to the smallest GDY nanoribbon. This aims at introducing also the effect to the two-dimensional extension of the fragments with respect to simple one-dimensional conjugation represented by the other models.

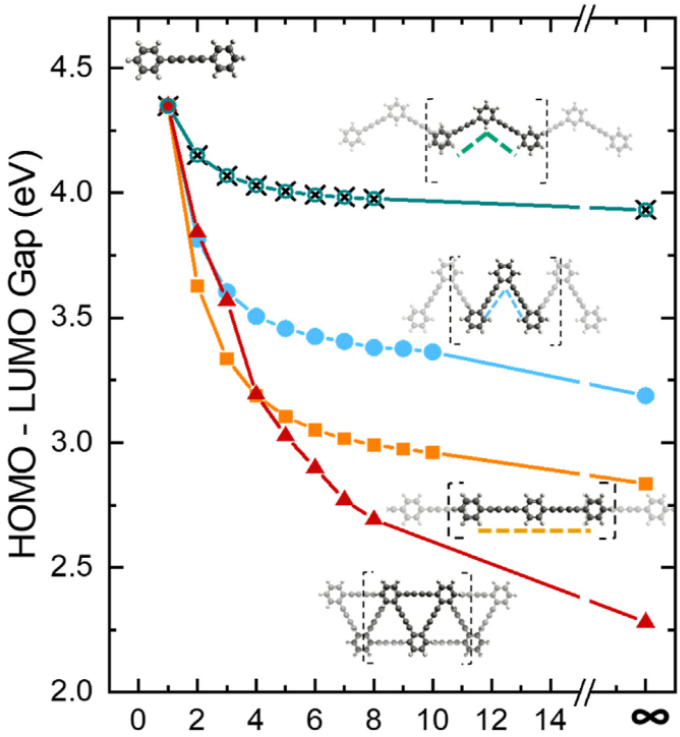

Figure 4.2: *Modulation of the DFT-computed HOMO-LUMO gaps (in eV) of one dimensional fragments (up to the 1D infinite polymer) formed by connecting N diacetylenic units in ortho-, para-, metha-positions or forming triangular rings. The single T1 ring corresponds to a value N = 2 on the x-axis and T2C to N = 3, the related sketches are reported in the figure. In the case of meta-connected units, both cis- and trans-configurations, represented respectively by empty circles and black crosses, have been considered but the associated values are superimposed thus not showing any configuration-dependent effect on the gap. The ∞ symbol stands for the infinite polymeric 1D case, whose gap value has been calculated with periodic boundary conditions Density Functional Theory simulations at the same level of theory (PBE0/6- 31G(d,p)).*

In all the cases a general decrease of the gap is observed when increasing the number of units. When moving from the monomer to the oligomer with two diacetylenic units, it is clear that the conjugation is larger (gap is lower) for para-conjugated units (gap drops from 4.35 to 3.63 eV moving from N = 1

to N = 2), followed by ortho-conjugated units (3.81 eV) and finally by meta-conjugated fragments with a gap exceeding 4 eV (4.15 eV). By increasing the number of units in the case of meta-conjugation the trend rapidly converges with no difference for trans or cis configuration. Meta-conjugation strongly limits the extent of conjugation across aromatic 6-membered units, thus preventing the modulation of the gap to lower values. Conversely, para and ortho connections can promote a significant π-electron conjugation across different units and a saturation effect is observed in both cases only for 1D fragments longer than six or seven units. Para connections are the most effective ones in promoting a larger conjugation, with a HOMO-LUMO gap rapidly dropping to values below 3 eV. This is in agreement to what is observed in similar structures in which diacetylenic linkages are substituted by acetylenic ones [52]. The infinite polymers reveal indeed a band gap of 3.188 eV for the ortho case and of 2.836 eV for the para-one, both much lower than the value of 3.933 eV predicted for the meta-conjugation (for both cis and trans configurations).

Similar to the modulation of the gap, BLA values on the diacetylenic chains could be expected to be modulated by the different extent of π-electron conjugation. However, the modulation of the BLA is negligible. In fact, moving from the monomer to the two-unit oligomers the BLA value changes from 0.1387 Å to 0.1374 Å for para-connection, to 0.1376 Å for ortho-connections and 0.139 Å for meta-connections revealing that conjugation is almost prevented for meta-, while it is somehow relevant for para- and ortho-cases. In the two latter cases as soon as the oligomer length increases, no further relevant changes of BLA are predicted (in the para-conjugated polymer it is 0.1363 Å and in the ortho one 0.1368 Å), thus revealing that the modulation of the gap is not directly related to the modulation of the bond lengths in the sp-carbon domains. Indeed, carbon-carbon bonds in the diacetylenic linkages remain practically unchanged with the increasing of the oligomer length. Trends in the BLA for the different connectivity-types are reported in Fig. 4.3.

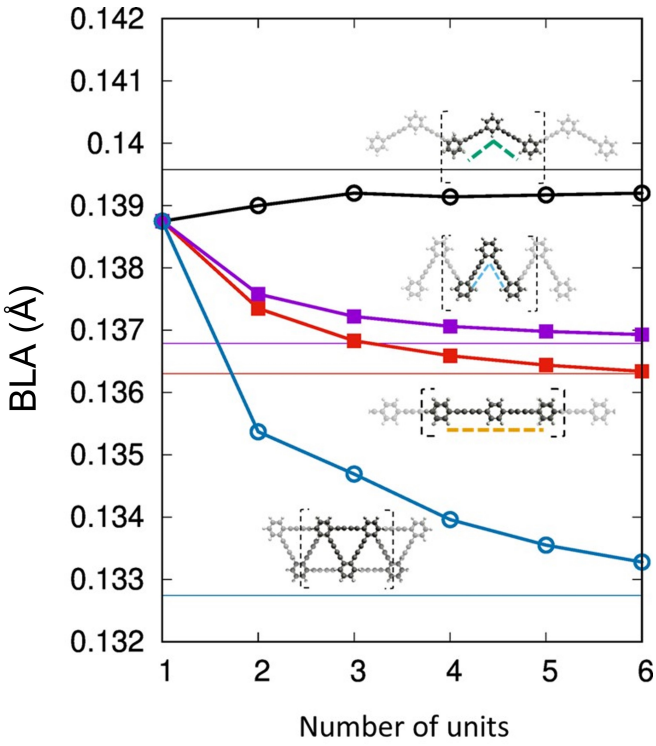

Figure 4.3: *Modulation of the average BLA values for one dimensional fragments (up to the 1D infinite polymer, whose gap is represented by the continuous line for each trend) formed by connecting N diacetylenic units in ortho-, para-, metha- positions or forming triangular rings.*

The case of oligomers formed by connected triangular units reveals further effects. For N = 2, the triangular structure is formed by only one triangular unit (T1) (see Fig. 4.2) in which the longest path consists in two diacetylenic units connected in ortho-position. In this fragment the gap (3.84 eV) equals the case of the ortho-oligomer having two units (3.81 eV). Moving to two condensed triangular units (T2C in Fig. 4.1-b, N = 3 in Fig. 4.2), the longest path is now formed by three ortho-conjugated diacetylenic units and a close correspondence in the gap (3.57 eV) is found with the ortho-oligomers of three units (3.60 eV). However, increasing again the number of condensed triangular units, a very peculiar effect is found. For N = 4 three triangular units are connected (T3C) forming both one ortho-path of four diacetylenic units and one para-path of two units. In this case, the gap (3.19 eV) is lower than the corresponding paths taken as single fragments (i.e. 3.51 eV and 3.63 eV, respectively). Increasing further the number of condensed triangular units, the HOMO-LUMO gap rapidly decreases at a much lower values than those predicted for the infinite para-conjugated polymer. This indicates that the length and type of the longest one-dimensional path in the fragment is not enough to

describe the trend in the gap. Indeed, conjugation affects the gap in a non-trivial way with more complicated conjugation paths playing an effective role. In fact, in condensed triangular units of increasing size both para- and ortho-conjugated paths of different lengths can be identified, but the predicted gap is very different from the one computed for the individual case of an ortho/para oligomer of the same length. This suggests the presence of combined effects involving both ortho and para paths that cannot be separated when larger fragments are considered. The band gap observed for the 1D system of connected triangular units presents a computed band gap value of 2.281 eV, well below the para-polymer, demonstrating again the importance of conjugation paths interacting in a 2D space. The present discussion based on a bottom-up approach becomes quite straightforward when adopting a top-down perspective, starting from the 2D infinite GDY crystal and introducing a confinement in one direction to form GDY nanoribbons (GDYNR) of decreasing width. Indeed, has been demonstrated since the first investigations of graphdiyne nanoribbons (GDYNR) [63–65] that the band gap of the 2D GDY crystal progressively increases going to GDYNR with decreasing width, reaching the highest value for the smallest width nanoribbon, that in this work corresponds to N = ∞ in Fig. 4.2. This modulation parallels what is also observed in graphene nanoribbons. However, in finite-length oligomers, different two-dimensional conjugation effects are present. This will be elucidated in the following section focused on the topological effects in 2D fragments.

4.2.2 Gap modulation in 2-D molecular fragments

Starting from the results reported in the previous section, molecular fragments extending in two dimensions are discussed here, considering in particular the different effects driven by para-, ortho- and meta paths. In sp-hybridized linear carbon system, the bond-length alternation (BLA) usually shows a very nice correlation with both the band gap and the vibrational frequency of longitudinal normal modes [37, 86, 87, 119, 120]. Conversely, in hybrid sp-sp^2 carbon GDY materials the BLA of di-acetylenic linkages is not significantly affected, as swhown in Fig. 4.3, in agreement with the case of GY fragments [52]. Substantial geometrical changes on bond lengths are found on the aromatic units connected by these di-acetylenic fragments in the different paths. In fact, carbon-carbon bonds of the sp^2 hybridized carbon atoms in the aromatic units are strongly affected by the different connections of the sp domains to the sp^2 ones. On this basis, as a structural index to correlate the topology with the computed HOMO-LUMO gap we evaluated the harmonic oscillator model of aromaticity (HOMA) parameter for the aromatic rings, calculated as suggested in Ref. [52], as defined in the original work by Krygowski et al. [117] and as discussed in the introduction. HOMA is shown to decrease by increasing the number of triangular rings (18-membered rings) in the molecular fragments due

to the elongation of conjugated bonds. Hence this parameter is able to describe all the topological effects which affect the structure of the aromatic ring, including conjugation effects responsible for modulating the HOMO-LUMO gap of the systems. Therefore, HOMA is a reliable index to show a correlation with the electronic gap, allowing to investigate relevant trends in topology-vs-gap relationship. As a reference we report graphene (i.e. completely fused aromatic rings) showing zero band gap and the lowest HOMA (0.755) amongst pure carbon systems. The upper limit is benzene with a gap of 7.24 eV and HOMA = 0.99, considered as the isolated aromatic units and thus presenting the higher gap correlated with the higher HOMA. All the systems here investigated can be viewed as aromatic rings interconnected in different geometries thus forming GDY fragments of different sizes whose HOMA values falling between these two limits (see Fig. 4.4).

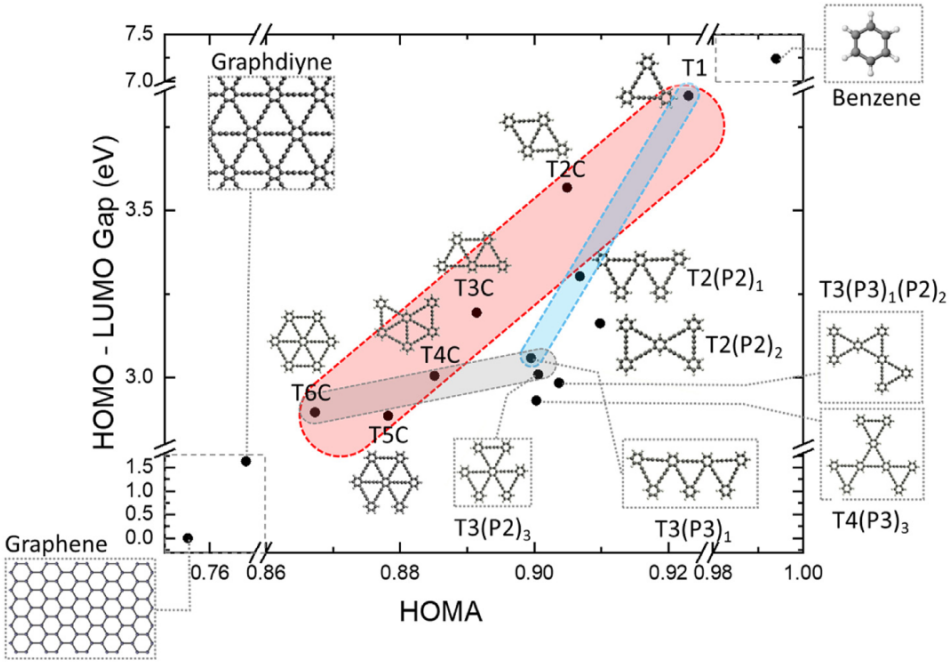

Figure 4.4: *Correlation between computed HOMO-LUMO gaps (in eV) and mean HOMA values of some of the 2D-GDY fragments investigated. Shaded areas show some peculiar trends discussed in the text. Graphene and benzene are reported as a reference [114].*

A general trend indicates smaller gap for smaller HOMA. Interestingly, considering only sp-sp^2 structures the two limits are represented by the single triangular molecule (T1) with a HOMO-LUMO gap of 3.84 eV and HOMA value of 0.92 and the infinite 2D γ-GDY crystal with a band gap of 1.63 eV and HOMA value of 0.77. γ-GDY has larger gap and HOMA values than graphene but lower than all the finite GDY fragments showing that HOMA is a reliable

index to correlate the electronic gap of these sp-sp^2 carbon systems with the degree of π-electron conjugation modulated by structural changes induced by topology. A clear relationship can be found by considering the subgroup of structures of condensed triangles of increasing number from the single triangle to the 6 condensed one (i.e. T1, T2C, T3C, T4C, T5C and T6C, highlighted in red). A progressive decrease of the gap is correlated to the decrease of the HOMA with increasing the number of fused triangular rings (that share at least one side of the triangular unit), which consist respectively of 1,2,3 4,5 and 6 triangles in these six structures. The first three cases correspond to the oligomers of the GDYNR already discussed in the previous section. In fact, moving from the triangular ring T1 to T2C an ortho-path of three diacetylenic units is formed, which is responsible for the decrease of the gap and of the HOMA. In T3C the GAP and HOMA are further lowered due to the dominating effect of para-conjugation, having a para-path of length 2 (i.e. made by 2 di-acetylenic units). T4C has a lower gap due to the increase in the number of these paths, which are now 2 of length 2, while T5C and T6C have the lowest gap values, presenting both 3 para-paths of length 2.

A similar trend with a different slope is found by considering an increasing number of triangular units linearly connected by sharing only one corner and namely starting from T1 and then considering T2(P2)$_1$ and T3(P3)$_1$ (Fig. 4.4, highlighted in light blue). The observed decrease of gap and HOMA with increasing the number of units can be related to the progressive lengthening of para-pathways respectively of length 2 and 3 in T2(P2)$_1$ and T3(P3)$_1$. However, the comparison between T2(P2)$_1$ and T3C reveals what happens in very similar structures both having one-para path of length 2. The lower gap in T3C results from the "closure" of the middle ring to form a system of three-fused ring instead of only two. The fact that the trends highlighted in red and in light blue respectively in Fig. 4.4 are slightly different can be related to the HOMA definition and its relationship to the structure topology. Indeed, in the fused structures highlighted in red the increase of the number of aromatic rings having more than two interconnected di-acetylenic bridges in ortho-position, affects the CC bond lengths in the aromatic rings. On the other hand, in the open structures highlighted in light blue in Fig. 4.4, most of the aromatic rings are connected only through two di-acetylenic chains connected in ortho-position, and this topology will even more significantly affect CC bond lengths in the rings, differently from the closed fragments. This subtle topological dependence of individual CC bond-lengths is therefore taken into account in the HOMA value.

Another interesting effect related to the type of connection between only two triangular rings can be understood looking at T2C, T2(P2)$_1$ and T2(P2)$_2$. T2C has no para paths and a larger gap, while the latter two structures have two triangular units connected at one corner but forming two different path of

length 2 in T2(P2)$_2$ instead of only one in T2(P2)$_1$. As expected, due to the increase in number of para-paths, T2(P2)$_2$ has a lower gap. Such structures show a decreasing gap at a substantially fixed HOMA (it shows only a slight increase). This behaviour can be discussed by the inspection of the topology of these structures. While in T2(P2)$_1$ all the aromatic units have multiple diacetylenic chains in ortho-position, in T2(P2)$_2$ the central aromatic ring possesses four diacetylenic bridges where two ortho- and two meta-connections can be identified. Differently than peripheral ortho-connected rings, the presence of meta-connections (which interrupt conjugation) do not affect the CC bond-leghts of these rings and the interplay between these ortho and meta-connections turns out to affect only slightly the HOMA value.

A further trend related to the existence of para-pathways is revealed by comparing T3(P3)$_1$ T4C, T3(P2)$_3$ and T6C (Fig. 4.4, highlighted in grey). The latter three models possess only para-paths of length 2, which are 2 in number for T4C and 3 for T3(P2)$_3$ and T6C, while T3(P3)$_1$ has only one para-path of length 3. Despite the longest path, the gap of T3(P3)$_1$ is larger than the other three, suggesting that a larger number of shortest path can decrease the gap more than the length of the para-conjugated segments. The case T4C further shows that even if only two para-paths of length 2 are present, by maximizing the number of fused triangular rings, conjugation will dominate over a larger length of the para-path. Considering now T3(P3)$_1$(P2)$_2$ and T4(P3)$_3$ (see Fig. 4.4), where now we have respectively one para-path of length 3 plus 2 para-path of length 2 in T3(P3)$_1$(P2)$_2$ and 3 para-path of length 3 in T4(P3)$_3$, a lower gap is found with respect to the previous models but they are both slightly larger than T6C (3 para-path of length 2 where the number of fused triangular rings is maximized). Very relevant is the comparison between T6C and T4(P3)$_3$: T6C has three para-path of length 2 while T4(P3)$_3$ has three para path of length 3. The latter should have a lower gap based on the assumption that the length and the number of para-paths mostly affect the gap value. However, they both present a very similar gap value, demonstrating that the formation of a multiply-fused structure has a dominating effect in reducing the band gap with respect to a more "open" one (with longer para-path). Our analysis reveals a subtle interplay of different topological effects in determining the degree of conjugation and hence the HOMO-LUMO gap in GDY fragments. We have shown that para pathways dominate over ortho and meta ones. The number of para pathways dominate over the length of each path and for the same number of para paths fused triangular structures showed a larger conjugation (i.e. smaller HOMA).

4.2.3 Modulation of the relevant marker bands in Raman spectra

The very intense Raman band related to longitudinal normal modes of vibration (collective CC stretchings on the linear sp-domains, ECC mode) [37, 86,

87, 119, 120] reveals a significant modulation for the different structures and it is another important experimental observable which could help in establishing structure-properties relationships in GDY-based system. For this reason, we calculated the Raman spectra of the investigated fragments to correlate electronic and vibrational properties and to assess the use of spectroscopic measurements to identify the presence of peculiar topologies (see Fig. 4).

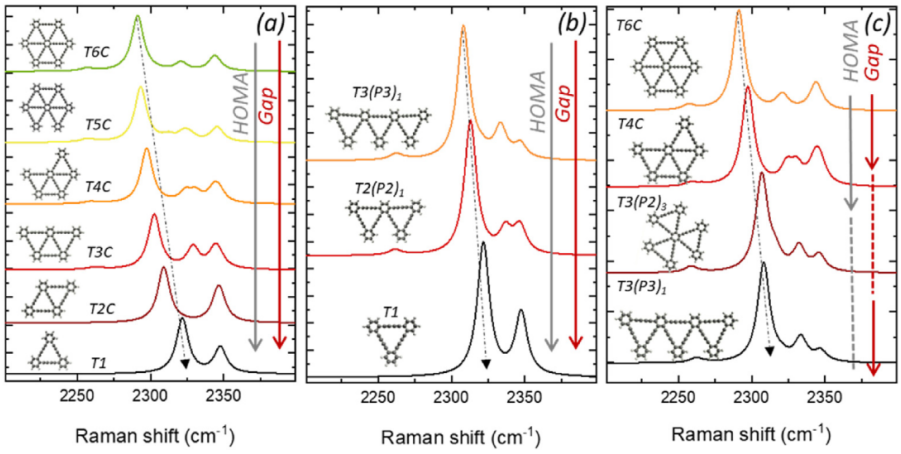

Figure 4.5: *DFT-computed Raman spectra of 2D-GDY molecular fragments for different subgroups of structures. The corresponding trend of HOMA and gap is represented by arrows (dotted line indicates no substantial variation).*

No clear correlation with the peculiar structure of the different fragments is found in the aromatic ring vibrations below 1700 cm^{-1} . Hence we focus on the main Raman active bands associated to stretching vibration of sp-carbon atoms falling in the 2000 and 2400 cm^{-1} spectral region which is a peculiar and intense marker band of sp-carbon systems. The normal mode related to this band is the ECC mode. This band is strongly related to π-delocalization along the sp-carbon domains and it is usually modulated by the BLA. As shown in Fig. 4.5-a, in fragments with increasing number of fused triangular rings the most intense ECC mode shows a progressive red shift in the frequency (more than 30 cm^{-1}). This redshift is accompanied by a decrease of both gap and HOMA. A similar trend is observed when increasing the length of a single para path as in T1, $T2(P2)_1$ and $T3(P3)_1$. The ECC mode frequency changes from 2322 cm^{-1} to 2308 cm^{-1} for increasing length of the para-conjugation pathway and with a parallel decrease of gap and HOMA (Fig. 4.5-b). More complex is what happens in Fig. 4.5-c for $T3(P3)_1$, $T3(P2)_3$, T4C and T6C. $T3(P2)_3$ and T4C. They have the same gap (3.009 and 3.005 eV respectively) but the main Raman peak of T4C is red-shifted in frequency with respect to $T3(P2)_3$ (10 cm^1, from 2307 to 2297 cm^1). This is correlated to the larger number of fused 6-membered rings that are observed in T4C. Moreover, $T3(P3)_1$ (band gap of

3.06 eV) has an intense Raman active peak whose normal mode is located at the same frequency of the main Raman active mode of T3(P2)$_3$, consistently with the very similar gap and the same HOMA values. Finally, the most intense peak associated to the ECC mode of T6C reveals to be the most red-shifted between the others (2291 cm^{-1}), again in very good agreement with the trends observed in the gap values. An impressive correlation is found between HOMA and ECC wavenumbers, with a relationship which is very close to linearity, as shown in Fig. 4.6. This indicates a close relation between the structural variations induced on the aromatic rings by the possible different topology and the vibrations of the linear sp-domains.

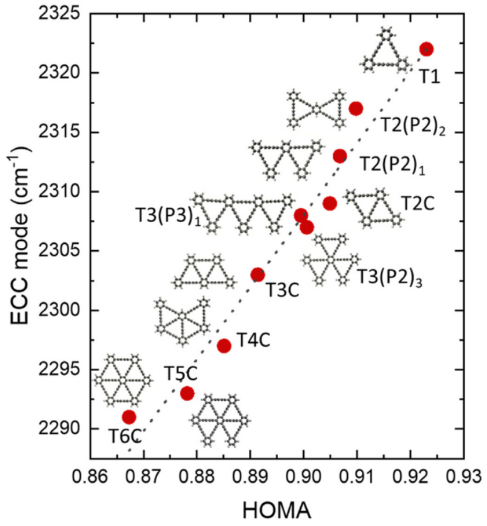

Figure 4.6: *Correlation between HOMA and ECC mode wavenumbers.*

In particular, we underline that sp-carbon chains vibrations are indirectly affected by geometry variations on the hexagonal rings, indicating further how these rings are the key connecting units in modulating the extent of π-electrons delocalization in these hybrid sp-sp^2 carbon materials. Therefore, the HOMA parameter turns out to be significant to investigate not only the trends in the electronic gap, but also in the vibrational features of these systems. In sp-carbon structures, the correlation between structural/vibrational/electronic properties is usually based on the BLA. In fact, BLA is a structural index which directly modulates the frequency of the ECC mode and is directly influenced by the degree of conjugation. In hybrid sp-sp^2 carbon materials studied here, the BLA predicted on the diacetylenic domains does not show remarkable difference. This means that conjugation has a more complex effect on the structural parameters responsible for modulating the gap and the Raman frequency of the ECC mode. It is indeed the HOMA index that is able to describe both the different gap and the variation in the ECC mode frequency as a function

of the different topology of the GDY fragments.

4.3 1D γ-graphdiyne nanoribbons (GDYNRs)

Following a bottom-up approach, we continued the analysis of these systems focusing our attention on graphdiyne-based nanoribbons (GDYNR). To present the results coming from DFT calculations of three series of nanoribbons, we refer to the nomenclature introduced in previous papers [47, 59, 63–65]. Armchair and zigzag are indicated by A(n)-GDYNR and Z(n)-GDYNR, respectively, where the index n refers to the width of GDYNR, which is an integer value for A(n)-GDYNR (n = 1,2, . . . ,5) and integer or half-integer value in the case of Z(n)-GDYNR (n=1,3/2, . . .,5), as depicted in Fig. 4.7.

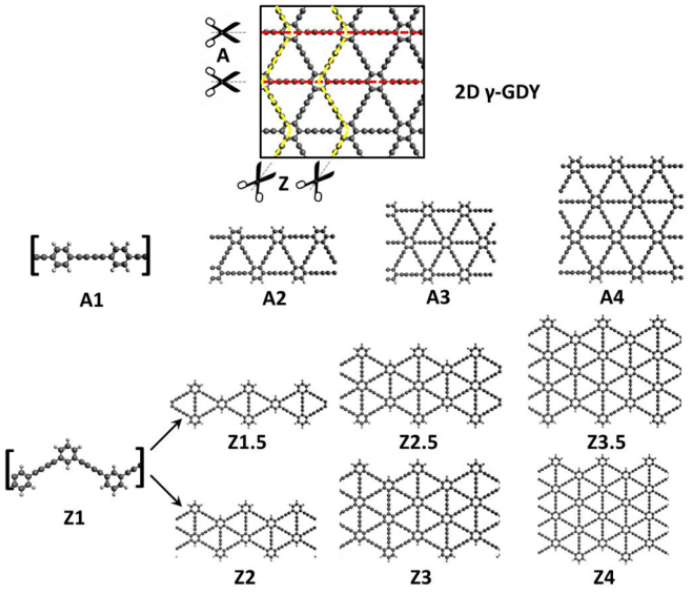

Figure 4.7: *Sketches of the armchair A(n)- and zigzag Z(n)-GDYNRs investigated in this work. n is the index representing the nanoribbon width.*

Such GDYNR models can be classified according to the proper line-symmetry groups, isomorphs to D_{2h} group in the case of A(n)-GDYNR and Z(n)-GDYNR with half-integer n. Z(n)-GDYNR with integer n, belong to the C_{2v} group. For all GDYNR, hydrogen atoms have been added at the edges as end groups, in agreement with most of the previous computational works [47, 59, 63–65]. This choice is reasonable also from the experimental point of view, based on the finite GDY fragments that have been synthetized in the past [51]. To assess the influence of the edge type on both electronic and vibrational properties, we have considered also the A(1) and Z(1) systems, which correspond to copolymers

formed by alternated diacetylenic and phenyl-rings units connected, respectively, in para- and meta-positions [52]. These two limiting cases represent a reference system formed by just the edge of A(n)- and Z(n)-GDYNR.

Geometry optimization, band-gap evaluation, and prediction of IR and Raman spectra have been carried out for GDYNR, treated as one-dimensional (1D) crystals, by employing DFT simulations and applying periodic boundary conditions in one dimensions, respectively. The CRYSTAL17 code [116] has been adopted to this aim, exploiting the possibility to employ hybrid exchange-correlation functionals together with Gaussian basis sets. PBE0/6-31G(d,p) and HSE06/6-31G(d,p) levels of theory have been then chosen to predict the gap of the different GDYNR of different width, while, among these, Raman spectra could be computed only at PBE0/6-31G(d,p) level in CRYSTAL17 since HSE06 is not yet implemented for Raman response. Previous experience in the prediction of the Raman response of several sp-carbon-based molecular systems shows that this functional provides a good agreement vs experimental data [37, 86, 87]. According to the discussion reported in Ref. [121], the exponent of the diffuse sp orbitals in 6-31G(d) basis set of carbon atoms have been increased from 0.1687144 to 0.187 bohr^{-2} to avoid convergence problems in the self-consistent field cycles, due to basis sets linear dependencies. For the same reason, when using the VTZ basis set, the exponent 0.12873135 bohr^{-2} of one of the s functions and the exponent 0.10084754 bohr^{-2} of one of the p functions have been changed to 0.153 and 0.12 bohr^{-2}, respectively. Considering other parameters of the CRYSTAL simulations, the tolerance on integral screening (TOLINTEG parameters) have been fixed to 9,9,9,9,80, while the shrink parameters defining Monkhorst-Pack sampling points have been fixed to 100 for the calculation of the band structures and gaps and 50 for the vibrational analysis.

4.3.1 Electronic properties of 1D γ-graphdiyne nanoribbons

Considering zigzag and armchair GDYNR, in Fig. 4.8 we plot the band gap of A(n)-GDYNR and Z(n)-GDYNR as a function of the n index (n$\leq$5) and compared with the values found for 2D-GDY (i.e., n $\rightarrow \infty$).

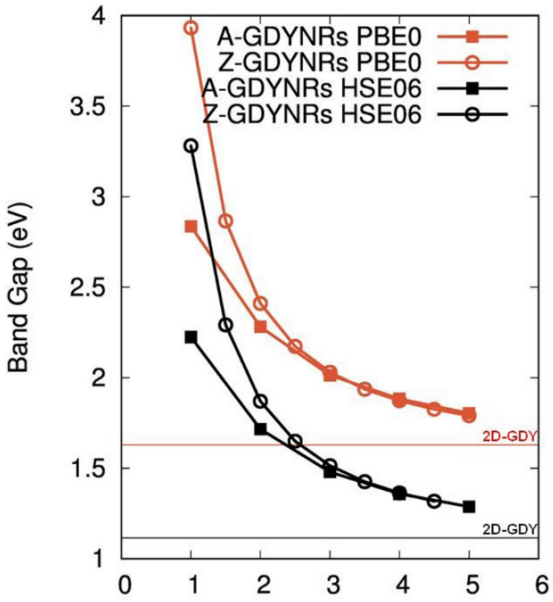

Figure 4.8: *Band gap (eV) of armchair and zigzag GDYNR as a function of width index (n) as obtained by PBE0/6-31G(d) (in red) and HSE06/6-31G(d) (in black) calculations. The value band gap of 2D-GDY is also indicated as a comparison by the horizontal lines. [115]*

Several works report that the gap of confined GDY is larger than the gap of the infinitely extended 2D GDY and decreases for increasing size, towards the limit of 2D-GDY [47,59,63–65]. Confinement effects caused by the finite width of GDYNR modulate the gap, similar to the behavior of graphene nanoribbons with respect to the graphene crystal. As shown in Fig. 4.8 this modulation of the gap spans a range of about 1 eV (for n$\leq$2). As expected, the values obtained with the HSE06 functional are systematically lower than those obtained with PBE0. However, both functionals essentially describe the same behavior. Interestingly, while for n $>$ 3 the trends are the same for both edges, for small widths (n $<$ 3), Z(n)-GDYNRs have a larger gap with respect to A(n)-GDYNRs. The reason for this is evident if we consider the gap values obtained for the limiting case (n = 1) of the 1D polymers A(1) and Z(1) (Fig. 4.7). Both polymers can be described as sp-carbon segments of four carbon atoms (i.e., diacetylenic units) interconnected by phenyl rings. The connection on these rings can be done along three different conjugation paths, corresponding to para-, meta-, and ortho- connections. As highlighted by Tahara et al. investigating the case of graphyne fragments [52], A(1) corresponds to a para-conjugated system where the delocalization of π electrons along the system occurs more efficiently, thus promoting the lowest gap. Conversely, the meta-conjugation characteristic of Z(1) reduces π-electron delocalization, which justifies the higher band gap. As expected, the influence of the edge type is effective for small widths, but rapidly decreases for increasing width.

For n > 3 the edge type (A or Z) has a very limited influence on the gap, even if the gap remains still quite far from the n $\rightarrow \infty$ limit of the 2D-GDY crystal.

4.3.2 Raman and IR spectra of GDYNRs: Markers of confinement

The detailed analysis of Raman and IR spectra of A- and Z- nanoribbons presented here aims at discussing the existence of marker bands that could be taken as signature of spatial confinement and/or edge type (A- or Z-). Computed wave numbers, IR intensities, Raman activities, and graphical representations of the normal modes of vibration of the main GDYNR markers discussed in the text are reported in the Supplementary Material of our work [115].

Raman spectra

Figure 4.9 compares Raman spectra of A(n)- and Z(n)-GDYNR for increasing widths with the spectrum of 2D-GDY, discussed in the previous section. Starting from n = 2, both A(n)- and Z(n)-GDYNR show strong bands which can be put in correspondence with the Raman bands of 2D-GDY. We discuss bands in the region of sp-carbon diacetilenic segments (2000-2400 cm^{-1} range) and in the region of sp^2 carbon of the phenyls (1400-1600 cm^{-1} range).

We can start the discussion with the 2000–2400 cm^{-1} region. At first, we have to define the main active bands appearing, concerning this region, in the Raman spectra of 2D γ-GDY crystal, whoose detailed vibrational treatment will be presented in the following chapter. Indeed, γ-GDY is characterized by the Y and Y' phonons that are, respectively, A_{1g} and E_{2g} collective CC stretching vibrations localized on its sp-carbon domains. The combination of the stretching coordinates of each i_{th} polyyne arm follows the characteristic pattern shown by the ECC mode. The properties of this mode have been widely discussed in the past [17] [24], extending the treatment of vibrational dynamics developed for polyconjugated polymers a few decades ago [119] [120]. In the A_{1g} Y mode (2276 cm^{-1}), all sp-carbon chains oscillate in-phase, according to the ECC coordinate. In the E_{2g} Y' mode (2335 cm^{-1}) the ECC vibrational pattern is repeated on the six polyyne segments with different relative phases, according to E_{2g} symmetry. For what concerns GDYNR, a strong doublet ($\approx$ 2300 cm^{-1}) correlates with the Y and Y' lines of 2D-GDY. The strongest A_{1g} band starts from 2307 cm^{-1} (2305 cm^{-1}) in A(2)-GDYNR [Z(2)-GDYNR], and in larger ribbons converges to a unique wave number (2285 cm^{-1}, about 10 cm^{-1} higher than Y line of 2D-GDY, and independent of edge topology, see Fig. 4.9). The remarkable frequency dispersion ($\approx$ 30 cm^{-1}) from n = 2 to n = ∞ (2D-GDY) suggests that this band is highly sensitive to π-electron delocalization, thus indicating that there is a strong interplay between the π electrons of the polyyne arms and those of the aromatic rings. The effect of edge topology on the Y line can be appreciated only considering very thin ribbons

(n = 1, 1.5). The higher wave-number component of such doublet correlates with the Y' E_{2g} line of 2D-GDY, and shows a less-pronounced dispersion [10 cm^{-1} for A(n)-GDYNRs and 20 cm^{-1} for Z(n)-GDYNRs] while it is more sensitive to the edge type. In the case n = 1, the Y-Y' doublet merges in a single band predicted at 2344 and 2371 cm^{-1} for A(1) and Z(1) species, respectively. This band corresponds to the ECC mode of the single unit of polyyne (one unit cell) in the sp-carbon segment. Moreover, calculation of the vibrational structure of a diphenyl polyyne consisting of a linear chain having 4 sp-hybridized carbon atoms capped with two phenyl groups (i.e., the smallest structural unit defining GDY) has been performed as a term of comparison. Remarkably, the wave number of this mode in A(1)- GDYNR is significantly lower than the corresponding mode of the diphenyl-polyyne model molecule (2368 cm^{-1}), while it almost coincides for Z(1)-GDYNR. This complies with the effect of conjugation between π electrons of the polyyne chain and π electrons of the aromatic ring being more effective in the case of the para- substitution (see the discussion above on the band gaps). A thorough discussion on the physical effects ruling this behavior can be found in Ref. [37]. The lowering of symmetry in GDYNR with respect to 2D-GDY concurs with the activation of different modes, close in frequency and mainly contributing to the two main Y and Y' bands. Sometimes, weak additional bands can be identified [e.g., A(4), A(5), Z(2), Z(4)]. The Y-Y' doublet cannot be taken as a characteristic marker of a ribbon, because of its clear relationship with the corresponding doublet of the 2D crystal. However, the remarkable redshift observed with increasing width for both families of GDYNR (Fig. 4.9) suggests that the position of Y and Y' could be a diagnostic tool regarding the width of GDYNR, at least qualitatively.

Focusing now on 850–1600 cm^{-1} region, γ-GDY crystal is mainly characterized by three signatures useful for the comparison with its nanoribbons: The G mode (1573 cm^{-1}) that involves stretching of the phenyl units' bonds with in phase contribution by the stretching vibration of single bonds linked to the aromatic units. The displacements pattern recalls that associated with the G line of graphene. The D line (1490 cm^{-1}) is assigned to a phonon decribed as the ring breathing coupled to the stretchings of the CC bonds linked to the aromatic moiety. These coordinates vibrate out of phase, with a pattern very similar to that of the phonon associated with the D line of graphite/graphene. Lastly, the B line (983 cm^{-1}) is associated with the breathing mode of the phenyl units, out-of-phase coupled with the stretching coordinates of the central CC bonds. Starting from A(3)-GDYNR and Z(2)-GDYNR, we clearly identify three bands: the first is very close to the G line of 2D-GDY (at 1571 cm^{-1}), the second to the D band (at 1490 cm^{-1}), and the third to the B band (at 983 cm^{-1}). Several satellite lines also show up, giving rise to a rather rich spectrum. This feature is ascribed to the presence of CH bonds on the edges

of the ribbons, whose characteristic bending frequencies lie in this spectral region. By analyzing the vibrational eigenvectors of A(n)-GYNRs, we observe that the band at about 1570 cm^{-1} corresponds to the G-mode vibration (ring stretching) of the "bulk" regions, whereas the band at about 1630 cm^{-1} is assigned to the same vibrational pattern, well localized on the edges and coupled to CH wagging vibrations. A similar situation is found for the two lines at 1452 and 1499 cm^{-1} : the latter corresponds to the D line of 2D-GDY, and is associated with a bulk normal mode, whereas the former shows the same vibrational pattern, mainly localized on peripheral rings and coupled with CH wagging vibrations. Therefore, the lines at 1452 and 1630 cm^{-1} can be taken as markers of armchair edges and, as expected, their relative intensity decreases with increasing the nanoribbon width n. These lines are rather intense and should allow a reliable identification of A(n)-GDYNRs. Remarkably, thanks to its A_{1g} symmetry, the 1630 cm^{-1} line shows a sizable Raman intensity also for the largest A(n)-GDYNR here investigated (n = 5). Considering Z(n)-GDYNRs, the inspection of Fig. 4.9 shows that the edge type significantly affects the shape of the Raman spectrum. In the Raman spectra of the thinner Z(n)-GDYNRs we observe two bands (1650, 1460 cm^{-1}) that are the counterparts of the satellite bands observed for A(n)-GDYNR. However, these lines are significantly weaker in Z(n)- than in A(n)-GDYNR, which would make more difficult the recognition of Z(n)-GDYNR based on the Raman pattern.

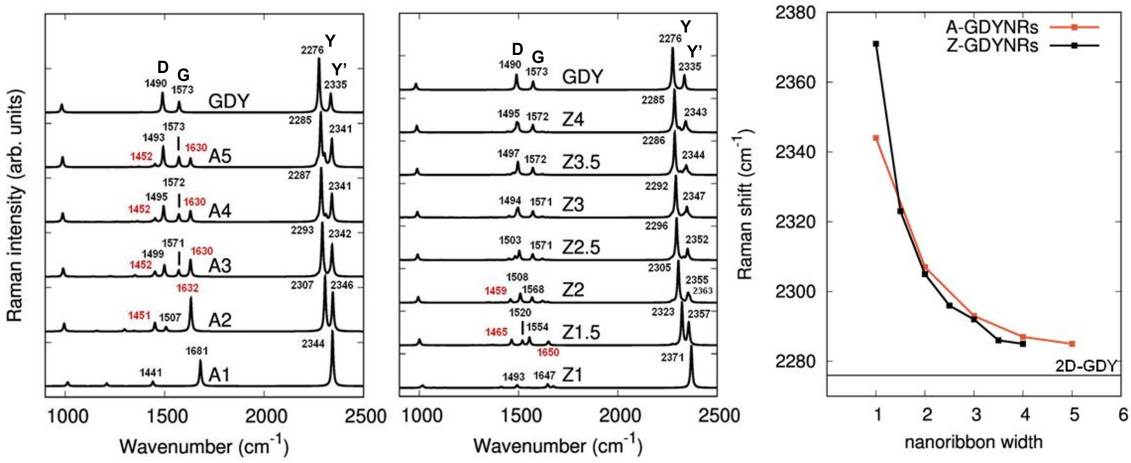

Figure 4.9: *Comparison among the DFT computed [PBE0/6-31G(d)] Raman spectra of 2D-GDY, A(n)-GDYNRs (left) and Z(n)-GDYNRs (center) having increasing widths. The wavenumber values are not scaled. (Right) Modulation of the DFT-computed [PBE0/6-31G(d), unscaled values] wave number of the Raman Y bands predicted for armchair and zigzag GDYNRs as a function of their width. The wavenumber computed for 2D-GDY is also reported as a comparison [115].*

IR spectra

In Fig. 4.10 we compare the IR spectra of A(n)- and Z(n) GDYNRs with the spectra of the 1D infinite polymers [A(1) and Z(1)] and 2D-GDY.

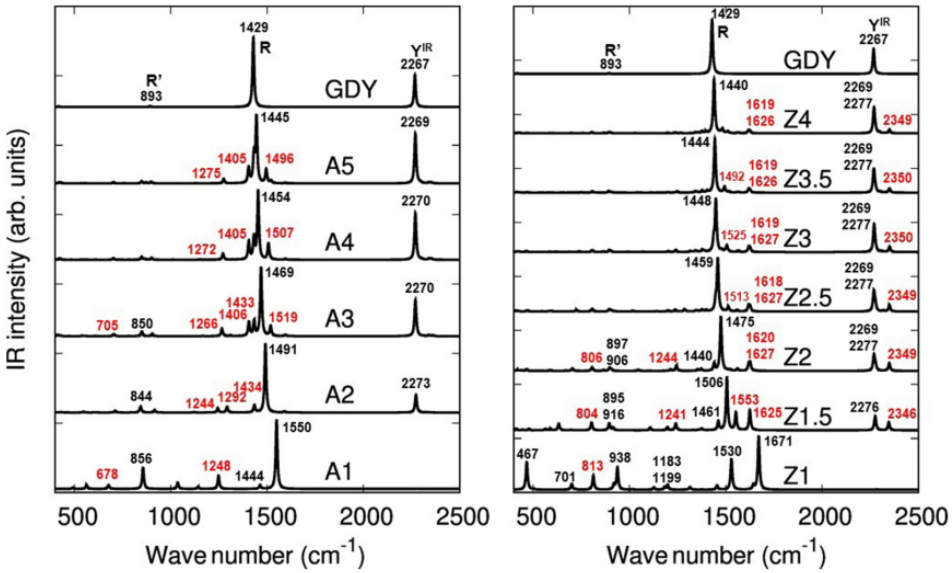

Figure 4.10: *Comparison among the DFT-computed [PBE0/6-31G(d)] IR spectra of 2D-GDY, A(n)-GDYNRs, and Z(n)-GDYNRs having increasing widths. The wave-number values are not scaled.*

Starting from the 2000–2400 cm^{-1} region, for both edge types, the polymers A(1) and Z(1) do not show any IR band of appreciable intensity in the sp-carbon region above 2000 cm^{-1}. Starting from A(2) a band raises at about 2270 cm^{-1} , very close to the Y^{IR} band of the 2D crystal characterized by out-of-phase combination of single and triple bonds stretching coordinates. Similarly, in the IR spectrum of Z(n)-GDYNRs we find a rather strong Y^{IR} band coming from two close phonons, computed at 2269 and 2277 cm^{-1}. Another IR peak at 2350 cm^{-1} is clearly observed for Z(n)-GDYNRs, corresponding to the IR-active ECC mode localized on the edges. On the opposite, only a very weak additional absorption band is present for A(n)-GDYNRs. This behavior makes this feature a potential marker of Z edges.

In the 850–1600 cm^{-1} region the strong R band of 2D-GDY (1429 cm^{-1}), which is mainly due to CC stretching of the bonds in the phenyl units with out-of-phase contribution of the stretching coordinates of single bonds linked to the aromatic unit, as well as the weak R' (893 cm^{-1}), mainly involving stretching coordinates of bonds inside the aromatic rings coupled in phase with the stretching of the bonds in the phenyl units, find a nice correspondence with two IR features of GYNRs, beginning with A(2) and Z(1.5). The bands

predicted at about 1270 and 700 cm^{-1} in the larger A(n)-GDYNRs, even if weak, are significant markers of confinement. While many intense bands are predicted for Z(1), the bands below 1400 cm^{-1} are weaker in Z(n)-GDYNRs: as in the Raman, markers of Z nanoribbons are difficult to identify, also with IR spectroscopy in this spectral region. A good marker of Z(n)-GDYNRs could be the band at about 1620 cm^{-1}, which results from the convolution of two bands computed at 1619 and 1626 cm^{-1}.

Effects of the edge groups

In addition to the spectral region above 1000 cm^{-1}, the IR spectra show another frequency range where significant features could be analyzed to discriminate between GDYNR with different edges. In particular, Ref. [122] showed that, similarly to CH stretching modes located in different intramolecular environments [123], also out-of-plane (opla) CH bending normal modes (600-900 cm^{-1} range) are influenced by the molecular topology. In the case of polycyclic aromatic hydrocarbons (PAHs), out-of-plane CH bending (hereafter referred as opla) modes bring significant information about the edge: Indeed, depending on the edge topology different "types" of vibrational patterns, associated with IR transitions, can be identified, each one at characteristic wave number. These vibrational patterns are sketched in Fig. 4.11 and are described as collective out-of-plane displacements of one, two, or three adjacent CH bonds. In the literature, they have been named SOLO, DUO, and TRIO [123].

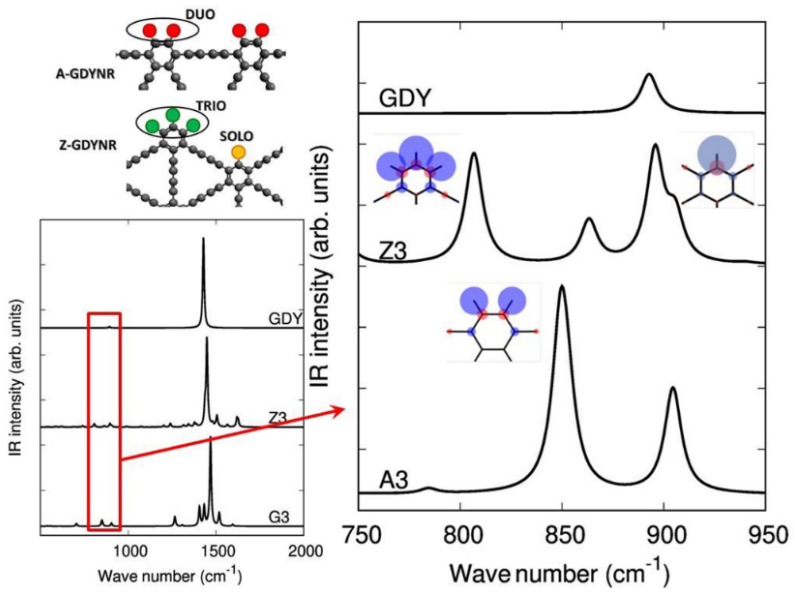

Figure 4.11: *(Top left) Definition of SOLO, DUO, and TRIO vibrational patterns associated to opla CH bending normal modes found in A- and Z-GDYNR. (Right) Comparison among the DFT-computed [PBE0/6-31G(d)] IR spectra of 2D-GDY, with A(3)- and Z(3)-GDYNR in the frequency range 750-950 cm^{-1} where opla CH bending vibrations of the edges are found. Sketches of the opla CH normal modes describing the different bands are reported in the figure: atomic displacements are indicated by red and purple circles with different colors indicating, respectively, opposite spatial phases of the motion. The amplitudes of the displacement are proportional to the diameter of the circle. The wave-number values are not scaled [115].*

In PAHs, TRIO modes are located at lower wave numbers than SOLO modes while DUO vibrations are located between these two extremes. Moreover, since these modes are out- of-plane vibrations (orthogonal to the plane of π-conjugated atoms) and are completely localized on terminal CH bonds, they are not affected by π-electron delocalization. Therefore, the same behavior observed in PAHs should be found also in the case of GDYNR. We report in Fig. 4.11 the analysis of the 750-950 cm^{-1} range for 2D-GDY, A(3)- and Z(3)-GDYNR. Even if the opla CH bending vibrations give contributions to the IR spectra weaker than the bands above 1250 cm^{-1} (see the bottom left panel of Fig. 4.11), the bands between 750 and 950 cm^{-1} are non-negligible and are potentially measurable. By analyzing more in detail this region, we observe significant differences between A(3)- and Z(3)-GDYNR. A(3)-GDYNR shows two bands at 850 and 905 cm^{-1} : the latter is reminiscent of a band found in 2D-GDY and it is due to a bulk mode of carbons atoms. As expected, the band at 850 cm^{-1} is an opla CH bending vibration, and it belongs to the DUO pattern. In the case of Z(n)-GDYNR, four IR bands are found (807, 863, 896, and 906 cm^{-1}). The bands at 863 and 896 cm^{-1} are related to bulk modes

of carbon domains, while the intense band at 807 cm^{-1} and the shoulder at 906 cm^{-1} are assigned to pure opla CH bending vibrations. In full agreement with the behavior of PAHs, the band at 807 cm^{-1} is associated with TRIO moieties and the band at 906 cm^{-1} with SOLO moieties. Based on these results, we infer that the analysis of IR spectra below 1000 cm^{-1} would allow one to detect useful markers able to clearly discriminate A(n)-GDYNR from Z(n)-GDYNR. We also note that a similar spectroscopic signature is predicted also for Raman-active opla CH bending vibrations. However, their Raman intensity is very weak and probably not measurable.

Spectroscopic marker bands of armchair and zigzag GDYNR

One possible question regarding the presented analysis of Raman and IR spectra of A- and Z- nanoribbons is about the existence of marker bands that could be taken as signature of the nanoribbon's edge type (A- or Z-). To this aim, In Figure 4.12 we directly compare the Raman and IR spectra of A(3)-GDYNR and Z(n)-GDYNR (n = 2.5, 3) with those of 2D-GDY to reveal the peculiar marker bands of A- and Z- GDYNR. As mentioned in the previous sections, while in the Raman spectra Z-edges do not show intense marker bands, A(3)-GDYNR presents a relevant marker bands at 1630 cm^{-1}, which can be considered not only as a marker of confinement, but also a reliable marker of the A edges presence. By comparing the Raman spectra of integer and half integer Z(n)-GDYNRs, we can notice small but clear differences. For instance, Z(3) shows one only band originated by the superposition of two normal modes located at 1490 cm^{-1} and at 1498 cm^{-1} while for Z(2.5), in the same spectral range, two individual components are computed, located at 1482 cm^{-1} and at 1503 cm^{-1} respectively, giving rise to a doublet of peaks . However, these bands find a clear correspondence with D line of 2D crystal and cannot be taken as marker band of the ribbons. Considering the IR spectrum, a reliable marker of Z(n)-GDYNRs can be found in the extra band predicted at about 2350 cm^{-1} , which does not appear in the case of for A(n)-GDYNRs. In addition, another marker of Z edge is the band at about 1620 cm^{-1} . On the other hand, A(n)-GDNRs display several marker bands at about 1270 and 1405 cm^{-1}.

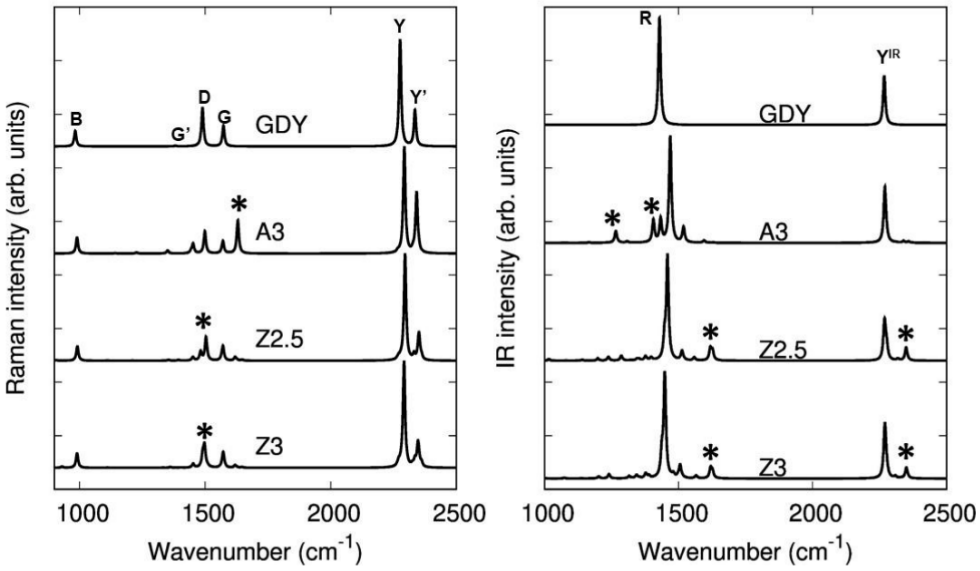

Figure 4.12: *Comparison among the DFT computed (PBE0/6-31G(d)) Raman and IR spectra of 2D-GDY, with GDYNRs having different edges and the same width. The wavenumber values are not scaled. The bands discussed in the text are marked by *.*

4.4 2D γ-graphdiyne (γ-GDY): electronic and vibrational properties

The final section of the chapter is dedicated to the investigation of the electronic structure of 2D γ-GDY and the prediction and assignment of its IR and Raman spectra using periodic DFT simulations (CRYSTAL17 code), similar to the case of GDYNR, and adopting different functionals and basis sets. Indeed, for γ-GDY crystal, for which reference theoretical data are already available in the literature both considering band gaps [47, 59] and Raman spectra [61], local-density approximation (LDA) (VWN), generalized gradient approximation (GGA) (PBE and BLYP), and hybrid functionals (PBE0, HSE06, B3LYP) have been considered with 6-31G(d,p) basis sets. For PBE0 and HSE06 only, also the more extended Ahlrichs VTZ+polarization basis set has been used. This allowed analyzing the reliability of different functionals, including hybrid ones, and the influence of basis set in the prediction of the band gap. The other computational parameters adopted were the same employed for the case of γ-GDY nanoribbons, whose treatment is reported in the previous section.

4.4.1 Electronic properties of 2D γ-graphdiyne

As first investigation, computation of the electronic structure of 2D γ-GDY by periodic DFT simulations has been done adopting different functionals and

basis sets. Indeed, as illustrated in previous papers [47] [59], the gap in the band structure of γ-GDY is found at the Γ point (Fig. 4.13). As in the case of other carbon-based polyconjugated materials, the correct prediction of the gap suffers from the limitations of current DFT pure functionals in describing accurately π-electron delocalization, with a tendency to overestimate its effect, thus causing unrealistically low predictions of the band gap. For instance, the gap of 2D γ-GDY reported in the literature changes from about 0.4 eV (LDA), 0.5 eV (GGA) to 0.9–1.1 eV when employing hybrid functionals or the GW method. The latter values are considered more reliable [47, 56, 59, 68]. In fact, it is well known that hybrid functionals significantly improve the accuracy in the description of π-electron delocalization, but their use is not convenient when employing plane waves and pseudopotential methods to carry out DFT calculations in periodic systems. A useful alternative is provided by Gaussian basis sets, which allow using hybrid functionals at an acceptable computational cost.

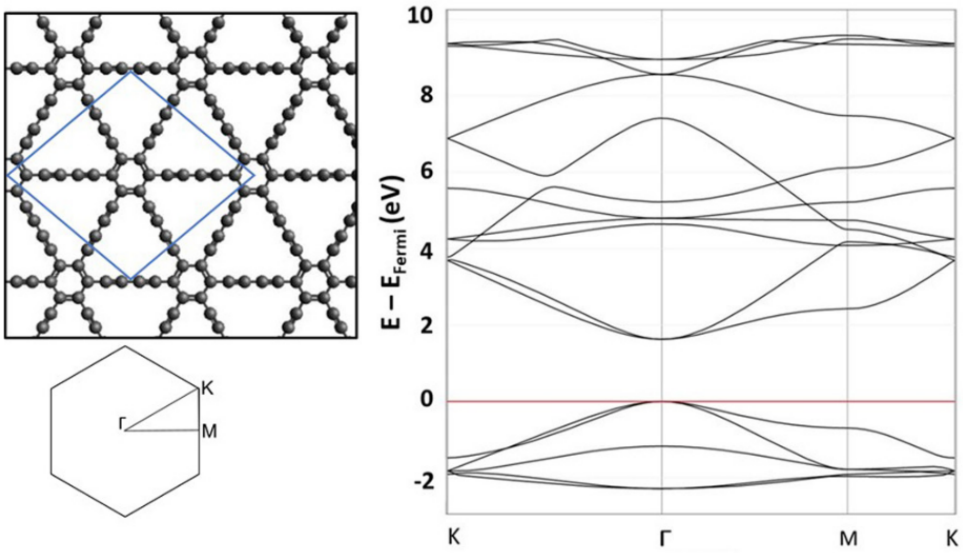

Figure 4.13: *Electronic band structure of 2D-GDY [PBE0/6-31G(d) DFT calculation] [115].*

In Tab. 4.1 band gaps computed by employing different LDA, GGA, and hybrid functionals are reported. For PBE0 and HSE06 I also provide the comparison of the results produced by a double-ζ basis set (6-31G(d)) vs a triple-ζ basis set (VTZ). We note that the effect of the basis set is less important than the choice of the functional: indeed, both for PBE0 and HSE06, adopting the more accurate VTZ basis set gives in both cases a gap which is just about 0.05 eV larger than the values obtained with the 6-31G(d) basis set. Therefore, we can suppose that the latter basis set is sufficiently accurate to model the prop-

erties of this system. Considering LDA and GGA functionals (PBE, BLYP), we obtain band gaps of 0.4 (LDA), 0.45 (PBE), and 0.48 eV (BLYP), in full agreement with previous calculations. As expected, hybrid functionals provide higher values of the band gap: 1.6 eV (PBE0), 1.4 eV (B3LYP), and 1.1 eV (HSE06). The latter value agrees with the result of GW calculations, usually taken as an accurate reference value. This also agrees with the fact that HSE06 has been found to give a more accurate prediction of band gaps with respect to the parent PBE0 functional [124].

XC functional	Basis set	Band gap (eV)
PBE0	6-31G(d)	1.63
	VTZP	1.67
HSE06	6-31G(d)	1.11
	VTZP	1.16
B3LYP	6-31G(d)	1.40
BLYP	6-31G(d)	0.48
PBE	6-31G(d)	0.45
LDA (VWN)	6-31 G(d)	0.40

Table 4.1: Band gaps of 2D-GDY computed by employing different exchange-correlation functionals and Gaussian basis sets.

4.4.2 Vibrational spectra and optically active phonons of 2D γ-GDY

The phonons of 2D-GDY at the Γ point can be classified according to the D_{6h} point group, which is isomorphic to the *P6/mmm* layer group of the crystal. The structure of the representation of the D_{6h} point group in the vibrational space is:

$$\Gamma^{vib} = 3A_{1g}+2A_{2g}+3B_{2g}+3E_{1g}+6E_{2g}+2A_{2u}+5E_{1u}+3B_{1u}+3B_{2u}+3E_{2u} \quad (4.3)$$

A_{1g}, E_{1g} and E_{2g} phonons are Raman active, whereas A_{2u} and E_{1u} are IR active; the rest of the irreducible representations (A_{2g}, B_{2g}, B_{1u}, B_{2u}, E_{2u}) are inactive. Therefore, 12 peaks (9 of which are double degenerate) are expected in the first-order Raman spectrum, and 7 absorption bands (5 double degenerate) in the IR spectrum. Furthermore, since the D_{6h} point group possesses inversion symmetry, there is mutual exclusion between IR and Raman transitions. The Raman and IR spectra of 2D-GDY computed by DFT are reported in Fig. 4.14.

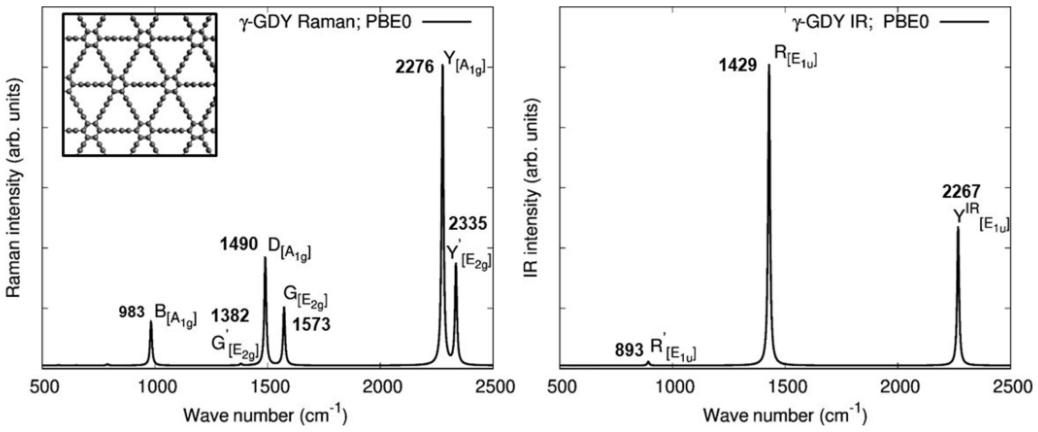

Figure 4.14: *DFT-computed [PBE0/6-31G(d)] Raman and IR spectra of 2D-GDY. The wavenumber values are not scaled [115].*

Our calculations provide a pattern of the Raman spectrum which is similar to the one determined by Zhang et al. adopting LDA and plane-wave pseudopotential method [61]. The labels used in Fig. 4.14 to identify the different Raman lines have been chosen analyzing the related vibrational eigenvectors, to suggest possible correlations with the vibrational transitions of related materials (e.g., G and D Raman lines of graphene). In Fig. 4.15 and 4.16, sketches of the normal modes of vibration associated to the main Raman and IR active bands of γ-GDY are reported in order to support the Raman and IR assignment discussion present in the following section.

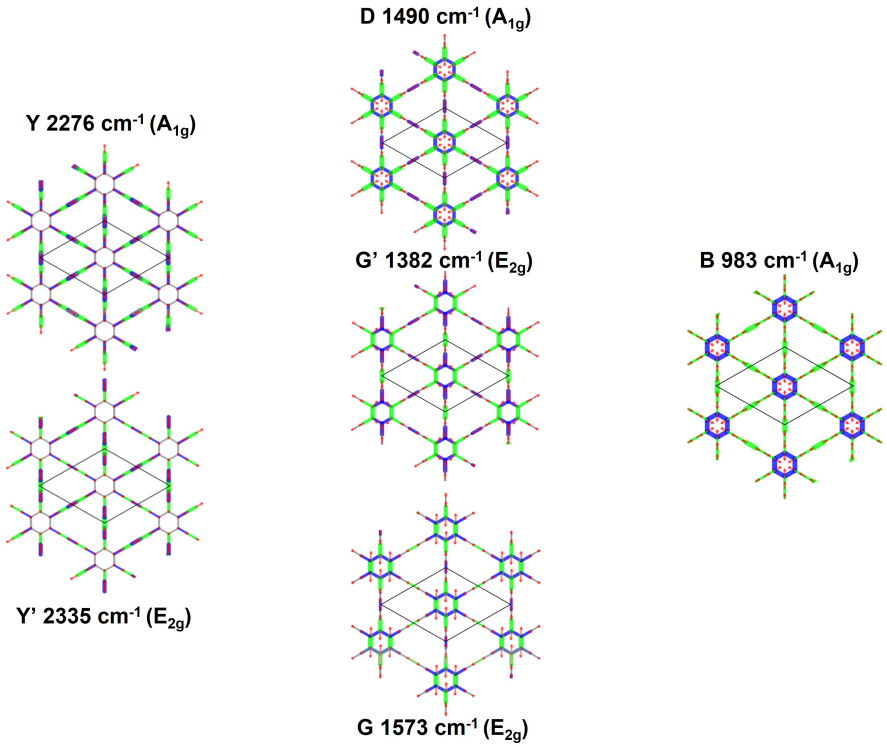

Figure 4.15: *Sketches of DFT computed [PBE0/6-31G(d)] Raman active normal modes of 2D-GDY. Red arrows indicate atomic displacements while green and blue colors indicate the active bond stretching vibrations in each normal mode. The different colors indicate different phases of the vibration, while the line width is proportional to its amplitude.*

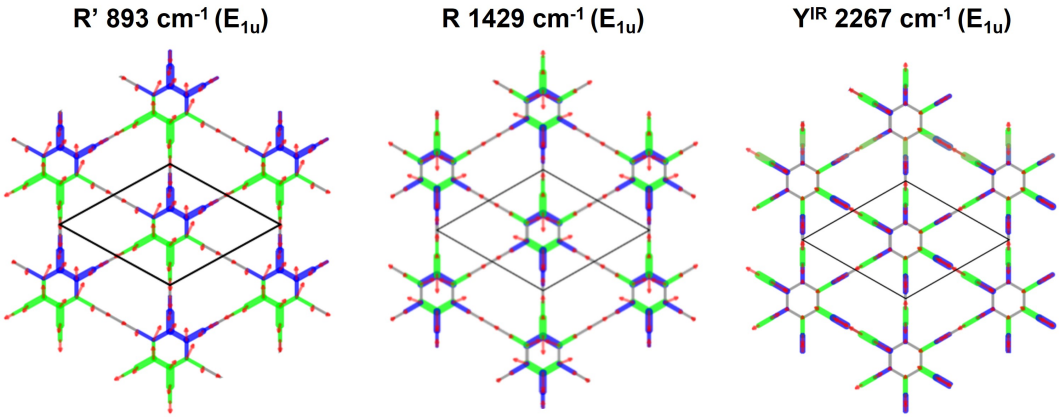

Figure 4.16: *Sketches of DFT computed [PBE0/6-31G(d)] IR active normal modes of 2D-GDY. Red arrows indicate atomic displacements while green and blue colors indicate the active bond stretching vibrations in each normal mode. The different colors indicate different phases of the vibration, while the line width is proportional to its amplitude.*

4.4.3 Raman and IR assignment

It is well known that the marker bands of sp-hybridized CC bonds are found in the 2000-2400 cm^{-1} range [3, 24]. Indeed, the Y and Y' phonons are, respectively, A_{1g} and E_{2g} collective CC stretching vibrations localized on the sp-carbon domains of GDY, as already described in the previous section. The combination of the stretching coordinates of each i_{th} polyyne arm follows the characteristic pattern shown by the ECC mode of polyynes. In the A_{1g} Y mode (2276 cm^{-1}), all sp-carbon chains oscillate in-phase, according to the ECC coordinate. In the E_{2g} Y' mode (2335 cm^{-1}) the ECC vibrational pattern is repeated on the six polyyne segments with different relative phases, according to E_{2g} symmetry. The sizable difference in wave number of these two phonons (59 cm^{-1}) indicates a non-negligible coupling among adjacent polyyne chains, caused by the interaction among the π electrons of the phenyl unit and of the attached sp chains. Indeed, the ECC mode of a diphenyl polyyne is computed at 2368 cm^{-1}, much higher than the Y and Y' bands of GDY, supporting the evidence of a non-negligible coupling of adjacent sp-carbon chains and proving the occurrence in GDY of significant π electron delocalization across phenyl groups. In Fig. 4.15, sketches of the normal modes of vibration associated to the main Raman active bands of γ-GDY are reported in order to support the discussion. The region below 1600 cm^{-1} is commonly assigned to stretching vibrations of the aromatic rings. However, phonons involving these stretching coordinates always show a remarkable coupling with "single" bonds stretchings of the polyyne arms. The phonons of A_{1g} symmetry are associated with the following Raman bands:

(i) The D line (1490 cm^{-1}) is assigned to a phonon decribed as the ring breathing coupled to the stretchings of the CC bonds linked to the aromatic moiety. These coordinates vibrate out of phase, with a pattern very similar to that of the phonon associated with the D line of graphite/graphene.

(ii) The B line (983 cm^{-1}), associated with the breathing mode of the phenyl units, out-of-phase coupled with the stretching coordinates of the central CC bonds coordinate. Stretching of the single bonds linked to the aromatic units is also involved, with a minor contribution.

Symmetry selection rules for A_{1g} phonons tell us that only the three diagonal elements of the Raman polar tensor, namely ($\alpha_{xx} = \alpha_{yy}, \alpha_{zz}$), are nonvanishing. According to the calculations reported in our paper [115] all relevant Raman transitions listed above show a neligible out-of-plane α_{zz} component. So, the intensity of these Raman lines is determined by the value $|\alpha_{xx}|^2 = |\alpha_{yy}|^2$. This implies that for 2D-GDY sheets deposited on a substrate (x, y plane), Raman experiment in backscattering geometry at normal incidence (z direction) will provide the same intensity pattern, independently of the polarization of the incident and scattered light, because the symmetry of the Raman

tensors does not allow assessing the orientation of the sheet in the x, y plane. A proof of the orientation of the sheet with respect to the substrate should be obtained with normal incidence and collection of the scattered photons at 90° (e.g. x direction). In this case A_{1g} bands should vanish for z polarization of the scattered photons.

The E_{2g} Raman transitions are the following:

(i) The G mode (1573 cm^{-1}): it involves coordinates of the phenyl units with in phase contribution by the stretching coordinates of single bonds linked to the aromatic units. The displacements pattern recalls that associated with the G line of graphene.

(ii) The weak G' mode (1382 cm^{-1}): it also involves the stretching coordinates of the phenyl unit, as the G mode; the contribution from the polyyne chain involves coordinates of the central single bonds and, to lesser extent, single bonds linked to the aromatic units.

(iii) A very weak E_{2g} band at 790 cm^{-1}, corresponding to another different linear combination of all the single bonds stretching coordinates (phenyl, central single and single attached to phenyls) with non-negligible bending contributions.

(iv) Two very weak bending phonons (573, 394 cm^{-1}).

Considering a degenerate pair for each E_{2g} phonon, the nonvanishing elements of the Raman tensor are α_{xx} = -α_{yy} and α_{xy}, respectively, with $|\alpha_{xx}|^2 = |\alpha_{xy}|^2$. Accordingly, the polarization properties of the E_{2g} bands of 2D-GDY sheets deposited on a substrate result to be the same as for A_{1g} transitions: for backscattering geometry, one expects independence of the Raman intensity vs the polarization direction within the xy plane. In the IR spectrum, since the 2 A_{2u} modes practically show almost zero intensity we essentially observe E_{1u} phonons, namely:

(i) The Y^{IR} band (2267 cm^{-1}) assigned to the out-of-phase combination of single and triple bonds stretching coordinates; focusing on individual polyyne arms, it can be described as the ECC mode with a node, located on the central CC bond (Fig. 4.16);

(ii) The R band (1429 cm^{-1}), which is mainly due to CC stretching of the bonds in the phenyl units with out-of-phase contribution of the stretching coordinates of single bonds linked to the aromatic unit (Fig. 4.16);

(iii) The very weak R' transition (893 cm^{-1}); it mainly involves stretching coordinates of bonds inside the aromatic rings, coupled in phase with the stretching of the bonds in the phenyl units. A careful inspection of the vibrational patterns shows that a non-negligible contribution by bending displacements affects the R' phonon (Fig. 4.16);

(iv) Two very weak bending phonons are computed at 419 and 171 cm^{-1}.

Considering a degenerate pair for each E_{1u} phonon, the nonvanishing elements of the associated dipole derivatives are μ_x and μ_y, respectively, with $|\mu_x|^2 = |\mu_y|^2$. The above relationship tells us that IR experiment with polarized light at normal incidence on the GDY plane cannot discriminate between oriented and unoriented sheets in the plane.

Chapter 5

Designing All Graphdiyne Materials: Topologically Driven Modulation of Electronic and Vibrational Properties

5.1 Introduction

Once the study of electronic and vibrational properties of γ-GDY system has been performed, ranging from molecular fragments to the 2D crystal, some questions arise: are there any other sp-sp^2 GDY-based systems, different from the γ ones, that are worth to be studied for their peculiar electronic and vibrational properties? If yes, how these properties are modulated by connectivity between sp and sp^2 domains, by the number of carbon atoms with that hybridizations and by the topology that can be created by using these carbon atoms? In this last chapter, in order to answer these questions, we explored the development of an algorithm to systematically generate new hybrid sp-sp^2 carbon structures as modifications of graphene by introducing linear diacetylenic units. By DFT calculations on the geometries so generated, we performed geometry optimization, evaluation of the relative stability, and prediction of the electronic band structure, gap, and density of states (DOS), together with the investigation of their Raman and IR spectra. We analyzed a total of 26 structures, more than half not previously identified, and we outlined metallic, semimetallic with Dirac cones, and semi-conducting systems grouped on the basis of topological features. Moreover, the analysis of the vibrational response enabled the identification of different marker bands in the Raman and IR spectra of these systems and gave the possibilility to investigate peculiar physicochemical effects, together with the possibility to discriminate between materials with different structural topology. The identification of new 2D car-

bon structures and the topology-based electronic and vibrational properties give further insights into the design and understanding of new hybrid sp-sp^2 carbon 2D materials [125].

5.1.1 Theoretical Details

Periodic boundary condition (PBC) DFT simulations have been carried out by employing CRYSTAL17 [116] to optimize the geometry (both the atomic position and cell parameters) and compute the electronic band structure, DOS, Raman and IR spectra. To this end, we adopted the PBE0 hybrid exchange-correlation functionals together with 6-31G(d) Gaussian basis sets [126]. This level of theory has been chosen according to our previous investigations on the structural and vibrational properties of γ-GDY and related nanoribbons, reported in previous chapters, where the results obtained using different functionals and basis sets have been compared [115]. Considering the other simulation parameters, the tolerance on integral screening has been fixed to 9,9,9,9,80 (TOLINTEG parameters), while the shrink parameters defining Monkhorst-Pack and Gilat sampling points have been fixed to 100 and 200 for the calculation of the band structure and DOS, respectively. For vibrational frequency and Raman/IR analysis, shrink parameters was also set to 100. Depending on the crystalline structure (orthorhombic, monoclinic, and hexagonal), the main three paths and special points in the Brillouin zone were chosen. Band structures and DOS were plotted using the program CRYSPLOT [127], a visualization environment for plotting properties of crystalline solids as computed through the CRYSTAL code (http://crysplot.crystalsolutions.eu/). Similar to [57], the data here reported have been obtained using the PBE0 functional, taking advantage of the improvement obtained by means of hybrid functionals in the description of ground-state electronic properties. Even if a further improvement could be obtained by employing the HSE06 functional [124], in our previous investigation on γ-GDY and its nanoribbons, we verified if both PBE0 and HSE06 are able to describe the same trends for band gaps, with a larger overestimation of PBE0 ones with respect to benchmark values computed by the GW method [128]. For some peculiar structures, full geometry optimization and band structure and DOS calculations have been carried out also using the HSE06 functional and compared with PBE0 results.

5.1.2 Construction of GDY Crystals as Graphene Derivatives and Analysis of their Relative Energies

We developed an approach to generate and classify all possible GDY 2D structures. We considered stable graphene derivatives by inserting linear diacetylene (C_4) groups for a given number of 3-coordinated carbon atoms (sp^2 like) per primitive cell. We limited the analysis to a maximum of eight sp^2 carbon

atoms per primitive cell to avoid too large cells and to focus on structures that are more likely to be experimentally synthesized. This limit is enough to find all previously reported and many other GDY-like structures. Our approach is based on removing edges from the graphene structure and substituting them with linear diacetylenic units. The starting set of honeycomb layers with deleted edges was made of about 40,000 structures with a maximum of eight carbon atoms per primitive cell (four times that of the original cell). With the help of the topological classification tools in ToposPro, we extracted 332 topologically distinct patterns containing 6-membered rings with one or more missing edges. Geometrical considerations led to the possibly derived hexagons with deleted edges (from one to six), as shown in Figure 5.1. For each configuration, there is a "dual" one with reverse deleted edges, leaving 12 possible distinct patterns.

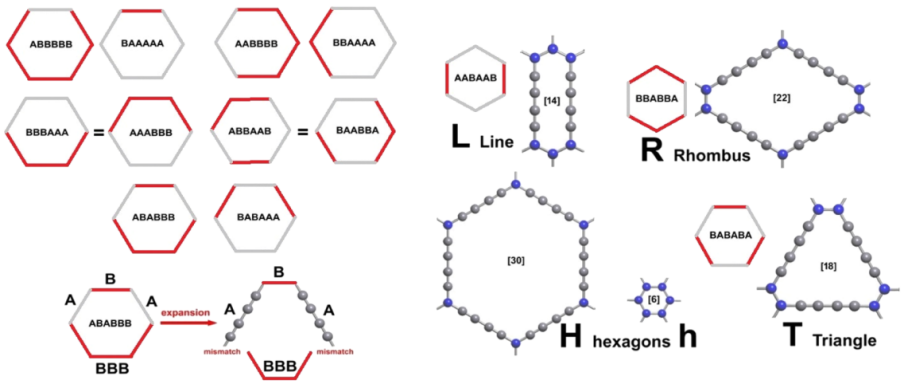

Figure 5.1: *(Left) The eight distinct possible configurations that upon expansion give highly distorted hexagons that are discarded in our generation of GDY-like layers. A and B indicate non-equivalent sides of the hexagon units: B should be considered as a true CC bond, while A represents the diacetylene unit (C_4) of four sp carbon atoms. The configurations are shown as "dual" couples, that is, reversing the role of A vs B. Two couples do not generate a new configuration, for example, BBBAAA = AAABBB. (Right) Four configurations that upon expansion gave undistorted six-sided polygons. The value in the square bracket is the total number of carbon atoms in the ring that uniquely define each building block, h=[6], H=[30]; L=[14]; T=[18], and R=[22]. Line (L) and rhombus (R) blocks are "dual", so for each layer containing them, we can substitute each L with an R without significant distortions. The definition proposed here follows the one reported in the work by Park et al. [54]*

In Figure 5.1 on the left, we show the eight patterns that after the introduction of C_4 edges will not allow the closure of the 6-membered ring without a large angular distortion (see the detail for one case). Only the four remaining configurations shown in Figure 5.1 on the right allow expansion by the insertion of C_4 linear structures without substantial distortion, that is, keeping all the angles around 120°. These four configurations and the original unaltered aromatic ring constitute five building blocks, here called as h,H,R,T,L (small

and large hexagon h and H, respectively, rhombus R, triangle T, and line L), as suggested by Park et al. [54]. From the 332 patterns, we extracted only those containing some of the five possible building blocks that allow to tile the plane without a large distortion, obtaining 26 structures that are GDY-like (of which 17 are new), as described in Figures 5.2 and 5.3. Due to the "dual" properties of L/R and h/H, the 26 structures can be grouped in 12 couples plus a self-dual layer. Based on this classification, structures are called as 6-h^{n}L^{m}T^{o}R^{p}H^q, where 6 represents the number of carbon atoms along the longest edge and the superscript on the building block symbols represents the number of each block appearing in a primitive unit cell (e.g., the primitive cell of c2mm 6-h^{2}L contains two small C_6 h-rings and one C_{14} L-ring, and all the edges are either between two or six carbon atoms).

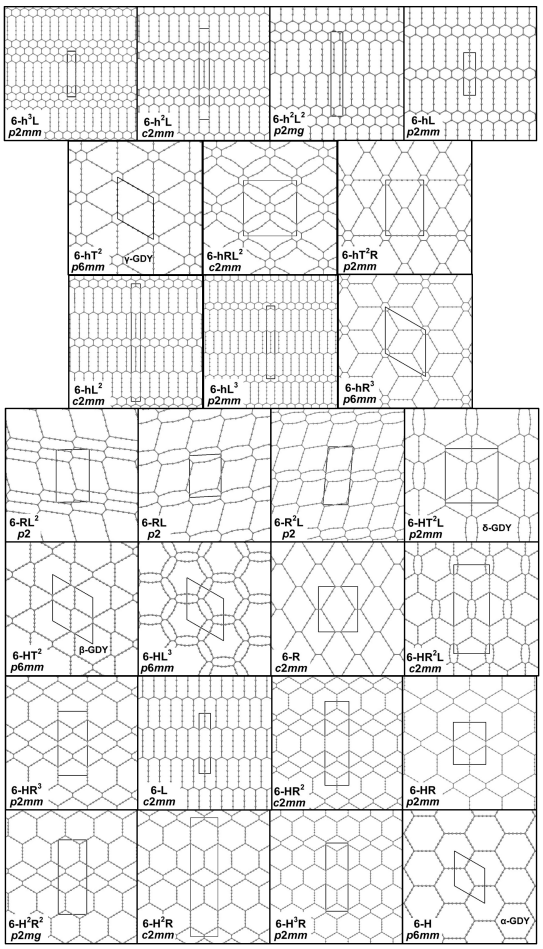

Figure 5.2: *Representation of the 26 2D structures identified and investigated in this work. The unit cells and the plane groups are indicated. α-, β-,γ-, and δ-GDY are also labeled.*

name	rel. energy kcal/mol	plane group	Pearson symbol	sp/sp^2 ratio	electronic character (PBE0)
6-h^{3}L	14.15	*p2mm*	oP12	0.50	metal
6-h^{2}L	16.81	*c2mm*	oS20	0.66	metal
6-h^{2}L^2	20.55	*p2mg*	oP16	1.00	metal
6-hL	20.59	*p2mm*	oP8	1.00	metal
6-hT^2 γ-GDY	21.13	*p6mm*	hP18	2.00	B.G. = 1.63 eV
6-hRL^2	22.65	*c2mm*	oS48	2.00	0 B.G.
6-hT^{2}R	22.69	*p2mm*	oP28	2.50	B.G. = 0.83 eV
6-hL^2	23.11	*c2mm*	oS28	1.33	metal
6-hL^3	24.06	*p2mm*	oP20	1.50	metal
6-hR^3	24.07	*p6mm*	hP32	3.00	0 B.G.
6-RL^2	24.73	*p2*	mP22	2.66	0 B.G.
6-RL	24.73	*p2*	mP16	3.00	0 B.G.
6-R^{2}L	25.03	*p2*	mP26	3.33	0 B.G.
6-HT^{2}L δ-GDY	25.07	*p2mm*	oP36	3.50	B.G. = 0.18 eV
6-HT^2 β-GDY	25.40	*p6mm*	hP30	4.00	B.G. = 1.14 eV
6-HL^3	25.41	*p6mm*	hP32	3.00	0 B.G.
6-R	25.48	*c2mm*	oS20	4.00	0 B.G.
6-HR^{2}L	25.85	*c2mm*	oS80	4.00	0 B.G.
6-HR^3	26.11	*p2mm*	oP44	4.50	0 B.G.
6-L	26.18	*c2mm*	oS12	2.00	metal
6-HR^2	26.30	*c2mm*	oS68	4.66	0 B.G.
6-HR	26.63	*p2mm*	oP24	5.00	0 B.G.
6-H^{2}R^2	26.63	*p2mg*	oP48	5.00	0 B.G.
6-H^{2}R	26.92	*c2mm*	oS76	5.33	0 B.G.
6-H^{3}R	27.05	*p2mm*	oP52	5.50	0 B.G.
6-H α-GDY	27.39	*p6mm*	hP14	6.00	0 B.G.

Figure 5.3: *Summary of the 26 Structures Investigated Here: Reporting Name, Relative Energy with Respect to Graphene, Plane Group, Pearson Symbol, sp/sp^2 Ratio, and Electronic Characters (Band Gap Reported for Semiconductors)*

5.2 Relative Energies of 2D Crystals

After the full geometry optimization of the 26 structures and of the reference 2D graphene structure, we studied their stability by calculating the relative energy per carbon atom with respect to graphene according to the following:

$$E^i_{rel} = \frac{E^i_{tot}}{N^i} - \frac{E^{graphene}_{tot}}{N^{graphene}} \tag{5.1}$$

where E_{tot} is the DFT-computed total energy and N is the number of atoms in the unit cell for the i_{th} structure and graphene ($N^{graphene}$=2). This value of E_{rel} gives the relative cohesive energy per carbon atom and allows us to identify the most stable structures. Relative energy values are plotted as a function of the sp/sp^2 ratio, calculated as the ratio of sp and sp^2 carbon atom numbers in the unit cell (see Figure 5.4). This ratio ranges from 0 in the case of graphene up to 6 in the case of α-GDY, the largest values possible for the periodic 2D

hybrid sp/ sp^2 carbon nanostructures investigated here where the sp domains are formed by diacetylenic units.

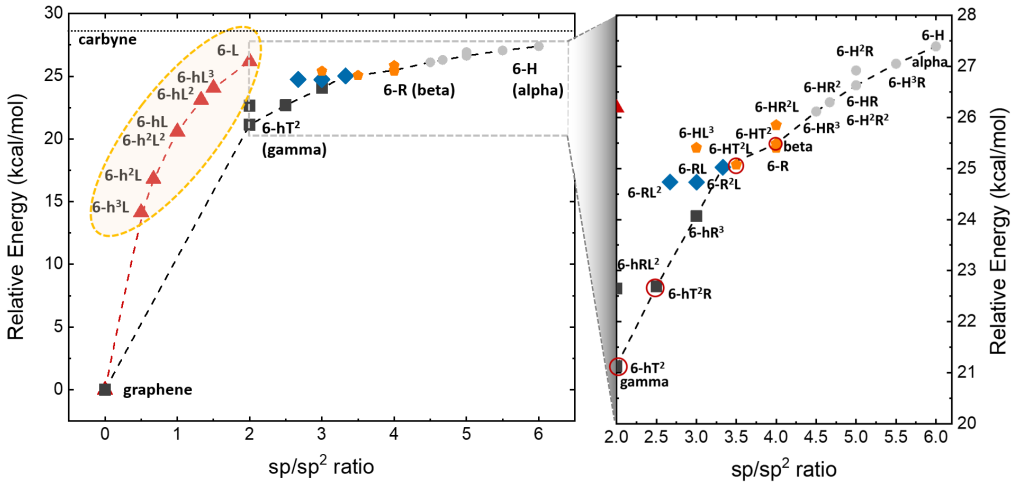

Figure 5.4: *Relative energies plots of the 26 structures investigated with respect to graphene as a function of sp-sp^2 ratios. In the first panel, the two distinct trends are analyzed, while in the second panel, the members of the second trends are collected in different classes, depending on the peculiar topology identified. The seven metallic systems are all in the left panel and grouped in the elongated ellipsoid, while semiconductors with finite band gaps are circled in red. As a term of comparison, the computed energy of the 1D infinite carbyne is reported as an asymptotic limit of the curve (28.41 kcal/mol).*

The increasing amount of sp carbon atoms with respect to graphene (i.e., a larger sp/sp^2 ratio) increases the energy of the whole system, consistently with chemical intuition. However, in Figure 5.4, two different trends can be identified. The first trend (red line) is continuous and smooth and contains all the structures formed by different combinations of 6-atom hexagons (h) and line polygons (L) and, namely, 6-h^3L, 6-h^2L, 6-hL, 6-h^2L^2, 6-hL^2, 6-hL^3, 6-L and graphene (6-h). The lowest-energy structure is 6-h^3L, formed by graphene ribbons having a width of three aromatic units and interconnected by diacetylenic bridges. 6-h^2L and 6-hL formed by graphene ribbons having a width of two and one aromatic units, respectively, and interconnected by diacetylenic bridges show an increase in relative energy. Hence, by reducing the width of graphene ribbons (i.e., as far as we progressively move away from the graphene limit), an increase in the relative energy is observed. Similarly, a further increase in energy is found in 6-hL^2 and 6-hL^3 which have, as in 6-hL, graphene nanoribbons of width 1 but which are interconnected by two and three L polygons (bridges

of two and three diacetylenic units), respectively. Therefore, both the number of condensed aromatic hexagons (width of graphene ribbons) and the spacing between the graphene ribbons (h polygons) set by the number of diacetylenic domains (L polygons) modulate the relative energy of these systems with respect to graphene. The maximum energy is reached in 6-L where no h units are present at all. As a general rule, considering structures 6-h^{n}L^m in which graphene nanoribbons of width "n" are connected by "m" diacetylenic units, the lower energy is found by increasing n and decreasing m, clearly tending closer and closer to the graphene case. Interestingly, these two parameters seem to have similar importance; in fact, the same energy is obtained in 6-hL with the smallest graphene ribbon and single diacetylenic unit and in 6-h^{2}L^2 in which the increase in energy given by doubling the diacetylenic units is counterbalanced by doubling the graphene ribbon width. The structures of these groups are known in literature as "grazynes" [129]. Our analysis underlines a clear trend in the energy that can be easily generalized for similar structures for predictive purposes. A different trend in Figure 5.4 is indicated by the black dotted curve. In this group, we find the widely studied polymorphs of GDY, usually labeled as α-GDY (structure 6-H), β-GDY (structure 6-HT^2), and γ-GDY (structure 6-hT^2). γ-GDY has gathered more attention in the recent years, also from the experimental point of view, and has been deeply investigated in the previous chapter. Among all the structures belonging to this trend, it has the lowest energy with respect to graphene, consistently with its low sp/sp^2 ratio (sp/sp^2 = 2). On the other hand, α-GDY is the highest-energy structure among all of those which are investigated here, again consistently with the highest sp/sp^2 ratio (sp/sp^2 = 6). β-GDY with sp/sp^2 = 4 is in between these two limiting cases. Apart from these widely studied polymorphs, the structures belonging to this second group can be further classified based on their topology and structure. The description of their geometry is based on their building units, similarly to the method proposed by Park et al. [54] As shown in Figure 5.4, the four lowest-energy structures 6-hT^2 (γ-GDY), 6-hRL^2 , 6-hT^{2}R, and 6-hR^3 form one subgroup themselves, since they all share the presence of h polygons in their geometry, that is, a last reminiscence of the graphene structure. On the other hand, the highest-energy structures 6-HR^3 , 6-HR^2, 6-HR, 6-H^{2}R^2, 6-H^{2}R, 6-H^3 and 6-H (α-GDY) form another subgroup, and they can be all described as α-GDY ribbons connected with different widths and interconnections, tending indeed toward the upper limit of α-GDY. In the intermediate case, two clusters of structures can be identified: one collects structures 6-HL^3, 6-HT^{2}L, 6-R, 6-HR^{2}L, and 6-HT^2 (β-GDY) and the other one collects the structures 6-RL, 6-RL^2, and 6-R^{2}L. The members in the first group are all characterized by the presence of isolated α-GDY units (i.e., large 30-atom hexagons H with all sizes characterized by diacetylenic units), while in the second group, the systems are structurally pe-

culiar, since they are formed only by units which can be described as rhombus R and lines L according to the definition in Figure 5.1. It should be noticed that in many of the structures containing L units, the diacetylenic bridges are usually bent and not linear, as also found in the calculations by Belenkov et al. [130]. Moreover, the energy values of 6-HR/6-H^2R^2 and 6-hL/6-h^2L^2 seem to overlap between each other, even if they are not exactly the same values. Such close values could be due to the fact that they contain the same structural units (H and R for the former two and h and L for the latter) in the same ratio, suggesting the role of topology in determining the energetic and electronic behavior of these systems. The energy trend can be summarized as follows:

(1) As expected, the relative energy with respect to graphene increases for an increasing sp/sp^2 ratio.

(2) The closer the structural resemblance to graphene, the lower the relative energy of the 2D structures. This is clearly shown in crystals made of graphene ribbons having diacetylenic-connected bridges: the more we approach the graphene structures (the lower the sp/sp^2 ratio), the lower the relative energy.

(3) Considering the other trends, the lowest-energy structures are those where the graphene h unit (hexagon of sp^2 carbon) is still present in the structure.

(4) The energy increases when the number of α-GDY units (H hexagon) increases up to the limiting case of 2D α-GDY.

These trends in relative energy are consistent with the cohesive energies reported by Park et al. [54] and with the sublimation energy given by Belenkov et al. [130] by considering that a larger relative energy corresponds to a lower cohesive and sublimation energy. Our work shows that α-GDY has the lowest stability, while γ-GDY is the most stable. On the other hand, the semiempirical calculations by Belenkov et al. [130] predict the largest sublimation energy (i.e., lower relative energy) for the system called $\gamma 2$, which corresponds to 6-L in our work. For 6-L, we find a larger relative energy than γ-GDY even if they share the same sp/sp^2 ratio value. Our work includes systems that were already investigated in the literature and several novel ones, thus revealing the wide range of possibilities available in the design of 2D sp-sp^2 carbon systems. As a term of comparison, we carried out a simulation, adopting the same level of theory, of the 1D carbyne chain, the limiting case in which the sp/sp^2 tends to infinity, and we found a relative energy of 28.41 kcal/mol, which is, as expected, the largest energy value found and should be intended as an asymptotic limit when increasing the sp/sp^2, as can be seen in Figure 5.4. Indeed, it can be

considered as the limiting case for all the possibly generated 2D hybrid sp/sp^2 carbon structures.

5.3 Electronic Properties: Band Structure and DOS

After the discussion about energy and stability, we decided to explore how topological elements affect the band structure and the electronic properties of GDY crystals, on the basis of their peculiar crystal structure. As a starting point, different families previously identified can be recovered also here. Indeed, Figure 5.4 reports seven structures that show a metallic behavior, grouped with an elongated ellipsoid, while the finite band gap semiconducting crystals are circled in red. All the other 2D carbon systems are zero-band gap semiconductors. In Figure 5.5, the band structure of graphene is compared with that of the three widely investigated α-, β-, and γ-polymorphs of GDY. α-GDY shows a very similar band structure to that of graphene, with the occurrence of Dirac cones at the K-point, which makes both of them zero-gap semiconductors or semimetals, in agreement with previous studies [55, 56].

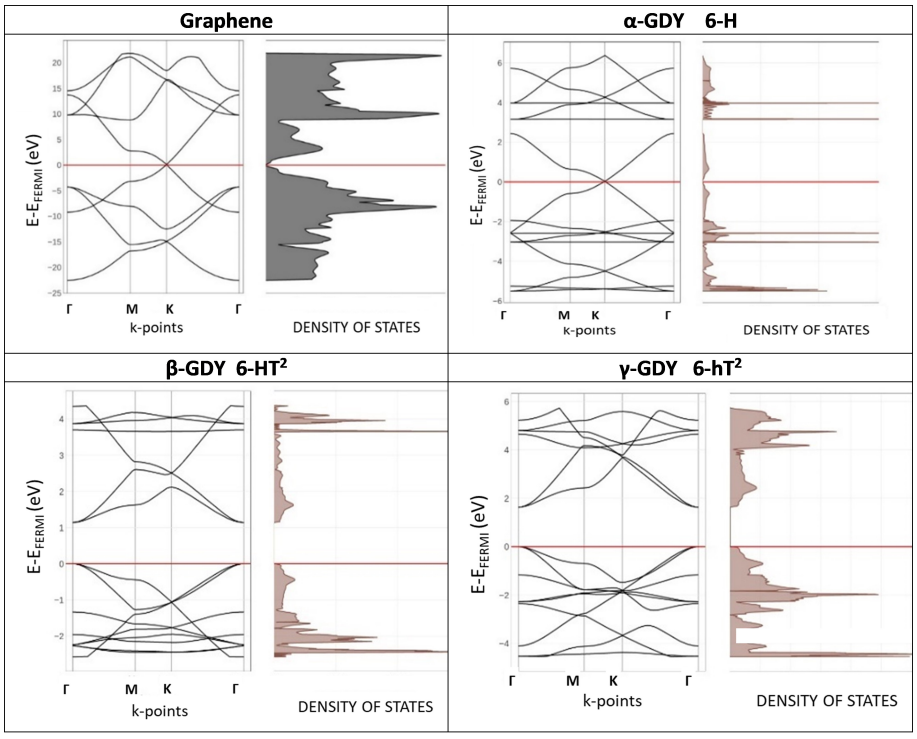

Figure 5.5: *Comparison of DFT-computed band structures and DOS of graphene and α-, β-, and γ-GDY polymorphs.*

Graphene and α-GDY have the same crystal structure and layer group (p6mm), differing only in the number of carbon atoms in the primitive cell (2 and 14 in graphene and α-GDY, respectively), highlighting the topology dependence of the band structure. In α-GDY band structure, is worth noting the appearance of both occupied and empty flat bands, that is another typical topology-dependent feature found for 2D COFs [57, 58]. On the other hand, β-GDY and γ-GDY are finite-gap semiconductors, showing a band gap of 1.14 and 1.63 eV, respectively. Their structures are similar: based on the algorithm we adopted to build the structures, β-GDY and γ-GDY are indeed dual ones to the other (see also Figures 5.1 and 5.2), respectively, 6-HT^2 and 6hT^2, demonstrating the topology dependence of the band structure. Further results can be obtained by extending the analysis to all the systems investigated here. The band structure and DOS of all these structures can be classified into three classes: finite-gap semiconductors (such as β- and γ-GDY), metals, and zero-gap semiconductors (see Figure 5.6). For each class, the band structure and DOS of only one representative structure are reported.

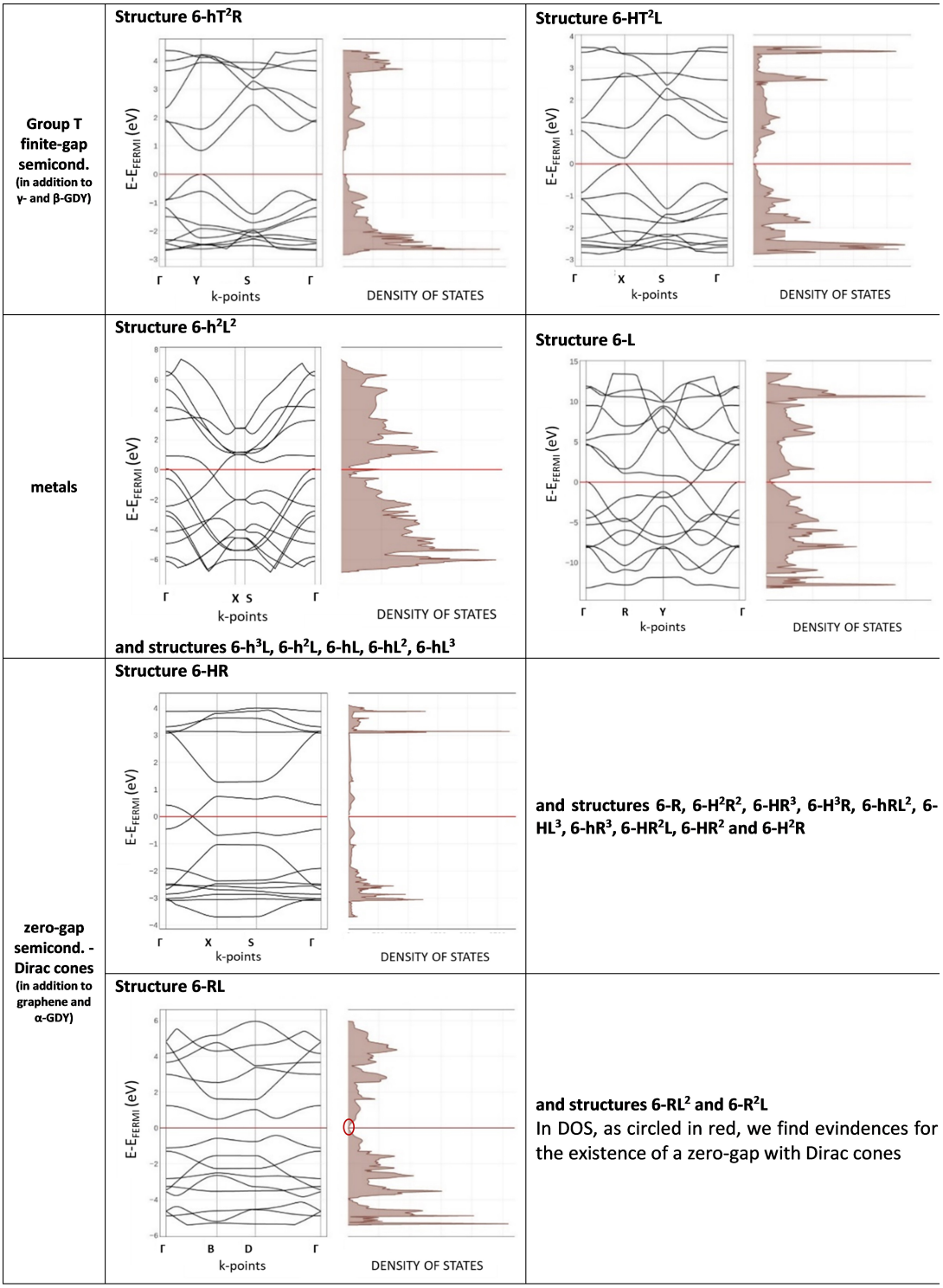

Figure 5.6: *Comparison of DFT-computed band structures and DOS of all the other structures investigated here.*

Finite-gap semiconductors include β- and γ-GDY (1.14 eV and 1.63 eV respectively) and only two other structures, 6-hT^{2}R and 6-HT^{2}L, presenting a finite gap of 0.8327 and 0.1789 eV, respectively. These geometries are dual ones with respect to the other, as for β- and γ-GDY (Figure 5.1). Among the 26 structures investigated here, these are the only ones containing a T-shaped unit, suggesting that T units would induce electronic effects, leading to the rise of a band gap the band structure. The second class is formed by metallic systems and include structures made of graphene ribbons interconnected by diacetylenic groups (here called as hL), also described as grazynes [129]. All these crystals (i.e., 6-h^{3}L, 6-h^{2}L, 6-hL, 6-h^{2}L, 6-hL^2, 6-hL^3 and 6-L) share the same trend in the band structure. They present a half-filled band and a Dirac cone immediately below the Fermi energy. In this class, we find also structure 6-L, the limiting case of a 2D crystal formed by line units only. The third class, collecting the largest number of different geometries, is characterized by zero-gap semiconductors presenting Dirac cones at the Fermi energy. In this class, two subclasses with a slightly different behavior are presented: the first one, including structures 6-R, 6-HR, 6-H^{2}R^2, 6-HR^3, 6-H^{3}R, 6-hRL^2, 6-HL^3, 6-hR^3, 6-HR^{2}L, 6-HR^2 and 6-H^{2}R, collects 2D crystals that, from the point of view of the band structure, present a pattern similar to that of α-GDY, with a Dirac cone along one of the special directions in the BZ. The second subclass (RL) collects structures 6-RL, 6-RL^2 and 6-R^{2}L, which already formed a cluster in relative energy: for these three crystals, Dirac cones cannot be identified along the three main paths in the BZ but are located elsewhere in the Brillouin zone. The presence of Dirac cones is outlined by the linear behavior of the DOS close to the Fermi energy. Even for these structures sharing a peculiar topology (they are crystals formed only by rhombus R and line L units), 6-RL^2 and 6-R^{2}L are dual ones with respect to the other, and 6-RL is self-dual. To support the significance of these results, for some structures, geometry optimization and band structure/DOS calculations have been repeated using the HSE06 functional together with the same 6-31G(d) basis set, in order to check the effect related to the functional choice. As also demonstrated in the previous chapter, this functional can indeed give a more accurate quantitative evaluation of the band gap, in agreement with benchmark GW-computed values, even if the qualitative trends are the same obtained with PBE0. As expected, HSE06 band gap values are lower: 1.11 versus 1.63 eV for 6-hT^2 (γ-GDY), 0.34 versus 0.83 eV for 6-hT^{2}R, and 0.68 versus 1.14 eV for 6-HT^2 (β-GDY); however, they still confirm that these structures are finite band gap semi-conductor. A discrepancy is found, however, for the 6-HT^{2}L structure, showing a very small (0.18 eV) but finite band gap with PBE0, while it is predicted as a zero-band gap semiconductor with HSE06. This result shows that in the presence of very small band gaps, the choice of the theoretical method could play an important role. These trends reveal the topology-related shape of the band structure

and the metallic, finite- or zero-gap semiconductor behavior. An inspection of the geometry of these structures allows further insights into how the building units (Figure 5.1) determine the behavior of the 2D carbon materials. A finite band gap can be the consequence of the presence of T units, while hexagonal units (h and H) are present in zero-band gap semiconductors with Dirac cones, as evidenced by the limiting case of graphene (h units only) and α-GDY (H units only). R units (see the case of 6-R) are similar to h and H, promoting the occurrence of zero-gap semiconducting behavior with Dirac cones, while L units, as in the case of 6-L (only L building blocks), occur in structures showing a metallic band structure. We can conclude that whenever h, H, or R units are present, there would be a tendency toward zero-gap semiconductors showing Dirac cones, and when L units are present, there would be a tendency toward metallic structures, while, on the other hand, T units are related to a gap opening between valence and conduction bands. All metallic structures are formed by systems where only h and L units are present, and the effect of L seems to dominate that of h in affecting the band structure. Zero-gap structures all contain H and/or R, and for some of them, also, h and L units can be present: in any case, H/R units seem to dominate the behavior of the band structure. Finally, T units seem to dominate over all the other units in affecting the band structure, promoting a band gap. Interestingly, 6-HT^{2}L represents a limiting case, showing a balance between the opposite effects of T and L units. The dominating effect seems to be related to the functional choice, since we find 0.18 eV for PBE0 and zero gap for HSE06. For the systems already reported in the literature, our results are consistent and describe the same behavior [54]. However, the band gap values are lower than the ones reported here for 6-HT^2 and 6-hT^2, probably due to the use of a pure GGA functional (PBE) with respect to the hybrid one used in our calculation. A discrepancy is found for the 6-hT^{2}R structure, for which we predict a gap of 0.83 eV with PBE0 (and 0.34 eV with HSE06), while a zero-gap semiconductor is predicted by Park et al. [54]. This points out again that for semiconductive systems having a small band gap (i.e., below 1 eV), the choice of the functional could be relevant to predict the behavior of the materials in terms of their electronic structure. Based on the role of the different h, H, R, L, and T units and considering the results for 6-HT^{2}L with PBE0 and HSE06, the choice of the functional is relevant in predicting the smaller or larger dominating effect of the different units in affecting the band structure behavior. This is not a primary effect when large band gaps are present, but some peculiar cases could require more attention to the theoretical method.

5.4 Vibrational Properties: Raman and IR spectra

The investigation of 2D graphdiyne-based crystals is concluded with the study of their vibrational patterns through the analysis of Raman and IR spectra. In this section, I decided to focus firstly our attention on 6-L, 6-H and 6-R structures, characterized by the simplest topologies of a single repeating unit, i.e. line (L), hexagon (H) and rhombus (R), and on 6-hT^2 and 6-HT^2 systems that are widely studied polymorphs of graphdiyne. This first family will be hereafter referred as GDY. A second family of 2D crystals (hereafter referred as grazdiynes, GZY) contain linear diacetylene chains (L) and extended sp^2 domains forming zig-zag sequences of CC bonds like polyacetylene and/or ribbons made by condensed aromatic rings with L chains linked to the zig-zag edges. All these systems are sketched in Figs. 5.7 and 5.8. In Tab. 5.1, the main properties related to all the investigate systems are reported and discussed in the following sections. 6-H, 6-HT^2 and 6-hT^2 are referred respectively as α-GDY, β-GDY and γ-GDY in literature [47, 59, 131]. To ease the comparison among the different crystals, we adopted the same Cartesian reference system with the z axis orthogonal to the 2D crystal plane. When useful, a local reference system (x', y', z') is introduced for the description of physical quantities characteristic of the linear diacetylene branches: the x' axis oriented along the sp chain and z' parallel to the z axis of the crystal.

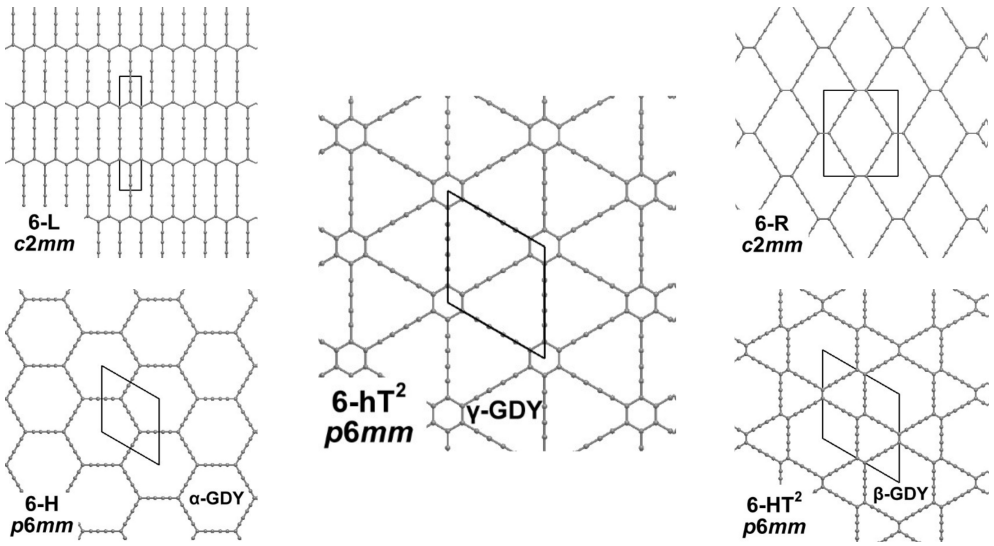

Figure 5.7: *Sktches of GDY systems (6-H, 6-L, 6-R, 6-HT^2, 6-hT^2)*

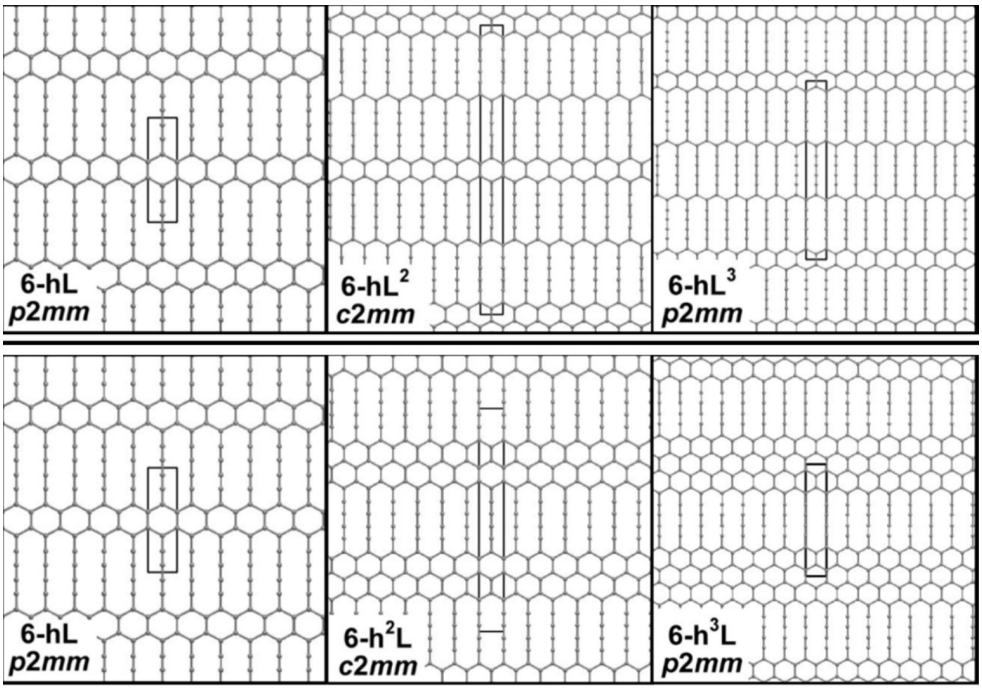

Figure 5.8: *Sketches of the two Grazynes families analyzed in this paper. Above: systems with increasing width of L layers, here named GZY-I. Below: systems with increasing width of graphene-like ribbons, GZY-II.*

Since the vibrational spectra (and especially the Raman ones) of sp carbon chains is very sensitive to the delocalization properties of the electrons, as well as they feel end group effects, we decided to analyse in detail and in comparative way spectra predicted for GDY and GYZ, mainly focusing on the vibrational transitions which involve the diacetylene branches.

species	point group space group	n. of chains	ΔE (kcal/mol)	BLA (Å)	ECC modes
6-H α-GDY	D_{6h} p6mm	3(i)	27.39	0.142	$1A_g$+$1E_{2g}$
6-L	D_{2h} c2mm	centred: 2 primitive: 1(i)	26.18	0.136	$1A_g$
6-R	D_{2h} c2mm	centred: 4 primitive: 2(i)	25.48	0.154	$1A_g$+$1B_{1g}$
6-HT^2 β-GDY	D_{6h} p6mm	6	25.40	0.156	$1A_g$+$2E_{2g}$
6-hT^2 γ-GDY	D_{6h} p6mm	3(i)	21.13	0.167	$1A_g$+$1E_{2g}$
6-hL	D_{2h} p2mm	1(i)	20.59	0.138	$1A_g$
6-hL^2	D_{2h} c2mm	centred: 4 primitive: 2	23.11	0.136	$2A_g$
6-hL^3	D_{2h} p2mm	3 i(central chain only)	24.06	0.135	$3A_g$
6-h^2L	D_{2h} c2mm	centred: 2 primitive: 1(i)	16.81	0.139	$1A_g$
6-h^3L	D_{2h} p2mm	1(i)	14.15	0.138	$1A_g$

Table 5.1: *Table reporting space group and point group symmetry (factor group at* Γ *point of BZ), number of polyyne chains belonging to the unit cell, energy contribution per carbon atom, referred to graphene (E), and bond alternation parameter (BLA) of the polyyne units. (i) in the fourth column indicates that inversion symmetry centres are located on the polyyne chains. The number and symmetry species of polyyne ECC phonons are also listed in the table.*

5.4.1 Vibrational spectra of GDY

Preliminary to a detailed spectra analysis, it is useful to define internal and symmetry CC stretching coordinates of the diacetylene branches. This allows establishing, without the need of any calculation, which peculiar group vibrations of the chains are involved in the Raman and IR active q=0 phonons. For each diacetylene branch (labelled by the index i) we consider the sequence of the five CC bonds forming the chain, and we define the relative stretching coordinates (r_i, r'_i, T_i, T'_i, P_i) as indicated in Figure 5.9. We also define the group coordinates $\{S_i\}$ sketched in Figure 5.9: the symmetric (T_i^+) and the antisymmetric (T_i^-) combination of quasi-triple CC bonds stretching; the symmetric (r_i^+) and the antisymmetric (r_i^-) combination of quasi-single terminal CC bonds stretching; and the stretching (P_i) of the central quasi-single CC

bond. The group coordinates defined above are symmetry coordinates for the diacetylene fragment, showing an inversion centre in the middle of the central CC bond.

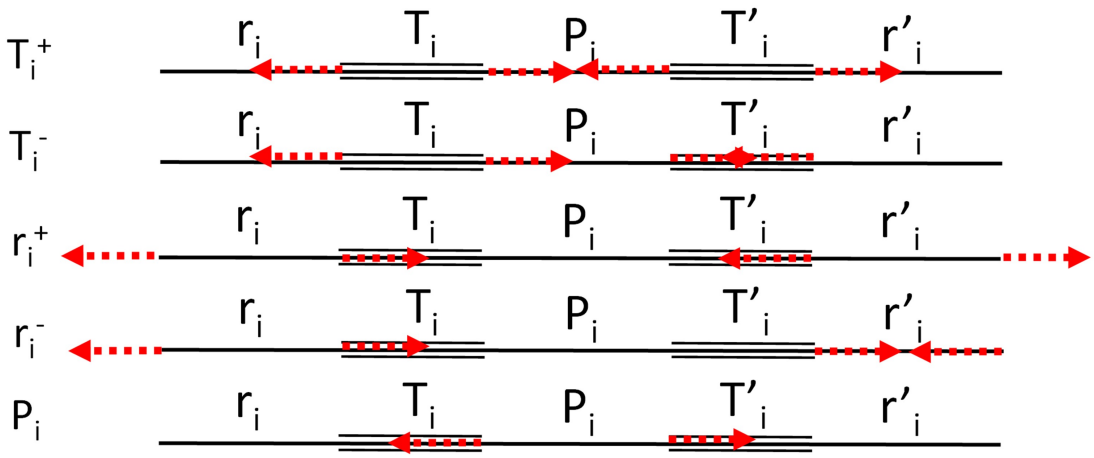

Figure 5.9: *Definition of the CC stretching internal coordinates and sketches of their symmetry adapted combinations* $\{S_k\}$.

In most crystal structures illustrated in Fig. 5.7, the inversion centres carried by each diacetylene unit are preserved, so the collection of the sets S_i define a symmetry adapted internal coordinates basis set, useful for the rationalization of the spectral features. This happens for crystals 6-H, 6-L, 6-R and 6-hT^2, while in 6-HT^2 the inversion centres located on the chains are lost. Remarkably, for all the crystals but 6-HT^2, we can state that among S_i only the gerade coordinates $\{S_k\}^g = \{r_i^+ , T_i^+, P_i\}$ are involved in Raman active phonons, while ungerade coordinates $\{S_k\}^u = \{r_i^-, T_i^-\}$ are involved in the IR active phonons. This feature is independent on the number of diacetylene chains in the unit cell and on the kind of the chemical group linking the chains. On other hand, the symmetry of the crystal and the number of chains will determine the suitable symmetry combinations of the $\{S_k\}^g$ of the different chains, giving Raman active phonons. $\{S_k\}^g$ combination of A_{1g} and E_{2g} species characterize Raman phonons of the crystals showing D_{6h} symmetry (6-H, and 6-hT^2), while in 6-L and 6-R structures (D_{2h} symmetry) they give rise to B_{1g} and A_g phonons. Combinations of $\{S_k\}^u$ give E_{1u} phonons and B_{3u}/B_{2u} phonons for D_{6h} and D_{2h} structures, respectively. Vibrational displacements located in the sp^2 domains will also concur to the definition of the vibrational trajectories associated to the phonons, giving rise to rather complex patterns of collective atomic displacements. Luckily, the definition of the sets $\{S_k\}^g$ and $\{S_k\}^u$ greatly eases the analysis of the spectral features of the more informative spectral region above 2000 cm^{-1}, mainly involving vibrations of the diacetylene

branches.

In Figure 5.10 we report the computed Raman and IR spectra for the GDY series.

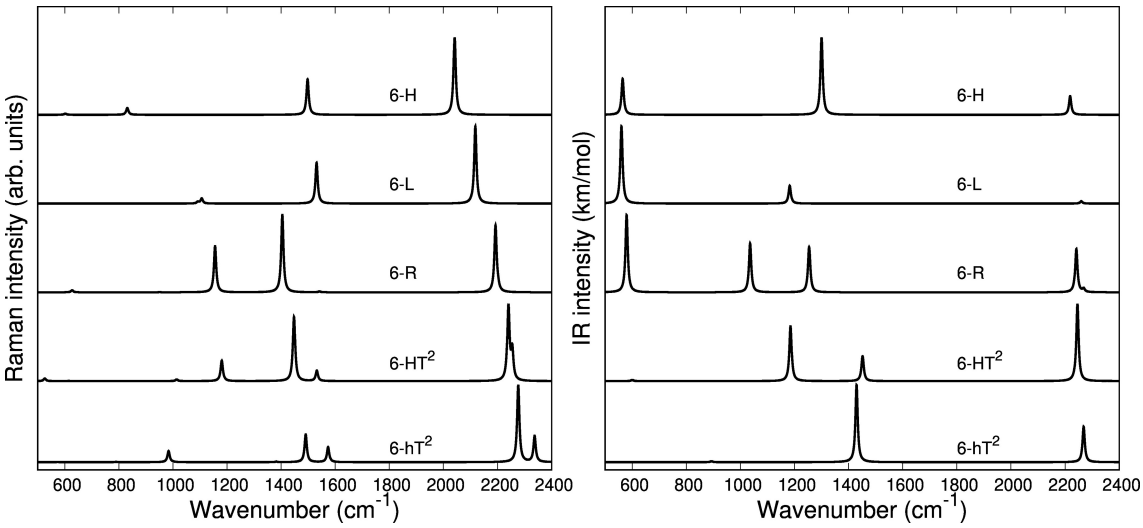

Figure 5.10: *Computed Raman and IR spectra of GDY systems (6-H, 6-L, 6-R, 6-HT^2, 6-hT^2)*

The vibrational spectra of GDYs present two characteristic regions, as already discussed for the γ one in previous sections. The interval 2000-2400 cm^{-1} is typical of stretching modes of CC triple bonds: indeed, vibrations of the sp chains give rise to strong Raman active bands above 2000 cm^{-1}, which can be considered the marker bands of the diacetylenic units. In the lower frequency region, between 800 -1600 cm^{-1}, we find Raman active bands assigned to stretching vibrations of CC bonds linking sp^2 hybridized carbon atoms, i. e., bonds belonging to aromatic rings (case 6-hT^2) or the CC bonds linking the polyynes branches in 6-L, 6-R, 6-HT^2. These phonons always involve additional contributions from the stretching of the quasi-single bonds belonging to the sp chains.

Let us first analyse the higher frequency region of the Raman spectrum, which shows a remarkable modulation of the frequency of the main line, corresponding to the strongest transition of the whole Raman spectrum, for the GDY family. According to our symmetry analysis, for D_{6h} structures (6-H and 6-hT^2) we can predict two Raman active phonons resulting from the A_{1g} and E_{2g} (doubly degenerate) combination of the symmetric triple bond stretching (T_i^+) of the three diacetylene chains belonging to the hexagonal cell. For 6-R and L crystals, we have two (A_g and B_{1g}) transition and one only A_g transition, respectively, according to the number of chains in the primitive cell (two and one chain, respectively). A peculiar case is that of 6-HT^2 crystal, with a

cell containing six diacetylene branches, which lost their local inversion centre in the crystal. In this case, we obtain one A_{1g} and two E_{2g} bands, with the lower frequency E_{2g} transition and the A_{1g} transitions showing accidental degeneracy in frequency. In 6-HT^2 the two E_{2g} phonons mix T_i^+ and T_j^- group coordinates of different chains, while the A_{1g} phonon corresponds to the in phase combination of the six T_i^+ , as for the other GDYs (see Fig. 5.11).

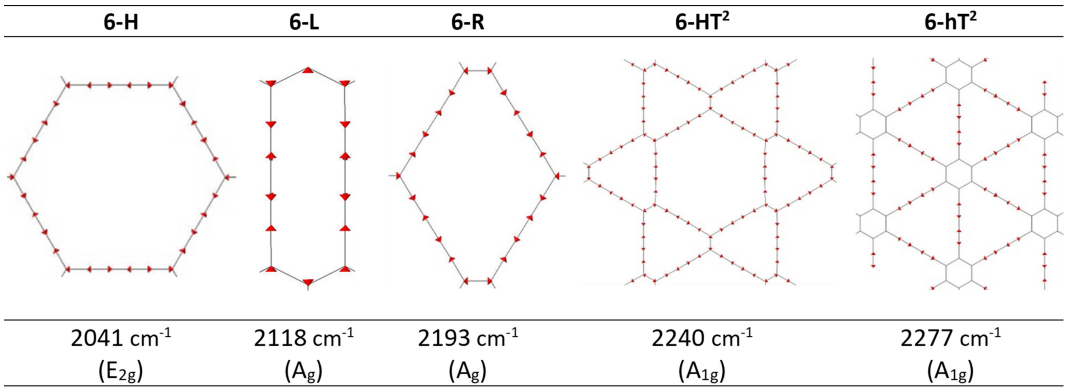

Figure 5.11: *Sketches of the vibrational eigenvectors associated to the strongest ECC phonons of GDYs. In the last row the corresponding vibrational wavenumbers and symmetry species are reported.*

With the only exception of the E_{2g} vibrations of 6-HT^2, the Raman active phonons in the 2000-2400 cm^{-1} region show, for all the diacetylene branches, the characteristic pattern of the ECC mode. Indeed, the group coordinates T_i^+ are dynamically coupled with the other stretching degrees of freedom of the sp chain, thus giving rise to collective vibrations, involving also stretching vibrations of the quasi single CC bonds, namely of the sub-sets of coordinates $\{r_i^+ , P_i\}$, which oscillate out-of-phase with T_i^+, during the ECC vibration. The strong dynamic coupling between triple and single bonds stretching in sp chain, resulting in ECC-modes, is a well recognized phenomenon, encountered for a wide variety of polyyne oligomers, irrespectively to their chain length and end groups [120], and also already deeply discussed in the previous chapters of this thesis. The strong Raman activity of ECC modes and the remarkable sensitivity to π-electrons conjugation of their frequency are reported as the signature of the strong electron-phonon interaction, taking place along the peculiar ECC vibrational trajectory. In fact, the ECC vibration can be described as the oscillation of the bond length (BLA) alternation parameter, which is the key nuclear parameter affecting the electronic structure of Carbon chains with polyconjugated π electrons. Interestingly, in the case of GDY crystals, the occurrence of a shrinking of the C-C bonds of the sp chain simultaneous with the C≡C stretching not only depends on the dynamical coupling, but is

a direct consequence of the translational symmetry of the crystal. It requires that q=0 phonons are such that the atoms displacements do not modify the cell volume, at any time. Indeed, during ECC vibrations, the shrinking of C-C bonds, does guarantee the fulfilment of the above symmetry constraint when the two C≡C bonds stretches in phase. Looking to Figure 5.10, we observe for the 6-hT^2 system two distinct bands at rather different frequencies associated respectively to the A_{1g} symmetry ECC phonon (2277 cm^{-1}) and to the E_{2g} ECC phonon (weaker band at 2337 cm^{-1}). In a previous chapter, we showed that the sizeable difference in wavenumber of these two phonons (60 cm^{-1}) is due to the interaction among adjacent diacetylene chains, linked through the CC bond belonging to the phenyl unit. The separation in frequency between ECC modes is smaller for other GDY crystals, while in the most cases the intensity of the totally symmetric A_{1g} (or A_g) line is the largest one. However, 6-H represents a peculiar exception in GDY family: in this case, the ECC E_{2g} phonon has the largest Raman activity, as can be seen in Fig. 5.10, while the A_{1g} phonon is practically silent (it is 10-5 times weaker than the E_{2g} ECC phonon). Interestingly, for 6-H the frequency of the E_{2g} phonon is very low (2041 cm^{-1}), and remarkably lower than that of the A_{1g} mode, at 2361 cm^{-1}, up-shifted of 320 cm^{-1}. These features indicate that, differently from the other GDY systems, one only sp^2 carbon atom is no more able to decouple the sp chains and their interaction cannot be described no more as a perturbation. interaction between the effect of the interactions through one only sp^2 carbon atom cannot anymore described as a perturbation of the physics of the individual sp chains. In other words, the vibrational dynamics and Raman response of 6-H is heavily affected by the extended network of conjugated π-electrons involving all the diacetylene branches, linked by only one sp^2 C atom forming the threefold branching. As result of the different behaviours commented above, the higher frequency region of the GDY series shows a very simple Raman pattern, with a strong ECC line, which, in 6-hT^2 and 6-HT^2 cases, is accompanied by only one clearly observable weaker satellite band, located at higher frequency (see Fig. 5.10). Fig. 5.10 shows that the main ECC line follows a decreasing frequency trend according to the crystal structure, spanning a wide interval of about 300 cm^{-1}, in the sequence: 6-hT^2, 6-HT^2, 6-R, 6-L and 6-H, from the higher to the lower ECC. This trend parallels the increasing π-conjugation of the diacetylene chains, as far as ECC softens. This frequency behaviour is commonly observed in conjunction with the equalization of the equilibrium bond lengths (BLA) in the polyyne chains (see BLA values in Tab. 5.1) and, more generally, in polyconjugated sp^2 chain molecules.

As already discussed in the previous section, a comparative study of the energy of several GDY crystals is reported. The crystal energy, normalized to the number of C atoms, is referred to the case of graphene, showing that the introduction of diacetylene units has an energy cost (positive E, see values in

Tab. 5.1). Moreover, E values for the GDY series show a marked dependence on the crystal structure, e. g. on the relative abundance of sp^2 and sp phase and bonds topology: the most stable system is 6-hT^2, while the higher energy system is 6-H. In Figure 5.12 we report the plot of ECC vs E showing a nice correlation: ECC softens as E increases. Considering the high reactivity of the sp carbon chains characterized by a cumulene-like structure (i.e. a sp chain approaching an ideally linear sequence of double bonds), we expect that the systems showing higher E values present also a chain structure with more equalized CC bonds. The BLA parameter, which measure the average degree of bond alternation in the sp chains, provides an estimate of this property. BLA parameter have been obtained as difference between the average bond length of quasi single bonds and the average bond length of the triple ones: BLA = $\frac{1}{3}(r_0+r_0'+P_0) - \frac{1}{2}(T_0+T_0')$ where r_0, P_0 and T_0 are the equilibrium bond length values of CC bond belonging to the diacetylene chains (see Figure 5.9 for the meaning of the symbols). The BLA values of GDYs, reported in Tab. 5.1, are compared to E in the plot in Fig. 5.12, showing the expected correlation. This plot nicely explains the observed correlation between energy and ECC frequency: as a matter of fact, the usual trend among ECC and BLA values is indeed verified (Figure 5.12). A closer look to Figure 5.12, shows that there is a frequency value which does not follow an approximately linear trend with BLA corresponding to 6-H structure, showing a ECC frequency remarkably low in comparison with its BLA. Moreover, also in the plot E vs. BLA of Figure 5.12 6-H crystal is not in trend. It seems that the predicted chain geometry does not fully reflect the very high electron delocalization described by ECC and E. Notice moreover that the 6-H structure showed peculiar vibrational features, which deserve a deepening in the future.

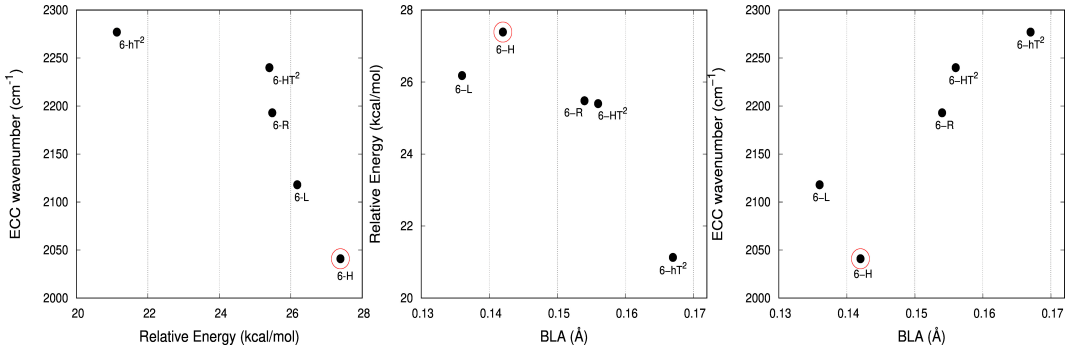

Figure 5.12: *Correlation between physical quantities sensitive to π-electrons conjugation. Left: ECC phonon wavenumber vs. Relative Energy. Center: E vs. BLA parameter. Right: ECC phonon wavenumber vs BLA. The data corresponding to 6-H crystal are highlighted by a red circle.*

We tried to rationalize the origin of the different degree of electrons conju-

gation in GDYs, by considering the different characteristic of the sp^2 links. As already reported in literature [115] and discussed in the previous sections, the high aromatic character of the phenyl units prevents an effective conjugation of the π^z-system of the ring with the π^z-electrons of the grafted diacetylenic chains, thus resulting in a remarkably large BLA and a rather high frequency of the ECC Raman band of 6-hT^2. Instead, the sp chains belonging to structures 6-HT^2 and 6-R, are linked each other through one only CC bond between two sp^2 C atoms, i.e., through a formally double bond, that is more prone to share its π^z electrons with the π^z-electrons systems of the diacetylene units. Thus, 6-HT^2 and 6-R show intermediate ECC frequency and BLA values. Also in the case 6-L, which presents arrays of sp^2 C atoms forming zig-zag chains with equalized CC bond length, a polyacetylene-like chain, one can identify pathways consisting of an infinite sequence of sp chains bridged by one CC bond involving sp^2 C atoms. In this case the p^z electrons of the sp^2 carbon atoms belong to a fully delocalized π system, along the zig-zag chain, and result to be more effective in promoting π^z-electrons conjugation with the sp branches. 6-L structure is at the second place if one considers the trend of E and of ECC frequency from lower to higher frequency values. A furtherly enhanced tendency toward conjugation is observed for the structure 6-H, with one only sp^2 C atom acting as a three-branches node of the network, showing the lower ECC frequency, in correspondence with the higher instability of the crystal (higher energy). We can also observe that for the most GDY systems ECC shifts toward lower values as far as the ratios between the number of sp and sp^2 C atoms (sp/sp^2) decreases. On the other hand, as already observed in the previous section and in our paper [125], sp/sp^2 ratio correlates also with the relative energy, showing a general increase with the increase of the sp phase content. The only one exception to this trend is the 6-L crystal, which possesses a very low ECC and a high E value but, in contrast, a low sp/sp^2 carbon ratio: this observation tells us that also the topology of the sp^2 phase can play a very important role.

The infrared spectra of the higher frequency region is characterized by phonons involving the antisymmetric stretchings of the triple bonds (T_i^-) accompanied by out of phase contributions of (r_i^-). Because of the inversion symmetry, IR active phonons cannot involve the stretching of the central CC bonds. We find one only IR active, doubly degenerate, E_{1u} phonon for the D_{6h} systems showing three sp branches in the cell (6-H, 6-hT^2) and one additional E_{1u} phonon in the case of 6-HT^2 (six sp branches). 6-L and 6-R crystals show one only B_{3u} transition and two (B_{3u} and B_{2u} transition) respectively, according to the number of branches belonging to the primitive cell. Looking to the IR intensity values, it's immediate to realize that, also in presence of two IR active modes, one only band is strong enough to be identified in the plot of predicted IR spectra. In the framework of ECC theory, such IR active modes

have been described as the BLA oscillation with a node in the middle of the chain. Differently from the collective ECC modes, the vibrational frequency of these modes is little sensitive to the degree of conjugation of the chain, moreover their frequency is always higher than ECC. The above characteristics is reflected also in the spectral trend, showing a modest dependence of the position of the high frequency IR bands on the different crystal structures of the GDY series.

For what concerns the region below 1600 cm^{-1}, Raman transitions correspond to phonons involving the stretching of the "quasi" single bonds of the sp chains. For a given i-th sp chain, r_i^+ and P_i coordinates are involved in out-of-phase combination, which fulfils the requirement that the cell volume is preserved during the vibrational displacements. The stronger Raman line in this region has a frequency value in the range 1480-1550 cm^{-1} and belong to the total symmetric species for all the crystal, but for 6-H structure showing a strong E_{2g} transition, of the same symmetry species as its intense ECC mode.

GDY	6-R	6-HT^2	6-hT^2	6-H	6-L
P(Å)	1.343	1.345	1.351	1.336	1.329
r(Å)	1.398	1.399	1.406	1.391	1.381
ν(C-C) (cm^{-1})	1404	1448	1491	1498	1531

Table 5.2: *Bond length of the quasi single CC bonds belonging to the diacetylene branches, for GDY structures. For meaning of bond labels, see Figure 5.9*

Table 5.2 shows that there is a nice correlation between the strength of the quasi single CC bonds belonging to the sp chain and the frequencies of the associated CC stretching phonons for the series 6-R, 6-H, 6-R: the shorter the bonds, the higher is the frequency. 6-HT^2 and 6-hT^2 do not follow this trend, likely for the coupling with ring breathing vibration in 6-hT^2 and because of the more complex vibrational structure for the crystal with a largest cell (6-HT^2). However, the vibrational eigenvectors become much more complex in presence of bonds linking sp^2 carbon atoms, which are possibly subjected to strong dynamical coupling with r_i stretchings. However, also vibrational modes rather localized in the sp^2 domain can occur, as in the case of 6-hT^2 crystal, for which the nature of these vibrations has already discussed deeply in our paper [115] and in previous sections of this thesis work. In particular, the three bands located at 1382, 1491 and 1574 cm^{-1} show large contributions by stretching vibrations of the phenyl units. The collective character of the phonons of GDYs in the lower frequency region (below 1400 cm^{-1}) makes difficult to propose a comparative discussion. We limit ourselves to the observation that 6-R and 6-HT^2, which share the property of the presence of isolated sp^2 CC bonds between diacetylene chain, present a strong band close to 1100 cm^{-1} characterized by a vibrational eigenvector showing a remarkable contribution of the sp^2 CC bond.

Shifting to the analysis of the IR spectra in the region below 1600 cm^{-1}, we focus our attention on the possibility to identify different marker bands for the different 2D structures. For the 6-H crystal one can find a very intense IR active band at 1300 cm^{-1}. Also for 6-hT^2, the peak with the highest IR intensity is located below 1500 cm^{-1}: we predict a strong band at 1429 cm^{-1} with contributions from stretching vibrations of the bonds of the phenyl units. The marked difference in frequency between 6-H and 6-hT^2 bands ($\Delta\nu$ = 129 cm^{-1}) gives the possibility to distinguish between the two structures. Both IR spectra of 6-HT^2 and 6-R, show the presence of two strong IR-active bands, well separated in frequency and located at different positions for the two systems. Looking at the vibrational eigenvectors, we can describe these vibrations as mainly characterized by the in phase T_i^- and r_i^-. Also for these systems, IR spectroscopy shows strong distinctive features, useful for their identification. 6-L structure shows an isolated band located at 1182 cm^{-1} very close to the 6-HT^2 one (1185 cm^{-1}). However, for 6-HT^2, the presence of the additional strong band 6-HT^2 of at 1452 cm^{-1}, allows distinguishing among the two crystals. Moreover, the whole intensity pattern is different for the two structures.

In the lower frequency region (< 600 cm^{-1}, see Figure 5.10) it is possible to identify different marker bands. Indeed, a very intense IR active peak appears for 6-R, 6-L and 6-H, located respectively at 580 cm^{-1}, 560 cm^{-1} and 565 cm^{-1}. Through the analysis of the vibrational eigenvectors associated to these bands it is possible to state that these phonons are characterized by collective in-plane bending of the CC bonds of the sp chains.

5.4.2 Vibrational spectra of GYZ

The second class of crystals studied in this work consists in the series known in literature as grazynes [129]. They are 2D materials that show the presence of L units (diacetylene chains) and condensed aromatic rings forming ribbons with different widths (Figure 5.8) [129]. For the analysis of the Raman and IR spectra of GZY we will focus our attention on the evolution of the spectra inside two different families, whose structures are depicted in Figure 5.8. The first one (GZY-I) (6-hL, 6-hL^2, 6-hL^3) shows a topology made by ribbons consisting in an infinite sequence of condensed h units (1 only h unit in the height, forming a polyacene chain), intercalated by layers formed by L units. These layers have different height, depending on the number n of L units (n =1,2,3), running parallel to the layer width (x axis direction) and linked each other through a zig-zag polyacetylene-like sp^2 chains. The crystal 6-L, already discussed as member of the GDY group, is a limiting case of this family and will be considered in our comparative analysis. The second family (GYZ-II) is characterized by a layer of parallel L segments (the layer thickness corresponds to one only L unit) intercalated to nanoribbons formed by condensed h units, with different widths, according to the notation: 6-hL, 6-h^{2}L, 6-h^{3}L. Graphene can be considered a

limiting case, belonging to this family. In Fig. 5.13 we report the Raman spectra and the infrared spectra calculated for GZY-I and GZY-II groups.

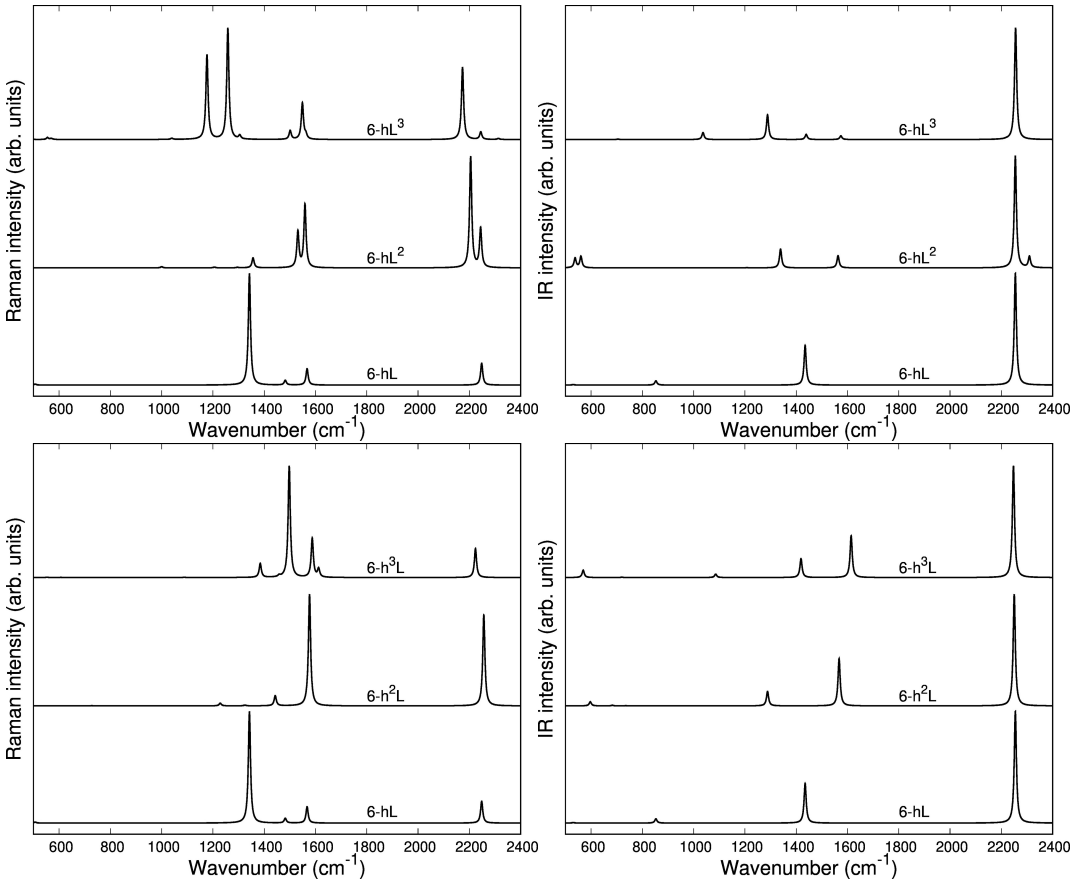

Figure 5.13: *Calculated Raman and IR spectra of GZY-I (top) and GZY-II(bottom).*

GZY spectra show features typical of the sp phase, which is the main responsible of the characteristic vibrational features in the high frequency (above 2000 cm^{-1}) and of the graphene-like ribbons, giving rise to features below 1600 cm^{-1}. The interplay between the two (sp and sp^2) phases influences the degree of electrons delocalization in the whole crystal and is expected to have a signature especially in the Raman spectra, which cannot be regarded by a mere superposition of the spectroscopic response of the L layers and of the h ribbons. Because of the complex trajectories of the phonons below 1600 cm^{-1}, involving atomic displacements in both sp and sp^2 phase, the following discussion will be focused on the vibrational features coming from vibrations mainly localized on the diacetylene branches, i.e., on the 2000–2400 cm^{-1} region. GZY-I q=0 phonons are classified according to the D_{2h} symmetry: Raman transitions in the high frequency range are associated to A_g phonons. As in the case of GDY, one strong Raman line, possibly accompanied by satellite lines located

in the higher frequency side, dominates the sp spectral region (Fig. 5.13). The eigenvectors analysis (Fig. 5.14) shows that only chains which carry a symmetry inversion centre develop a collective ECC vibration, namely the symmetric stretching of CC quasi triple bonds (T_i^+) accompanied by out-of-phase vibration of the quasi single CC bonds (r_i^+, R_i). This happens for crystals 6-hL, and for the central chains of the L layer in the case 6-hL^3. Chains which lost the inversion centre contribute to the phonon eigenvetor with diplacements localized either on the triple bond close to the zig-zag chain, or to the polyacene ribbon. This is the case of the phonons of 6-hL^2 where the strongest lower frequency phonon describes a BLA fluctuation along a path crossing a CC bond belonging to the zig-zag chain, and does not involve the peripheral C≡C bond of the L^2 layer. Its low frequency and high intensity should be ascribed to electrons delocalization phenomena, which involve the CC bonds of the polyacetylene-like chain. In a similar way, we can justify the large Raman intensity (and low frequency) of the ECC-like mode of 6-hL^3. It can be described as due to the ECC vibration of the central chain (showing inversion centre) accompanied by an in phase BLA oscillation of the two adjacent chains, localized on the C-C≡C sequence close to the zig-zig chains. In the case of the family GZY-II the situation is simpler because all these structures contain only one L segment in the primitive unit cell, which is characterized by inversion centre. Thus this family shows one only A_g transition above 2000 cm^{-1}, corresponding to the ECC mode of the diacetylene chain, thus resulting in one only Raman line in the higher frequency region of the Raman spectrum. Interestingly, looking to the calculated Raman spectra we can see that GZY-II series shows a little dispersion of the ECC line, while for the GZY-I series the ECC–like phonon shows a dispersion of 75 cm^{-1}, with a decreasing frequency trend as far as the number of L segments in the L layer increases. This is another evidence that the CC bonds belonging to the zig-zag chain bridges chains in such a way that sizeable electrons conjugation between the diacetylene segments occurs. As already observed in the case 6-hT^2, aromatic systems are less prone to share electrons with the sp system, and this explains why the frequencies of their ECC bands are rather high and little sensitive to the width of the graphene-like ribbons. As a last observation, we notice that the modulation of the ECC phonon frequency is remarkably stronger in the case of GDY (dispersion of about 300 cm^{-1}) than in the whole GZY family (dispersion of 140 cm^{-1}).

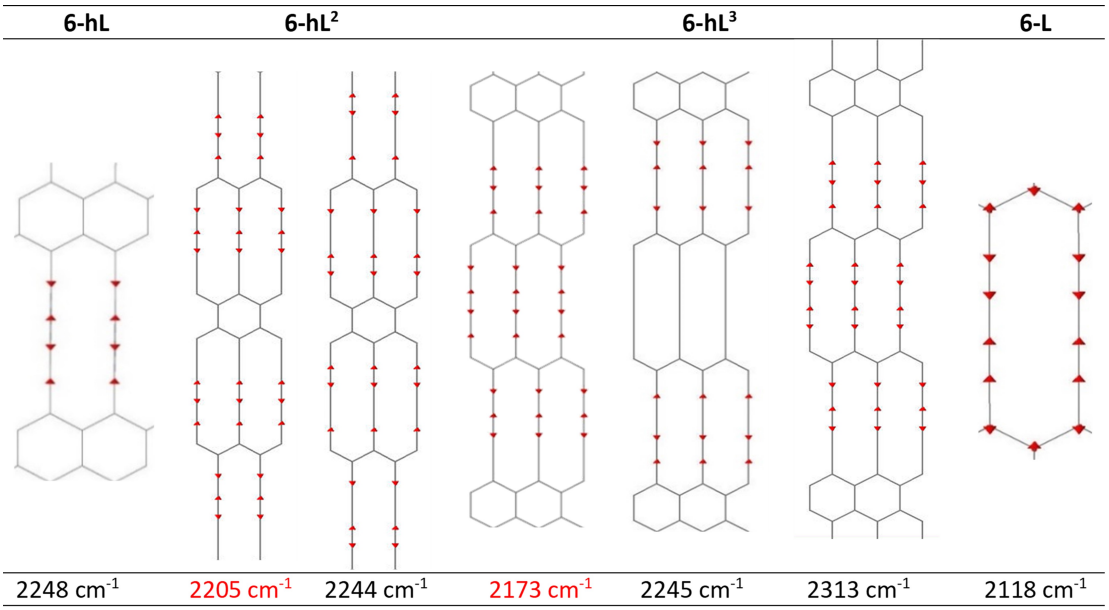

Figure 5.14: *Sketches of the vibrational eigenvectors associated to the Raman active (A_g) phonons of GZY-I group, in the spectral region above 2000 cm^{-1}. In the last row the corresponding vibrational wavenumbers are reported. Wavenumbers of the strongest bands are highlighted in red.*

In Figure 5.15 we illustrate the correlation between the frequency of the ECC line and the crystal relative energy E. Similar to the case of the GDY family, we find a decreasing trend of the frequency as far as the crystal become less stable. Also in this case larger E values correspond to less stable sp chains, showing a more cumulene like character (more equalized CC bonds), as illustrated by Figure 5.15. In the same figure the expected trend of the ECC frequency versus the BLA parameters is also shown.

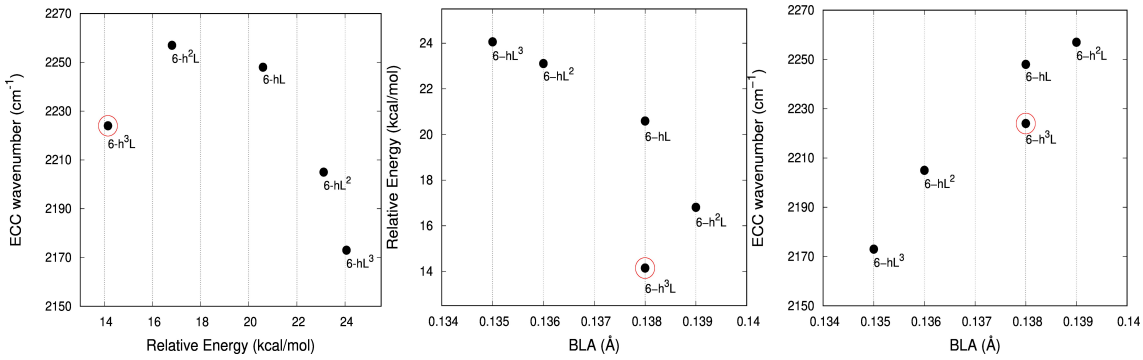

Figure 5.15: *Correlation between physical quantities sensitive to π-electrons conjugation. Left: ECC phonon wavenumber vs. E. Center: E vs. BLA parameter. Right: ECC phonon wavenumber vs BLA. The data corresponding to 6-h^{3}L crystal are highlighted by a red circle.*

Interestingly, also for the GZY family there is an outlier, namely 6-h^{3}L, showing its ECC frequency (2224 cm^{-1}) rather low in comparison with its E. Moreover, also its BLA value does not correlate well with the energy value. A possible rationalization of such behaviour should consider the role of the sp^2 phase, that also contributes to E: notice that for 6-h^{3}L the parameter sp/sp^2 is the lower one (0.5).

Above 2000 cm^{-1} GZY crystals show IR active B_{3u} transitions characterized by dipole moment oscillation in the direction of the sp chains (x axis). Similar to their Raman counterpart, the number of IR active transitions equals the number of L units in the primitive cell. However, the IR spectrum shows one only band in the most cases because of the very low IR intensity of the other transitions. Only in the case 6-hL^2 a satellite band can be observed in the IR spectrum, at higher frequency with respect to the main line (Figure 5.13). The stronger IR line in this region corresponds, for all the GZY crystal, to the out of phase stretching (T_i^-) of the triple CC bonds of the chain. In cases with more than one chain per unit cell, it is described by the in phase combination of (T_i^-) of all the chains (see vibrational eigenvectors sketched in Fig. 5.16).

Interestingly, looking to the data reported in Fig. 5.16, we can realize that phonons corresponding to similar displacements of the sp carbon can have very different IR intensities in the different crystals. In particular, the structure 6-hL^3 shows a remarkably high IR intensity of the band at 2256 cm^{-1} which could be ascribed to relevant fluxes of charge associated to the collective vibration of the three L segments forming the L^3 layer. This last observation can be taken as a further evidence of the high delocalization of electrons along the sequence made by three diacetylene segments.

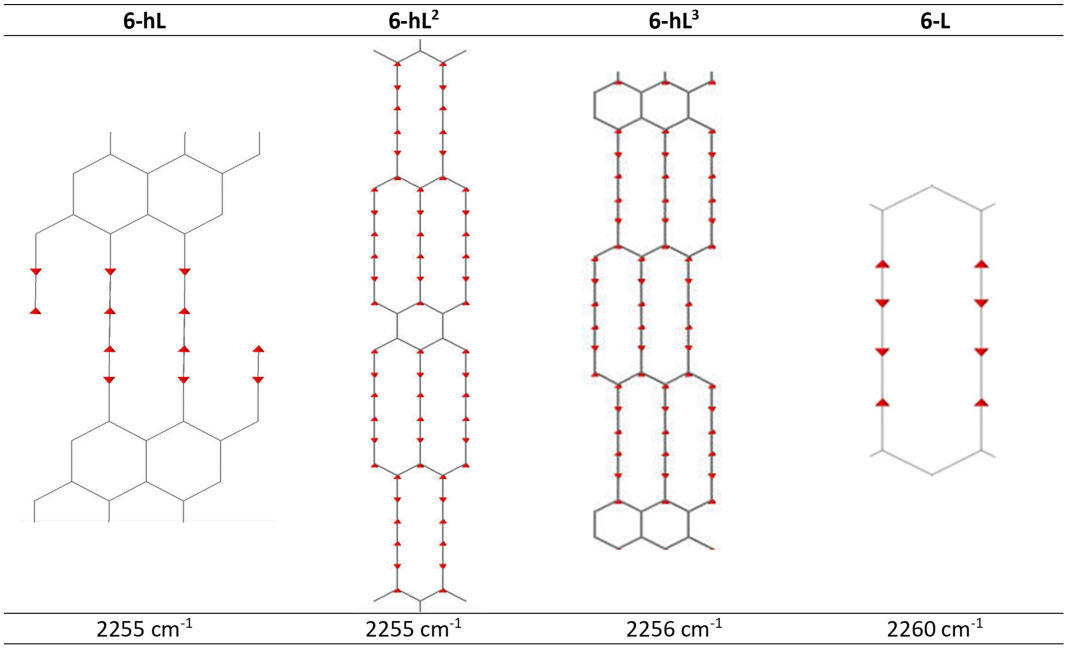

Figure 5.16: *Sketches of the vibrational eigenvectors associated to the strongest IR active (B_{3u}) phonons of GZY-I, in the spectral region above 2000 cm^{-1}. In the last row the corresponding vibrational frequencies (cm^{-1}) are reported.*

Conclusions and Future Perspectives

In conclusion, in my thesis work a computational investigation of sp and hybrid sp-sp^2 carbon nanostructures has been performed by means of Density Functional Theory through the use of Gaussian and Crystal packages. The first class of investigated systems were sp-hybridized carbon atom wires (CAWs). I started with the investigation of polyynes, by analyzing their optical, electronic and vibrational properties through the computation of UV-Vis and Raman spectra, to understand how they are affected by chain length and by different terminal groups. To this aim, hydrogen- methyl- and cyano-terminated polyynes with chain length ranging from 6 to 16 have been investigated. Indeed, Raman and UV-Vis absorption responses revealed to be strongly modulated by these parameters, enabling an easy characterization of carbon atom wires with these spectroscopic techniques. Indeed, both Raman and UV-Vis peaks suffer a red-shift, in vibrational frequency and wavelength respectively, increasing the number of carbon atoms in the chain, confirming the increase in π-electron conjugation typical for π-conjugated systems when the dimension of the conjugated backbone is increased. Moreover, strong dependency of both Raman and UV-Vis spectra on the end-capping group was shown, revealing higher electronic conjugation for cyano-terminated polyynes with respect to methyl- and hydrogen-terminated ones at constant number of carbon atoms. Comparison with experimental spectra was also performed to confirm the results. Interaction between polyynes, having different length and terminations, and metal nanoparticles was also studied through the analysis of the interaction energy between the chain and the cluster and of the Raman spectra computed for the polyyne+cluster system. The aim was to better understand how this interaction can be modulated by the dimension of the metal nanoparticle and by the carbon chain length, but also to give a better interpretation of the experimental SERS spectra. The first investigated systems consisted in hydrogen-terminated polyynes of length 4 and 8 (i.e. HC_4H and HC_8H) interacting with clusters made by 4 and 8 atoms (i.e. Ag_4 and Ag_8). Indeed, I initially focused on finding a good computational setup able to correctly interpret the interaction between the two systems. Once the computational setup has been

chosen, I moved to the investigation of HC_4H and HC_8H interacting with Ag_4 and Ag_8. From the analysis, I found strong dependencies of the interaction energy on chain length and cluster size, demonstrating an increase of this energy increasing the size of the cluster and/or of the chain. On the other hand, with the analysis of the Raman spectra, I was also able to explain the appearance of a low frequency band in the experimental SERS spectra, attributing this phenomenon to the peculiar interaction between chain and nanoparticle, but also to interpret its modulation by changing different parameters (cluster size, chain length, chain termination...). Then, to complete the analysis of CAWs, I passed to the analysis of a series of end-capped cumulenes, characterized by vinylidene-[H], phenyl-[Ph], di-tert-butylphenyl-[tBuPh], mesityl-[Mes] and fluorene-[Fl] terminals. For each species, regardless the end-groups, I observed the appearance of a low energy broken-symmetry DFT solution of the singlet ground state. Such solution started to appear for chain lengths longer than five carbon bonds ($n \geqslant 5$), and it is the fingerprint of a diradicaloid (open-shell singlet) character of the electronic structure, thus underlying a multi-reference configuration of the ground state wavefunction. The appearance of BS solutions goes on par with the presence of low-lying triplet states, while FOD analysis and the evaluation of the di-/tetra-radical (y_0,y_1) indexes further supported the presence of open-shell singlet BS-DFT solutions, revealing strong electron correlation effects and multireference character of the ground state electronic structure of cumulenic chains. The evidence of an open-shell singlet (BS-DFT) diradicaloid ground state of cumulenes is the appearance of a marked bond length alternation of the carbon chain, thus inducing a single-/triple-like bond pattern contrary to the canonical (equalized) double-bonds one. We have discovered that Fluorene ([Fl]) end-group induces the highest bond length alternation of the chain, leading to a large diradicaloid character. Diaryl-mesityl ([Mes]) end group instead shows the lowest bond length alternation, while diphenyl ([Ph]) and diaryl-tert-butyl- ([tBuPh]) feature intermediate BLAs between [Mes] and [Fl]. The modulation of the BLA and diradicaloid character for different end-capped cumulenes can be attributed by the fine interplay, namely the electronic coupling, between the sp-carbon chain and the terminal groups. A correlation between the BLA parameter and the dihedral angle of the terminal groups was also found. The larger is the end-group dihedral angle, the lower is the BLA parameter, hence the lower is the diradicaloid character. In this frame, [Fl] end-capped chains showed the highest diradicaloid character with high bond length alternation of the chain, featuring an overall planar structure and allowing the π-electrons to delocalize over the end groups while [Mes] end-capped chains showed high dihedral angles, hindering the over-delocalization of the electronic structure on the terminals and reducing the diradicaloid character. The computed spin densities for the open-shell singlet BS-DFT further corroborate this finding, showing an

enhanced delocalization over the end groups for [Fl] species rather than [Mes]. For the same set of molecules, with the addition of the hydrogen-terminated polyynes, transport properties have been investigated with a vision of applying these systems as active materials in organic electronics devices. To this aim, reorganization energies have been analyzed for carbon atom wires with different lenght and end-capping groups. Calculated energies, whose values reflect the ability of a molecule in taking or giving electronic charge, revealed to be very dependent on the lenght and termination of the polyynic and cumulenic species, showing decreasing value for an increasing lenght of the chain, but also a strong dependence on the end-capping groups. Indeed, starting from the simplest systems, i.e. hydrogen-terminated polyynes and vinylidene-capped cumulenes, we found quite similar reorganization energy values for both systems, and also a strong dependence on the exchange-correlation functional adopted. Moreover, anionic reorganization energies showed lower values with respect to the cationic ones for vinylidene-capped cumulenes, while for hydrogen-terminated polyynes the situation is reversed. Evaluation of N_{FOD} indices also revealed a strong diradical character also for the charged state of these systems; in particular, polyynes showed multireferencial character only in their charged states, while the ground state is well described by using single reference DFT calculations. The analysis of distortions suffered by the molecule when subjected to positive or negative charge-transfer process, both in terms of bond lengths and dihedral angles, confirmed the reorganization energy values obtained for polyynic and cumulenic species. Then, also for n[Ph], n[tBuPh], n[Mes] and n[Fl] reorganization energy values were calculated depending on the cumulenic chain length. For these systems, the effect of the end-capping groups showed to be very important in determining the energy values. Indeed, lower values were obtained for n[Fl] species, also reflected by the lower distortions suffered by molecules when positively or negatively charged. On the contrary, n[Mes] systems are characterized by the highest energy values and higher distortions, while n[Ph] and n[tBuPh] showed intermediate values between the two extremes. Moreover, the dependency of the energies from the end-capping groups go on par with the tendency of the molecule to show a marked diradical character. For a high number of carbon atoms in the chain (n=9), very low reorganization energy values are obtained (<0.1 eV), demonstrating the marked facility for these systems in transporting charge carriers.

After the investigation of carbon atom wires, I passed to the analysis of more extended molecular systems based on mixed sp-sp^2 hybridization. To this aim, structure/properties relationships of γ-GDY based molecular fragments have been studied to find the connection between the molecular structure and their fundamental physicochemical properties. Indeed, HOMO-LUMO gap, molecular structure/topology and Raman response of GDY fragments have been shown to display some peculiar and general trends, giving useful information

for the design of new promising systems. One-dimensional models allow to verify the dependence of the gap on the type of conjugation path (para, ortho or meta) where para-path shows the largest conjugation. Indeed, the length and number of para-pathways significantly modulate the HOMO-LUMO gap among the other possible conjugation pathways (ortho and meta), in agreement with what observed in GY [52]. However, we found that the number of "condensed" triangular units can be even more important in reducing the gap. Despite these effects, the gap appears to reach a stable value as the number of "triangular" units is increased in the fragments, suggesting that to approach the limit of infinite 2D GDY very large fragments are required, thus possibly making the use of bottom-up chemical synthetic routes unfeasible. The Raman frequencies associated to vibrational stretching modes localized on the sp-carbon domains show a correlation with the predicted HOMO-LUMO gaps. In particular, a red shift of the frequency is found for systems possessing a lower gap. These correlations can be used, at least qualitatively, to evaluate the modulation of the gap for molecules characterized by different structures and topologies possibly in relation to spectral measurement of previously synthetized systems. Then, since the study of molecular GDY systems was completed, my focus was oriented towards more extended GDY-based systems like 1D γ-GDY nanoribbons (GDYNR). Indeed, calculations have been used here to compute the band gap and the vibrational response of nanoribbons with different widths and edge type. For these systems, the trends of the band gap as a function of the GDYNRs width, for both armchair (A) and zigzag (Z) edge can be rationalized based on the different structures, and comply with the band gaps of the polymers A(1)-GDYNR and Z(1)-GDYNR, taken as the n = 1 width limit. Moreover, Raman and IR spectra have been computed for GDYNRs with different width and edge. We have unveiled Raman markers of A(n)-GDYNR at 1630 and 1450 cm^{-1}, whereas the weak bands computed at 700, 1270, and 1405 cm^{-1} are IR markers. In the case of Z(n)-GDYNRs, Raman markers are too weak to be of experimental interest, while the most significant markers are found in the IR spectrum at about 1620 and 2350 cm^{-1}. The Raman bands above 2200 cm^{-1} display an evident redshift for increasing GDYNRs width; hence their position can be useful for a qualitative assessment of the GDYNR width. Apart from minor details, no significant difference has been found in the spectroscopic response of integer vs half-integer Z(n)-GDYNRs. Finally, IR-active CH out-of-plane modes have been found to have a characteristic dependence on the edge type, providing another significant marker for the characterization of GDYNR. The analysis ends with the investigation of the 2D γ-GDY crystalline system. For this material, The band gap computed at HSE06/6-31G(d) level of theory (hybrid functional, Gaussian basis set) provides a reliable value (1.11 eV), in very good agreement with the value of 1.1 eV obtained by using the GW method. Moreover, Raman and

IR spectra of 2D-GDY have been computed, assigned, and discussed in detail, showing a good agreement with available literature data. These spectra can be taken as a reference for the investigation of confined systems and for the interpretation of experimental measurements.

Finally, once the γ-GDY-based systems have been deeply explored, both in molecular and crystalline 1D and 2D forms, I proposed a computational investigation aimed at the molecular design of new sp-sp^2 carbon 2D crystals, different from the γ-GDY system, focusing in particular on the importance of the structure and topology in modulating the relative energies and the band structure with respect to graphene. The adopted approach is able to predict all the possible sp-sp^2 crystals as graphene derivatives. By restricting the search to all the sp-sp^2 carbon crystals with a maximum number of eight sp^2 carbon atoms per unit cell, we generated 26 2D crystals. DFT simulations revealed some peculiar trends both in relative energy and electronic properties, which can be described in terms of general topological effects. In all the cases, an increase in the sp-sp^2 carbon ratio produced an increase in relative energies with respect to graphene, with two peculiar trends. A first one is constituted by graphene stripes interconnected by diacetylenic bridges (grazdiynes), which have been also predicted to have a metallic behavior. The second trend collects 2D crystals (including α-, β-, and γ-GDY), which can be described in terms of common geometrical units formed by the carbon atoms, including h and H hexagons, L lines, R rhombus, and T triangles. Describing the crystals in terms of these units allowed us to rationalize both relative energies and the band structure: the higher the similarity to graphene units (i.e., h), the lower the relative energies; on the other hand, H units increase the relative energies up to the limiting case of α-GDY and are a characteristic of zero-gap semiconductors with Dirac cones. These different units can play a role in determining the electronic behavior of the material: triangular T units are indeed the structural/topological factor which promotes semiconductive materials with a finite band gap; on the other hand, L units would promote metallic structures, while h, H, and R units tend to induce zero-gap semiconducting behavior with Dirac cones. As a general rule, in structures formed by different units, L is found to have a larger effect than h, while H and R dominate over L, and finally, T seems to dominate all over the other units, even if these relative effects have been shown to have a non-negligible dependence on the DFT functional choice, in particular for some peculiar structures. Therefore, I demonstrated that the local topology is strongly responsible for the metallic/semiconductive behavior, while the formation of long conjugation pathways, along which a larger/lower conjugation can occur, seems to play only a minor role, in agreement with the behavior of γ-GDY molecular fragments. For the same systems, the Raman and IR response of the most representative 2D structures were also investigated. I decided to focus my attention on two families, the first

characterized by 6-L, 6-H, 6-R, 6-hT^2 and 6-HT^2 GDY structures while the second consisting in linear diacetylene chains (L) connected to extended sp^2 domains forming the so called grazdiynes systems (GYZ). Concerning the first family, the dependence of the vibrational pattern, rapresented by Raman and IR active bands, on peculiar topology and structure of the different crystals has been deeply investigated. Indeed, a strong frequency shift of the ECC Raman active phonon depending on different structural features has been showed, focusing in particular on how diacetylenic units are able to couple between each other and with different sp^2 domains. Interestingly, ECC phonon vibrational frequency revealed to be coupled also with stability of the different systems, suffering a red-shift for increasing instability of the 2D materials. For this reason, 6-hT^2 showed the highest value of ECC vibrational frequency while 6-H showed the lowest one. Moreover, we found a strong correlation between ECC, BLA of the diacetylenic linkages and relative energies for these systems, assessing again the strong connection between structural, electronic and vibrational properties in sp-sp^2 hybridized carbon-based materials. Finally, IR spectra analysis demonstrated the existence of different marker bands which make possible the unambigous characterization of these systems. Focusing on the second family of these 2D crystals (GZY), composed by 6-hL, 6-hl^2, 6-hL^3, 6-h^{2}L and 6-h^{3}L systems, looking at the calculated Raman spectra we can see that GZY-II series, characterized by 6-hL, 6-h^{2}L and 6-h^{3}L structures, shows a little dispersion of the ECC line, while for the GZY-I series, composed by 6-hL, 6-hl^2, 6-hL^3 systems, the ECC–like phonon shows a dispersion of 130 cm^{-1}, with a decreasing frequency trend as far as the number of L segments in the L layer increases. This is another evidence that the CC bonds belonging to the zig-zag chain bridges chains in such a way that sizeable electrons conjugation between the diacetylene segments occurs. A similar nice correlation between ECC, BLA and energy can be appreciated also for GZY families and, as for the case of GDYs, IR spectra resulted to be very useful in the characterization of these materials.

Based on these results, various perspectives of my PhD work can be opened. At first, the possibility to extend the investigation towards longer carbon atom wires having different end-capping groups could open the opportunity to modulate even more the optical and electronic properties of these materials, giving tha chance to reach a more red-shifted absorption spectra towards the visible range of wavelengths. Moreover, fluorescence phenomenon could be studied and explored for these molecules, also with a vision of applying them as fluorescent probes. On the other hand, transport properties investigation could be completed with the computation of the electronic coupling integrals between molecules, having the access to their crystalline data, with the aim of computing the mobility for the entire material. Then, future investigations could be realized by extending of the dimension of the studied GDY fragments

and nanoribbons to understand how the electronic and vibrational properties are furtherly affected. Morevoer, the possibility to evaluate potential multireferential character in these systems would be a very challenging analysis. This analysis could be extended also to GDY-based 2D systems with various topology, to understand how topology can affect diradical character of the investigated materials. For the same set of GDY crystals, transport properties could be investigated to obtain mobility values able to discriminate between systems with higher charge carriers velocity. Moreover, structure and topology effects can be pushed even further, by analyzing structures with longer sp-carbon based linkages, as graphtriyne, graphfouryne and so on, to understand how the increase in the length of these units can affect the properties of hybrid sp-sp^2 materials.

All the results obtained during my PhD, and reported in this thesis work, are characterized by the common objective of applying sp and hybrid sp-sp^2 systems in different engineering fields, from energy to electronics, having a vision for an all carbon-based science and technology.

List of Figures

List of Tables

Bibliography

[1] A. Hirsch. The era of carbon allotropes. *Nature materials*, 9:868–71, 11 2010.

[2] R.H. Baughman. Dangerously seeking linear carbon. *Science*, 312(5776):1009–1010, 2006.

[3] C.S. Casari and A. Milani. Carbyne: from the elusive allotrope to stable carbon atom wires. *MRS Comm.*, 8:207–219, 2018.

[4] F. Cataldo. *Polyynes: Synthesis, Properties, and Applications*. Taylor and Francis, 2005.

[5] S.C. Brand M.M. Haley and J.J. Pak. Carbon networks based on dehydrobenzoannulenes: Synthesis of graphdiyne substructures. *Angewandte Chemie International Edition in English*, 36(8):836–838, 1997.

[6] J.J. Pak W.B. Wan, S.C. Brand and M.M. Haley. Synthesis of expanded graphdiyne substructures. *Chem. Eur. J.*, 6(11):2044–2052, 2000.

[7] G.J. Palmer J.A. Marsden and M.M. Haley. Synthetic strategies for dehydrobenzo[n]annulenes. *Eur. J. Org. Chem.*, (13):2355–2369, 2003.

[8] J. A. Marsden and M.M. Haley. Carbon networks based on dehydrobenzoannulenes. 5. extension of two-dimensional conjugation in graphdiyne nanoarchitectures. *J. Org. Chem.*, 70(25):10213–10226, 2005.

[9] C. A. Johnson E. L. Spitler and Michael M. Haley. Renaissance of annulene chemistry. *Chem. Rev.*, (106):5344–5386, 2006.

[10] M.M. Haley. Synthesis and properties of annulenic subunits of graphyne and graphdiyne nanoarchitectures. *Pure Appl. Chem.*, 80(3):519–532, 2008.

[11] K. Suenaga Y. Niimi J. Kotakoski J.C. Meyer H. Peterlik M. Wanko S. Cahangirov A. Rubio Z.J. Lapin L. Novotny P. Ayala L. Shi, P. Rohringer and T. Pichler. Confined linear carbon chains as a route to bulk carbyne. *Nat. Mater.*, 15:634–639, 2016.

[12] W.A. Chalifoux and R.R. Tykwinski. Synthesis of polyynes to model the sp-carbon allotrope carbyne. *Nature Chemistry*, 2(11):967–971, 2010.

[13] S. Yang and M. Kertesz. Linear cn clusters: are they acetylenic or cumulenic? *The Journal of Physical Chemistry A*, 112(1):146–151, 2008.

[14] L. Y. Antipina A. K. Singh P. B. Sorokin†, H. Lee† and B. I. Yakobson. Calcium-decorated carbyne networks as hydrogen storage media. *Nano Lett.*, 11(7):2660–2665, 2011.

[15] H. Lee† F. Xu† M. Liu, V. I. Artyukhov† and B. I. Yakobson. Carbyne from first principles: Chain of c atoms, a nanorod or a nanorope. *ACS Nano*, 7(11):10075–10082, 2013.

[16] M. Wang and S. Lin. Ballistic thermal transport in carbyne and cumulene with micron-scale spectral acoustic phonon mean free path. *Scientific Reports*, 5(18122):1–10, 2016.

[17] R.R. Tykwinski A. Milani C.S. Casari, M. Tommasini. Carbon-atom wires: 1-d systems with tunable properties. *Nanoscale*, 8:4414–4435, 2016.

[18] H.Bai Y. Zhu and Y. Huang. Electronic property modulation of one-dimensional extended graphdiyne nanowires from a first-principle crystal orbital view. *ChemistryOpen*, 5:78–87, 2016.

[19] S. Dag S. Tongay, R. T. Senger and S. Ciraci1. Ab-initio electron transport calculations of carbon based string structures. *Phys. Rev. Lett.*, 93(13):136404–1 – 136404–4, 2004.

[20] N. W. Ashcroft and N. D. Mermin. *Solid State Physics*. Saunders, 1976.

[21] F. Cataldo, I.E. Castelli N. Manini G. Onida L. Ravagnan, E. Cinquanta, and P. Milani. Synthesis, characterization, and modeling of naphthyl-terminated sp carbon chains: Dinaphthylpolyynes. *The Journal of Physical Chemistry B*, 114(46):14834–14841, 2010.

[22] V. Barbieri A. Lucotti V. Russo F. Cataldo C.S. Casari A. Milani, M. Tommasini. Semiconductor-to-metal transition in carbon-atom wires driven by sp^2 conjugated end groups. *The Journal of Physical Chemistry C*, 121(19):10562–10570, 2017.

[23] A. Milani F. Innocenti and C. Castiglioni. Can raman spectroscopy detect cumulenic structures of linear carbon chains? *Journal of Raman Spectroscopy*, 41(2):226–236.

[24] V. Russo A.Li Bassi A. Lucotti F. Cataldo A. Milani, M. Tommasini and C. S. Casari. Raman spectroscopy as a tool to investigate the structure and electronic properties of carbon-atom wires. *Beilstein J. Nanotechnol.*, 6:480–491, 2015.

[25] C.D. Methfessel F.Hampel J. A. Januszewski, D. Wendinger and R. R. Tykwinski. Synthesis and structure of tetraarylcumulenes: Characterization of bond-length alternation versus molecule length. *Angew. Chem. Int. Ed.*, 52(6):1817–1821, 2013.

[26] J. A. Januszewski and R. R. Tykwinski. Synthesis and properties of long [n]cumulenes (n≥5). *Chem.Soc.Rev.*, 43:3184–3203, 2014.

[27] H. D. Hartzler. Di-Íerí-butylvinylidenecarbene, tetra-fm-butylbutatriene, tetra- ferí-butylhexapentaene, and t etrakis (di-rm-butylvinylidene) cyclobutane. *J.A.C.S.*, 93:4527–4531, 1971.

[28] P. D. Jarowski K. N. Houk A.Auffrant, B.Jaun and F. Diederich. Peralkynylated buta-1,2,3-trienes: Exceptionally low rotational barriers of cumulenic c=c bonds in the range of those of peptide c-n bonds. *Chem. Eur. J.*, 10:2906–2911, 2004.

[29] Z. Wei Z. Zhou R. R. Tykwinski S. N. Spisak, M. U. Bühringer and M. A. Petrukhina. Structural and electronic effects of stepwise reduction of a tetraaryl[3]cumulene. *Angewandte Chemie*, 131:2045–2050, 2019.

[30] P. Pinter and D. Munz. Controlling möbius-type helicity and the excited-state properties of cumulenes with carbenes. *J. Phys. Chme. A*, 124:10100–10110, 2020.

[31] P. Pinter M. M. Hansmann D. Munz J. Messelberger, A. Grünwald. Carbene derived diradicaloids-building blocks for singlet fission? *Chemical Science*, 9:6107–6117, 2018.

[32] D. Munz M. M. Hansmann, M. Melaimi and G. Bertrand. Modular approach to kekulé diradicaloids derived from cyclic (alkyl)(amino)carbenes. *J.A.C.S.*, 140:2546–2554, 2018.

[33] J. Messelberger P. Haines R. Kaur M. M. Hansmann D. Munz T. Ullrich, P. Pinter and D. M. Guldi. Singlet fission in carbene-derived diradicaloids. *Angewandte Chemie*, 132:7980–7988, 2020.

[34] C. Kollmar. Electronic structure of diradical and dicarbene intermediates in short-chain polydiacetylene oligomers. *J. Chem. Phys.*, 98:7210–7228, 1993.

[35] G. Trinquier C. Lepetit F. Allouti M. E. Alikhani R. Chauvin C. Poidevin, J. P. Malrieu. Towards magnetic carbo-meric molecular materials. *Chem. Eur. J.*, 22:5295–5308, 2016.

[36] S. J. Goodner A. Grünwald and D. Munz. Isolating free carbenes, their mixed dimers and organic radicals. *J. Vis. Exp.*, 146, 2019.

[37] M. Tommasini A. Milani and G. Zerbi. Carbynes phonons: A tight binding force field. *J. Chem. Phys.*, 128(064501):1–7, 2008.

[38] D. Fazzi M. Del Zoppo W. A. Chalifoux M. J. Ferguson G. Zerbi A. Lucotti, M. Tommasini and R. R. Tykwinski. Evidence for solution-state nonlinearity of sp-carbon chains based on ir and raman spectroscopy: Violation of mutual exclusion. *J. Am. Chem. Soc.*, 131(12):4239–4244, 2009.

[39] F. Cataldo. Simple generation and detection of polyynes in an arc discharge between graphite electrodes submerged in various solvents. *Letters to the Editor / Carbon*, 41:2653 – 2689, 2003.

[40] R. B. Heimann Y. P. Kudryavtsev and S. E. Evsyukov. Carbynes: advances in the field of linear carbon chain compounds. *J. Mat. Sc.*, 31:5557–5571, 1996.

[41] B. Guseva G. Babaev Y. P. Kudryavtsev, S. E. Evsyukov and V. V. Khvostov. Carbyne - the third allotropic form of carbon. *Russ. Chem. Bull.*, 42(3):399–413, 1993.

[42] R. C. Livingston P. Siemsen and F. Diederich. Acetylenic coupling: A powerful tool in molecular construction. *Angew. Chem. Int. Ed.*, 39(3):2632–2657, 2000.

[43] S. Szafert and J. A. Gladysz. Carbon in one dimension: Structural analysis of the higher conjugated polyynes. *Chem. Rev.*, 103(11):4175-4205, 2003.

[44] M. Jevric and M. B. Nielsen. Synthetic strategies for oligoynes. *Asian J. Org. Chem.*, 4(4):286–295, 2003.

[45] S. Hayashi H. Tabata, M. Fujii. Laser ablation of diamond particles suspended in ethanol: Effective formation of long polyynes. *Carbon*, 44(3):522–529, 2006.

[46] V. Cadierno and J. Gimeno. Allenylidene and higher cumulenylidene complexes. *Chem. Rev.*, 109(8):3512–3560, 2009.

[47] A.L. Ivanovskii. Graphynes and graphdyines. *Progress in Solid State Chemistry*, 41(1):1 – 19, 2013.

[48] D. Wang X. Gao, H. Liu and J. Zhang. Graphdiyne: synthesis, properties, and applications. *Chem Soc Rev*, 48:908–936, 2019.

[49] J. Bjork S. Klyatskaya M. Ruben F. Klappenberger, Y. Zhang and J. V. Barth. On-surface synthesis of carbon-based scaffolds and nanomaterials using terminal alkynes. *Acc. Chem. Res.*, 48(7):2140–2150, 2015.

[50] H. Ma C. Yuan Q. Sun, L. Cai and W. Xu. Dehalogenative homocoupling of terminal alkynyl bromides on au(111): Incorporation of acetylenic scaffolding into surface nanostructures. *ACS Nano*, 10(7):7023–7030, 2016.

[51] F. Diederich and M. Kivala. All-carbon scaffolds by rational design. *Advanced Materials*, 22(7):803–812.

[52] M. Sonoda Y. Tobe K. Tahara, T. Yoshimura and R.V. Williams. Theoretical studies on graphyne substructures: geometry, aromaticity, and electronic properties of the multiply fused dehydrobenzo[12]annulenes. *The Journal of Organic Chemistry*, 72(4):1437–1442, 2007.

[53] A. L. Ivanovskii A. N. Enyashin. Graphene allotropes. *Phys. Status Solidi*, 248(8):1879–1883, 2011.

[54] H. Lee M. Park, Y. Kim. Design of 2d massless dirac fermion systems and quantum spin hall insulators based on sp-sp^2 carbon sheets. *npj Comput. Mater.*, 4(54):541-549, 2018.

[55] F. Vines D. Malko, C. Neiss and A. Gorling. Competition for graphene: Graphynes with direction-dependent dirac cones. *Phys. Rev. Lett.*, 108(8):086804 – 1–4, 2012.

[56] Q. Yan Q. Zheng H.Cui, X. Sheng and G.Su. Strain-induced dirac cone-like electronic structures and semiconductor- semimetal transition in graphdiyne. *Phys. Chem. Chem. Phys.*, 15(21):8179–8185, 2013.

[57] C. Zhong M. Matsumoto W. R. Dichtel S. Thomas, H. Li and J. L. Bredas. Electronic structure of two-dimensional π-conjugated covalent organic frameworks. *Chem. Mater.*, 31(9):3051–3065, 2019.

[58] E. Hamzehpoor O. MacLean M. Rajeswara Rao Y. Chen L. V. Besteiro D. Dettmann L. Ferrari F. Frezza P. M. Sheverdyaeva R. Liu A. K. Kundu P. Moras M. Ebrahimi M. C. Gallagher F. Rosei D. F. Perepichka G. Galeotti, F. De Marchi and G. Contini. Synthesis of mesoscale ordered two-dimensional π-conjugated polymers with semiconducting properties. *Nat. Mater.*, 19:874–880, 2020.

[59] H. Liu Y. Li, L. Xu and Y. Li. Graphdiyne and graphyne: from theoretical predictions to practical construction. *Chem. Soc. Rev.*, 43:2572–2586, 2014.

[60] D.L.Mafra M.S.C. Mazzoni L.M. Malard, M.H.D. Guimaraes and A. Jorio. Group-theory analysis of electrons and phonons in n-layer graphene systems. *Phys. Rev. B*, 79:125426, 2009.

[61] Z. Li R. Zhao L. Tong Z. Liu J. Zhang S. Zhang, J. Wang and Z. Liu. Raman spectra and corresponding strain effects in graphyne and graphdiyne. *The Journal of Physical Chemistry C*, 120(19):10605–10613, 2016.

[62] J. Campos-Delgado F. Lopez-Urias Y. I. Vega-Cantu F. J. Rodriguez-Macias A. L. Elias E. Munoz Sandoval A. G. Cano-Marquez J. C.Charlier H. Terrones M.Terrones, A. R. Botello-Mendez. Graphene and graphite nanoribbons: Morphology, properties, synthesis, defects and applications. *Nano Today*, 5(4):351–372, 2010.

[63] D. Wang Y. Li Z. Shuai M. Long, L. Tang. Electronic structure and carrier mobility in graphdiyne sheet and nanoribbons: Theoretical predictions. *ACS Nano*, 5(4):2593–2600, 2011.

[64] B.Q. Song S.X. Du L.D. Pan, L.Z. Zhang and H.-J. Gao. Graphyne- and graphdiyne-based nanoribbons: Density functional theory calculations of electronic structures. *Applied Physics Letters*, 98(17):173102, 2011.

[65] W. Qiao H. Bai, Y. Zhu and Y. Huang. Structures, stabilities and electronic properties of graphdiyne nanoribbons. *RSC Adv.*, 1:768–775, 2011.

[66] C. Sun and D.J. Searles. Lithium storage on graphdiyne predicted by dft calculations. *The Journal of Physical Chemistry C*, 116(50):26222–26226, 2012.

[67] M. Hankel Z. Zhu V. Rudolph Y. Jiao, A. Du and S.C. Smith. Graphdiyne: a versatile nanomaterial for electronics and hydrogen purification. *Chem. Commun.*, 47:11843–11845, 2011.

[68] J. E. Halpert X. Lai Y. Liu H. Cao R. Yu D. Wang S. Wang, L. Yi and Y. Li. A novel and highly effcient photocatalyst based on p25–graphdiyne nanocomposite: Incorporation of acetylenic scaffolding into surface nanostructures. *Small*, 8(2):265–271, 2012.

[69] B. Liu Q. Feng X. Li M.Huang Z. Liu J. Zhang C. Tung L. Wu J. Li, X. Gao. Graphdiyne: A metal-free material as hole transfer layer to fabricate quantum dot-sensitized photocathodes for hydrogen production. *J. Am. Chem. Soc.*, 138(12):3954–3957, 2016.

[70] S. Lin and M.J. Buehler. Mechanics and molecular filtration performance of graphyne nanoweb membranes for selective water purification. *Nanoscale*, 5:11801–11807, 2013.

[71] A. Szabo and N.S. Ostlund. *Modern Qantum Chemistry: introduction to Advanced Electronic Structure Theory*. Dover Pubns, 1996.

[72] J.K. Labanowski. Simplified and biased introduction to density functional approches in chemistry, 1996.

[73] J. Kohanoff and N.I. Gidopoulos. *Density functional theory: basics, new trends and applications*. Wiley-Blackwell, 1 2003. Chapter Number: 26.

[74] R. G. Parr and Y. Weitao. *Density-Functional Theory of Atoms and Molecules*. Oxford University press, 1995.

[75] J.P. Perdew and S. Kurth. *Density functionals for non-relativistic Coulomb system*. Oxford University press, 2003.

[76] C. Adamo and V. Barone. Toward reliable density functional methods without adjustable parameters: The pbe0 model. *The Journal of Chemical Physics*, 110(13):6158–6170, 1999.

[77] Ira N. Levine. *Quantum Chemistry*. Pearson, 2013.

[78] F. Colonna J. Toulouse and A. Savin. Long-range–short-range separation of the electron-electron interaction in density-functional theory. *PHYSICAL REVIEW A*, 70(062505):1–16, 2004.

[79] T. Yanai H. Iikura, T. Tsuneda and K. Hirao. A long-range correction scheme for generalized-gradient-approximation exchange functionals. *J. Chem. Phys.*, 115(8):3540–3544, 2001.

[80] J. C. Sancho-García E. Bremond, Á. J. Perez-Jimenez and C. Adamo. Range-separated hybrid density functionals made simple. *J. Chem. Phys.*, 150(201102):1–6, 2019.

[81] W.J. Hehre; J. A. Pople R. Ditchfield. Self-Consistent Molecular-Orbital Methods. IX. An Extended Gaussian-Type Basis for Molecular-Orbital Studies of Organic Molecules. *J. Chem. Phys.*, 54(2):724–728, 1971.

[82] T. H. Dunning. Gaussian basis sets for use in correlated molecular calculations. I. The atoms boron through neon and hydrogen. *J. Chem. Phys.*, 90(2):1007–1023, 1989.

[83] S. Grimme and A. Hansen. A Practicable Real-Space Measure and Visualization of Static Electron-Correlation Effects. *Angew. Chem. Int. Ed.*, 54:12308 –12313, 2015.

[84] D. Fazzi M. Tommasini-C. Castiglioni W.A. Chalifoux N. R. Agarwal, A. Lucotti and R. R. Tykwinski. Structure and chain polarization of long polyynes investigated with infrared and raman spectroscopy. *Journal of Raman Spectroscopy*, 44(10):1398–1410.

[85] H. B. Schlegel-G. E. Scuseria M. A. Robb J. R. Cheeseman G. Scalmani V. Barone G. A. Petersson H. Nakatsuji X. Li M. Caricato A. Marenich J. Bloino B. G. Janesko R. Gomperts B. Mennucci H. P. Hratchian J. V. Ortiz A. F. Izmaylov J. L. Sonnenberg D. Williams-Young F. Ding F. Lipparini F. Egidi J. Goings B. Peng A. Petrone T. Henderson D. Ranasinghe V. G. Zakrzewski J. Gao N. Rega G. Zheng W. Liang M. Hada M. Ehara K. Toyota R. Fukuda J. Hasegawa M. Ishida T. Nakajima Y. Honda O. Kitao H. Nakai T. Vreven K. Throssell J. A. Montgomery Jr. J. E. Peralta F. Ogliaro M. Bearpark J. J. Heyd E. Brothers K. N. Kudin V. N. Staroverov T. Keith R. Kobayashi J. Normand K. Raghavachari A. Rendell J. C. Burant S. S. Iyengar J. Tomasi M. Cossi J. M. Millam M. Klene C. Adamo R. Cammi J. W. Ochterski R. L. Martin K. Morokuma O. Farkas J. B. Foresman M. J. Frisch, G. W. Trucks and D. J. Fox. Gaussian 09. http://gaussian.com/, 2009.

[86] A. Milani M. Del Zoppo-C. Castiglioni M. Tommasini, D. Fazzi and G. Zerbi. Intramolecular vibrational force fields for linear carbon chains through an adaptative linear scaling scheme. *J. Phys. Chem. A*, 111:11645–11651, 2007.

[87] M. Del Zoppo C. Castiglioni A. Milani, M. Tommasini and G. Zerbi. Carbon nanowires: phonon and π-electron confinement. *Phys. Rev. B*, 74:153418 1–4, 2006.

[88] http://cccbdb.nist.gov.

[89] A. Facibeni A. Milani P. Serafini G. Cerrato A. Lucotti M. Tommasini D. Fazzi C. Castiglioni V. Russo A. Li Bassi S. Peggiani, A. Senis and C. S. Casari. Size-selected polyynes synthesised by submerged arc discharge in water. *Chemical Physics Letters*, 740(137054):1–7, 2020.

[90] R. A. Lotti A. Facibeni P. Serafini A. Milani V. Russo A. L. Bassi S. Peggiani, P. Marabotti and C. S. Casari. Solvent-dependent termination, size and stability in polyynes synthesized via laser ablation in liquids. *Physical Chemistry Chemical Physics*, 22(45):26312–26321, 2020.

[91] S. Ehrlich S. Grimme, J. Antony and H. Krieg. A consistent and accurate ab initio parametrization of density functional dispersion correction (dft-d) for the 94 elements h-pu. *The Journal of Chemical Physics*, 132(15):154104, 2010.

[92] N. Russo S. Chiodo and E. Sicilia. Lanl2dz basis sets recontracted in the framework of density functional theory. *The Journal of Chemical Physics*, 125(10):104107, 2006.

[93] D. Wendinger and R. R. Tykwinski. Odd [n]cumulenes (n = 3, 5, 7, 9): Synthesis, characterization, and reactivity. *Accounts of Chemical Research*, 50:1468–1479, 2017.

[94] K. Yamaguchi. The electronic structures of biradicals in the unrestricted hartree-fock approximation. *Chemical Physics Letters*, 33:330–335, 1975.

[95] J. Casado S. Canola and F. Negri. The double exciton state of conjugated chromophores with strong diradical character: Insights from tddft calculations. *Physical Chemistry Chemical Physics*, 20:24227–24238, 2018.

[96] A. S. Ichimura P. M. Lahti and J. A. Sanborn. Methodologies for computational studies of quininoidal diiminediyls: Biradical vs dinitrene behavior. *J. Phys. Chem. A*, 105:251–260, 2001.

[97] T. P. Ruoko K. Meerholz D. Fazzi, S. Fabiano and F. Negri. Polarons in π-conjugated ladder-type polymers: A broken symmetry density functional description. *Journal of Materials Chemistry C*, 7:12876–12885, 2019.

[98] M. Nakano and B. Champagne. Nonlinear optical properties in open-shell molecular systems. *WIREs Comput. Mol. Sci.*, 6:198–210, 2016.

[99] A. Dorigo K. Yamaguchi, F. Jensen and K. N. Houk. A spin correction procedure for unrestricted hartree-fock and moller-plesset wavefunctions for singlet diradicals and polyrdicals. *Chem. Phys. Lett.*, 149:537–542, 1988.

[100] Y. Dai S. Canola and F. Negri. The low lying double-exciton state of conjugated diradicals: Assessment of tdudft and spin-flip tddft predictions. *Computation*, 7:1–13, 2019.

[101] N. Hansen; S. Rimme; J. Dedicatedtoprofessor C. A. Bauer and G. Erker. The fractional occupation number weighted density as a versatile analysis tool for molecules with a complicated electronic structure. *Chem. Eur. J.*, 23:6150–6164, 2017.

[102] A. Hansen J. G. Brandenburg, C. Bannwarth and S. Grimme. B97-3c: A revised low-cost variant of the b97-d density functional method. *Journal of Chemical Physics*, 148:064104, 1–13, 2018.

[103] S. Evangelisti T. Leininger C. Angeli, R. Cimiraglia and J. P. Malrieu. Introduction of n-electron valence states for multireference perturbation theory. *Journal of Chemical Physics*, 114:10252, 2018.

[104] F. Neese. Software update: The orca program system, version 4.0. *WIREs Comput Mol Sci*, 8:1327, 2018.

[105] M. Nakano and B. Champagne. Theoretical design of open-shell singlet molecular systems for nonlinear optics. *J. Phys. Chem. Lett.*, 6:3236–3256, 2015.

[106] F. Negri C. Bertarelli C. Castiglioni D.Fazzi, E. V. Canesi. Biradicaloid character of thiophene-based heterophenoquinones: The role of electron–phonon coupling. *ChemPhysChem*, 11:3685–3695, 2010.

[107] D. Fazzi D. C. Castiglioni E. V. Canesi S. di Motta, F. Negri. Biradicaloid and polyenic character of quinoidal revealed by the presence of a-lying double-exciton state. *J. Phys. Chem. Lett.*, 1:3334–3339, 2010.

[108] F. Neese. Definition of corresponding orbitals and the diradical character in broken symmetry dft calculations on spin coupled systems. *Journal of Physics and Chemistry of Solids*, 65:781–785, 2004.

[109] Prediction of molecular properties and molecular spectroscopy with density functional theory: From fundamental theory to exchange-coupling. *Coordination Chemistry Reviews*, 253(5):526–563, 2009.

[110] L. Noodleman. Valence bond description of antiferromagnetic coupling in transition metal dimers. *The Journal of Chemical Physics*, 74(10):5737–5743, 1981.

[111] H. Fukui K. Yamaguchi and T. Fueno. Molecular orbital (mo) theory for magnetically interacting organic compounds. ab-initio mo calculations of the effective exchange integrals for cyclophane-type carbene dimers. *Chemistry Letters*, 15(4):625–628, 1986.

[112] C. J. Calzado C. de Graaf J. Paul Malrieu, R. Caballol and N. Guihe. Magnetic interactions in molecules and highly correlated materials: Physical content, analytical derivation, and rigorous extraction of magnetic hamiltonians. *Chem. Rev.*, 114(1):429–492, 2014.

[113] A. Heil C. M. Marian and M. Kleinschmidt. The dft/mrci method. *WIREs Computational Molecular Science*, 9(2):e1394, 2018.

[114] M. Tommasini C. E. Bottani C. S.Casari P. Serafini, A. Milani. Topology-dependent conjugation effects in graphdiyne molecular fragments. *Carbon*, 180:265–273, 2021.

[115] Patrick Serafini, Alberto Milani, Matteo Tommasini, Chiara Castiglioni, and Carlo S. Casari. Raman and ir spectra of graphdiyne nanoribbons. *Phys. Rev. Materials*, 4:014001, 2020.

[116] R. Orlando C. M. Zicovich-Wilson B. Civalleri L. Maschio M. Rerat S. Casassa J. Baima S. Salustro B. Kirtman. R. Dovesi, A. Erba. 8(4), 2018.

[117] T.M. Krygowski. Crystallographic studies of inter- and intramolecular interactions reflected in aromatic character of x-electron systems. *J. Chem. Inf. Comput. Sci.*, 33:70–78, 1993.

[118] V. Russo M. Tommasini F. Cataldo A. Li Bassi A. Milani, A. Lucotti and C.S. Casari. Charge transfer and vibrational structure of sp-hybridized carbon atomic wires probed by surface enhanced raman spectroscopy. *J. Phys. Chem. C*, 115:12836–12843, 2011.

[119] J.M. Chalmers P.R. Griffiths G. Zerbi, in: N.J. Everall. *Vibrational Spectroscopy of Polymers: Principles and Practice*. Wiley, 2007.

[120] M. Tommasini C. Castiglioni and G. Zerbi. Raman spectroscopy of polyconjugated molecules and materials: confinement effect in one and two dimensions. *Phil. Trans. Roy. Soc. Lond.*, 362:2425–2459, 2004.

[121] L. Maschio M. Sgroi M. Lorenz, B. Civalleri and D. Pullini. Benchmarking dispersion and geometrical counterpoise corrections for cost-effective large-scale dft calculations of water adsorption on graphene. *Journal of Computational Chemistry*, 35(24):1789–1800.

[122] M. Alfe A. Ciajolo M. Tommasini, A. Lucotti and G. Zerbi. Fingerprints of polycyclic aromatic hydrocarbons (pahs) in infrared absorption spectroscopy. *Spectrochim. Acta A*, 152:134–148, 2016.

[123] T. Renouard L. Gherghel C. Mathis K. Mullen A. Centrone, L. Brambilla and G. Zerbi. Structure of new carbonaceous materials: The role of vibrational spectroscopy. *Carbon*, 43:1593–1609, 2005.

[124] G. E. Scuseria J. Heyd, J. E. Peralta and R. L. Martin. Energy band gaps and lattice parameters evaluated with the heyd-scuseria-ernzerhof screened hybrid functional. *J. Chem. Phys.*, 123:174101, 2005.

[125] D. M. Proserpio P. Serafini, A. Milani and C. S. Casari. Designing all graphdiyne materials as graphene derivatives: Topologically driven modulation of electronic properties. *J. Phys Chem. C*, 125:18456-18466, 2021.

[126] H. Horn A. Schäfer and R. Ahlrichs. Fully optimized contracted gaussian basis sets for atoms li to kr. *J. Chem. Phys.*, 97:2571-2577, 1992.

[127] B. Civalleri G. Beata, G. Perego. Crysplot: A new tool to visualize physical and chemical properties of molecules, polymers, surfaces, and crystalline solids. *J. Chem. Comp.*, 40:2329–2338, 2019.

[128] H. Zhang X. Wang Y. Xi Z. Wang H. Bu, M. Zhao. Isoelectronic doping of graphdiyne with boron and nitrogen: Stable configurations and band gap modification. *J. Phys. Chem. A*, 116(15):3934-3939, 2012.

[129] F. Vines S. Kamalinahad and P. Gamallo. Grazynes: Carbon-based two-dimensional composites with anisotropic properties. *J. Phys. Chem. C*, 123(44):27140-27149, 2019.

[130] T. E. Belenkova E. A. Belenkov, V. v. Mavrinskii and V. M. Chernov. Structural modifications of graphyne layers consisting of carbon atoms in the sp- and sp^2-hybridized states. *J. Exp. Theor. Phys.*, 120(44):820-830, 2015.

[131] H. Eckhardt R. H. Baughman and M. Kertesz. Structure-property predictions for new planar forms of carbon: Layered phases containing sp^2 and sp atoms. *J. Chem. Phys.*, 87(11):6687–6699, 1987.